



HAL
open science

simulation des propriétés optiques non-linéaires du second ordre de systèmes organiques : de la molécule isolée aux nanoparticules

Laurie Lescos

► To cite this version:

Laurie Lescos. simulation des propriétés optiques non-linéaires du second ordre de systèmes organiques : de la molécule isolée aux nanoparticules. Chimie organique. Université de Bordeaux, 2021. Français. NNT : 2021BORD0245 . tel-03543963

HAL Id: tel-03543963

<https://theses.hal.science/tel-03543963>

Submitted on 26 Jan 2022

HAL is a multi-disciplinary open access archive for the deposit and dissemination of scientific research documents, whether they are published or not. The documents may come from teaching and research institutions in France or abroad, or from public or private research centers.

L'archive ouverte pluridisciplinaire **HAL**, est destinée au dépôt et à la diffusion de documents scientifiques de niveau recherche, publiés ou non, émanant des établissements d'enseignement et de recherche français ou étrangers, des laboratoires publics ou privés.

THÈSE

présentée pour obtenir le Grade de

DOCTEUR

DE L'UNIVERSITÉ DE BORDEAUX
ÉCOLE DOCTORALE DES SCIENCES CHIMIQUES
SPÉCIALITÉ: CHIMIE PHYSIQUE

par

Laurie LESCOS

**SIMULATION DES PROPRIÉTÉS OPTIQUES
NON-LINÉAIRES DU SECOND ORDRE DE
SYSTÈMES ORGANIQUES: DE LA MOLÉCULE
ISOLÉE AUX NANOPARTICULES**

Directeur de thèse : Prof. Frédéric CASTET

Soutenue le : 25 Octobre 2021

Devant la commission d'examen formée de :

Prof. Vincent RODRIGUEZ	Université de Bordeaux	Président
Prof. Josep Maria LUIS	Université de Gérone	Rapporteur
Prof. Patrick TROUILLAS	Université de Limoges	Rapporteur
Prof. Benoît CHAMPAGNE	Université de Namur	Examineur
Prof. Luca MUCCIOLI	Université de Bologne	Examineur

THESIS

submitted to the

UNIVERSITY OF BORDEAUX

DOCTORAL SCHOOL OF CHEMICAL SCIENCES

by

Laurie LESCOS

in fulfillment for the Degree of

DOCTOR OF PHILOSOPHY

in CHEMICAL PHYSICS

**SIMULATION OF SECOND-ORDER NONLINEAR
OPTICAL PROPERTIES OF ORGANIC SYSTEMS:
FROM THE ISOLATED MOLECULE TO
NANOPARTICLES**

Thesis Director : Prof. Frédéric CASTET

Defense date : 25 October 2021

Review committee members :

Prof. Vincent RODRIGUEZ	University of Bordeaux	President
Prof. Josep Maria LUIS	University of Girona	Reviewer
Prof. Patrick TROUILLAS	University of Limoges	Reviewer
Prof. Benoît CHAMPAGNE	University of Namur	Examiner
Prof. Luca MUCCIOLI	University of Bologna	Examiner

Remerciements

Mes premiers remerciements vont évidemment à toi Fred, le meilleur directeur de thèse dont on puisse rêver. Merci pour ta patience, ton écoute et ta pédagogie. Tu as su me pousser hors de ma zone de confort avec beaucoup de bienveillance. Merci également pour ta disponibilité et ton soutien sans faille.

Je souhaite également remercier les membres de mon jury de thèse, les professeurs Vincent RODRIGUEZ, Josep Maria LUIS, Patrick TROUILLAS, Benoît CHAMPAGNE et Luca MUCCIOLI, pour avoir accepté d'être membre du jury le jour de ma soutenance afin d'évaluer mon travail.

Mes remerciements s'adressent également aux membres du groupe THEO pour la bonne ambiance qui y règne. Je me rappellerai des raclettes, couscous et autres repas de groupe. Je tiens en particulier à remercier Pascal, Raph et Philippe, tant pour leur sympathie et leur bonne humeur que pour l'aide qu'ils ont pu me procurer au cours de ces trois années. Merci aux doctorants qui ont égayé mes années de thèse : Cesar, Miguel, Diana, Alejandro, Alberto et Ridel.

Je tiens à remercier Luca pour le stage de Master que j'ai effectué avec lui à Bologne, qui m'a donné goût à la chimie théorique et qui m'a menée jusqu'à cette thèse. Je te suis aussi reconnaissante pour toute l'aide que tu m'as apportée. Je remercie chaleureusement Benoît pour m'avoir accueillie pendant deux mois à Namur et pour avoir continué à m'aider et à me conseiller par la suite. Merci à Pierre pour toute son aide et sa patience. Merci également à Emna, sans toi mon séjour n'aurait pas été aussi merveilleux. Merci pour ces bons moments, ces visites et surtout ces dégustations de gaufres.

Un immense merci à mes amies. Sophie, merci pour les pauses-café, les midis passés ensemble et ta gaieté. Merci à Anne-So L. pour les bons moments de rigolade et les apéros. Merci à Anne-So B. pour les bons moments passés ensemble et ton soutien infailible. Enfin, merci à Aurore pour toutes ces années d'amitié. Et surtout merci pour mon super EVJF!

Mes remerciements sont aussi destinés à ma famille. En particulier, un grand merci à mes futurs beaux-parents, Eric et Laurence, qui ont toujours été là pour moi et me bichonnent depuis bientôt 6 ans. Merci pour votre convivialité, vos valeurs et votre porte toujours ouverte. Merci à mon futur beau-frère Micka, et j'insiste sur « futur », pour les repas, les soirées, les entraînements à la salle et tous ces moments passés ensemble et auxquels j'ai survécu. Merci à Nath pour son grand cœur et à mon petit frère Maxence pour ses bonnes blagues. Un merci tout particulier à mes parents pour avoir fait de moi ce que je suis. Merci pour votre amour, votre fierté et votre soutien depuis toujours. Papa, merci de me connaître et de me comprendre comme tu le fais. Et merci pour ton humour de Lescos, qui ne fait sûrement rire que moi. Maman, merci de me soutenir et de me rassurer dans mes moments de doutes et de me dire les mots que j'ai besoin d'entendre. Et surtout merci pour les massages des pieds!

Mes derniers remerciements s'adressent à mon chéri, Jérémy. Merci de m'avoir toujours soutenue et encouragée pendant ma thèse, et de m'avoir mis un coup de pied aux fesses quand j'en ai eu besoin. Merci de m'aider chaque jour à devenir meilleure et à sortir de ma zone de confort. Je suis fière de la femme que je suis devenue à tes côtés. Merci pour les magnifiques voyages que nous avons fait ensemble, et ça ne fait que commencer. Merci de m'avoir donné le goût du sport. Merci d'essuyer mes larmes, merci de me faire rire, merci pour nos projets et merci pour ton amour. Je t'aime et j'ai hâte de devenir ta femme.

Résumé

La thèse a pour objectif l'implémentation d'approches computationnelles dédiées à l'étude des propriétés optiques non linéaires (ONL) du second ordre de molécules organiques π -conjuguées de type "push-pull" dans leurs états solvato et agrégé. Dans une première partie, la première hyperpolarisabilité de quatre séries de mérocyanines fortement dipolaires est calculée en utilisant la théorie de la fonctionnelle de la densité (DFT) avec différentes fonctionnelles d'échange-corrélation (FXCs). En particulier, les performances de FXCs hybrides appartenant à la famille "Minnesota 2006", ainsi que les FXCs à séparation de portée LC-BLYP, ω B97X-D et CAM-B3LYP, sont analysées par rapport à des valeurs de référence obtenues à partir de calculs Møller–Plesset du second ordre, et à des données expérimentales provenant de mesures de diffusion Hyper-Rayleigh (HRS). Cette étude se concentre principalement sur deux effets : l'influence du taux d'échange Hartree-Fock exact inclus dans la FXC sur l'intensité des réponses HRS statiques, et l'impact de l'optimisation du paramètre de séparation de portée dans les FXCs à séparation de portée, effectuée selon une procédure non-empirique et spécifique au système considéré. Les effets de dispersion en fréquence sont également étudiés, ainsi que leur rôle crucial dans la comparaison entre données théoriques et expérimentales. La deuxième partie de la thèse présente une étude de l'organisation structurale et les propriétés ONL du second ordre de nanoparticules organiques fluorescentes (FONs) formées de chromophores dipolaires π -conjugués. Des simulations de dynamique moléculaire sont couplées à des calculs DFT afin d'étudier le processus d'agrégation moléculaire, l'orientation moléculaire des chromophores dipolaires au sein des nanoparticules, ainsi que l'effet des fluctuations dynamiques sur leurs propriétés ONL. Ces calculs permettent de rationaliser la forte augmentation de la première hyperpolarisabilité induite par l'agrégation, et mettent en évidence l'impact des effets de polarisation mutuelle et des couplages intermoléculaires sur les réponses ONL.

Abstract

The present thesis aims to implement computational approaches dedicated to the investigation of the second-order nonlinear optical (NLO) properties of π -conjugated push-pull organic molecules in their solvated and aggregated states. In a first part, the performance of various density functional theory (DFT) exchange-correlation functionals (XCFs) to evaluate the first hyperpolarizability of four series of highly dipolar merocyanines is reported. In particular, the performance of the 2006 Minnesota family of hybrid XCFs, as well as the LC-BLYP, ω B97X-D and CAM-B3LYP long-range (LR) corrected XCFs, is discussed in regard to reference second-order Møller–Plesset calculations and experimental data obtained from Hyper-Rayleigh Scattering (HRS) measurements. This study focuses on two particular effects: the influence of the amount of exact Hartree-Fock exchange included in the XCF on the magnitude of the static HRS responses, as well as to the impact of tuning the range-separation parameter in LR-XCFs, according to a system-specific non-empirical procedure. Frequency dispersion effects are also investigated, as well as their crucial role in the comparison between theoretical and experimental data. In a second part, the structural organization and second-order NLO properties of fluorescent organic nanoparticles (FONs) based on dipolar chromophores incorporating a hydrophobic triphenylamine electron-donating unit and a slightly hydrophilic aldehyde electron-withdrawing unit at their extremities are studied. Molecular dynamics simulations are coupled with quantum chemical calculations in order to study the molecular aggregation process, the molecular orientation of the dipolar dyes within the nanoparticles and the dynamical behavior of their NLO properties. The strong enhancement of the first hyperpolarizability upon aggregation of the dyes is evidenced, as well as the high impact of mutual polarization effects and intermolecular couplings on the NLO responses.

Résumé en français

Le développement de composés organiques présentant de fortes réponses optiques non-linéaires (ONL) du second ordre a suscité de nombreux travaux de recherche au cours des trente dernières années, en raison de leur application potentielle dans les domaines de l'opto-électronique et de la (bio)imagerie. Les molécules organiques capables de générer des premières hyperpolarisabilités (β) importantes sont par exemple utilisées en tant qu'éléments actifs dans les systèmes à base de polymères pour la modulation électro-optique, ou comme sondes en imagerie par génération de seconde harmonique (SHG) de lipides et membranes cellulaires. Bien que les systèmes octupolaires peuvent également avoir de fortes réponses ONL quadratiques, les grandes valeurs de β sont plus souvent associées aux chromophores dipolaires de type "push-pull", possédant une structure de type D- π -A dans laquelle un groupe électro-donneur (D) interagit avec un groupe électro-attracteur (A) par l'intermédiaire d'un pont π -conjugué. Ces molécules présentent en général un transfert de charge important entre les sites donneur et accepteur, donnant lieu à une absorption intense dans le domaine du visible. En variant la nature des groupes D et A ou la longueur du pont conjugué, il est possible de moduler l'amplitude des réponses ONL.

Au delà de la conception de molécules capables de générer des réponses ONL importantes, de nombreuses applications requièrent le développement d'architectures plus complexes telles que des surfaces fonctionnalisées et des nanoparticules (NPs), qui permettent de concentrer spatialement un grand nombre de diffuseurs moléculaires. Maîtriser les propriétés de tels édifices supramoléculaires représente un défi important, tant sur le plan expérimental que de la simulation numérique. Cette thèse a pour objectif l'étude théorique des propriétés ONL du second ordre de différents systèmes organiques de type push-pull, depuis la molécule isolée jusqu'aux nanoparticules constituées de plusieurs centaines d'unités moléculaires. Dans une première partie, la première hyperpolarisabilité de chromophores individuels est déterminée à différents niveaux de calcul. En particulier, les performances de différentes fonctionnelles d'échange-corrélation (FXCs) utilisées dans la théorie de la fonctionnelle de la densité (DFT) sont analysées par rapport à des valeurs de référence obtenues à partir de calculs *ab initio* et à des données expérimentales provenant

de mesures de diffusion Hyper-Rayleigh (HRS). Dans une seconde partie, des nanoparticules organiques formées de chromophores dipolaires sont étudiées en combinant des simulations de dynamique moléculaire et des calculs DFT, afin de rationaliser le rôle des fluctuations dynamiques et des interactions intermoléculaires sur les réponses ONL. Ce chapitre rédigé en français constitue un résumé des principaux résultats obtenus lors de ces deux études. Les résultats détaillés sont présentés dans le corps du manuscrit, après une brève introduction des principes de l'optique non linéaire et des méthodes théoriques utilisées.

Performance des fonctionnelles DFT pour le calcul des premières hyperpolarisabilités de mérocyanines fortement dipolaires

Dans cette étude, nous avons évalué les performances de différentes fonctionnelles d'échange-corrélation pour le calcul des réponses ONL quadratiques de mérocyanines dipolaires récemment synthétisées dans le groupe de M. Blanchard-Desce (Université de Bordeaux). Ces dernières comportent des groupes accepteurs de type tricyanopropylidène connectés à des groupes donneurs de type dihexylaminophényle ou dihexylaminothiophényle par des chaînes polyéniques de différentes longueurs (Figure 1). Des mesures de diffusion Hyper-Rayleigh (HRS) ont démontré que ces molécules fortement dipolaires possèdent de grandes premières hyperpolarisabilités. En particulier, le dérivé **II'**[4], incluant des substituants terminaux dihexylaminothiophényle et tricyanopropylidène, présente une valeur record de première hyperpolarisabilité, ainsi qu'une alternance de longueur de liaison (*Bond length Alternation*, BLA) négligeable le long du pont conjugué, en apparence contradiction avec le paradigme associant les fortes réponses ONL quadratiques à une valeur optimale non nulle de BLA.

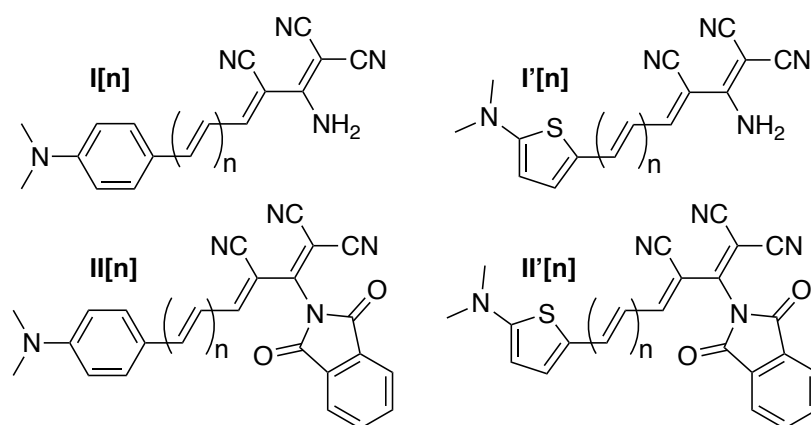


Figure 1 – Structures des mérocyanines de type tricyanopropylidène étudiées dans ce travail. La longueur de la chaîne polyénique varie de $n = 0$ à $n = 4$.

La description précise des premières hyperpolarisabilités (β) de tels chromophores, qui présentent un fort transfert de charge à l'état fondamental ainsi que des états excités de basse énergie, constitue un challenge pour la théorie de la fonctionnelle de la densité (DFT). Dans cette étude, nous avons évalué la précision de FXCs hybrides incorporant différents taux d'échange Hartree-Fock (XHF), ainsi que celle de FXCs hybrides à séparation de portée (SP), dont les domaines à courte et longue portées sont définis à l'aide d'un paramètre (ω). Suite à différentes études ayant démontré que l'optimisation de ω améliorerait la description des premières hyperpolarisabilités des composés à transfert de charge, nous avons comparé les hyperpolarisabilités calculées avec les valeurs standards de ω à celles calculées avec des valeurs de ω ajustées selon une procédure non-empirique et spécifique à la molécule considérée.

La performance des différentes fonctionnelles est évaluée en fonction de leur capacité à reproduire les données HRS expérimentales, ainsi que les valeurs de β calculées en utilisant la méthode Møller-Plesset à l'ordre 2 (MP2). Des études théoriques antérieures ont en effet montré que le niveau MP2 inclut la majeure partie des effets de corrélation électronique et reproduit correctement les premières hyperpolarisabilités de systèmes π -conjugués obtenues avec la méthode CCSD(T). Les valeurs β_{HRS}^{MP2} sont donc utilisées en tant que références théoriques par la suite. Par ailleurs, nous avons également mené des calculs au niveau CPHF (Coupled-Perturbed Hartree-Fock), afin d'évaluer l'ampleur des effets de corrélation électronique sur les valeurs de β . Dans la série de molécules étudiées, la corrélation électronique exalte la première hyperpolarisabilité d'un facteur compris entre 1.97 et 3.43. Le rapport $\beta_{HRS}^{MP2}/\beta_{HRS}^{CPHF}$ est dépendant du système, ce qui démontre la nécessité d'inclure les effets de corrélation électronique dans les calculs, car ces derniers introduisent une correction non systématique des valeurs de β_{HRS} qui pourrait affecter les interprétations qualitatives. Comme affiché Figure 2, les ratios $\beta_{HRS}^{MP2}/\beta_{HRS}^{CPHF}$ augmentent de manière progressive avec la taille n du pont polyénique jusqu'à une valeur maximale obtenue pour $n = 3$, et ensuite diminuent légèrement. Bien qu'elle suive la même tendance, la série **II'**[**n**] , qui contient la plus forte paire D/A, montre de plus fortes variations du rapport $\beta_{HRS}^{MP2}/\beta_{HRS}^{CPHF}$ en fonction de n .

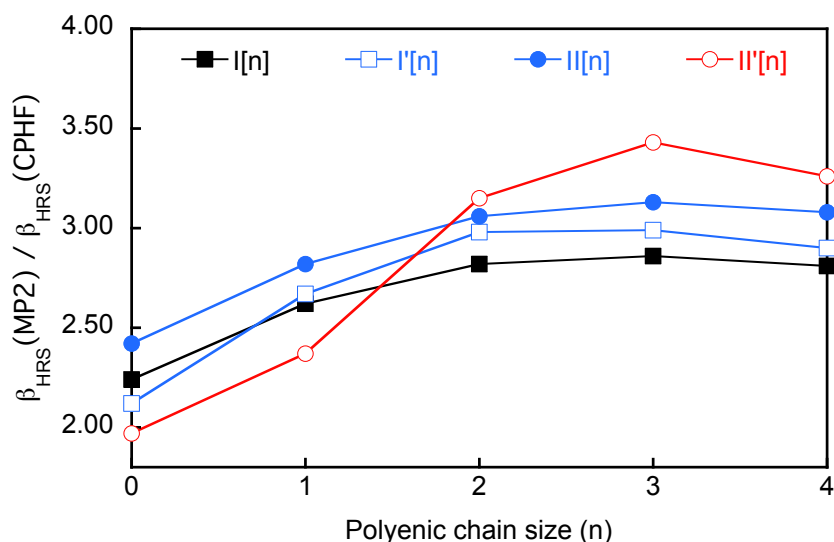


Figure 2 – Ratio $\beta_{HRS}^{MP2} / \beta_{HRS}^{CPHF}$ en fonction de la longueur de la chaîne dans les quatre séries de dérivés mérocyanines.

Les premières hyperpolarisabilités calculées avec les fonctionnelles hybrides de la famille Minnesota-2006, ainsi que les FXCs à SP, sont comparées aux résultats HF et MP2 *ab initio* et aux données expérimentales issues des mesures HRS. L'évolution des réponses β_{HRS} en fonction de la nature des substituants terminaux ou de la longueur du pont conjugué est rationalisée à partir de l'approximation à deux états, dont la fiabilité concernant les interprétations qualitatives a été démontrée.

Les hyperpolarisabilités statiques calculées avec les FXCs à SP se situent globalement entre les valeurs calculées au niveau couplé perturbé Hartree-Fock (CPHF) et celles calculées au niveau MP2 (Figure 3). Le plus souvent, les valeurs de β_{HRS} calculées aux niveaux LC-BLYP et ω B97X-D avec des paramètres de SP optimisés sont plus proches des résultats MP2 que celles obtenues avec les valeurs standards de ω , bien que cette amélioration ne soit pas systématique et dépende du système. Contrairement à ce qui a été montré avec LC-BLYP et ω B97X-D, l'optimisation du paramètre de SP dans CAM-B3LYP se traduit par une augmentation des valeurs de ω , et donc du taux d'échange HF dans la fonctionnelle, ce qui diminue légèrement l'accord avec les résultats MP2.

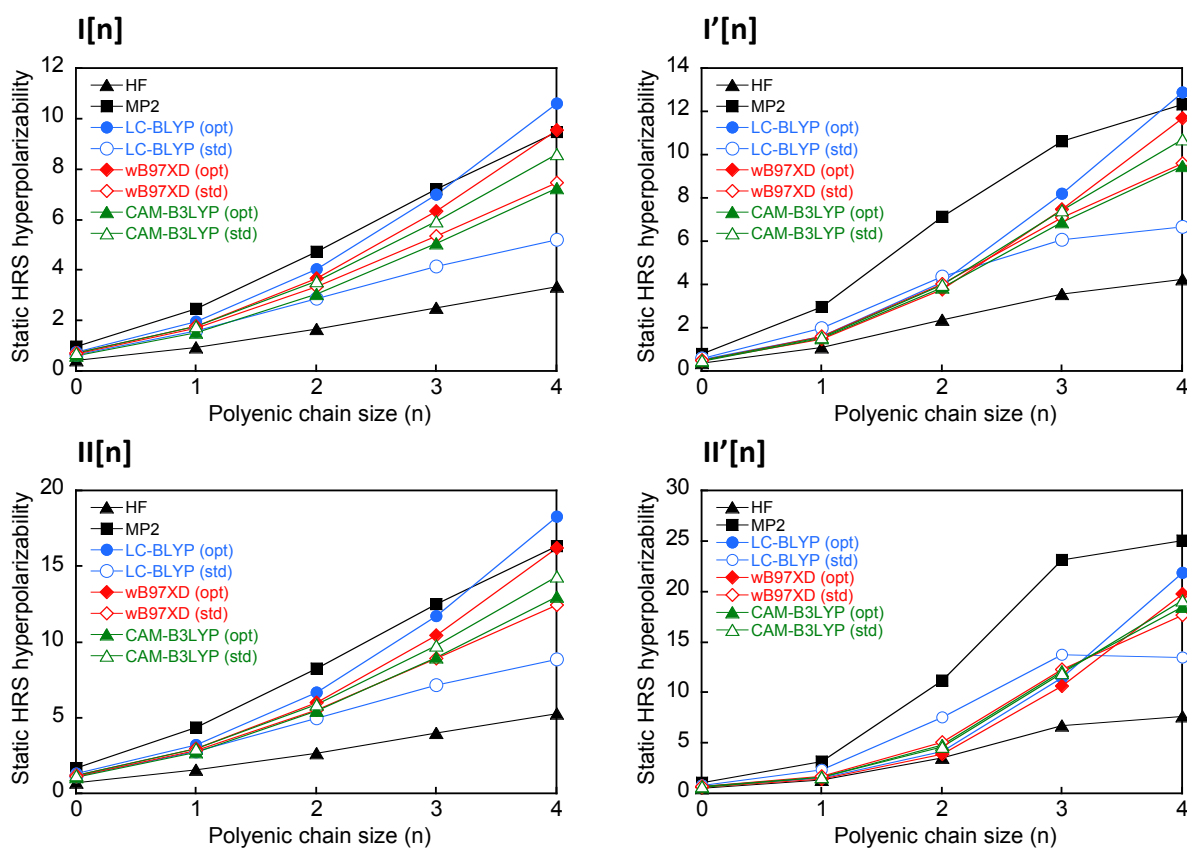


Figure 3 – Evolution des hyperpolarisabilités HRS statiques (en 10^4 u.a.) avec la longueur de la chaîne polyénique dans les quatre séries de mérocyanines, calculées dans le chloroforme aux niveaux HF et MP2, combinés avec la base 6-311+G(d), ainsi qu’au niveau DFT en utilisant des FXCs à séparation de portée avec des paramètres de SP standards (std) et optimisés (opt).

Les calculs effectués avec les fonctionnelles de la famille Minnesota montrent que le pourcentage d’échange HF dans la FXC impacte fortement l’ampleur des réponses β_{HRS} . M06-2X présente des valeurs de β_{HRS} proches de celles obtenues avec les FXC à SP optimisées, ce qui indique qu’un pourcentage proche de 50% d’échange HF constitue le meilleur compromis pour calculer les propriétés ONL de ces chromophores "push-pull" conjugués fortement dipolaires (Figure 4).

De manière générale, ces calculs illustrent également la difficulté de comparaison entre les premières hyperpolarisabilités dynamiques calculées et les données expérimentales mesurées dans des conditions de résonance. Aucune des FXCs de DFT considérées dans cette étude ne reproduit de façon satisfaisante l’intensification des réponses β_{HRS} à la fréquence de résonance, ce qui entrave toute comparaison quantitative de leur évolution relative en fonction de la longueur de la chaîne. L’utilisation d’un modèle à deux états atténué pour extrapoler les hyperpolarisabilités statiques expérimentales ne permet pas d’améliorer l’accord entre les réponses théoriques et expérimentales de cette série de composés hautement dipolaires.

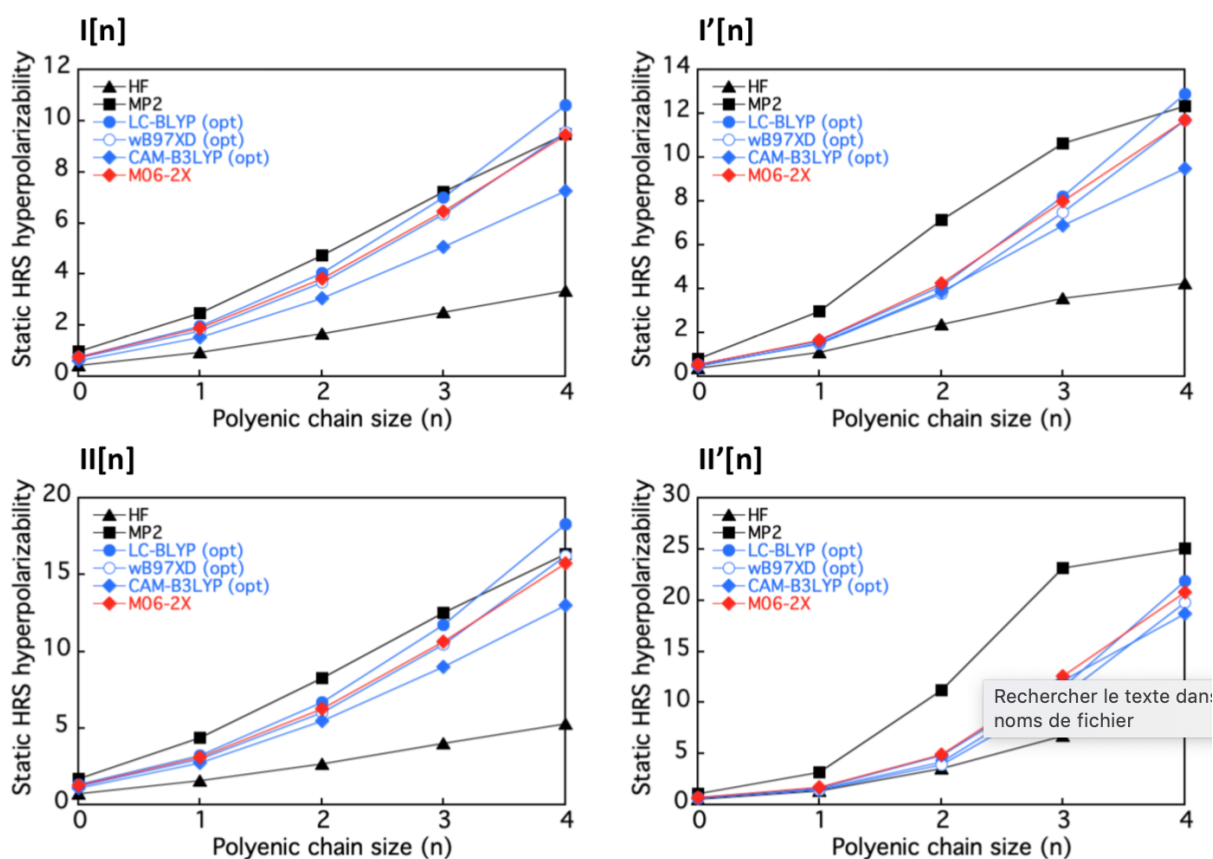


Figure 4 – Evolution des hyperpolarisabilités HRS statiques (en 10^4 u.a.) avec la longueur de la chaîne polyénique dans les quatre séries de mérocyanines, calculées dans le chloroforme en utilisant des FXCs corrigées à longue portée avec des paramètres de SP optimisés et la base 6-311+G(d). Les résultats obtenus aux niveaux HF, MP2 et M06-2X sont également reportés pour comparaison.

Agrégation, structure et propriétés optiques non linéaires de nanoparticules organiques dans l'eau

La deuxième partie de la thèse présente l'étude de nanoparticules organiques formées de chromophores de type "push-pull" incluant un fort groupe électro-attracteur. En changeant la nature de ce groupe électro-accepteur (parmi lesquels l'aldéhyde, légèrement hydrophile, comme illustré Figure 5) et celle des systèmes π -conjugués, des nanoparticules (NP) possédant une émission ajustable (du vert au proche infrarouge) et une bonne stabilité colloïdale dans l'eau ont été synthétisées dans le groupe de M. Blanchard-Desce. L'analyse des spectres d'émission de fluorescence et des durées de vie de ces NPs a suggéré la possibilité d'une orientation locale spécifique des chromophores au voisinage de la surface des NPs. Cette hypothèse a été confirmée par des mesures de seconde harmonique de NPs formées à partir de la molécule dipolaire schématisée Figure 5. Ces mesures ont montré que, contrairement à ceux des molécules constitutives, les signaux de diffusion de seconde harmonique (SHS) des NP proviennent exclusivement de la partie dipolaire de l'hyperpolarisabilité, avec une contribution négligeable de la partie octupolaire. Ces

résultats ont été attribués à la présence d'arrangements polaires de type H des molécules à l'interface avec l'eau, avec le groupe terminal hydrophobe triphénylamine pointant vers le centre de la NP et le groupe formyle pointant vers l'eau.

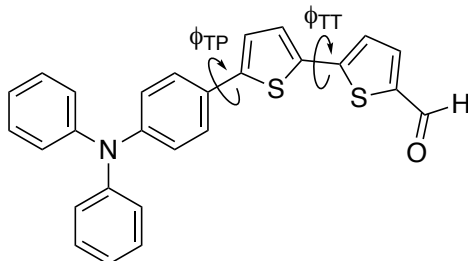


Figure 5 – Structure chimique de la molécule dipolaire étudiée dans cette thèse, avec les angles dièdres $\phi_{TT} = \text{S-C-C-S}$ et $\phi_{TP} = \text{C-C-C-S}$.

L'objectif de cette étude théorique est de compléter ces investigations expérimentales en corroborant ou non leurs conclusions. Des simulations de dynamique moléculaire (MD) de la formation des NPs dans l'eau pure sont associées à des calculs quantiques (QM) basés sur la DFT, afin d'offrir un aperçu du processus de formation des nanoparticules, de l'orientation des molécules dipolaires au sein des agrégats et de leurs propriétés ONL. Les réponses ONL de NPs composés d'une centaine de chromophores sont évaluées en utilisant une implémentation simplifiée de la méthode DFT dépendante du temps (sTD-DFT-vTB). Cette approche permet une réduction drastique des ressources calculatoires et le calcul des réponses optiques de structures composées de plusieurs milliers d'atomes.

Les simulations de dynamique moléculaire confirment la formation spontanée de NPs amorphes à base de molécules dipolaires organiques en solution aqueuse, ainsi que l'apparition de domaines à l'interface avec l'eau dans lesquels les chromophores développent des interactions intermoléculaires de type π -stacking. Les NPs finales ont une forme ellipsoïdale plus ou moins allongée, dont la structure globale fluctue largement au cours de la dynamique. (Figure 6).

L'orientation des molécules dipolaires à l'intérieur d'une NP représentative est illustrée Figure 7. Les groupes triphénylamine hydrophobes des molécules pointent majoritairement vers le centre de la NP, alors que les groupes formyles (hydrophiles) pointent vers l'extérieur. Cette orientation préférentielle est également illustrée sur le graphique de la Figure 7, qui reporte la concentration des différents groupes atomiques en fonction de la distance avec le centre de la NP.

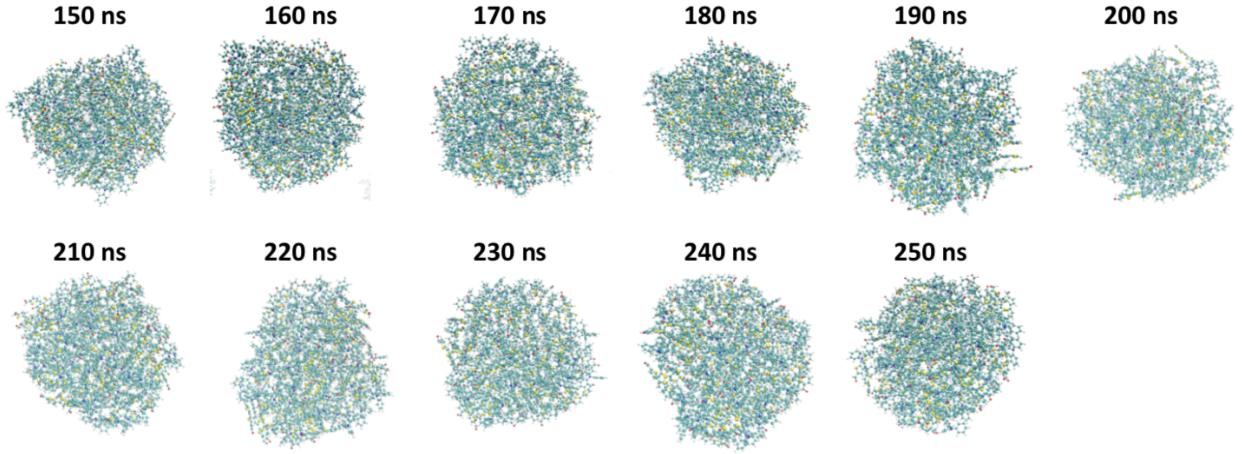


Figure 6 – Evolution temporelle de la nanoparticule 1 au cours de la simulation MD.

L'évolution de la densité moyenne de voisins $N(r_{ij})$ à l'intérieur des NPs en fonction de la distance r_{ij} entre les centres de masse des molécules (Figure 8) révèle que les premiers voisins d'une molécule sont situés en moyenne à une distance d'environ 6 Å. Il est à noter qu'après 50 Å, $N(r_{ij})$ tombe à zéro lorsque la distance excède la taille de l'agrégat, ce qui permet d'estimer la taille moyenne des NPs à environ 5 nm. L'évolution du cosinus moyen de l'angle θ_{ij} entre dipôles moléculaires, également illustré Figure 8, donne des informations complémentaires sur l'orientation des molécules à l'intérieur des NPs, avec des valeurs positives (négatives) correspondant à une orientation parallèle (antiparallèle). Comme indiqué Figure 8, la valeur moyenne $\langle \cos \theta_{ij} \rangle$ est positive à la distance correspondant aux premiers voisins, suggérant un arrangement parallèle à l'origine des moments dipolaires globalement non nuls des NPs. A de plus grandes distances, $\langle \cos \theta_{ij} \rangle$ est proche de zéro, indiquant que cette corrélation orientationnelle a disparu. L'ordre parallèle préférentiel à courte portée des molécules dipolaires est confirmé par la distribution des valeurs de $\langle \cos \theta_{ij} \rangle$ pour des molécules plus proches que 7.5 Å, qui montre un léger maximum pour $\langle \cos \theta_{ij} \rangle = 1$. Il est à noter que la distribution présente un deuxième maximum à $\langle \cos \theta_{ij} \rangle = -1$, montrant également la propension des chromophores à adopter une configuration antiparallèle.

La nature flexible des NPs permet des variations de forme importantes (Figure 6), qui se reflètent dans de larges fluctuations temporelles de leurs réponses ONL. Dans une première approche, nous avons évalué le tenseur de première hyperpolarisabilité des NPs évalué comme la somme des tenseurs des molécules individuelles constitutives calculés au niveau TD-DFT. Bien que cette approximation néglige les couplages électroniques intermoléculaires et les effets de polarisation, elle intègre les effets liés à l'organisation spatiale des molécules à l'intérieur des NPs, et à leurs fluctuations géométriques. Les premières hyperpolarisabilités statiques calculées pour 8 NPs (NP1-8) présentent une vaste gamme de valeurs, avec des écarts-types importants dans leurs distributions :

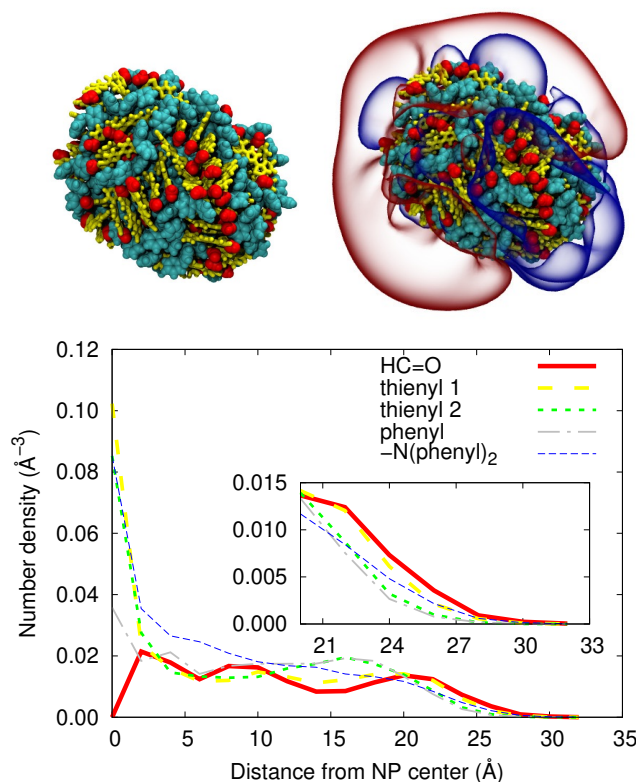


Figure 7 – En haut à gauche: Exemple de NP ellipsoïdale composée de 100 molécules agrégées illustrant l’orientation des groupes formyle (en rouge) vers l’extérieur, et les domaines d’empilements π (en jaune); En haut à droite: Potentiel électrostatique calculé à partir de la distribution des charges atomiques (les isovaleurs varient de -4 (bleu) à $+4$ (rouge) kT/e , avec $T = 300$ K); En bas: Densité radiale des différents fragments moléculaires en fonction de la distance depuis le centre de la NP (valeurs moyennées sur les 100 molécules des 8 NPs finales (NP1-NP8)).

$\langle \beta_{HRS} \rangle = (43.8 \pm 11.9)10^3$ u.a. Les valeurs des β_{HRS} dynamiques, incluant les effets de la dispersion en fréquence, sont environ trois fois plus élevées que les valeurs statiques ($\langle \beta_{HRS} \rangle = (189.1 \pm 70.5)10^3$ u.a.) avec une plus large distribution. L’impact de la dispersion en fréquence sur les rapports de dépolarisation (DR) est moins systématique, soit augmentant soit diminuant les valeurs des DR selon la NP considérée. Malgré ces fluctuations irrégulières, les DR statiques et dynamiques moyens sont très proches (4.5-4.6), indiquant que les réponses ONL de ces structures supramoléculaires présentent globalement un caractère 1D, typique des systèmes pour lesquels le tenseur d’hyperpolarisabilité est dominé par une seule composante diagonale. Les réponses ONL des NPs individuelles au sein d’une même simulation montrent également de fortes fluctuations temporelles, induites par les fluctuations géométriques au cours de la simulation de MD. L’évolution dans le temps des moyennes cumulatives des β_{HRS} et des DR est illustrée Figure 9 pour les NP1, 5, 7 et 8, en commençant à partir de l’instant où les 100 molécules s’agrègent en une seule structure. Pour la NP5, même si les valeurs individuelles varient fortement au cours du temps, les moyennes cumulatives convergent à $\langle \beta_{HRS} \rangle = 204$ u.a. et $\langle DR \rangle = 4.3$.

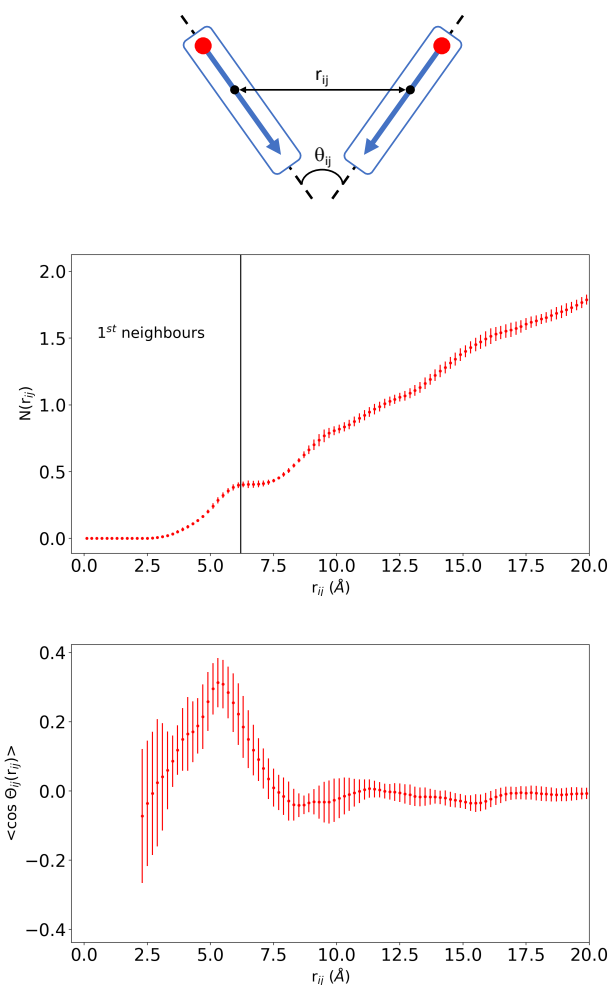


Figure 8 – Définition de l'angle θ_{ij} entre dipôles moléculaires et la distance r_{ij} entre leurs centres de masse (haut), et évolution de la densité moyenne de voisins $N(r_{ij})$ (milieu) et du cosinus moyen de θ_{ij} (bas) en fonction de r_{ij} .

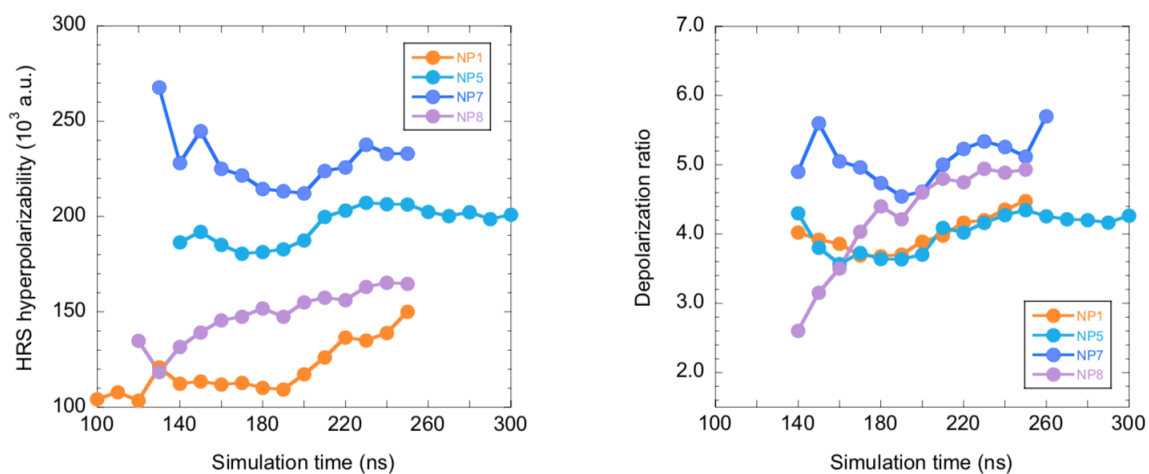


Figure 9 – Evolution temporelle des moyennes cumulatives du β_{HRS} (gauche) et du DR (droite) pour les NP1, 5, 7 et 8, calculés à partir de l'approximation du tenseur somme au niveau TD-DFT:M06-2X/6-311+G(d).

A l'exception de la NP7, les valeurs des β_{HRS} et des DR statiques évaluées à partir de l'approximation du tenseur somme au niveau sTD-DFT-vTB sont très proches de celles estimées en utilisant le niveau TD-DFT complet. Dans le cas des calculs dynamiques, la valeur moyenne du β_{HRS} obtenue avec sTD-DFT-vTB est 1.7 fois plus grande que celle obtenue en TD-DFT (Tableau 4.2), alors que le DR moyen augmente de 4.6 à 5.0. Comparer les données sTD-DFT-vTB évaluées à partir de l'approximation du tenseur somme avec celles issues des calculs sur la totalité de la structure supramoléculaire donne une mesure directe des effets des interactions intermoléculaires. Dans le cas statique, tenir compte des interactions intermoléculaires induit une baisse de 20% de l'hyperpolarisabilité HRS. Au contraire, en raison des effets de résonance, les valeurs des β_{HRS} dynamiques présentent des variations très grandes et non systématiques, allant d'une baisse de $\sim 80\%$ pour la NP7 à une augmentation de $\sim 900\%$ pour la NP1. En considérant les données moyennées sur les 8 NPs, les interactions intermoléculaires amplifient globalement la réponse β_{HRS} dynamique d'un facteur 3, alors que le DR est abaissé de 5.0 à 4.2. Nous soulignons cependant que les très fortes valeurs β_{HRS} calculées pour les NP1 et NP4, et donc la valeur moyenne de β_{HRS} , devraient être interprétées avec prudence, puisque les réponses divergent à la fréquence harmonique induisant ainsi des instabilités numériques.

Table 1 – Premières hyperpolarisabilités dynamiques ($\lambda = 1064$ nm, β_{HRS} en 10^3 u.a.) et rapports de dépolarisation (DR) des nanoparticules finales issues des 8 trajectoires de MD, évaluées en utilisant l'approximation du tenseur somme aux niveaux TD-DFT et sTD-DFT-vTB, ainsi que des calculs sTD-DFT-vTB réalisé sur les nanoparticules entières.

	TD-DFT ^a (tenseur somme)		sTD-DFT-vTB ^b (tenseur somme)		sTD-DFT-vTB ^b (calcul complet)	
	β_{HRS}	DR	β_{HRS}	DR	β_{HRS}	DR
NP1	317.0	6.3	325.8	5.8	3194.5	4.8
NP2	112.0	3.7	248.2	3.4	106.4	3.0
NP3	110.7	3.0	161.2	3.8	616.9	3.6
NP4	160.1	5.1	238.9	5.2	2259.4	5.1
NP5	237.6	5.9	343.1	7.2	369.9	4.7
NP6	185.0	3.6	238.7	4.5	212.7	4.9
NP7	234.0	3.4	827.6	5.0	156.6	2.1
NP8	156.4	5.5	167.9	5.3	634.3	5.0
av.± std. dev.	189.1 ± 70.5	4.6 ± 1.3	318.9 ± 215.4	5.0 ± 1.2	943.8 ± 1145.4	4.2 ± 1.1

^a M06-2X/6-311+G(d) en phase gas.

^b En utilisant $y_J = 4.0$, $y_K = 2.0$ et $E_{th} = 5.0$ eV.

La forte augmentation de la première hyperpolarisabilité mesurée au moment de l'agrégation des molécules est bien reproduite par l'implémentation de la méthode sTD-DFT-vTB, employée ici pour la première fois pour caractériser les propriétés ONL de NPs en tenant pleinement compte de leurs fluctuations dynamiques grâce à un schéma MD+QM séquentiel. Cette approche permet de mettre en évidence le fort impact des effets de polarisation mutuelle et des couplages intermoléculaires sur les réponses ONL. En particulier, les interactions intermoléculaires sont à l'origine de l'émergence d'états excités de faible énergie entrant en résonance avec le faisceau lumineux à la fréquence de seconde harmonique. Ces états sont responsables de la forte augmentation du signal SHS

lors de l'agrégation des molécules.

Cette thèse montre également la difficulté de comparer les réponses ONL calculées et expérimentales de telles assemblées supramoléculaires grandes et flexibles. Les limites de la méthodologie computationnelle sont principalement liées à l'échelle temporelle et à la taille des objets qui peuvent être étudiés, aux instabilités numériques dues aux effets de résonance, ainsi qu'à la probable sous-estimation de l'amplitude des champs électriques locaux puisque la première couche de solvatation n'est pas prise en compte. Par conséquent, ce travail ne constitue qu'une première étape vers la simulation rigoureuse des réponses ONL de grandes architectures moléculaires.

Contents

Introduction	1
1 General aspects of nonlinear optics	6
1.1 Origin of optical nonlinearities in dielectric media	6
1.1.1 At the microscopic level	6
1.1.2 At the macroscopic level	8
1.2 Common second-order NLO processes	9
1.3 Second Harmonic Generation	10
1.4 Importance of symmetry	11
1.4.1 Intrinsic symmetry of permutation	11
1.4.2 Kleinman's symmetry	12
1.4.3 Molecular symmetry	12
1.5 Experimental measurements of molecular second-order NLO responses . . .	13
1.5.1 Electric Field-Induced Second Harmonic Generation	13
1.5.2 Hyper-Rayleigh Scattering	15
1.6 Examples of organic molecules with large second-order NLO properties . .	22
1.6.1 π -conjugated donor-acceptor molecules	22
1.6.2 Octupolar molecules	25
2 Theoretical methods	33
2.1 Wavefunction methods	33
2.1.1 Schrödinger equation and wavefunction	33
2.1.2 Born-Oppenheimer approximation	35
2.1.3 Hartree-Fock method	35
2.1.4 Roothaan-Hall approximation	38
2.1.5 Electron correlation and post Hartree-Fock methods	39
2.1.6 Møller-Plesset Perturbation Theory	40
2.2 Density Functional Theory	42
2.2.1 Hohenberg-Kohn theorems	42
2.2.2 Kohn-Sham formalism	43

2.2.3	Exchange-correlation functionals	45
2.3	Calculation of the first hyperpolarizability	49
2.3.1	Coupled Perturbed Hartree-Fock (CPHF) and Coupled Perturbed Kohn-Sham (CPKS)	49
2.3.2	Time-Dependent Hartree-Fock (TDHF) and Time-Dependent DFT (TD-DFT)	54
2.3.3	Simplified Linear-Response TD-DFT	57
2.3.4	Finite-field method	58
2.3.5	Sum-over-states method and the two-state model	60
2.4	Basis sets	61
2.5	Solvent effects: the polarizable continuum model	64
2.6	Molecular dynamics simulations	66
3	Performance of DFT functionals for calculating the second-order NLO properties of dipolar merocyanines	77
3.1	Introduction	77
3.2	Levels of approximation	78
3.3	Optimal tuning of the range separation parameter	79
3.4	Experimental reference data	81
3.5	Molecular structures	82
3.6	Static first hyperpolarizabilities	83
3.6.1	Reference <i>ab initio</i> calculations	83
3.6.2	Two-state approximation	86
3.6.3	Effect of the amount of exact HF exchange	86
3.6.4	Optimal tuning of the range-separation parameter in RS-XCFs . . .	91
3.7	Frequency dispersion effects	93
3.8	Comparison to experiments	94
3.9	Conclusions	98
4	Self-assembling, structure and nonlinear optical properties of fluorescent organic nanoparticles in water	104
4.1	Introduction	104
4.2	Molecular dynamics simulations	105
4.3	Calculation of second-order NLO properties	106
4.4	Aggregation and structural properties	107
4.4.1	Aggregation energy of molecular pairs in water	107
4.4.2	Self-aggregation of the dyes in water	108
4.4.3	Structure of the nanoparticles	109
4.5	Nonlinear optical properties	115
4.5.1	NLO responses of solvated dyes	115
4.5.2	NLO responses of the nanoparticles	117

4.6	Absorption properties	119
4.7	Comparison to experiments and further discussion	120
4.8	Conclusions and perspectives	122
Conclusions and perspectives		129
Appendices		132
A Supporting information of Chapter 3		132
A.1	Molecular geometries	132
A.2	Optimal range separation parameters	133
A.3	Absorption optical properties	136
A.4	Static nonlinear optical properties	150
A.5	Dynamic nonlinear optical properties	163
A.6	Two-state approximation	179
B Supporting information of Chapter 4		193
B.1	Force field parameterization and MD simulations	193
B.1.1	Validation of the force field used for water	193
B.1.2	Torsional energy profiles of organic chromophores	195
B.1.3	MD simulations of organic chromophores in water	196
B.2	Determination of the optimal parameters of the sTD-DFT method	197
B.2.1	Test molecular and supramolecular geometries	197
B.2.2	Optimization of the sTD-DFT-xTB parameters	198
B.2.3	Optimization of the sTD-DFT-vTB parameters	203
B.3	Free energy of pairs of chromophores in water	209
B.4	Morphology of the nanoparticles	209
B.4.1	Global shape of the nanoparticles	209
B.4.2	Characterization of the shape of the nanoparticles	210
B.4.3	Time-evolution and statistical distributions of structural and elec- tronic properties	212
B.4.4	π -aggregation of the molecular units	213
B.5	NLO properties of the nanoparticles	214
B.5.1	NLO properties of the final nanoparticles of each MD run	214
B.5.2	Evolution in time of the NLO properties	216
B.6	Absorption properties of π -stacked dimers	219
B.6.1	Comparison between TD-DFT and sTD-DFT-vTB calculations	219
B.6.2	Diabatization of low-lying excited states	222
B.7	Assessment of M06-2X with respect to MP2	227

Introduction

The design of organic compounds that exhibit large quadratic second-order nonlinear optical (NLO) responses has fueled a number of research works over the past thirty years, owing to their broad field of applications ranging from smart materials (including optical telecommunications, data storage, information and signal processing) to biology (including in vivo bioimaging and therapy). In particular, organic compounds exhibiting large first hyperpolarizabilities (β) are used as active elements in electric field poled polymer-based systems for electro-optic modulation,^[1] or as probes for second-harmonic generation (SHG) imaging of lipids and cell membranes.^[2, 3, 4, 5] Although octupolar systems can also display large quadratic NLO responses,^[6, 7] high β values are most often associated to dipolar push-pull chromophores having a D- π -A architecture, in which an electron-donating group (D) interacts with an electron-withdrawing group (A) through a π -conjugated linker. These molecules usually display significant charge transfer between the D and A sites giving rise to intense absorption in the visible region. Varying the nature of the D and A groups or the length of the conjugated bridge by chemical design allows to modulate the magnitude of the second-order NLO responses.^[8, 9, 10, 11, 12]

Since they provide insights on the relationships linking the chemical structure of the chromophores to their optical properties, computational approaches are highly useful to design novel NLO materials, by providing rational guidelines for eventual syntheses. In particular, computational chemistry provides insights on various factors not individually accessible from experiments, including the impact of the nature of D and A groups, of the size of the π -conjugated linker, as well as of frequency-dispersion and solvent effects. The present thesis aims to implement computational approaches dedicated to the investigation of the NLO properties of different organic systems, ranging from solvated molecules to supramolecular aggregates composed of several hundreds of chromophores.

The first Chapter presents a detailed introduction to the nonlinear optical phenomena, from their mathematical description to examples of molecules possessing large second-order NLO responses. This Chapter also includes a brief description of the experimental tools allowing the determination of the NLO properties. Then, the basic concepts

of the computational methods employed in this work, including quantum chemistry and classical force-field methods, are reviewed in Chapter 2.

Chapter 3 presents an accurate investigation of the second-order NLO responses of a series of recently designed dipolar merocyanines. As detailed in this Chapter, the size of these systems prohibits using highly accurate *ab initio* methods such as coupled-cluster, so that density functional theory (DFT) remains the only alternative for investigating their NLO properties at a reasonable computational cost. However, the accurate description of such NLO chromophores, which exhibit large ground-state charge transfer as well as low-lying charge-transfer excited states, is highly challenging for DFT, and the various approximations introduced through the exchange-correlation functional (XCFs) have to be carefully assessed. In this Chapter, we report an extensive study of the performance of various XCFs for describing the first hyperpolarizabilities of these systems, including the 2006 Minnesota family of hybrids, as well as the LC-BLYP, ω B97X-D and CAM-B3LYP long-range (LR) corrected XCFs. Particular focus is given to the influence of the amount of exact Hartree-Fock exchange included in the XCF on the magnitude of the NLO responses, as well as to the impact of tuning the range-separation parameter in LR-XCFs, according to a system-specific nonempirical procedure. Additional issues encompass the interpretation of the first hyperpolarizabilities by resorting to the two-state approximation and the analysis of their frequency dispersion. This work was conducted in collaboration with the group of Dr. Eduard Matito (University of San Sebastian) and of Prof. Benoît Champagne (University of Namur), and was the object of an article published in 2020 [*Phys. Chem. Chem. Phys.* 2020, 22, 16579–16594].

Finally, Chapter 4 reports a comprehensive study of fluorescent organic nanoparticles (FONs). In recent years, molecular-based organic nanoparticles emerged as highly promising systems in the fields of optoelectronics and biology, because they offer alternatives to inorganic ones that suffer from toxicity and biodegradability issues. Although a large number of studies were dedicated to the design and characterization of new systems with targeted absorption, fluorescence or nonlinear optical (NLO) properties, the complete and rational development of the field remains limited by the difficulty to support and guide the experimental investigations by theoretical simulations. Indeed, owing to the large size and flexible nature of such supramolecular assemblies, theoretical calculations remain highly challenging and out of the reach of standard computational schemes. In this Chapter, we propose a new modelling strategy that enables a drastic reduction of the computational cost. By combining molecular dynamics simulations with a simplified Time-Dependent DFT method, we were able to rationalize the Second-Harmonic Scattering (SHS) responses of nanoparticles based on organic dipolar chromophores, following a recent experimental investigation reported by the groups of Prof. Vincent Rodriguez and Dr. Mireille Blanchard-Desce.^[13] This theoretical approach allowed us to describe the

spontaneous formation of amorphous nanoparticles in water solution, as well as the onset of polar π -stacked domains at the water interface. We also disentangled the influence of the supramolecular organization of the dyes and of the polarization effects on the NLO responses. In particular, we demonstrated that intermolecular interactions are at the origin of the emergence of low-lying excited states entering into resonance with the second harmonic light, which are responsible for the experimentally observed enhancement of the SHS signal upon aggregation and for the appearance of a red shifted tail in the linear absorption spectrum. This work was carried out in collaboration with Dr. Marc de Wergifosse (University of Bonn) and the groups of Prof. Benoît Champagne (University of Namur) and Prof. Luca Muccioli (University of Bologna), and was recently published [*Phys. Chem. Chem. Phys.* 2021, 23, 23643–23654].

Bibliography

- [1] Dalton L. R., Sullivan P. A., and Bale D. H. Electric Field Poled Organic Electro-optic Materials: State of the Art and Future Prospects. *Chem. Rev.*, 110:25, 2010.
- [2] Campagnola P. J., Wei M.D., and Loew L. M. High-Resolution Nonlinear Optical Imaging of Live Cells by Second Harmonic Generation. *Biophys. J.*, 77:3341, 1999.
- [3] Moreaux L., Sandre O., Charpak S., Blanchard-Desce M., and Mertz J. Coherent Scattering in Multi-Harmonic Light Microscopy. *Biophys. J.*, 80:1568, 2001.
- [4] Dombek D. A., Blanchard-Desce M., and Webb W. W. Optical Recording of Action Potentials with Second-Harmonic Generation Microscopy. *J. Neurosci.*, 24:999, 2004.
- [5] Reeve J. E., Anderson. H. L., and Clays K. Dyes for biological second harmonic generation imaging. *Phys. Chem. Chem. Phys.*, 12:13484, 2010.
- [6] Lee Y-K, Jeon S-J, and Cho M. Molecular Polarizability and First Hyperpolarizability of Octupolar Molecules: Donor-Substituted Triphenylmethane Dyes. *J. Am. Chem. Soc.*, 120:10921, 1998.
- [7] Castet F., Blanchard-Desce M., Adamietz F., Poronik Y. M., Gryko D. T., and Rodriguez V. Experimental and Theoretical Investigation of the First-Order Hyperpolarizability of Octupolar Merocyanine Dyes. *ChemPhysChem*, 15:2575, 2014.
- [8] Kanis D. R., Ratner M. A., and Marks T. J. Design and construction of molecular assemblies with large second-order optical nonlinearities. Quantum chemical aspects. *Chem. Rev.*, 94:195, 1994.
- [9] Marder S. R., Cheng L.-T., Tiemann B. G., Friedli A. C., Blanchard-Desce M., Perry J.W., and Skindhøj J. Large First Fyperpolarizabilities in Push-Pull Polyenes by Tuning of the Bond Length Alternation and Aromaticity. *Science*, 263:511, 1994.
- [10] Meyers F., Marder S. R., Pierce B. M., and Brédas J.-L. Electric Field Modulated Nonlinear Optical Properties of Donor-Acceptor Polyenes: Sum-Over-States Investigation of the Relationship between Molecular Polarizabilities (α , β , and γ .) and Bond Length Alternation. *J. Am. Chem. Soc.*, 116:10703, 1994.
- [11] Plaquet A., Champagne B., Kulhánek J., Bureš F., Bogdan E., Castet F., Ducasse L., and Rodriguez V. Effects of the Nature and Length of the π -Conjugated Bridge on the Second-Order Nonlinear Optical Responses of Push-Pull Molecules Including 4,5-Dicyanoimidazole and Their Protonated Forms. *ChemPhysChem*, 12:3245, 2011.
- [12] Klikar M., Le Poul P., Růžička A., Pytela O., Barsella A., Dorkenoo K. D., Robin-Le Guen F., Bureš F., and Achelle S. Dipolar NLO Chromophores Bearing Diazine Rings as π -Conjugated Linkers. *J. Org. Chem.*, 82:9435, 2017.

- [13] Daniel J., Bondu F., Adamietz F., Blanchard-Desce M., and Rodriguez V. Interfacial Organization in Dipolar Dye-Based Organic Nanoparticles Probed by Second-Harmonic Scattering. *ACS Photonics*, 2:1209, 2015.

General aspects of nonlinear optics

We present in this chapter the physical and mathematical descriptions of nonlinear optical (NLO) properties of molecules and materials. We focus in particular on the molecular second-order NLO responses characterized by the first hyperpolarizability, and give emphasis on the consequences of symmetry aspects on the mathematical description of this property. After a review of some common second-order NLO processes, we focus on the second harmonic generation. In the last part of the chapter, we present few representative examples of molecules possessing nonlinear optical properties. Rather than providing an exhaustive review of the existing classes of NLO molecules, we aim here at highlighting some key aspects of the relationship between the chemical structure and the strength of the second-order NLO responses.

1.1 Origin of optical nonlinearities in dielectric media

1.1.1 At the microscopic level

In this section, we describe the response of a molecule to an external oscillating (or dynamic) electric field. The electric field is vectorial and composed of a static component and a time-oscillating component according to:

$$F_z(t) = \sum_{\omega} F_z^{\omega} (e^{-i\omega t} + e^{+i\omega t}) \quad (1.1)$$

where F_z^{ω} are the Fourier amplitudes of the electric field along the molecular axis z . In the presence of such a field, all charged particles in the molecule, electrons as well as atomic nuclei, experience a force that perturbs their motions. In a classical picture, the charges are expected to follow the time-oscillations of the laser field, their oscillations giving rise to an induced dipole moment that can be expressed to first order in terms of the linear electric polarizability:

$$\mu_i = \mu_i^0 + \underbrace{\alpha_{ij} F_j}_{\text{Induced dipole moment}} \quad (1.2)$$

where μ_i^0 is the permanent electric dipole moment of the molecule in the Cartesian direction i , F_j the optical field applied in direction j and α_{ij} the corresponding component of the linear electric polarizability tensor:

$$\alpha = \begin{pmatrix} \alpha_{xx} & \alpha_{xy} & \alpha_{xz} \\ \alpha_{yx} & \alpha_{yy} & \alpha_{yz} \\ \alpha_{zx} & \alpha_{zy} & \alpha_{zz} \end{pmatrix} \quad (1.3)$$

When the intensity of the applied field is large, the induced dipole moment is not anymore linear with respect to the electric field strength and can be expressed as a Taylor series^[1]:

$$\mu_i = \mu_i^0 + \alpha_{ij} F_j + \frac{1}{2!} \beta_{ijk} F_j F_k + \frac{1}{3!} \gamma_{ijkl} F_j F_k F_l + \dots \quad (1.4)$$

where β_{ijk} and γ_{ijkl} are the second- and third-order nonlinear polarizabilities, also referred to as the first and second hyperpolarizabilities. Similarly to the linear response, the vectorial property of the electric field implies that the first- and second-order hyperpolarizabilities are third-rank and fourth-rank tensors, respectively. Thus, the β tensor contains 27 components and is generally expressed as a rectangular 9x3 matrix:

$$\beta = \begin{pmatrix} \beta_{xxx} & \beta_{xyy} & \beta_{xzz} & \beta_{xyz} & \beta_{xzy} & \beta_{xxz} & \beta_{xxz} & \beta_{xxy} & \beta_{xyx} \\ \beta_{yxx} & \beta_{yyy} & \beta_{yzz} & \beta_{yyz} & \beta_{yzy} & \beta_{yzx} & \beta_{yxz} & \beta_{yxy} & \beta_{yyx} \\ \beta_{zxx} & \beta_{zyy} & \beta_{zzz} & \beta_{zyz} & \beta_{zzy} & \beta_{zzx} & \beta_{zxx} & \beta_{zxy} & \beta_{zyx} \end{pmatrix} \quad (1.5)$$

where the β tensor components can be calculated as:

$$\beta_{ijk} = \left. \frac{\partial^2 \mu_i}{\partial F_j \partial F_k} \right|_{F=0} = - \left. \frac{\partial^3 E}{\partial F_i \partial F_j \partial F_k} \right|_{F=0} \quad (1.6)$$

Due to the fact that the response of the oscillating charges in the molecules depends on the frequency of the electric fields, the linear and nonlinear polarizabilities also depend on the frequency of the applied fields. Inserting the expression 1.1 into equation 1.4 yields:

$$\begin{aligned} \mu_i &= \mu_i^0 + \sum_{\omega} \alpha_{ij}(-\omega, \omega) F_j^{\omega} (e^{-i\omega t} + e^{+i\omega t}) \\ &+ \frac{1}{2!} \sum_{\omega_1, \omega_2} \beta_{ijk}(-\omega_{\sigma}; \omega_1, \omega_2) F_j^{\omega_1} F_k^{\omega_2} (e^{-i\omega_{\sigma} t} + e^{+i\omega_{\sigma} t}) \\ &+ \frac{1}{3!} \sum_{\omega_1, \omega_2, \omega_3} \gamma_{ijkl}(-\omega_{\sigma}; \omega_1, \omega_2, \omega_3) F_j^{\omega_1} F_k^{\omega_2} F_l^{\omega_3} (e^{-i\omega_{\sigma} t} + e^{+i\omega_{\sigma} t}) + \dots \end{aligned} \quad (1.7)$$

where the frequency-dependence of the (hyper)polarizabilities has been exemplified. In this expression, ω_1 , ω_2 and ω_3 are the frequencies of the incident fields respectively ap-

plied in the j , k and l directions, while $\omega_\sigma = \sum_i \omega_i$. Equation 1.7 provides the fundamental origin of nonlinearities at the microscopic level.

It is worth mentioning that the Taylor series expansion in equation 1.4 is sometimes replaced by a simple power series expansion. In this case, the numerical factors $\frac{1}{n!}$ are implicitly integrated in the hyperpolarizability tensor components.

$$\mu_i = \mu_i^0 + \alpha_{ij}F_j + \beta_{ijk}F_jF_k + \gamma_{ijkl}F_jF_kF_l + \dots \quad (1.8)$$

These different conventions (referred to as the T convention for the Taylor expansion and B convention for the power series expansion) have often been causes of confusion in the community when comparing the hyperpolarizability values obtained from different experimental or computational tools.^[2] All hyperpolarizability values reported in this thesis are given in atomic units (1 a.u. of $\beta = 3.6310^{-42} \text{ m}^4\text{V}^{-1} = 3.2063 \times 10^{-53} \text{ C}^3\text{m}^3\text{J}^{-2} = 8.641 \times 10^{-33} \text{ esu}$) in the T convention.

1.1.2 At the macroscopic level

The collective reorganization of the electron density of the molecules under the effect of the external electrical field is characterized, at the macroscopic level, by the polarization P of the material. When neglecting electric field gradient effects, the macroscopic polarization can be expanded as power series of the Maxwell fields F :^[3]

$$P = \chi^{(1)}F + \chi^{(2)}F^2 + \chi^{(3)}F^3 + \dots \quad (1.9)$$

where the expansion coefficients $\chi^{(1)}$, $\chi^{(2)}$ and $\chi^{(3)}$ are respectively the linear susceptibility and the second- and third-order nonlinear susceptibilities. As their microscopic analogues, the optical susceptibilities are expressed as second-, third- and fourth-rank tensors, respectively. For example, for the second-order susceptibility:

$$\chi^{(2)} = \begin{pmatrix} \chi_{xxx}^{(2)} & \chi_{xyy}^{(2)} & \chi_{xzz}^{(2)} & \chi_{xyz}^{(2)} & \chi_{xzy}^{(2)} & \chi_{xzx}^{(2)} & \chi_{xxz}^{(2)} & \chi_{xxy}^{(2)} & \chi_{xyx}^{(2)} \\ \chi_{yxx}^{(2)} & \chi_{yyy}^{(2)} & \chi_{yzz}^{(2)} & \chi_{yyz}^{(2)} & \chi_{yzy}^{(2)} & \chi_{yzx}^{(2)} & \chi_{yxz}^{(2)} & \chi_{yyx}^{(2)} & \chi_{yyx}^{(2)} \\ \chi_{zxx}^{(2)} & \chi_{zyy}^{(2)} & \chi_{zzz}^{(2)} & \chi_{zyz}^{(2)} & \chi_{zzy}^{(2)} & \chi_{zzx}^{(2)} & \chi_{zxz}^{(2)} & \chi_{zxy}^{(2)} & \chi_{zyx}^{(2)} \end{pmatrix} \quad (1.10)$$

It is important to note that, as macroscopic quantities, P and F correspond to averages of their microscopic counterparts over a region of the material that is large with respect to its building blocks, but small enough with respect to the wavelengths of the applied fields. In particular, although the same notation F is used for the field in equations 1.4, 1.8 and 1.9, the macroscopic Maxwell field is in general different from the local field that is really felt by the molecule within its environment. This constitutes one of the main difficulties in predicting the optical properties of a material from the properties of its microscopic constituents.

1.2 Common second-order NLO processes

Original property of photons in comparison of other elementary particles is that they do not interact directly with one another. Therefore, when transformations of photons into others are observed, it always occurs through interaction with another element, namely the electrons that constitute the matter and that are characterized by discrete energetic levels. So, the matter can absorb, emit or scatter photons, and by consequence give rise to optical displacements. The scattering processes must be distinguished from the absorption processes in the sense that they do not imply electronic transitions towards any stationary electronic excited states of the system. By analogy to classical absorption processes, optical scattering is often defined as the "absorption" and re-emission of one or more photons through a virtual excited state. Second-order NLO scattering processes involve various forms of 3-waves mixing, by frequency summation or difference. The mixing of two optical waves within a medium can give rise to a scattered one, with frequency:

$$\omega_\sigma = \omega_1 \pm \omega_2 \quad (1.11)$$

where ω_1 and ω_2 are the frequencies of the incident beams. The above summation is noted $(-\omega_\sigma; \omega_1, \omega_2)$, where the minus sign traduces the energy conservation principle.

Different values of the frequencies ω_1 and ω_2 give rise to different second-order NLO phenomena. The most common ones are shown in Figure 1.1. Sum Frequency Generation (SFG, $\chi^{(2)}(-(\omega_1 + \omega_2); \omega_1, \omega_2)$) implies the creation of a photon of frequency equal to the sum of the frequencies of the incident fields. The particular case where the two incident fields are degenerated ($\omega_1 = \omega_2 = \omega$) corresponds to the phenomenon of Second Harmonic Generation (SHG, $\chi^{(2)}(-2\omega; \omega, \omega)$), in which the generated photon has a frequency which is exactly the double of the one of the applied fields. The Difference Frequency Generation (DFG, $\chi^{(2)}(-(\omega_1 - \omega_2); \omega_1, -\omega_2)$) process is related to the generation of a photon of frequency corresponding to the difference between the frequencies of the incident fields. Again, if the two incident fields are degenerated, this process is referred to as Optical Rectification (OR, $\chi^{(2)}(0; \omega, -\omega)$), where a static field ($\omega=0$) is generated. Finally, the Electro-Optical effect (EO, $\chi^{(2)}(-\omega; \omega, 0)$), also called Pockels effect, corresponds to the combination of a static field with an optical excitation field to provide an optical field response.

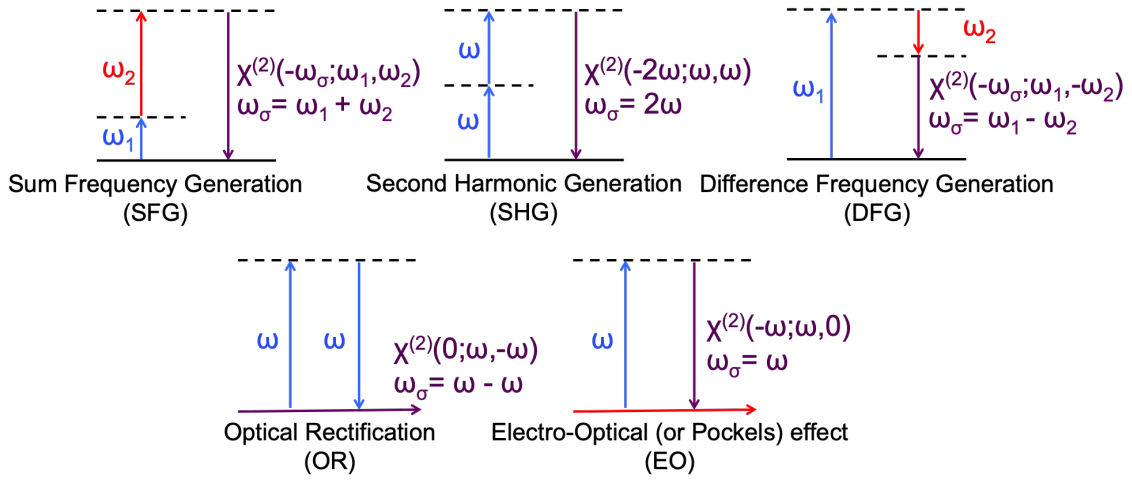


Figure 1.1 – Schemes of the most common second-order NLO phenomena. Horizontal arrows represent static fields ($\omega=0$).

1.3 Second Harmonic Generation

Among all the second-order phenomena, this thesis work mainly focuses on SHG, firstly demonstrated by Franken and his colleagues in 1961.^[4] As discussed in the previous section, SHG, also called frequency doubling, is a nonlinear optical process, in which photons interacting with a nonlinear material are effectively combined to form new photons having twice the frequency (or half the wavelength) of initial photons.

SHG has a broad field of applications, including photonics. One example of photonic application is the data storage. The possibility to store information in coumarin-based copolymer thin films by using photo-induced dimerization^[5, 6] have been recently demonstrated. Namely, the dimerization of coumarin moieties results in a local modification of the SHG efficiency, which is, in turn, used to store the data. Molecular NLO switches, namely nanoscale structures, including molecules, supramolecules, polymers, functionalized surfaces, and crystalline/amorphous solids, have high potential for applications in data storage, signal processing, and sensing.^[7] They can commute between two or more forms, displaying contrasts in their NLO properties. SHG is also widely used in electro-optic (EO) devices.^[8, 9] In particular, EO modulators based on organic materials are preferred because of their ultra-high bandwidth and ultra-low energy.

Another very interesting application of SHG is the imaging microscopy. The first biological sample observed by the SHG microscope was a rat-tail tendon, which has a non-centrosymmetric structure owing to the alignment of polar collagen.^[10] As the SHG microscope is able to selectively observe the region in a sample where the spatial inversion symmetry is broken, it is a valuable tool for investigating the molecular ordering and structural organization in biological samples.^[11, 12] The main sources of endoge-

nous SHG in biological samples are collagen,^[13, 14] myosin^[15, 16] and microtubule,^[17] since their polar structures are organized by non-centrosymmetric structural proteins. SHG microscope has also been used for various medical applications such as the diagnosis of collagen-related diseases and the detection of tumor-associated collagen as a cancer biomarker.^[18, 19] Besides imaging by endogenous SHG, exogenous staining enables visualization of the plasma membranes and monitoring the change in the membrane potential under the SHG microscope.^[20, 21, 22, 23, 24, 25, 16] The distribution of lipid molecules between the outer and inner leaflet of the membrane bilayer is asymmetric.^[26, 27] This implies that the cellular membranes are non-centrosymmetric, i.e., SHG-active. However, the SHG signal generated by these membranes is not strong enough to be observed. To enhance the SHG signal, the membranes are stained with amphiphilic polar dye molecules whose chromophore consists of one π -conjugated chain terminated by electron donating and accepting moieties (D- π -A conjugation).^[28] Compared to two-photon absorption, the advantages of SHG microscopy are the absence of saturation (limitation in the maximum number of photons that can be emitted in a given time), bleaching (destructive process that arises when the dye is excited to a reactive state) and blinking (fluctuation in the fluorescence from a transition to a dark state that cannot emit photons).^[29]

1.4 Importance of symmetry

Both for molecules or materials, symmetry is a key aspect in the description of NLO properties. In general, the number of independent components in the β or $\chi^{(2)}$ tensors (equations 1.5 and 1.10) are completely determined by symmetry. Hyperpolarizabilities and macroscopic susceptibilities exhibit various types of symmetry: permutation symmetry, time-reversal symmetry and symmetry in space.^[30] The time-reversal and permutation symmetries are fundamental properties of the NLO properties themselves, whereas the spatial symmetry reflects the structural properties of the molecule/material. The consequences of these three types of symmetry on the form of the β tensor are discussed below in the case of a molecular SHG process.

1.4.1 Intrinsic symmetry of permutation

In the most general case, where the two excitations are non degenerate, the first hyperpolarizability tensor contains 27 independent components, collected in a 9×3 matrix (equation 1.5). In the case of two indiscernible incident photons, the following permutation can be applied on the components of the β tensor:

$$\beta_{ijk} = \beta_{ikj} \tag{1.12}$$

Consequently, the number of independent components in the β can be reduced from 27 to 18:

$$\beta = \begin{bmatrix} \beta_{xxx} & \beta_{xyy} & \beta_{xzz} & \beta_{xyz} & \beta_{xxz} & \beta_{xxy} \\ \beta_{yxx} & \beta_{yyy} & \beta_{yzz} & \beta_{yyz} & \beta_{yxz} & \beta_{yxy} \\ \beta_{zxx} & \beta_{zyy} & \beta_{zzz} & \beta_{zyz} & \beta_{zxx} & \beta_{zxy} \end{bmatrix} \quad (1.13)$$

1.4.2 Kleinman's symmetry

If the frequencies (incident and scattered ones) implied in NLO processes are far from any absorption band of the molecule under study, the overall permutation symmetry can be applied on the Cartesian components of the hyperpolarizability tensor, without any changes of their values. This property is known as the time-reversal symmetry and was first introduced by Kleinman:^[31]

$$\beta_{kji} = \beta_{ijk} \quad (1.14)$$

Assuming the Kleinman's conditions, the number of independent (nonzero) components in the β tensor is reduced to 10:

$$\beta = \begin{bmatrix} \beta_{xxx} & \beta_{xyy} & \beta_{xzz} \\ \beta_{yxx} & \beta_{yyy} & \beta_{yzz} \\ \beta_{zxx} & \beta_{zyy} & \beta_{zzz} \end{bmatrix} + [\beta_{xyz}] \quad (1.15)$$

Note that the Kleinman's permutation rule is an approximation, which is strictly verified only in the static limit ($\omega = 0$).

1.4.3 Molecular symmetry

Finally, the number of independent components in the β tensor also depends on the symmetry of molecules. Let's consider first the particular case of centrosymmetric molecules, i.e. possessing a symmetry of inversion. Under this symmetry, the atomic coordinates transform as:

$$x \rightarrow -x, \quad y \rightarrow -y, \quad z \rightarrow -z \quad (1.16)$$

Consequently, the induced dipole and electric field components transform as:

$$\begin{aligned} \mu_x &= -\mu_x, & \mu_y &= -\mu_y, & \mu_z &= -\mu_z \\ F_x &= -F_x, & F_y &= -F_y, & F_z &= -F_z \end{aligned} \quad (1.17)$$

Let's now examine the effect of this symmetry on the β tensor components. From equation 1.8:

$$-\mu_i = -\mu_i^0 + \alpha_{ij}(-F_j) + \beta_{ijk}(-F_j)(-F_k) + \gamma_{ijkl}(-F_j)(-F_k)(-F_l) + \dots \quad (1.18)$$

or

$$\mu_i = \mu_i^0 + \alpha_{ij}F_j - \beta_{ijk}F_jF_k + \gamma_{ijkl}F_jF_kF_l + \dots \quad (1.19)$$

In virtue of the Neumann principle^[32], which states that if a system is invariant with respect to certain symmetry elements, any of its physical properties must also be invariant with respect to the same symmetry elements, equalizing equations 1.8 and 1.19 leads necessary to $\beta_{ijk} = 0$ whatever i, j and k . As a general rule, all even-order nonlinear properties vanish in centrosymmetric systems.

To obtain all non-vanishing β tensor components for each group of symmetry, F. G. Fumi has derived a simple scheme^[33] called the “direct inspection method” based on the fact that the components of a tensor always transform as the product of their respective coordinates. As a consequence, a tensor component will be zero if its index changes sign after a symmetry operation. As illustrative examples, the hyperpolarizability tensors for the T_d , C_{3v} , C_{2v} and $C_{\infty v}$ point groups are given below:

$$\beta(T_d) = \begin{pmatrix} 0 & 0 & 0 & \beta_{xyz} & \beta_{xyz} & 0 & 0 & 0 & 0 \\ 0 & 0 & 0 & 0 & 0 & \beta_{xyz} & \beta_{xyz} & 0 & 0 \\ 0 & 0 & 0 & 0 & 0 & 0 & 0 & \beta_{xyz} & \beta_{xyz} \end{pmatrix} \quad (1.20)$$

$$\beta(C_{3v}) = \begin{pmatrix} 0 & 0 & 0 & 0 & 0 & \beta_{xzx} & \beta_{xzx} & -\beta_{yyy} & -\beta_{yyy} \\ -\beta_{yyy} & \beta_{yyy} & 0 & \beta_{xxz} & \beta_{xxz} & 0 & 0 & 0 & 0 \\ \beta_{zxx} & \beta_{zxx} & \beta_{zzz} & 0 & 0 & 0 & 0 & 0 & 0 \end{pmatrix} \quad (1.21)$$

$$\beta(C_{2v}) = \begin{pmatrix} 0 & 0 & 0 & 0 & 0 & \beta_{xzx} & \beta_{xzx} & 0 & 0 \\ 0 & 0 & 0 & \beta_{yyz} & \beta_{yyz} & 0 & 0 & 0 & 0 \\ \beta_{zxx} & \beta_{zyy} & \beta_{zzz} & 0 & 0 & 0 & 0 & 0 & 0 \end{pmatrix} \quad (1.22)$$

$$\beta(C_{\infty v}) = \begin{pmatrix} 0 & 0 & 0 & 0 & 0 & \beta_{xzx} & \beta_{xzx} & 0 & 0 \\ 0 & 0 & 0 & \beta_{xxz} & \beta_{xxz} & 0 & 0 & 0 & 0 \\ \beta_{zxx} & \beta_{zxx} & \beta_{zzz} & 0 & 0 & 0 & 0 & 0 & 0 \end{pmatrix} \quad (1.23)$$

1.5 Experimental measurements of molecular second-order NLO responses

1.5.1 Electric Field-Induced Second Harmonic Generation

Historically, the first technique developed to measure molecular second-order NLO responses is the Electric Field-Induced Second Harmonic (EFISH) generation. EFISH has been first observed in solids in 1962^[34] and in gases few years later (1971).^[35, 36] The first hyperpolarizability β of chromophores in solution were measured for the first time by Levine and Bethea in 1975.^[37, 38] In the EFISH technique, the centrosymmetry is broken by applying a static external electric field. By action of this external static field, the

dipolar molecules align themselves along the direction of the field. The light intensity scattered by this oriented solution is then measured at a frequency twice the fundamental frequency of an incident laser pulse. (Figure 1.2)

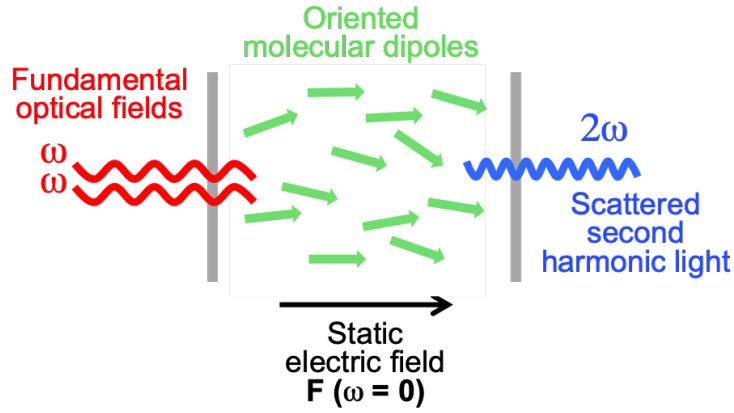


Figure 1.2 – Principle of the EFISH technique.

Since three external fields (one static and two optical) are implied in the process, EFISH is a third-order technique. The intensity of the light at 2ω is thus proportional to the square of the third-order term γ_{EFISH} :

$$I_{2\omega} \propto (\gamma_{EFISH})^2 \quad (1.24)$$

The γ_{EFISH} term can be written as the sum of two contributions:

$$\gamma_{EFISH} = \gamma_{\parallel}(-2\omega; \omega, \omega, 0) + \frac{\mu\beta_{\parallel}(-2\omega; \omega, \omega)}{3kT} \quad (1.25)$$

where the first term is a third-order contribution, implying two optical fields at frequency ω and a static field ($\omega = 0$). The second term is a second-order contribution, which depends on the temperature and implies the dipole moment of the dyes and the quantity β_{\parallel} . β_{\parallel} is the projection of the β vector onto the dipole moment axis of the molecules, and can be expressed as:

$$\beta_{\parallel}(-2\omega; \omega, \omega) = \frac{3}{5} \sum_i^{x,y,z} \frac{\mu_i \beta_i}{\|\vec{\mu}\|} = \frac{1}{5} \sum_i^{x,y,z} \frac{\mu_i}{\|\vec{\mu}\|} \sum_j^{x,y,z} (\beta_{ijj} + \beta_{jij} + \beta_{jji}) \quad (1.26)$$

where $\|\vec{\mu}\|$ is the norm of the dipole moment, μ_i are the components of the dipole moment and β_i are the components of the vector representation of β , which are expressed by a simple sum of the β -tensor components ($\beta_i = \beta_{ijj} + \beta_{jij} + \beta_{jji}$).

In order to experimentally obtain the two contributions of the γ_{EFISH} response, γ_{\parallel} and β_{\parallel} , experiments should be carried out at different temperatures. However, this is scarcely done because the range of accessible temperatures is narrow and because, in

practice, the third-order contribution $\gamma_{//}$ is considered as negligible with respect to the second-order term. In many experimental data analyses, the EFISH response is thus interpreted as an effective second-order response:

$$\gamma_{EFISH} \equiv \frac{[\mu\beta_{//}(-2\omega; \omega, \omega)]_{eff}}{3kT} \quad (1.27)$$

Note that, although this assumption was substantiated for highly dipolar compounds with large β responses, recent calculations demonstrated that the $\gamma_{//}$ contribution cannot be always omitted because it can be large, or even dominant with respect to the $\beta_{//}$ counterpart.^[39]

1.5.2 Hyper-Rayleigh Scattering

Unlike EFISH, the Hyper-Rayleigh Scattering (HRS) technique enables direct estimates of the second-order NLO properties of molecules, without contamination of higher-order responses. In HRS experiments, the first hyperpolarizability is derived from the intensity of the scattered light at optical frequency 2ω on incidence of a laser pulse at ω . Contrary to EFISH, the HRS signal originates from incoherent fluctuations of individual molecules that do not exhibit specific phase relations with respect to the others. Another important advantage of HRS over EFISH lies in the fact that it is applicable to nonpolar and ionic molecules. The principle of HRS is illustrated on Figure 1.3, where (X,Y,Z) is the laboratory frame.

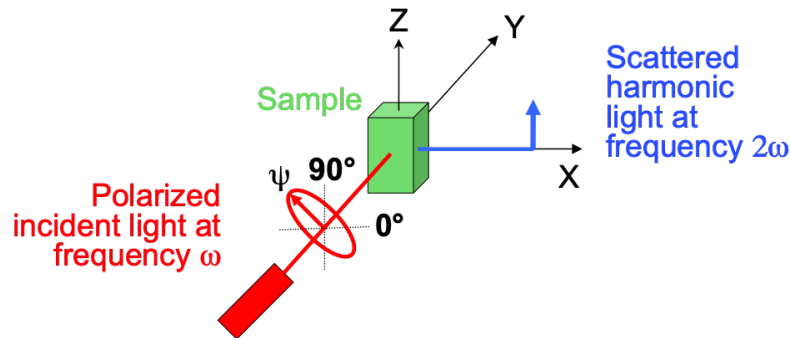


Figure 1.3 – Principle of the HRS technique.

1.5.2.1 Intensity of the harmonic light

For a non-polarized incident light of frequency ω , the intensity of the vertically polarized (parallel to the Z axis of the laboratory frame) SHG signal, scattered at 90° with respect to the propagation direction (parallel to the Y axis), is proportional to the square of the HRS hyperpolarizability:

$$\beta_{HRS}(-2\omega; \omega, \omega) = \beta_{HRS} = \sqrt{\langle \beta_{HRS}^2 \rangle} = \sqrt{\langle \beta_{ZZZ}^2 \rangle + \langle \beta_{ZXX}^2 \rangle} \quad (1.28)$$

where $\langle \beta_{ZZZ}^2 \rangle$ and $\langle \beta_{ZXX}^2 \rangle$ are averages of β tensor components that describe the isotropic distribution of molecular orientations in dilute solutions. The $\langle \beta_{ZZZ}^2 \rangle$ and $\langle \beta_{ZXX}^2 \rangle$ quantities are respectively related to the scattered HRS intensities obtained when the incident light is vertically (V) polarized (parallel to the Z axis, *i.e.* for a polarization angle $\Psi = 90^\circ$) and horizontally (H) polarized (parallel to the X axis, with $\Psi = 0^\circ$). For a sample made of two components, a solute and a solvent, the intensity of the second-harmonic light in the VV and HV configurations is given as a simple sum of contributions of both species:

$$I_{2\omega}^{VV} = G f_L^2 \left[\left\langle (\beta_{ZZZ}^S)^2 \right\rangle C_S + \left\langle (\beta_{ZZZ}^X)^2 \right\rangle C_X \right] I_\omega^2 10^{-A(2\omega)C_X} \quad (1.29)$$

$$I_{2\omega}^{HV} = G f_L^2 \left[\left\langle (\beta_{ZXX}^S)^2 \right\rangle C_S + \left\langle (\beta_{ZXX}^X)^2 \right\rangle C_X \right] I_\omega^2 10^{-A(2\omega)C_X} \quad (1.30)$$

where G includes all the experimental factors, C_S and C_X are respectively the solvent and solute concentrations, I_ω is the intensity of the incident light, and the term $10^{-A(2\omega)C_X}$ accounts for the possible absorption at frequency 2ω . f_L is a local field correction, which accounts for the effects of induced dipoles in the medium through electronic polarization. It is usually approximated using the high frequency Lorentz–Lorenz spherical cavity expression, which includes the refractive indices of the liquid at the optical frequencies ω and 2ω .^[40]

In order to obtain solely the β response of the solute, the contribution of the solvent has to be removed. To this end, two methods can be used. The first and most simple one is the internal reference method, which consists in using a series of samples with different concentrations C_X . According to equations 1.29 and 1.30, the intensity at 2ω plotted against C_X gives a straight line whose intercept corresponds to the contribution of the solvent. Note that this method can only be employed when the solvent has a significant HRS signal. If the solvent has no or weak HRS response, a molecule with a known HRS response is used as external reference.

As also demonstrated by equations 1.29 and 1.30, the intensity of the second-harmonic light has a quadratic dependence on the intensity of the incident light and a linear dependence on the solute concentration. The evolution of the HRS intensity with respect to the solute concentration and to the incident power is illustrated in Figure 1.4. Orientational averages of the molecular tensor components, $\langle \beta_{ZZZ}^2 \rangle$ and $\langle \beta_{ZXX}^2 \rangle$, are extracted from the best fit (blue surface) to experimental results in the VV and HV geometries, respectively.

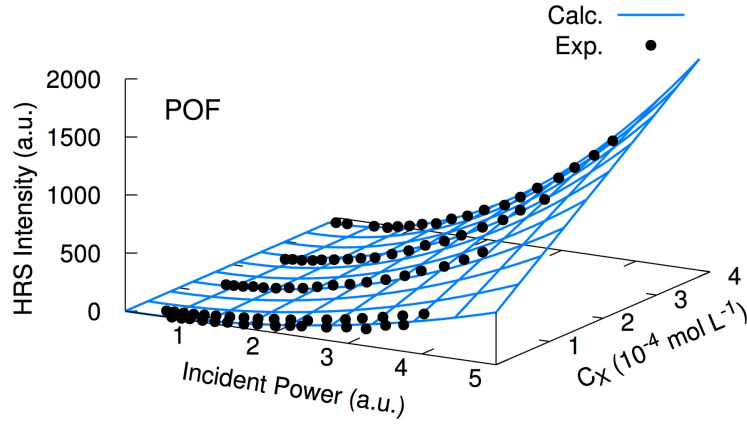


Figure 1.4 – Experimental (points) and fitted curves (lines) of the second-harmonic light intensity, as a function of the incident power and concentration of a typical NLO chromophore.

Assuming a more general elliptically polarized incident light and a phase retardation of $\pi/2$ (in accordance with the setting used by our collaborators), the intensity of the harmonic light collected perpendicular to the incident beam and vertically (V) polarized is given by the following expression:^[41]

$$\begin{aligned}
 I_{2\omega}^{\Psi V} &\propto \langle \beta_{ZXX}^2 \rangle \cos^4 \Psi + \langle \beta_{ZZZ}^2 \rangle \sin^4 \Psi + \langle (\beta_{ZXZ} + \beta_{ZZX})^2 - 2\beta_{ZZZ}\beta_{ZXX} \rangle \cos^2 \Psi \sin^2 \Psi \\
 &= \langle \beta_{ZXX}^2 \rangle \cos^4 \Psi + \langle \beta_{ZZZ}^2 \rangle \sin^4 \Psi + (7\langle \beta_{ZXX}^2 \rangle - \langle \beta_{ZZZ}^2 \rangle) \cos^2 \Psi \sin^2 \Psi
 \end{aligned}
 \tag{1.31}$$

The evolution of the HRS intensity $I_{2\omega}^{\Psi V}$ with respect to the polarization angle Ψ of the incident light is exemplified in Figure 1.5 for a typical NLO chromophore.

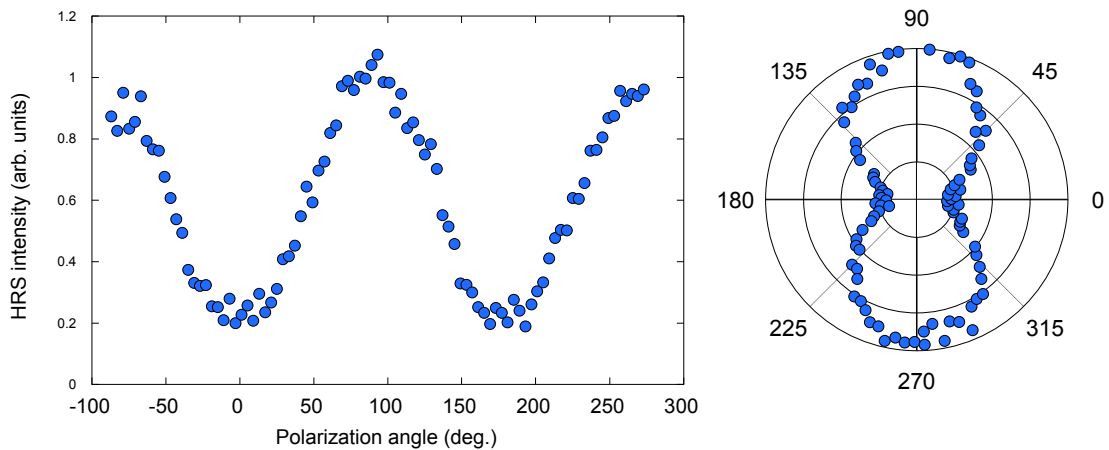


Figure 1.5 – Experimental points corresponding to the normalized second-harmonic light intensity with respect to the polarization angle of the incident light of a typical NLO chromophore.

The orientationally averaged tensor quantities $\langle \beta_{ZZZ}^2 \rangle$, $\langle \beta_{ZXX}^2 \rangle$ and $\langle (\beta_{ZXZ} + \beta_{ZZX})^2 - 2\beta_{ZZZ}\beta_{ZXX} \rangle$ can be expressed in terms of molecular β tensor components by the equations below:

$$\begin{aligned}
\langle \beta_{ZZZ}^2 \rangle &= \frac{1}{7} \sum_{\zeta}^{x,y,z} \beta_{\zeta\zeta\zeta}^2 + \frac{4}{35} \sum_{\zeta \neq \eta}^{x,y,z} \beta_{\zeta\zeta\eta}^2 + \frac{2}{35} \sum_{\zeta \neq \eta}^{x,y,z} \beta_{\zeta\zeta\zeta} \beta_{\zeta\eta\eta} \\
&+ \frac{4}{35} \sum_{\zeta \neq \eta}^{x,y,z} \beta_{\eta\zeta\zeta} \beta_{\zeta\zeta\eta} + \frac{4}{35} \sum_{\zeta \neq \eta}^{x,y,z} \beta_{\zeta\zeta\zeta} \beta_{\eta\eta\zeta} + \frac{1}{35} \sum_{\zeta \neq \eta}^{x,y,z} \beta_{\eta\zeta\zeta}^2 \\
&+ \frac{4}{105} \sum_{\zeta \neq \eta \neq \xi}^{x,y,z} \beta_{\zeta\zeta\eta} \beta_{\eta\xi\xi} + \frac{1}{105} \sum_{\zeta \neq \eta \neq \xi}^{x,y,z} \beta_{\eta\zeta\zeta} \beta_{\eta\xi\xi} \\
&+ \frac{4}{105} \sum_{\zeta \neq \eta \neq \xi}^{x,y,z} \beta_{\zeta\zeta\eta} \beta_{\xi\xi\eta} \\
&+ \frac{2}{105} \sum_{\zeta \neq \eta \neq \xi}^{x,y,z} \beta_{\zeta\eta\xi}^2 + \frac{4}{105} \sum_{\zeta \neq \eta \neq \xi}^{x,y,z} \beta_{\zeta\eta\xi} \beta_{\eta\zeta\xi}
\end{aligned} \tag{1.32}$$

$$\begin{aligned}
\langle \beta_{ZXX}^2 \rangle &= \frac{1}{35} \sum_{\zeta}^{x,y,z} \beta_{\zeta\zeta\zeta}^2 + \frac{4}{105} \sum_{\zeta \neq \eta}^{x,y,z} \beta_{\zeta\zeta\zeta} \beta_{\zeta\eta\eta} - \frac{2}{35} \sum_{\zeta \neq \eta}^{x,y,z} \beta_{\zeta\zeta\zeta} \beta_{\eta\eta\zeta} \\
&+ \frac{8}{105} \sum_{\zeta \neq \eta}^{x,y,z} \beta_{\zeta\zeta\eta}^2 + \frac{3}{35} \sum_{\zeta \neq \eta}^{x,y,z} \beta_{\zeta\eta\eta}^2 - \frac{2}{35} \sum_{\zeta \neq \eta}^{x,y,z} \beta_{\zeta\zeta\eta} \beta_{\eta\zeta\zeta} \\
&+ \frac{1}{35} \sum_{\zeta \neq \eta \neq \xi}^{x,y,z} \beta_{\zeta\eta\eta} \beta_{\zeta\xi\xi} - \frac{2}{105} \sum_{\zeta \neq \eta \neq \xi}^{x,y,z} \beta_{\zeta\zeta\xi} \beta_{\eta\eta\xi} \\
&- \frac{2}{105} \sum_{\zeta \neq \eta \neq \xi}^{x,y,z} \beta_{\zeta\zeta\eta} \beta_{\eta\xi\xi} \\
&+ \frac{2}{35} \sum_{\zeta \neq \eta \neq \xi}^{x,y,z} \beta_{\zeta\eta\xi}^2 - \frac{2}{105} \sum_{\zeta \neq \eta \neq \xi}^{x,y,z} \beta_{\zeta\eta\xi} \beta_{\eta\zeta\xi}
\end{aligned} \tag{1.33}$$

$$\begin{aligned}
\langle (\beta_{ZXZ} + \beta_{ZZX})^2 - 2\beta_{ZZZ}\beta_{ZXX} \rangle &= \frac{3}{35} \sum_{\zeta}^{x,y,z} \beta_{\zeta\zeta\zeta}^2 - \frac{1}{105} \sum_{\zeta \neq \eta}^{x,y,z} \beta_{\zeta\zeta\zeta} \beta_{\zeta\eta\eta} + \frac{2}{70} \sum_{\zeta \neq \eta}^{x,y,z} \beta_{\zeta\zeta\zeta} \beta_{\eta\eta\zeta} \\
&+ \frac{38}{105} \sum_{\zeta \neq \eta}^{x,y,z} \beta_{\zeta\zeta\eta}^2 + \frac{2}{35} \sum_{\zeta \neq \eta}^{x,y,z} \beta_{\zeta\eta\eta}^2 + \frac{2}{70} \sum_{\zeta \neq \eta}^{x,y,z} \beta_{\zeta\zeta\eta} \beta_{\eta\zeta\zeta} \\
&- \frac{1}{21} \sum_{\zeta \neq \eta \neq \xi}^{x,y,z} \beta_{\zeta\eta\eta} \beta_{\zeta\xi\xi} + \frac{8}{105} \sum_{\zeta \neq \eta \neq \xi}^{x,y,z} \beta_{\zeta\zeta\xi} \beta_{\eta\eta\xi} - \frac{13}{105} \sum_{\zeta \neq \eta \neq \xi}^{x,y,z} \beta_{\zeta\zeta\eta} \beta_{\eta\xi\xi} \\
&+ \frac{11}{105} \sum_{\zeta \neq \eta \neq \xi}^{x,y,z} \beta_{\zeta\eta\xi}^2 + \frac{8}{105} \sum_{\zeta \neq \eta \neq \xi}^{x,y,z} \beta_{\zeta\eta\xi} \beta_{\eta\zeta\xi}
\end{aligned} \tag{1.34}$$

1.5.2.2 Depolarization ratio

The depolarization ratio, corresponding to the ratio between the HRS intensities collected in the VV and HV optical geometries, is also measured as an important indicator of the symmetry of the NLO response:

$$\text{DR} = \frac{\langle \beta_{ZZZ}^2 \rangle}{\langle \beta_{ZXX}^2 \rangle} \quad (1.35)$$

As discussed in section 1.4.3, in the T_d symmetry, β_{xyz} is the only non-zero component. Therefore, the orientationally averaged tensor quantities $\langle \beta_{ZZZ}^2 \rangle$ and $\langle \beta_{ZXX}^2 \rangle$ are calculated as:

$$\langle \beta_{ZZZ}^2 \rangle = \frac{36}{105} \beta_{xyz}^2 \quad (1.36)$$

$$\langle \beta_{ZXX}^2 \rangle = \frac{24}{105} \beta_{xyz}^2 \quad (1.37)$$

which gives:

$$\text{DR} = \frac{36}{105} \times \frac{105}{24} = 1.50 \quad (1.38)$$

The DR value of 1.5 thus corresponds to the response of a purely octupolar system.

Another typical example is the C_{2v} symmetry, which is often assumed for describing planar push-pull molecules. For a molecule lying in the xz plane with z the charge transfer axis, β_{zxx} , β_{zyy} and β_{zzz} are the three independent tensor components. Assuming that the out-of-plane component is negligible with respect to the in-plane components ($\beta_{zyy} = 0$), the DR can be written as:

$$\text{DR} = \frac{15 + 18R + 27R^2}{3 - 2R + 11R^2} \quad (1.39)$$

with $R = \beta_{zxx}/\beta_{zzz}$. In the limit case where $R \rightarrow 0$, i.e. when the hyperpolarizability tensor is reduced to its single diagonal component along z , the corresponding DR is equal to 5.00, and the system is said to have a 1D NLO response.

If we look now at the $C_{\infty v}$ symmetry, β_{zxx} and β_{zzz} are the two independent tensor components, and the DR becomes:

$$\text{DR} = \frac{15 + 36R + 72R^2}{3 - 4R + 20R^2} \quad (1.40)$$

with $R = \beta_{zxx}/\beta_{zzz}$. Again, when $R \rightarrow 0$, the corresponding DR is equal to 5.00 and the system has a 1D NLO response, while when $R = 1/3$, the DR is equal to 9.00 and the response is said to be purely dipolar. The evolution of the DR with respect to R in the case of the C_{2v} and $C_{\infty v}$ symmetries is illustrated in Figure 1.6.

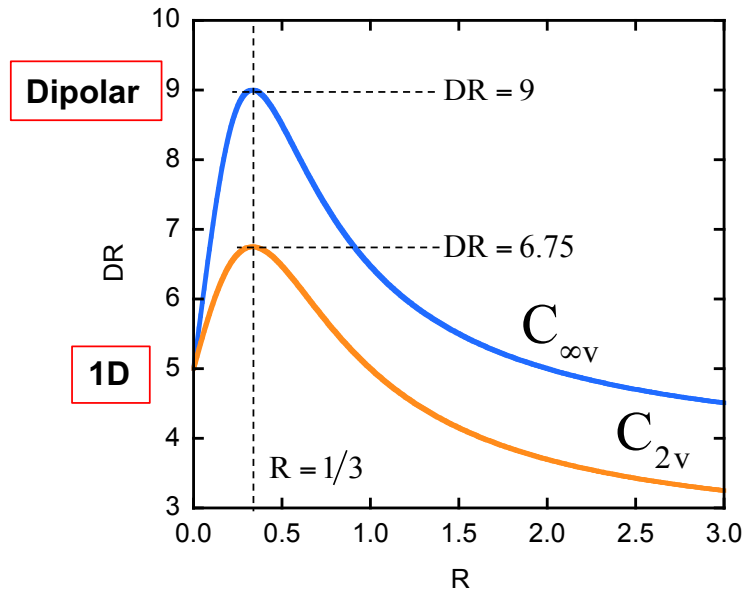


Figure 1.6 – Evolution of the depolarization ratio (DR) with respect to R in the case of the C_{2v} and $C_{\infty v}$ symmetries.

The DR, and more globally the shape of the normalized HRS intensity with respect to the polarization angle of the incident laser beam, provide therefore important information on the symmetry of the NLO-responsive part of the molecule. This is illustrated in Figure 1.7 for a set of small reference molecules, differing by their symmetry.^[42] As the symmetry is progressively decreased from CCl_4 (which has a pure octupolar symmetry and a T_d point group) to acetonitrile (which is almost a pure dipolar molecule if we consider that the methyl group has a negligible contribution to the NLO response), the DR increases from 1.5 to 9. Accordingly, the shape of the normalized HRS intensity as a function of the polarization angle of the incident beam is changing progressively from a four-lobes to a two-lobes pattern.

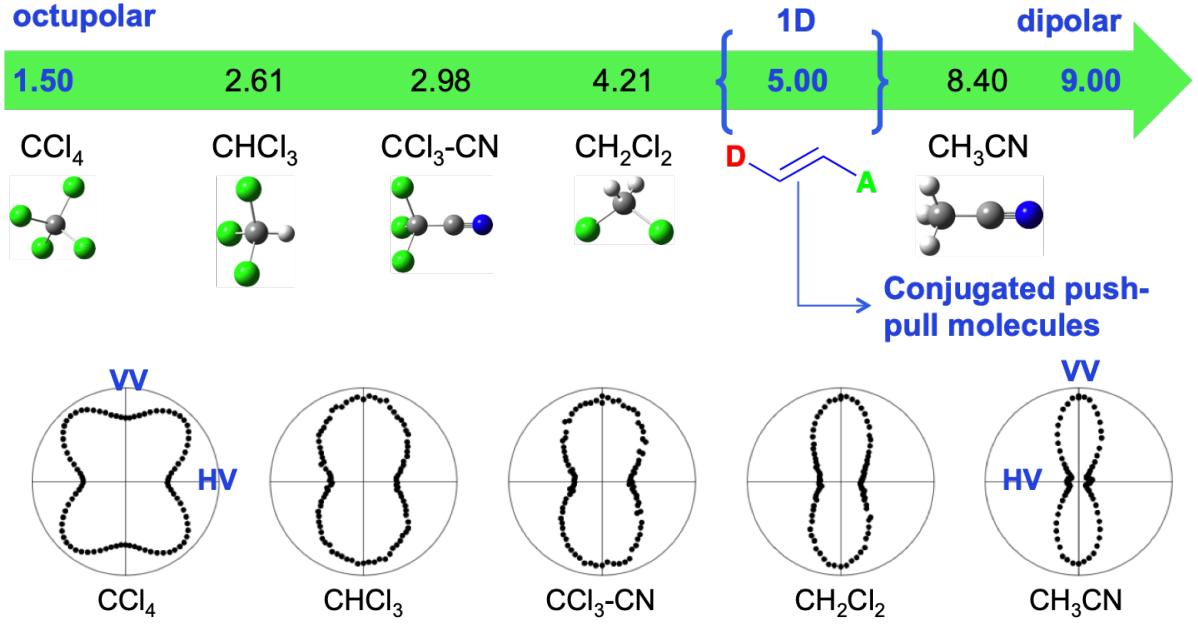


Figure 1.7 – DR (up) and normalized HRS intensity (down) of small reference molecules.

1.5.2.3 Irreducible spherical representation of the hyperpolarizability

From an experimental point of view, there are several obvious drawbacks to use Cartesian coordinates to study isotropic media. Indeed, the use of Cartesian coordinates implies symmetry assumptions about the different β -components of the molecules. On the other hand, the arbitrary orientation of the Cartesian axes used in theoretical calculations is a possible source of misfit with experimental data. For low-symmetry structures, it is often more convenient to use the irreducible spherical representation of the hyperpolarizability β tensor based on a mixed spherical-Cartesian formalism to analyze HRS measurements in terms of multipolar components. The use of spherical invariants allows the β -tensor to be decomposed as the sum of dipolar ($\beta_{J=1}$) and octupolar ($\beta_{J=3}$) tensorial components. With this formalism, the three HRS invariants $\langle \beta_{ZZZ}^2 \rangle$, $\langle \beta_{ZXX}^2 \rangle$ and $\langle (\beta_{ZXZ} + \beta_{ZZX})^2 - 2\beta_{ZZZ}\beta_{ZXX} \rangle$ involved in equation 1.31 can be rewritten as:

$$\langle \beta_{ZZZ}^2 \rangle = |\beta_{J=1}|^2 \left(\frac{9}{45} + \frac{6}{105} \rho^2 \right) \quad (1.41)$$

$$\langle \beta_{ZXX}^2 \rangle = |\beta_{J=1}|^2 \left(\frac{1}{45} + \frac{4}{105} \rho^2 \right) \quad (1.42)$$

$$\langle (\beta_{ZXZ} + \beta_{ZZX})^2 - 2\beta_{ZZZ}\beta_{ZXX} \rangle = |\beta_{J=1}|^2 \left(-\frac{2}{45} + \frac{22}{105} \rho^2 \right) \quad (1.43)$$

and equation 1.31 becomes:

$$I_{\Psi V}^{2\omega} \propto |\beta_{J=1}|^2 \left(\frac{1}{45} + \frac{4}{105} \rho^2 \right) \times [\cos^4 \Psi + (\text{DR}) \sin^4 \Psi + (7 - \text{DR}) \cos^2 \Psi \sin^2 \Psi] \quad (1.44)$$

where the nonlinear anisotropy parameter, $\rho = |\beta_{J=3}|/|\beta_{J=1}|$ denotes the relative magnitude of the octupolar and dipolar contributions to the first hyperpolarizability tensor, and provides an alternative to DR for classifying the studied systems in terms of their octupolar or dipolar character. The relationships between β_{HRS} and DR and the multipolar contributions are the following:

$$\beta_{HRS} = |\beta_{J=1}| \sqrt{\frac{2}{3} \left(\frac{1}{3} + \frac{1}{7} \rho^2 \right)} \quad (1.45)$$

$$\text{DR} = \frac{9(1 + \frac{2}{7} \rho^2)}{1 + \frac{12}{7} \rho^2} \quad (1.46)$$

1.6 Examples of organic molecules with large second-order NLO properties

In their review of 1994,^[43] Kanis, Ratner and Marks proposed to categorize the materials displaying NLO properties in three generic classes: multilayered semiconductors, molecular based macroscopic assemblies and inorganic solids, each class possessing its own fields of potential or existent application. Traditionally the NLO materials of choice were the inorganic solids, such as LiNbO_3 and KH_2PO_4 for example. However, many research works conducted in the last 20 years showed that the organic π -electron assemblies possess attractive NLO characteristics, which can be combined with their intrinsic advantages such as flexibility, tailored synthesis, low cost or easy processing.^[44, 45, 46, 47, 48] We give here a short review of the main classes of organic compounds that have been shown of interest regarding their second-order NLO properties.

1.6.1 π -conjugated donor-acceptor molecules

Organic chromophores having the ability to deliver high β values are most often associated to dipolar push-pull chromophores having a D- π -A architecture, in which an electron-donating group (D) interacts with an electron-withdrawing group (A) through a π -conjugated linker. These molecules usually display significant charge transfer between the D and A sites giving rise to intense absorption in the visible region. A large series of such push-pull chromophores were studied according to their second-order nonlinear properties, including benzobisthiazoles,^[49] phthalocyanines,^[50] polyaniline oligomers,^[43] push-pull polyenes^[51, 52, 53] and polymethineimines.^[54] Figure 1.8 reports information on the magnitude of second-order responses in some representative π -conjugated molecules, in relation with their structural properties. These data evidence that second-order NLO responses can be enhanced either by increasing the electronic asymmetry (using stronger donating or accepting moieties), or by increasing the conjugation length between the substituents.

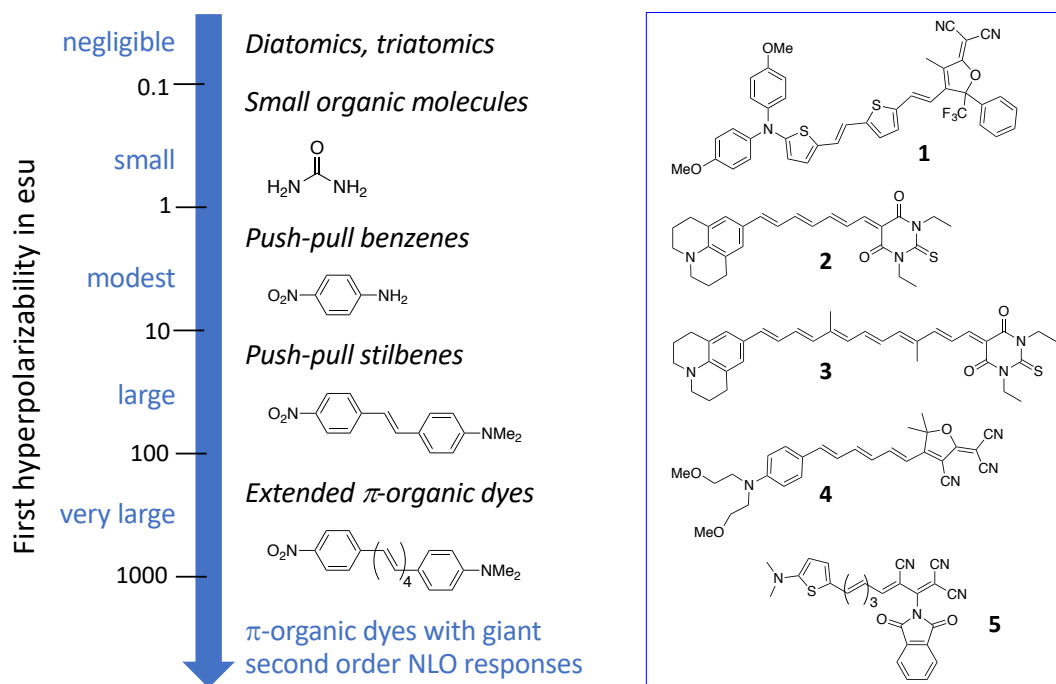


Figure 1.8 – Magnitude of second-order responses for representative organic molecules. β values (in $10^{-30} \text{ cm}^5 \text{ esu}^{-1}$) of small compounds were obtained from EFISH measurements using an incident laser beam of 1910 nm (ref. [43]). Compounds with very large second-order NLO responses are taken from Refs. [55] (1), [56] (2,3), [57] (4) and [58] (5).

Another related structural parameter having a direct impact on the first hyperpolarizability of push-pull molecules is the bond-length alternation (BLA) along the conjugated backbone, *i.e.* the average difference in length between single and double bonds. For instance, considering the polyene oligomers with the resonance structures shown in Figure 1.9, the BLA can be defined as the difference between the average length of the C=C bonds and the average length of the C–C bonds. By performing semi-empirical calculations on the $\text{Me}_2\text{N}-(\text{CH}=\text{CH})_n\text{-CHO}$ oligomers, Marder and collaborators first evidenced the structure-property relationship linking the first hyperpolarizability to the BLA.^[59, 60] As a representative example, the evolution of β with the BLA for $n = 5$ is reported in Figure 1.9 and shows that β exhibits a positive peak between the neutral (a) and the cyanine (b) limits, crosses through zero at roughly the cyanine limit, and exhibits a negative peak between the cyanine and zwitterionic (c) limits.

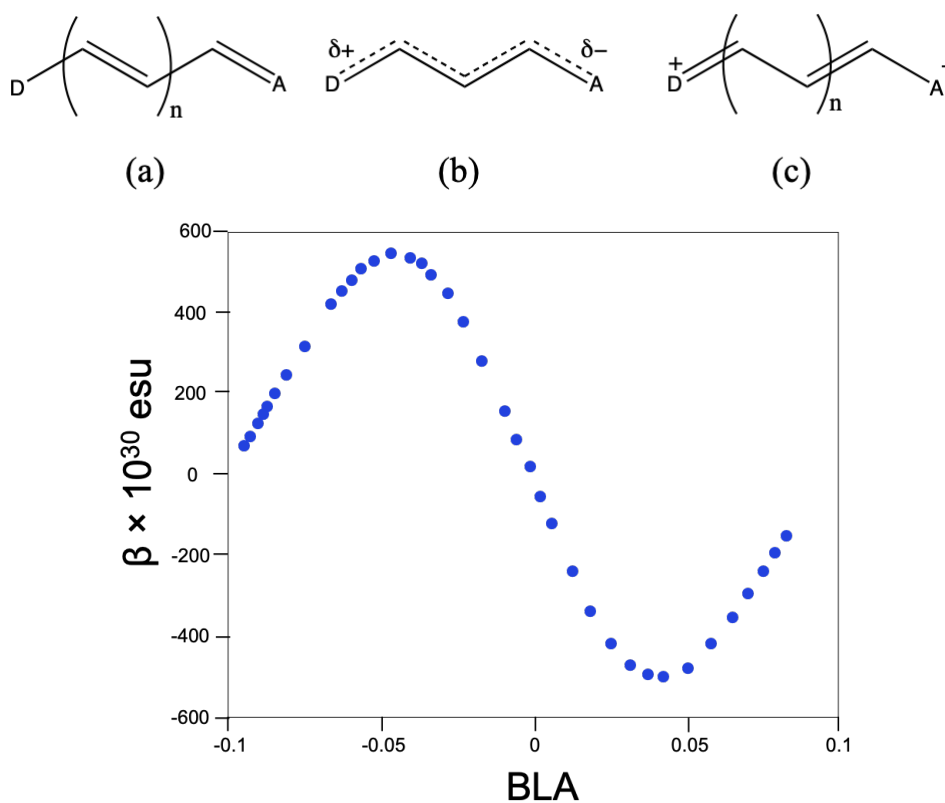


Figure 1.9 – Top: Neutral (a), cyanine (b) and zwitterionic (c) resonance structures that contribute to the electronic structure of polyene molecules. Bottom: Correlation of the first-hyperpolarizability with BLA in the $Me_2N-(CH=CH)_5-CHO$ molecule (adapted from ref. [60]).

The relationship between the BLA and the magnitude of the β responses was also evidenced recently in merocyanine derivatives^[61] (see Figure 1.10). In this case, a quasi-linear β -BLA relationship was evidenced when varying the nature of the chemical substituents. The larger β values and more positive BLA are associated with a more aromatic structure whereas the opposite trend corresponds to a quinoid ring structure.

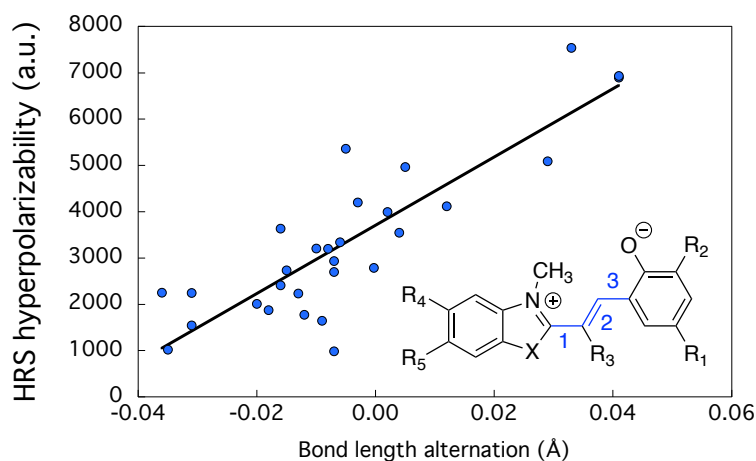


Figure 1.10 – Relationship between the bond length alternation (defined as $BLA = \frac{1}{2}(d_1 + d_3 - 2d_2)$) and β in a series of merocyanine derivatives varying by the nature of their chemical substituents R_{1-5} and X (adapted from ref. [61]).

The change in the BLA is also often invoked in experimental works to explain the dependence of the NLO responses on the solvent. In fact, interactions with solvent induce geometrical changes in the conjugated part of the solute, resulting in changes in the BLA, which in turn lead to a modification of its NLO properties. This is also true in the case of the second hyperpolarizability γ . For instance, the solvent-dependent second hyperpolarizabilities observed in a variety of unsaturated organic compounds by Marder and collaborators were associated with changes in the BLA, from a highly bond-length alternated structure for a formyl-substituted compound in non-polar solvents to a cyanine-like structure, with little bond-length alternation, for a dicyanovinyl-substituted compound in polar solvents.^[62]

1.6.2 Octupolar molecules

Whereas there have been countless efforts in the optimization of the NLO dipolar derivatives, octupolar derivatives have been much less investigated. Yet, compared to their dipolar counterparts, they possess several characteristics that are quite favorable for electro-optical applications: increased transparency, absence of dipole moment, and insensitivity to polarization. Among octupolar derivatives, two-dimensional derivatives with ternary symmetry have proven to be of major interest, leading to potentially very high β values. A typical example of this type of molecules is the 1,3,5-triamino-2,4,6-trinitro-benzene (TATB) shown in Figure 1.11. Theoretical investigations carried out by Brédas et al.^[63] have shown that the β response of the TATB is twice larger than the one obtained for the paranitroaniline (pNA) molecule, its dipolar counterpart.

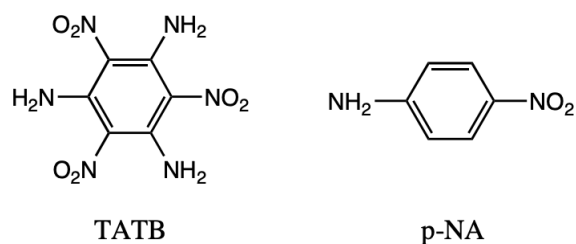


Figure 1.11 – Structure of the 1,3,5-triamino-2,4,6-trinitrobenzene (a) and paranitroaniline (b) molecules.

Other examples of octupolar NLO-phores have been designed. As shown in Figure 1.12, they are generally built from either an electron-withdrawing core (such as tricyano or trinitrobenzene, triazines, isocyanurates, boroxines, truxenone, etc.)^[64] or an electron-donating core (trimethoxy-benzene, triphenylbenzene, triphenylamine, etc.).^[64] Crystal violet (CV in Figure 1.12), the prototypical compound of this kind, has been studied by Wenseleers and collaborators by means of tunable wavelength HRS measurements.^[65] Octupolar merocyanine dyes **1-4** displayed in Figure 1.12 were also shown to exhibit high HRS responses.^[66]

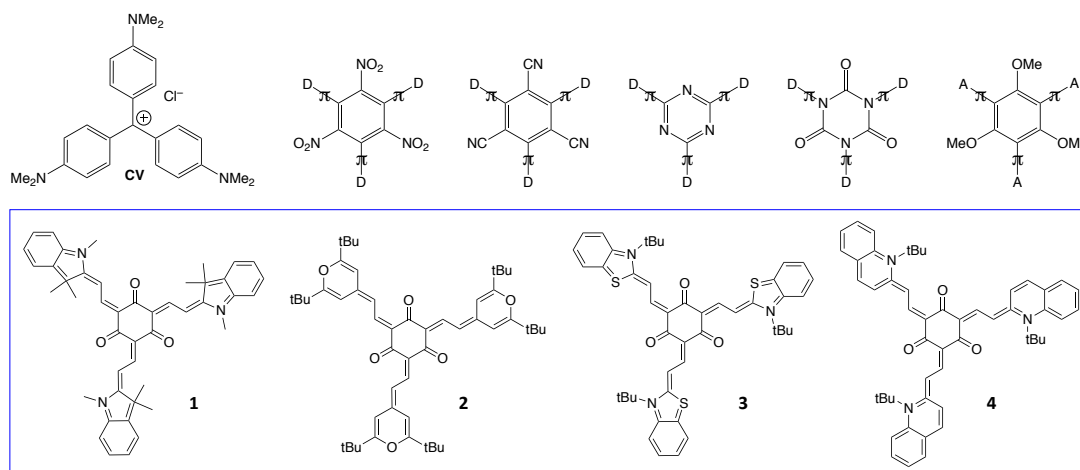


Figure 1.12 – Structure of the prototypical octupole crystal violet (CV) and examples of ternary octupoles built from an electron-withdrawing core (top) or electron-donating core (bottom) and merocyanine octupolar dyes investigated in ref. [66] (framed).

Bibliography

- [1] Armstrong J. A., Bloembergen N., Ducuing J., and Pershan P. S. Interactions between light waves in a nonlinear dielectric. *Phys. Rev.*, 127:1918, 1962.
- [2] Willetts A., Rice J. E., Burland D. M., and Shelton D. P. Problems in the comparison of theoretical and experimental hyperpolarizabilities. *J. Chem. Phys.*, 97:7590, 1992.
- [3] Suponitsky K. Y., Timofeeva T. V., and Antipin M. Y. Molecular and crystal design of nonlinear optical organic materials. *Russ. Chem. Rev.*, 75:515, 2006.
- [4] Franken P. A., Hill A. E., Peters C. W., and Weinreich G. Generation of optical harmonics. *Phys. Rev. Lett.*, 7:118, 1961.
- [5] Gindre D., Iliopoulos K., Krupka O., Champigny E., Morille Y., and Sallé M. Image storage in coumarin-based copolymer thin films by photoinduced dimerization. *Opt. Lett.*, 38:4636, 2013.
- [6] Iliopoulos K., Krupka O., Gindre D., and Sallé M. Reversible two-photon optical data storage in coumarin-based copolymers. *J. Am. Chem. Soc.*, 132:14343, 2010.
- [7] Castet F., Rodriguez V., Pozzo J-L, Ducasse L., Plaquet A., and Champagne B. Design and Characterization of Molecular Nonlinear Optical Switches. *Acc. Chem. Res.*, 46:2656, 2013.
- [8] Liu J., Xu G., Liu F., Kityk I., Liu X., and Zhen Z. Recent advances in polymer electro-optic modulators. *RSC Adv.*, 5:15784, 2015.
- [9] Wu J., Li Z., Luo J., and Jen A. K-Y. High-performance organic second- and third-order nonlinear optical materials for ultrafast information processing. *J. Mater. Chem. C*, 8:15009, 2020.
- [10] Freund I. and Deutsch M. Second-harmonic microscopy of biological tissue. *Opt. Lett.*, 11:94, 1986.
- [11] Campagnola P. J., Millard A. C., Terasaki M., Hoppe P. E., Malone C. J., and Mohler W. A. Three-dimensional high-resolution second-harmonic generation imaging of endogenous structural proteins in biological tissues. *Biophys. J.*, 82:493, 2002.
- [12] Mohler W., Millard A. C., and Campagnola P. J. Second harmonic generation imaging of endogenous structural proteins. *Methods*, 29:97, 2003.
- [13] Campagnola P. J. *3D SHG imaging and analysis of fibrillar collagen, Second harmonic generation imaging*. Boca Raton, London, New York: CRC Press, Taylor & Francis Group, 2013.

- [14] Mansfield J. C., Mandalia V., Toms A., C. P. Winlove, and Brasselet S. Collagen reorganization in cartilage under strain probed by polarization sensitive second harmonic generation microscopy. *J. R. Soc. Interface*, 16:20180611, 2019.
- [15] Yokota H., Kaneshiro J., and Uesu Y. Optical second harmonic generation microscopy as a tool of material diagnosis. *Phys. Res. Int.*, 2012:704634, 2012.
- [16] Vanzi F., Sacconi L., Cicchi R., Stringari C., and Pavone F. S. *Molecular structure and order with second-harmonic generation microscopy, Second harmonic generation imaging*. Boca Raton, London, New York: CRC Press, Taylor & Francis Group, 2013.
- [17] Kwan A. C. *Second-harmonic generation imaging of microtubules, Second harmonic generation imaging*. Boca Raton, London, New York: CRC Press, Taylor & Francis Group, 2013.
- [18] Karsten König, editor. *Multiphoton Microscopy and Fluorescence Lifetime Imaging: Applications in Biology and Medicine*. De Gruyter, 2018.
- [19] Campbell K. R., Chaudhary R., Handel J. M., Patankar M. S., and Campagnola P. J. Polarization-resolved second harmonic generation imaging of human ovarian cancer. *J. Biomed. Opt.*, 23:1, 2018.
- [20] Campagnola P. J., Wei M. D., Lewis A., and Loew L. M. High-resolution nonlinear optical imaging of live cells by second harmonic generation. *Biophys. J.*, 77:3341, 1999.
- [21] Moreaux L., Sandre O., and Mertz J. Membrane imaging by second-harmonic generation microscopy. *J. Opt. Soc. Am. B*, 17:1685, 2000.
- [22] Dambrin V Blanchard-Desce M Mertz J Moreaux L, Pons T. Electro-optic response of second-harmonic generation membrane potential sensors. *Opt. Lett.*, 28:625, 2003.
- [23] Dombeck D. A., Blanchard-Desce M., and Webb W. W. Optical recording of action potentials with second-harmonic generation microscopy. *J. Neurosci.*, 24:999, 2004.
- [24] Nuriya M., Jiang J., Nemet B., Eisenthal K. B., and Yuste R. Imaging membrane potential in dendritic spines. *Proc. Natl. Acad. Sci. U. S. A.*, 103:786, 2006.
- [25] Nuriya M., Fukushima S., Momotake A., Shinotsuka T., Yasui M., and Arai T. Multimodal two-photon imaging using a second harmonic generation-specific dye. *Nat. Commun.*, 7:11557, 2016.
- [26] Bretscher M. S. Membrane structure: some general principles. *Science*, 181:622, 973.
- [27] Murate M., Abe M., Kasahara K., Iwabuchi K., Umeda M., and Kobayashi T. Transbilayer distribution of lipids at nano scale. *J. Cell. Sci.*, 128:1627, 2015.

- [28] Reeve J. E., Anderson H. L., and Clays K. Dyes for biological second harmonic generation imaging. *Phys. Chem. Chem. Phys.*, 12:13484, 2010.
- [29] Pantazis P., Maloney J., Wu D., and Fraser S. E. Second harmonic generating (SHG) nanoprobe for in vivo imaging. *Proc. Natl. Acad. Sci.*, 107:14535, 2010.
- [30] Verbiest T., Clays K., and Rodriguez V. *Second-Order Nonlinear Optical Characterization Techniques: An Introduction*. CRC Press, Taylor and Francis Group, Boca Raton, London, NY, 2009.
- [31] Kleinman D. A. Nonlinear Dielectric Polarization in Optical Media. *Phys. Rev.*, 126:1977, 1962.
- [32] Neumann F. E. *Vorlesungen über die Theorie der Elastizität der festen Körper und des Lichtäthers*. Eds. O.E. Meyer, Leipzig, B.G. Teubner-Verlag, 1885.
- [33] Fumi F. G. Matter tensors in symmetrical systems. *Acta Cryst.*, 5:44, 1942.
- [34] Terhune R. W., Maker P. D., and Savage C. M. Optical harmonic generation in calcite. *Phys. Rev. Lett.*, 8:2550, 1962.
- [35] Finn R. S., Ward J. F., Ward F., and Finn R. S. DC-induced optical second-harmonic generation in the inert gases. *Phys. Rev. Lett.*, 26:285, 1971.
- [36] Hauchecorne G., Kerhervé F., and Mayer G. Measurement of light wave interactions in various substances. *J. Phys. (France)*, 32:47, 1971.
- [37] Levine B. F. and Bethea C. G. Molecular hyperpolarizabilities determined from conjugated and nonconjugated organic liquids. *App. Phys. Lett.*, 24:445, 1974.
- [38] Levine B. F. and Bethea C. G. Second and third order hyperpolarizabilities of organic molecules. *J. Chem. Phys.*, 63:2666, 1975.
- [39] Pielak K., Tonnelé C., Sanguinet L., Cariati E., Righetto S., Muccioli L., Castet F., and Champagne B. Dynamical behavior and second harmonic generation responses in acido-triggered molecular switches. *J. Phys. Chem. C*, 122:26160, 2018.
- [40] Lorentz H. A. *The theory of the electrons and its applications to the phenomena of light and radiant heat*. Dover Publications, Inc., New York, 2nd edition, 1952.
- [41] Bersohn R., Pao Y., and Frisch H. L. Double Quantum Light Scattering by Molecules. *J. Chem. Phys.*, 45:3184, 1966.
- [42] Castet F., Bogdan E., Plaquet A., Ducasse L., Champagne B., and Rodriguez V. Reference molecules for nonlinear optics: A joint experimental and theoretical investigation. *J. Chem. Phys.*, 136:024506, 2012.

- [43] Kanis D. R., Ratner M. A., and Marks T. J. Design and construction of molecular assemblies with large second-order optical nonlinearities. Quantum chemical aspects. *Chem. Rev.*, 94:195, 1994.
- [44] Prasad N. P. and William D. J. *Introduction to Nonlinear Optical Effects in Molecules and Polymers*. Wiley: NY, 1991.
- [45] Brédas J. L. and Silbey R. J. *Conjugated Polymers: the Novel Science and Technology of Highly Conducting and Nonlinear Optically Active Materials*. Kluwer: Dordrecht, Neth, 1991.
- [46] Messier J., Kajar F., Prasad P., and D. R. Ulrich. *Nonlinear Optical Effects in Organic Polymers*. Kluwer Academic Publishers, Dordrecht, 1989.
- [47] Chemla D. S. and Zyss J. *Nonlinear Optical Processes in Organic Materials*. Academic Press, NY, 1987.
- [48] Nalwa H. S. and Miyata S. *Nonlinear Optics of Organic Molecules and Polymers*. CRC Press, London, 1996.
- [49] Sales T. R. M., de Melo C. P., and Dossantos M. C. Semi-empirical calculations of hyperpolarizabilities of polyaniline oligomers. *Synt. Met.*, 43:3751, 1991.
- [50] Li D. Q., Ratner M. A., and Marks T. J. Molecular and macromolecular nonlinear optical materials. Probing architecture/electronic structure/frequency doubling relationships via an SCF-LCAO MECI π electron formalism. *J. Am. Chem. Soc.*, 110:1707, 1988.
- [51] de Melo C. P. and Silbey R. Variational-perturbational treatment for the polarizabilities of conjugated chains. II. Hyperpolarizabilities of polyenic chains. *J. Chem. Phys.*, 88:2567, 1988.
- [52] Ramasesha S. and Das P. K. Second harmonic generation coefficients in push-pull polyenes: a model exact study. *Chem. Phys.*, 145:343, 1990.
- [53] Ramasesha S. and Albert I.D.L. A comparative theoretical study of higher harmonic generation and electro-optic effects in polyene systems. *Chem. Phys. Lett.*, 196:287, 1992.
- [54] Albert I.D.L., Das P. K., and Ramasesha S. Second-harmonic generation and electronic structure of polymethineimines: a theoretical study. *Chem. Phys. Lett.*, 176:217, 1991.
- [55] Davies J. A., Elangovan A., Sullivan P. A., Olbricht B. C., Bale D. H., Ewy T. R., Isborn C. M., Eichinger B. E., Robinson B. H., Reid P. J., Li X., and Dalton L. R.

- Rational Enhancement of Second-Order Nonlinearity: Bis-(4-methoxyphenyl)heteroaryl-amino Donor-Based Chromophores: Design, Synthesis, and Electrooptic Activity. *J. Am. Chem. Soc.*, 130:10565, 2008.
- [56] Marder S. R., Cheng L-T, Tiemann B. G., Friedli A. C., Blanchard-Desce M., Perry J. W., and Skindhøj J. Large First Hyperpolarizabilities in Push-Pull Polyenes by Tuning of the Bond Length Alternation and Aromaticity. *Science*, 263:511, 1994.
- [57] Jang S-H, Luo J., Tucker N. M., Leclercq A., Zojer E., Haller M. A., Kim T-D, Kang J-W, Firestone K., Bale D., Lao D., Benedict J. B., Cohen D., Kaminsky W., Kahr B., Brédas J-L, Reid P., Dalton L. R., and Jen A. K-Y. Pyrroline Chromophores for Electro-Optics. *Chem. Mater.*, 18:2982, 2006.
- [58] Parthasarathy V., Pandey R., Stolte M., Ghosh S., Castet F., Würthner F., Das P. K., and Blanchard-Desce M. Combination of Cyanine Behaviour and Giant Hyperpolarisability in Novel Merocyanine Dyes: Beyond the Bond Length Alternation (BLA) Paradigm. *Chem. Eur. J.*, 21:14211, 2015.
- [59] Gorman C. B. and Marder S. R. Effect of Molecular Polarization on Bond-Length Alternation, Linear Polarizability, First and Second Hyperpolarizability in Donor-Acceptor Polyenes as a Function of Chain Length. *Chem. Mater.*, 7:215, 1995.
- [60] Bourhill G., Bredas J-L, Cheng L-T, Marder S. R., Meyers F., Perry J. W., and Tiemann B. G. Experimental Demonstration of the Dependence of the First Hyperpolarizability of Donor-Acceptor-Substituted Polyenes on the Ground-State Polarization and Bond Length Alternation. *J. Am. Chem. Soc.*, 116:2619, 1994.
- [61] Plaquet A., Guillaume M., Champagne B., Castet F., Ducasse L., Pozzo J-L, and Rodriguez V. In silico optimization of merocyanine-spiropyran compounds as second-order nonlinear optical molecular switches. *Phys. Chem. Chem. Phys.*, 10:6223, 2008.
- [62] Marder S. R., Gorman C. B., Tiemann B. G., Perry J. W., Bourhill G., and Mansour K. Relation between bond-length alternation and second electronic hyperpolarizability of conjugated organic molecules. *Science*, 261:186, 1993.
- [63] Bredas J. L., Meyers F., Pierce B. M., and Zyss J. On the second-order polarizability of conjugated π -electron molecules with octupolar symmetry: the case of triaminotrinitrobenzene. *J. Am. Chem. Soc.*, 114:4928, 1992.
- [64] Kim H. M. and Cho B. R. Second-order nonlinear optical properties of octupolar molecules structure-property relationship. *J. Mater. Chem.*, 19:7402, 2009.
- [65] Campo J., Painelli A., Terenziani F., Van Regemorter T., Beljonne D., Goovaerts E., and Wenseleers W. First Hyperpolarizability Dispersion of the Octupolar Molecule Crystal Violet: Multiple Resonances and Vibrational and Solvation Effects. *J. Am. Chem. Soc.*, 132:16467, 2010.

- [66] Castet F., Blanchard-Desce M., Adamietz F., Poronik Y. M., Gryko D. T., and Rodriguez V. Experimental and Theoretical Investigation of the First-order Hyperpolarizability of Octupolar Merocyanines Dyes. *Chem. Phys. Chem.*, 15:2575, 2014.

Theoretical methods

This chapter reviews the theoretical methods employed in this thesis, based on quantum mechanics and classical dynamics. The principles of these methods, as well as the key equations are given to facilitate the understanding. First, the wavefunction methods are introduced from the Schrödinger equation. Then, one of the earliest method, the Hartree-Fock (HF) method, is described, followed by post HF methods accounting for electron correlation. Next, Density Functional Theory (DFT) is described. Methods to evaluate and analyze the second-order NLO properties are presented, the Time-Dependent DFT approach (TD-DFT), a simplified TD-DFT approach and the Finite Field (FF) approach. In the last part, the principles of classical Molecular Dynamics (MD) simulation are presented.

2.1 Wavefunction methods

At the end of the 19th century, electromagnetism and classical mechanics were successful in rationalising all physical phenomena. However, it became soon clear that the behaviour of elementary particles was not governed by classical laws. The Planck “quantisation” (1900)^[1] being the first crack of the classical edifice, it was not long before Newton’s old suggestion of light consisting in particles revived through Einstein’s key experiment of the photoelectric effect (1905)^[2] and subsequent avant-garde light quantum hypothesis. Unravelling the schizophrenic behaviour of light paved the way for the ground breaking proposition of De Broglie who postulated that matter was also subject to the so-called wave-particle duality (1924).^[3] The need for a wave equation to support a wave theory of matter was fulfilled two years later when Schrödinger came up with the most fundamental equation of quantum mechanics.

2.1.1 Schrödinger equation and wavefunction

As a consequence of the probabilistic aspect of the quantum theory, a new mathematical tool, the wavefunction Ψ , was introduced to treat the possible positions of the

particles. This function depends on all the space (\mathbf{r}_i) and spin (σ_i) coordinates of the particles i constituting the system, as well as on the time t . For a system of N particles, the notation $\Psi(\mathbf{x}, t)$ is used in the following, where $\mathbf{x} = \{\mathbf{x}_1, \dots, \mathbf{x}_N\}$ is a contraction of the 4 spin-space coordinates of particle i . Having no physical meaning itself, the square modulus of Ψ represents the probability density for the particles to be distributed in given points of space $\mathbf{r} = \{\mathbf{r}_1, \dots, \mathbf{r}_N\}$ at a time t . Because of this probabilistic interpretation, a normalization constraint is imposed to the wavefunction at any time t :

$$\langle \Psi(\mathbf{x}, t) | \Psi(\mathbf{x}, t) \rangle = \int \dots \int |\Psi(\mathbf{x}, t)|^2 d\mathbf{x} = 1 \quad (2.1)$$

As stated by the first postulate of quantum mechanics, the wavefunction completely defines the state of the system of particles and is sufficient to calculate any of its properties. Considering a typical molecular system composed of N electrons and M nuclei (of coordinates $\mathbf{R} = \{\mathbf{R}_1, \dots, \mathbf{R}_M\}$), the wavefunctions $\Psi(\mathbf{x}, \mathbf{R}, t)$ are found by solving the time-dependent Schrödinger equation:

$$i\hbar \frac{\partial}{\partial t} \Psi(\mathbf{x}, \mathbf{R}, t) = \hat{H}(\mathbf{r}, \mathbf{R}, t) \Psi(\mathbf{x}, \mathbf{R}, t) \quad (2.2)$$

with \hbar the reduced Planck constant and $\hat{H}(\mathbf{r}, \mathbf{R}, t)$ the Hamiltonian of the system. However, one is usually dealing with stationary states so that the \hat{H} operator does not explicitly depend on time. The Schrödinger equation reduces then to its time-independent formulation:^[4]

$$\hat{H}_{tot} \Psi(\mathbf{x}, \mathbf{R}) = E_{tot} \Psi(\mathbf{x}, \mathbf{R}) \quad (2.3)$$

where $\Psi(\mathbf{x}, \mathbf{R})$ is the time-independent wavefunction, E_{tot} is the total energy and \hat{H}_{tot} the total Hamiltonian of the system. The latter can be written as the sum of the kinetic and potential energies of the nuclei and electrons:

$$\hat{H}_{tot} = \hat{T}_n + \hat{T}_e + \hat{V}_{ne} + \hat{V}_{ee} + \hat{V}_{nn} \quad (2.4)$$

with \hat{T}_n and \hat{T}_e the nuclear and electronic kinetic energy operators, \hat{V}_{ne} the attractive interaction between nuclei and electrons, \hat{V}_{ee} the repulsive electron-electron interaction and \hat{V}_{nn} the repulsive interaction between nuclei. In atomic units, \hat{H}_{tot} is defined as:

$$\begin{aligned} \hat{H}_{tot} = & - \sum_{a=1}^M \frac{1}{2m_a} \nabla_a^2 - \sum_{i=1}^N \frac{1}{2} \nabla_i^2 - \sum_{i=1}^N \sum_{a=1}^M \frac{Z_a}{r_{ia}} \\ & + \sum_{i=1}^N \sum_{j>i}^N \frac{1}{r_{ij}} + \sum_{a=1}^M \sum_{b>a}^M \frac{Z_a Z_b}{R_{ab}} \end{aligned} \quad (2.5)$$

where m_a is the mass of the atom a , Z_a and Z_b the nuclei charges of atom a and b respectively, R_{ntab} the distance between the nuclei a and b , r_{ia} the distance between the nucleus a and electron i and r_{ij} the distance between electrons i and j .

Because of the complexity associated with interdependency in the motion of the particles, exact solutions of the Schrödinger equation only exist for a small set of simple quantum systems such as the hydrogen atom or hydrogenoid ions. Therefore, several approximations are typically used, as described below.

2.1.2 Born-Oppenheimer approximation

Considering that the nuclei are moving much more slowly than the electrons, because neutrons and protons are more than 1800 times heavier in mass than electrons, one can assume that the electronic cloud somehow instantaneously adapts to the molecular geometry. Born and Oppenheimer proposed in 1927 to decouple the electronic and nuclear motions.^[5] This approximation, referred to as the Born-Oppenheimer or adiabatic approximation, results in neglecting the kinetic energy of the nuclei (T_n) and considering the interactions between nuclei (V_{nn}) to be a constant for a given geometry. The remaining electronic Hamiltonian depends explicitly on the electron coordinates (only parametrically on the nuclear positions) and is defined as:

$$\hat{H}_{el} = \hat{T}_e + \hat{V}_{ne} + \hat{V}_{ee} \quad (2.6)$$

The total molecular wavefunction can then be factorized as follows:

$$\Psi_{BO}(\mathbf{r}, \mathbf{R}) = \Psi_{elec}(\mathbf{r}, \mathbf{R})\Psi_{nuc}(\mathbf{R}) \quad (2.7)$$

with Ψ_{elec} the electronic wavefunction and Ψ_{nuc} the nuclear wavefunction. Ψ_{elec} is determined by solving the Schrödinger equation for the electrons alone in the field of the fixed nuclei. In this picture, nuclei are moving on a potential energy surface (PES) that is solution of the electronic Schrödinger equation.

In the framework of the Born-Oppenheimer approximation, one still cannot find solutions to the electronic Schrödinger equation for polyatomic systems containing more than one electron and further approximations have to be introduced.

2.1.3 Hartree-Fock method

Based on the variational principle,^[6] which states that the energy of an approximate wavefunction is always higher than the exact energy E_0 , the Hartree-Fock model^[7, 8] allows the determination of the “best” electronic wavefunction Ψ_{elec} , considering that it can be approximated by an antisymmetrised product of N one-electron wavefunctions, *i.e.*, a

unique Slater Determinant:

$$\Psi^{\text{HF}}(\mathbf{x}_1, \dots, \mathbf{x}_N) = \frac{1}{\sqrt{N!}} \begin{vmatrix} \phi_1(\mathbf{x}_1) & \phi_2(\mathbf{x}_1) & \dots & \phi_N(\mathbf{x}_1) \\ \phi_1(\mathbf{x}_2) & \phi_2(\mathbf{x}_2) & \dots & \phi_N(\mathbf{x}_2) \\ \dots & \dots & \dots & \dots \\ \phi_1(\mathbf{x}_N) & \phi_2(\mathbf{x}_N) & \dots & \phi_N(\mathbf{x}_N) \end{vmatrix} \quad (2.8)$$

where the spin-orbitals $\phi(\mathbf{x}_i)$ are defined as the product between a molecular orbital (MO) and a spin function: $\phi(\mathbf{x}_i) = \varphi(\mathbf{r}_i)\xi(\sigma_i)$. From a trial Slater Determinant, the variational principle can be applied to generate the “best” one that minimises the electronic energy, the expected energy being calculated as:

$$E = \langle \Psi_{\text{trial}}^{\text{HF}} | \hat{H} | \Psi_{\text{trial}}^{\text{HF}} \rangle \geq E_0 \quad (2.9)$$

The HF energy is the expectation value of the electronic Hamiltonian operator on the Ψ^{HF} wavefunction. Introducing equation 2.8 into 2.9 gives rise to the following expression:

$$E^{\text{HF}} = \sum_{i=1}^N h_{ii} + \sum_{i=1}^N \sum_{j=1}^N (J_{ij} - K_{ij}) \quad (2.10)$$

where the sums run over the N occupied spin-orbitals ϕ_i and where different integrals are introduced:

$$h_{ii} = \langle \phi_i(\mathbf{r}_i) | \hat{h} | \phi_i(\mathbf{r}_i) \rangle \quad (2.11)$$

is the average energy of an electron in the field of the nuclei (*i.e.*, the sum of the kinetic energy of the electron and the attractive interaction), where $\hat{h} = -\frac{1}{2}\nabla_i^2 - \sum_{a=1}^m \frac{Z_a}{r_{ia}}$ is the one-electron Hamiltonian from the independent model,

$$J_{ij} = \langle \phi_i(\mathbf{r}_i)\phi_j(\mathbf{r}_j) | \frac{1}{r_{ij}} | \phi_i(\mathbf{r}_i)\phi_j(\mathbf{r}_j) \rangle \quad (2.12)$$

is the Coulomb integral, describing the electrostatic repulsion between two the electronic density distributions $|\phi_i(\mathbf{r}_i)|^2$ and $|\phi_j(\mathbf{r}_j)|^2$ created by electrons i and j , and

$$K_{ij} = \langle \phi_i(\mathbf{r}_i)\phi_j(\mathbf{r}_i) | \frac{1}{r_{ij}} | \phi_j(\mathbf{r}_j)\phi_i(\mathbf{r}_j) \rangle \quad (2.13)$$

is the exchange integral, which has no classical equivalent and arises from the antisymmetry condition imposed to the wavefunction.

By minimising the expectation value of the energy via the variational method, one can show that the optimal spin-orbitals ϕ_i are eigenfunctions of the effective one-electron

Fock operator \hat{f}_i and satisfies the so-called Hartree-Fock equations:

$$\hat{f}_i \phi_i = \varepsilon_i \phi_i \quad (2.14)$$

where ε_i is the energy of the spin-orbital ϕ_i and the Fock operator is expressed as:

$$\hat{f}_i = \hat{h}_i + \sum_{j=1}^N (\hat{J}_j - \hat{K}_j) \quad (2.15)$$

in which \hat{J}_j and \hat{K}_j are the Coulomb and Exchange operators, defined below with respect to their action on a spin-orbital ϕ_i :

$$\hat{J}_j \phi_i(\mathbf{r}_i) = \left(\langle \phi_j(\mathbf{r}_j) | \frac{1}{r_{ij}} | \phi_j(\mathbf{r}_j) \rangle \right) \phi_i(\mathbf{r}_i) \quad (2.16)$$

$$\hat{K}_j \phi_i(\mathbf{r}_i) = \left(\langle \phi_j(\mathbf{r}_j) | \frac{1}{r_{ij}} | \phi_i(\mathbf{r}_j) \rangle \right) \phi_j(\mathbf{r}_i) \quad (2.17)$$

As evidenced by the above equations, the Coulomb operator, which accounts for the interaction between an electron at position \mathbf{r}_i and the average charge distribution of another electron in the spin-orbital ϕ_j , is multiplicative, while the exchange operator is non-multiplicative as it involves a permutation between the coordinates of electrons i and j .

The equations above clearly evidence that, in the HF framework, each electron is moving in the *average* electrostatic field created by all the other electrons. Moreover, one can notice that the term $i = j$ is allowed in the double summation of equation 2.9, meaning that the HF energy includes the interaction of an electron with itself. As a consequence, the Coulomb integral will not be equal to zero even if one computes the energy of a one-electron system, where there is obviously strictly no electron-electron repulsion. This physical nonsense, known as the self-interaction error, is well handled in the HF formalism as for $i = j$ Coulomb and exchange terms are strictly equal and therefore exactly cancel. But we will see in Section 2.2 that the balance between exchange and correlation becomes a major issue in the Density Functional Theory (DFT).

As the Fock operator depends on the orbitals that themselves enter the expression of the Coulomb and exchange operators, the problem has to be solved by an iterative procedure referred to as the Hartree-Fock Self-Consistent Field (SCF). Starting from a set of N trial spin-orbitals $\phi_i^{(trial)}$, the energy $E^{(trial)}$ is calculated. In a second step, the Fock operator $\hat{f}_i^{(1)}$ is formed and the Hartree-Fock equations solved, giving a new set of spin-orbitals $\phi_i^{(1)}$ that is used in the next iteration where a new energy $E^{(1)}$ is calculated, as well as a new Fock operator $\hat{f}_i^{(2)}$. This cycle continues until the new set of orbitals differs by less than a predefined threshold from the orbitals used to build the Fock operator, *i.e.*

until self-consistency is reached.

2.1.4 Roothaan-Hall approximation

If the method briefly described above is sufficient in the case of atoms and some diatomic molecules, one has to rely on the Roothaan-Hall approximation^[9, 10] to solve the Hartree-Fock equations for non linear molecules. In this formalism, the molecular orbitals φ_i are expanded as linear combinations of a finite number of known basis functions χ_p centered on the atomic nuclei, usually referred to as atomic orbitals even if their mathematical definition is more general:

$$\varphi_i = \sum_p^K C_{pi} \chi_p \quad (2.18)$$

The expansion coefficients C_{pi} gives the weight of the p-th atomic orbital χ_p in the i-th molecular orbital φ_i and K is the dimension of the basis set, *i.e.* the number of basis functions. Note that the use of a complete basis set (*i.e.* $K = \infty$) leads to the wavefunction corresponding to the lowest possible energy within the HF approach, referred to as the Hartree-Fock limit.

Substituting the MO expansion (equation 2.18) in the Hartree-Fock equations yields:

$$\hat{f}_i \left(\sum_p^K C_{pi} \chi_p \right) = \varepsilon_i \sum_p^K C_{pi} \chi_p \quad (2.19)$$

Multiplying by χ_q on both sides and integrating leads to the Roothaan-Hall equations:

$$\sum_p^K C_{pi} \langle \chi_p | \hat{f}_i | \chi_q \rangle = \varepsilon_i \sum_p^K C_{pi} \langle \chi_p | \chi_q \rangle \quad (2.20)$$

That can be expressed in the matrix form:

$$\mathbf{fC} = \varepsilon \mathbf{SC} \quad (2.21)$$

where \mathbf{S} is the overlap matrix with elements $S_{pq} = \langle \chi_p | \chi_q \rangle$ and \mathbf{f} is the Fock matrix with elements f_{pq} given by :

$$f_{pq} = \langle \chi_p | \hat{h} | \chi_q \rangle + \sum_j^N \left(2 \langle \chi_p | \hat{J}_j | \chi_q \rangle - \langle \chi_p | \hat{K}_j | \chi_q \rangle \right) \quad (2.22)$$

Using the expressions of the Coulomb and exchange operator (equations 2.16 and 2.17)

and the Roothan expansion of the MOs $\varphi_j(\mathbf{r}_j)$,

$$f_{pq} = h_{pq} + \sum_j^N \sum_r^K \sum_s^K C_{jr} C_{js} [2(pq|rs) - (pr|qs)] \quad (2.23)$$

where the first term $h_{pq} = \langle \chi_p | \hat{h} | \chi_q \rangle$ accounts for the one electron part, while the $(pq|rs)$ and $(pr|qs)$ terms correspond respectively to the two-electron Coulomb and exchange integrals, written using the standard chemist's notation:

$$(pq|rs) = \iint \chi_p(\mathbf{r}_i) \chi_q^*(\mathbf{r}_i) \frac{1}{r_{ij}} \chi_r(\mathbf{r}_j) \chi_s^*(\mathbf{r}_j) d\mathbf{r}_i d\mathbf{r}_j \quad (2.24)$$

The orbitals χ_p and χ_q associated to electron number 1 are centered on atoms p and q , and equivalently, the orbitals χ_r and χ_s associated to electron number 2 are centered on the atoms r and s .

The expansion coefficients obtained by solving the Roothaan-Hall equations also appear in the definition of the Fock operator, so that these coefficients serve as adjustable parameters in a SCF iteration procedure. Given a defined basis set, an initial guess is made for the C_{pi} coefficients and the f_{pq} elements are calculated. By diagonalisation of the $f_{pq} - \varepsilon_i S_{pq}$ matrix, one can determine the ε_i and generate a new set of expansion coefficients, used in turn to define a new Fock operator and so on. The procedure stops when a predefined convergence criterion is reached (generally comparing the difference in the “new” and “old” total energies).

2.1.5 Electron correlation and post Hartree-Fock methods

By considering, through the Fock operator, that each electron is moving in the average electrostatic field created by all the other electrons, the Hartree-Fock method improperly treats the correlation between the motion of the electrons, as the instantaneous repulsion between them is neglected. Consequently, electrons virtually get “too close” to one another and the electron-electron repulsion energy is overestimated, and so is the electronic energy. The difference between the HF limit E_{HF} and the exact energy E_{exact} is the so-called electron correlation energy:

$$E_{corr} = E_{exact} - E_{HF} \quad (2.25)$$

Two contributions to the correlation are generally distinguished: the Fermi correlation, that deals with electrons of same spin, and the Coulomb correlation, that accounts for interactions between all electrons. While the HF approximation accounts for exchange interactions (inherent to the antisymmetric nature of the wavefunction, *i.e.* the Slater Determinant) and Fermi correlation, the Coulomb correlation is completely neglected.

As a matter of fact, provided one is using an extended basis set to solve the HF equations, 99% of the total energy can be accounted for. However, the missing $\sim 1\%$ corresponding to Coulomb correlation may turn out to be determining in the description of some properties, including the NLO responses that are the subject of this thesis. Using HF method as starting point, several post Hartree-Fock methods^[11] have been developed to improve E_{corr} to various extents. Among these, the Møller-Plesset Perturbation Theory (MPx), used in this thesis, is reviewed in detail in the following section. Note that other approaches, not described here, are also available such as Configuration Interaction (CI), Multi-Configuration Self-consistent Field (MCSCF), and Coupled-Cluster Theory (CC).^[11, 12]

2.1.6 Møller-Plesset Perturbation Theory

The Møller-Plesset (MPx) Perturbation Theory method is based on the Rayleigh-Schrödinger perturbation theory. It treats electron correlation as a perturbation to the zeroth-order Hartree-Fock Hamiltonian. The total and exact Hamiltonian is divided into the unperturbed Hamiltonian \hat{H}_0 and the perturbation $\lambda\hat{H}'$, as follows:

$$\hat{H} = \hat{H}_0 + \lambda\hat{H}' \quad (2.26)$$

where λ is an ordering parameter that is eventually set equal to 1 and $\lambda\hat{H}'$ is small with respect to \hat{H}_0 . The unperturbed Hamiltonian \hat{H}_0 is defined as the HF Hamiltonian, expressed as the sum of Fock operators defined in equation 2.15:

$$\hat{H}_0 = \sum_{i=1}^N \hat{f}_i \quad (2.27)$$

Thus, the perturbation $\lambda\hat{H}'$ is the difference between the exact electronic Hamiltonian and the HF Hamiltonian. From the Schrödinger equation, the problem to be solved is:

$$(\hat{H}_0 + \lambda\hat{H}')|\Psi\rangle = E|\Psi\rangle \quad (2.28)$$

According to the Rayleigh-Schrödinger perturbation theory, the exact wavefunction and energy can be expanded in Taylor series of λ :

$$|\Psi\rangle = |\Psi^{(0)}\rangle + \lambda|\Psi^{(1)}\rangle + \lambda^2|\Psi^{(2)}\rangle + \lambda^3|\Psi^{(3)}\rangle + \dots \quad (2.29)$$

$$E = E^{(0)} + \lambda E^{(1)} + \lambda^2 E^{(2)} + \lambda^3 E^{(3)} + \dots \quad (2.30)$$

For non-degenerated states, the n^{th} -order energy terms $E^{(n)}$ are expressed in term of the $(n-1)^{\text{th}}$ order wavefunction $|\Psi^{(n-1)}\rangle$:

$$E^{(0)} = \langle \Psi^{(0)} | \hat{H}_0 | \Psi^{(0)} \rangle \quad (2.31)$$

$$E^{(1)} = \langle \Psi^{(0)} | \lambda \hat{H}' | \Psi^{(0)} \rangle \quad (2.32)$$

$$E^{(2)} = \langle \Psi^{(0)} | \lambda \hat{H}' | \Psi^{(1)} \rangle \quad (2.33)$$

...

Thus, the HF ground state energy is simply the sum of the zeroth- and first-order energies:

$$E^{\text{HF}} = E^{(0)} + \lambda E^{(1)} \quad (2.34)$$

The correlation energy can then be written as:

$$E_{\text{corr}} = \lambda^2 E^{(2)} + \lambda^3 E^{(3)} + \lambda^4 E^{(4)} + \dots \quad (2.35)$$

The first improvement to the HF energy, and the dominant one, is the second-order energy $E^{(2)}$, expressed as:

$$E^{(2)} = \sum_{i>j} \sum_{a>b} \frac{|\langle ab|ij\rangle - \langle ab|ji\rangle|^2}{\varepsilon_i + \varepsilon_j - \varepsilon_a - \varepsilon_b} \quad (2.36)$$

where i, j stand for occupied MOs, while a, b stand for unoccupied ones. $E^{(2)}$ contains the major part of the electron correlation correction. The highest order corrections are generally smaller. The MP2 energy is finally given by a sum of two terms:

$$E_{\text{MP2}} = E_{\text{HF}} + \lambda^2 E^{(2)} \quad (2.37)$$

MP n methods (MP2 and higher orders: MP3, MP4, ...) are known to demonstrate an oscillatory convergence behavior, in which the MP n energies can either underestimate or overestimate the exact energy as illustrated in Figure 2.1.

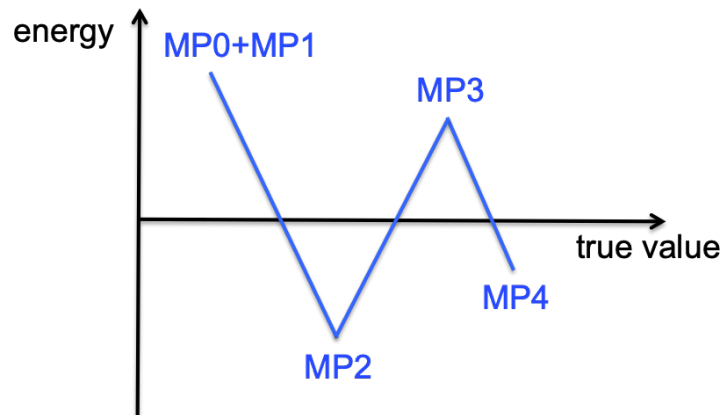


Figure 2.1 – Oscillating convergence behavior of the total ground state energy obtained with MP n methods. The true value is the exact electronic energy in the Born-Oppenheimer approximation (Figure inspired from ref. [13]).

2.2 Density Functional Theory

Although the wavefunction Ψ is the key to all information one would like to obtain about a particular system, this is a rather unintuitive and complex quantity that depends on three spatial and one spin coordinates for each electron. From now on, the coordinates of a single electron, previously noted \mathbf{r}_i and \mathbf{r}_j , will be written \mathbf{r} and \mathbf{r}' for simplicity. Recalling that the Hamiltonian only depends on the positions and charges of the nuclei and on the number of electrons in the system, the one-electron density of the system, $\rho(\mathbf{r})$, appears to be a good alternative to the N -electron wavefunction for describing the state of a system, since it is a function of only three spatial coordinates, which does not grow in complexity as a function of the number of electrons N . The integration of $\rho(\mathbf{r})$ over all space gives the total number of electrons N of the system:

$$\int \rho(\mathbf{r}) d\mathbf{r} = N \quad (2.38)$$

The year 1927 marks the very first step of electron density based approaches with the work of Thomas^[14] and Fermi.^[15] In their model, a classical expression is used for the nuclear-electron and electron-electron potentials while the kinetic energy of electrons, based on an uniform electron gas (*i.e.* constant electron density), is derived from a quantum statistical model. The Thomas-Fermi expression of the energy as a function of $\rho(\mathbf{r})$ yields:

$$E_{TF}[\rho] = \frac{3}{10}(3\pi^2)^{2/3} \int \rho(\mathbf{r})^{5/3} d\mathbf{r} - Z \int \frac{\rho(\mathbf{r})}{\mathbf{r}} d\mathbf{r} + \frac{1}{2} \iint \frac{\rho(\mathbf{r})\rho(\mathbf{r}')}{|\mathbf{r} - \mathbf{r}'|} d\mathbf{r}d\mathbf{r}' \quad (2.39)$$

Improvement was attempted by Dirac,^[16] who included an exchange term in the expression (first derived by Bloch^[17]), yielding the Thomas-Fermi-Dirac model, which proved to be still not satisfactory.^[18] Although these models are not showing themselves to be reliable and practically useful, as they predict molecules to be unstable relative to their separated constituents (no chemical bonds!), they constituted the first attempts to express the energy solely from the electron density of the system. Decades later, Hohenberg and Kohn were to lay the foundations of modern density functional theory.^[19]

2.2.1 Hohenberg-Kohn theorems

The first Hohenberg-Kohn theorem, often referred to as the “proof of existence”, states that, considering a system of electrons moving in an external field $v_{ext}(\mathbf{r})$, “*the external potential $v_{ext}(\mathbf{r})$ is (to within a constant) a unique functional of $\rho(\mathbf{r})$; since, in turn $v_{ext}(\mathbf{r})$ fixes \hat{H} we see that the full many particle ground state is a unique functional of $\rho(\mathbf{r})$* ”. In other terms, a given electron density $\rho(\mathbf{r})$ uniquely determines the Hamiltonian operator and consequently the wavefunction and all electronic properties of the system.

In this framework, the electronic energy is expressed as a functional of $\rho(\mathbf{r})$:

$$E[\rho] = \underbrace{T_e[\rho] + E_{ee}[\rho]}_{F_{HK}[\rho]} + E_{ne}[\rho] \quad (2.40)$$

While the nuclear-electron attractive potential $E_{ne}[\rho]$ is system dependent, the Hohenberg-Kohn functional $F_{HK}[\rho]$, constituted by the kinetic energy term and the repulsion between electrons, is a universal functional.

According to the second theorem, “ $E[\rho]$ assumes its minimum value for the correct $\rho(\mathbf{r})$, if the admissible functions are restricted by the condition $N = \int \rho(\mathbf{r}) d\mathbf{r}$ ”. It is nothing but a statement of the variational principle, already used in the wavefunction models, for the density. It implies that any trial electron density ρ_{trial} will always give an energy larger than the true ground-state energy. Assuming that the $F_{HK}[\rho]$ functional is exact, it delivers the ground-state energy minimum of the system if and only if the input electron density is the true ground-state density.

2.2.2 Kohn-Sham formalism

The main reason for the failure of Thomas-Fermi like approaches lies in the expression of the kinetic energy $T_e[\rho]$ within the homogeneous gas model as well as in the classical treatment of electron interactions. On the basis of the cornerstone’s HK theorems, Kohn and Sham^[20] proposed in 1965 an approach to recast the equations into a solvable and practical form.

Considering a fictitious system of N non-interacting electrons moving in an external potential $v_{ext}(\mathbf{r})$, that can be exactly represented by a Slater determinant of N spin-orbitals ϕ_i (referred to as the Kohn-Sham spin-orbitals), one can express the kinetic energy of the non-interacting system:

$$T_{ni} = \sum_{i=1}^N \langle \phi_i | -\frac{1}{2} \nabla_i^2 | \phi_i \rangle \quad (2.41)$$

and define its electronic density as:

$$\rho(\mathbf{r}) = \sum_{i=1}^N |\phi_i(\mathbf{r})|^2 \quad (2.42)$$

Even if, as already mentioned, the universal functional $F_{HK}[\rho]$ is unknown, one can define the effective potential $v_{eff}(\mathbf{r})$ that will render the density and energy of the fictitious non-interacting reference system identical to the one of the real interacting system such

that the energy functional can be written as:

$$E[\rho] = T_{ni}[\rho] + E_{ee}[\rho] + E_{ne}[\rho] + \Delta T[\rho] \quad (2.43)$$

where $T_{ni}[\rho]$ is the kinetic energy of the non-interacting system, $E_{ee}[\rho] = J[\rho] + E_{nc}[\rho]$ (with $J[\rho]$ the classical electron-electron repulsion and $E_{nc}[\rho]$ the non-classical part including exchange and electron correlation effects), $E_{ne}[\rho]$ is the nuclear-electron potential energy, and $\Delta T[\rho]$ the correction to the kinetic energy, necessary to account for the interacting nature of the electrons. One can rewrite the DFT energy as:

$$E[\rho] = T_{ni}[\rho] + J[\rho] + E_{ne}[\rho] + E_{xc}[\rho] \quad (2.44)$$

where $E_{xc}[\rho]$ is the so-called exchange-correlation term that exists, as demonstrated by the HK theorem, but whose exact expression remains unknown.

Assuming that $E_{xc}[\rho]$ is known, the problem can then be solved in a similar way as done for the HF model. The Kohn-Sham orbitals ϕ_i (linear combination of the basis functions) that minimise the energy satisfy the pseudo-eigenvalue equations:

$$\hat{f}_i^{KS} \phi_i = \varepsilon_i \phi_i \quad (2.45)$$

where the Kohn-Sham one-electron operator \hat{f}_i^{KS} is defined as:

$$\hat{f}_i^{KS} = -\frac{1}{2}\nabla_i^2 + v_{eff}(\mathbf{r}) \quad (2.46)$$

and the effective external potential $v_{eff}(\mathbf{r})$ is defined as:

$$v_{eff}(\mathbf{r}) = \int \frac{\rho(\mathbf{r}')}{|\mathbf{r} - \mathbf{r}'|} d\mathbf{r}' - \sum_a^{nuclei} \frac{Z_a}{r_{ia}} + v_{xc}(\mathbf{r}) \quad (2.47)$$

with:

$$v_{xc}(\mathbf{r}) = \frac{\partial E_{xc}[\rho]}{\partial \rho(\mathbf{r})} \quad (2.48)$$

The KS potential $v_{eff}(\mathbf{r})$ depends explicitly on the density via the Coulomb term and just like in HF, the problem has to be solved iteratively. Given a trial density, one can calculate the effective potential and solve the Kohn-Sham equations. The resulting orbitals ϕ_i give a new electron density (equation 2.42) that can be used to calculate a new effective potential and so on until a predefined threshold is reached. However, the exact expression of $E_{xc}[\rho]$ is unfortunately not known and its approximate determination constitutes the key issue to DFT improvement.

2.2.3 Exchange-correlation functionals

If $E_{xc}[\rho]$ was exactly known, one would be able to calculate the true energy of a system, electron correlation included. $E_{xc}[\rho]$ can formally be defined by making equivalent the energies of the real and fictitious systems:

$$E_{xc}[\rho] = (T_e[\rho] - T_{ni}[\rho]) + (E_{ee}[\rho] - J[\rho]) \quad (2.49)$$

Its name might be a bit misleading as it does not only account for the non classical portion of the electron-electron interaction, but also includes the correction for the self-interaction error, and the missing part of the true kinetic energy arising from the non-interacting electrons approximation. Up to now, its exact expression remains the holy grail of DFT and one has to rely on approximations, the quality of the resulting energy thus depending on the accuracy of the functional form chosen. There exists no systematic strategy to improve a functional, and even more dramatic, violation of required physical conditions in its expression does not necessarily lead to less accurate results.

Several improvements have been achieved since exchange-correlation functionals started being developed, and each new level of approximation has been associated by John P. Perdew to the mythical Jacob's ladder rungs,^[21] each one allowing to recover the results of lower rungs while adding capabilities (Figure 2.2).

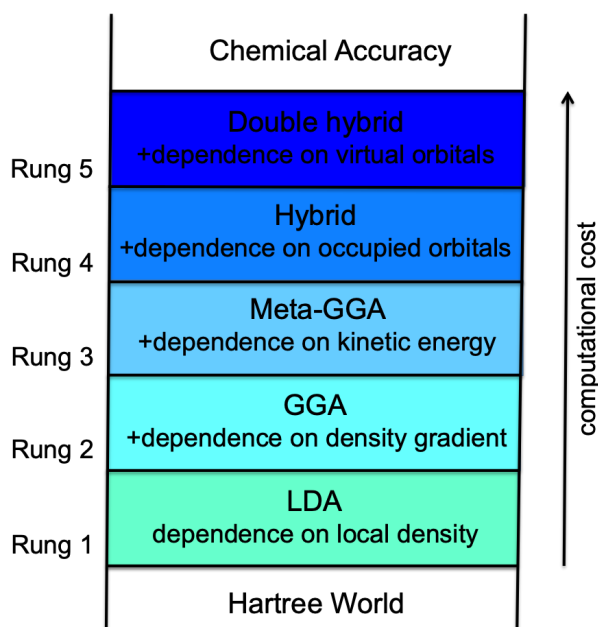


Figure 2.2 – Jacob's ladder of DFT.

The assumption is generally made that exchange and correlation contributions are separable and the exchange-correlation energy functional can conveniently be expressed as:

$$\begin{aligned}
E_{xc}[\rho] &= \int \rho(\mathbf{r})\varepsilon_{xc}[\rho(\mathbf{r})]\mathbf{d}\mathbf{r} \\
&= E_x[\rho] + E_c[\rho] \\
&= \int \rho(\mathbf{r})\varepsilon_x[\rho(\mathbf{r})]\mathbf{d}\mathbf{r} + \int \rho(\mathbf{r})\varepsilon_c[\rho(\mathbf{r})]\mathbf{d}\mathbf{r}
\end{aligned}
\tag{2.50}$$

where $\varepsilon_x[\rho(\mathbf{r})]$ and $\varepsilon_c[\rho(\mathbf{r})]$ are the exchange and correlation energy densities per particle.

2.2.3.1 Local (Spin) Density Approximation (L(S)DA)

The local density approximation is based on the model that gave birth to DFT, the uniform electron gas, where the density is considered to be locally constant, and it is assumed that the exchange and correlation potentials at a certain position depend only on the local value of this density, so that the exchange-correlation energy functional can be written as:

$$E_{xc}^{LDA}[\rho] = \int \rho(\mathbf{r})[\varepsilon_{xc}^{LDA}(\rho)]\mathbf{d}\mathbf{r} \tag{2.51}$$

where the exchange part (of a uniform electron gas) is exactly known and given by the Dirac formula^[15]:

$$E_x[\rho] = -\frac{3}{4} \left(\frac{3}{\pi}\right)^{1/3} \int \rho^{4/3}\mathbf{d}\mathbf{r} \tag{2.52}$$

while there is no explicit form known for the correlation energy. Monte Carlo simulations of the homogenous electron gas have been performed by Ceperley and Alder^[22] to numerically determine the correlation energy at very high accuracy. From this work, correlation functionals have been developed by Vosko, Wilk and Nusair^[23] (VWN) or Perdew and Wang (PW).^[24]

Explicit introduction of the spin is achieved by defining ε_{xc} respective to a sum of α and β densities:

$$E_{xc}^{LSDA}[\rho_\alpha, \rho_\beta] = \int \rho(\mathbf{r})[\varepsilon_{xc}^{LDA}(\rho_\alpha(\mathbf{r}), \rho_\beta(\mathbf{r}))]\mathbf{d}\mathbf{r} \tag{2.53}$$

Being based on the crude approximation of the uniform electron gas, which might be reasonable for metals, L(S)DA does not perform well for molecules, notably overestimating the bond energies and describing very poorly breaking or forming of bonds.

2.2.3.2 Generalized Gradient Approximation (GGA)

In molecular systems, the electronic density is far from being uniform and improvements over the L(S)DA have to account for the non-homogeneity of the true density. This is done within the Generalized Gradient Approximation by considering a dependency for

ε_{xc} not only on the density, but also on the gradient of the density $\nabla\rho$, *i.e.* allowing the density to locally change.

$$E_{xc}^{GGA}[\rho, \nabla\rho] = \int \rho(\mathbf{r})[\varepsilon_{xc}^{GGA}(\rho, \nabla\rho)]\mathbf{d}\mathbf{r} \quad (2.54)$$

The majority of the GGA exchange-correlation functionals are constructed by adding a correction term to the L(S)DA functional, treating separately exchange and correlation parts. Note that these functionals have a rather complicated mathematical form that is chosen upon the quality and accuracy of the results, not the physics behind. Two approaches for their development have to be distinguished: a semi-empirical one, with parameters fitted to reproduce experimental data, among which the popular BLYP functional (Becke exchange functional^[25] and Lee, Yang, Parr correlation functional^[26]), and a non-empirical one like PW91^[27] (Perdew and Wang) and PBE^[28] (Perdew-Becke-Ernzenhof).

A step further was achieved with the meta-GGA functionals, which include a dependency over the second-order derivatives of the density, though the associated computational cost and numerical stability problems do not necessarily translate into improved results. Although all these functionals constitute a great improvement over the L(S)DA method, some efforts were still to be made to reach better accuracy and this motivated the development of hybrid functionals.

2.2.3.3 Hybrid functionals

Both LDA and GGA functionals poorly describe the exchange part. To correct this shortcoming, Becke proposed to introduce a part of HF exchange into GGA exchange-correlation functionals, because HF exchange is non-local and presents the exact $-1/r$ asymptotic behavior (with $r = |\mathbf{r}-\mathbf{r}'|$), thus allowing to compensate the Coulomb part and to reduce the self-interaction error. That strategy provided the global hybrid functionals, in which the % of the HF exchange (a) is constant for any inter-electronic distances:

$$E_{xc}^{hybrid} = aE_x^{HF} + (1 - a)E_x^{DFT} + E_c^{DFT} \quad (2.55)$$

with $0 \leq a \leq 1$. When $a = 1$, the electrons are totally uncorrelated and, a single Slater Determinant of Kohn-Sham orbitals being the exact wavefunction of the system, the exchange energy that remains is given exactly by the HF theory. For $a = 0$, the fully interacting system can be approximated by L(S)DA or GGA functionals.

Several attempts have been made where additional parameters weighting the contributions of L(S)DA and GGA exchange and correlation are determined together with the parameter a . Among the wide panel of hybrid functionals available, the most famous

and widely used B3LYP^[29] functional, has the following expression:

$$E_{xc} = (1 - a)E_x^{LSDA} + aE_x^{HF} + b\Delta E_x^B + (1 - c)E_c^{LSDA} + cE_c^{LYP} \quad (2.56)$$

where the parameters a , b and c , set respectively to 0.2, 0.72 and 0.81, have not been optimised as they are simply taken from the older B3PW91 functional without further fitting of experimental data. E_x^{LSDA} and E_c^{LSDA} are the exchange and correlation at the LSDA level, E_x^{HF} the HartreeFock exchange, E_x^B the Becke exchange and E_c^{LYP} the Lee, Yang, Parr correlation energy. The average absolute error on atomisation energies (using a large basis set) of the B3LYP functional is only of about 2 kcal.mol⁻¹.^[30] However, in practice, one always has to chose the functional as carefully as possible accordingly to the system treated and the properties investigated.

2.2.3.4 Long-range corrected functionals

Certain failures of the aforementioned functionals, such as the inability to deal with charge-transfer excitations, are understood to arise from the incorrect long-range behaviour of the exchange potential. One way to achieve the correct asymptotic behaviour, is to introduce a partitioning of the Coulomb operator, in the exchange interaction, into short- and long-range components.

Contrary to global hybrids introduced in the previous section, in which the amount of exact HF exchange is fixed, long-range corrected (LRC) functionals, also referred to as range-separated (RS) hybrids, include HF exchange by means of a weighting function that depends on the interelectron distance r . The Coulomb operator is thus split into local and nonlocal parts using a smooth function, usually being the error function, together with a range separation parameter ω , which damps the exchange contribution from the density functional and complements it with exact HF exchange:

$$\frac{1}{r} = \frac{1 - \alpha_1 - \alpha_2 \text{erf}(\omega r)}{r} + \frac{\alpha_1 + \alpha_2 \text{erf}(\omega r)}{r} \quad (2.57)$$

with $0 \leq \alpha_1 + \alpha_2 \leq 1$ and $0 \leq \alpha_2 \leq 1$. The first term accounts for the short-range part of the Coulomb operator by DFT exchange while the second term describes long-range interactions with the exact HF exchange.

Thus, at long range, the amount of HF exchange equals $\alpha_1 + \alpha_2$, and subsequently the amount of DFT exchange equals $1 - \alpha_1 - \alpha_2$. The parameter α_1 allows, if non zero, to retain a fraction of DFT exchange in the asymptotic limit ($r \rightarrow \infty$) and corresponds to the amount of HF exchange at short range. The α_1 , α_2 and ω parameters of LRC functionals considered in this thesis are provided in Table 2.1. LC-BLYP^[31] appoints 100% of HF exchange at infinite distance and no HF exchange at distance zero, CAM-B3LYP^[32] uses the Coulomb-attenuating method and includes 19% of HF exchange at

short-range and 65% at long-range and ω B97X-D^[33] includes respectively 22.20% and 77.80% of HF exchange at short- and long-range. This last functional also incorporates empirical atom–atom dispersion corrections, though independent of applied external fields.

LRC functionals	α_1	α_2	ω_{std}
LC-BLYP	0.000	1.000	0.470
CAM-B3LYP	0.190	0.460	0.330
ω B97X-D	0.222	0.778	0.200

Table 2.1 – LRC functionals employed in this thesis, with their standard parameters α_1 , α_2 and ω_{std} (bohr⁻¹).

2.3 Calculation of the first hyperpolarizability

2.3.1 Coupled Perturbed Hartree-Fock (CPHF) and Coupled Perturbed Kohn-Sham (CPKS)

2.3.1.1 Static molecular properties

The CPHF and CPKS methods are applied in order to evaluate static molecular properties. Consider the unperturbed molecular Hamiltonian $\hat{H}_0 = \hat{T}_e + \hat{V}_{ne} + \hat{V}_{ee}$ and apply a static perturbation $\hat{V}(x)$:

$$\hat{H}(x) = \hat{H}_0 + \hat{V}(x) \quad (2.58)$$

where x represents the strength of the perturbation. The perturbation vanishes for $x = 0$, *i.e.* $\hat{V}(x = 0) = 0$. The perturbed energy for the perturbed state considered $\Psi(x)$ (usually the ground state) can be expanded with respect to x :

$$E(x) = \frac{\langle \Psi(x) | \hat{H}(x) | \Psi(x) \rangle}{\langle \Psi(x) | \Psi(x) \rangle} = E^{(0)} + E^{(1)}x + \frac{1}{2}E^{(2)}x^2 + \dots \quad (2.59)$$

where $E^{(0)}$ is the unperturbed energy and $E^{(1)}$, $E^{(2)}$, \dots are the energy derivatives with respect to x :

$$E^{(1)} = \left. \frac{\partial E}{\partial x} \right|_{x=0}; \quad E^{(2)} = \left. \frac{\partial^2 E}{\partial x^2} \right|_{x=0}; \quad \dots \quad (2.60)$$

These derivatives describe the static (or time-independent) molecular properties. In the case of electric properties, the perturbation strengths x are the components of the external static electric field F_i . The electric dipole moment, the polarizability and the first hyperpolarisability are thus given by:

$$\left. \frac{\partial E}{\partial F_i} \right|_{\mathbf{F}=\mathbf{0}} = -\mu_i \quad (2.61)$$

$$\left. \frac{\partial^2 E}{\partial F_i \partial F_j} \right|_{\mathbf{F}=\mathbf{0}} = -\alpha_{ij} \quad (2.62)$$

$$\left. \frac{\partial^3 E}{\partial F_i \partial F_j \partial F_k} \right|_{\mathbf{F}=\mathbf{0}} = -\beta_{ijk} \quad (2.63)$$

2.3.1.2 General static response theory

In order to compute such derivatives of the energy, two methods are available: finite field differentiation and analytical derivatives. Contrary to the finite-field method (discussed in Section 2.3.4) where finite field differentiation is used, the derivatives of the energy in the latter approach are calculated explicitly from analytical expressions. This method is more difficult to implement but is more precise, generally less computer-intensive and can also provide time-dependent molecular properties. A general static response theory is necessary to obtain these analytical expressions. In an electronic-structure method, the energy $E(x)$ is obtained by optimizing parameters $\mathbf{p} = (p_1, p_2, \dots)$ in an energy function $\varepsilon(x, \mathbf{p})$ for each fixed value of x . The energy is thus given by:

$$E(x) = \varepsilon(x, \mathbf{p}^o(x)) \quad (2.64)$$

where $\mathbf{p}^o(x)$ are the optimal values of the parameters. Note that the optimization is not necessarily variational. Nevertheless, in the case of Coupled Perturbed Hartree-Fock^[34, 35] (CPHF) and Coupled Perturbed Kohn-Sham (CPKS), the optimization is variational and \mathbf{p} are the orbital rotation parameters, that will be defined in the next section. The first-order derivative of $E(x)$ with respect to x is:

$$\frac{\partial E(x)}{\partial x} = \underbrace{\frac{\partial \varepsilon(x, \mathbf{p}^o)}{\partial x}}_{\text{explicit dependence on } x} + \underbrace{\sum_i \left. \frac{\partial \varepsilon(x, \mathbf{p})}{\partial p_i} \right|_{\mathbf{p}=\mathbf{p}^o}}_{\text{implicit dependence on } x} \frac{\partial p_i^o}{\partial x} \quad (2.65)$$

$\partial p_i^o / \partial x$ is called the linear-response vector and contains information about how the wavefunction changes when the system is perturbed. This term is not straightforward to calculate, since the explicit dependence of p_i^o on x is not known. If all the parameters are variational, the zero electronic gradient condition simplifies the derivative, and the linear-response vector does not need to be calculated owing to:

$$\left. \frac{\partial \varepsilon(x, \mathbf{p})}{\partial p_i} \right|_{\mathbf{p}=\mathbf{p}^o} = 0 \implies \frac{\partial E(x)}{\partial x} = \frac{\partial \varepsilon(x, \mathbf{p}^o)}{\partial x} \quad (2.66)$$

The second-order derivative of $E(x)$ is then expressed as:

$$\frac{\partial^2 E(x)}{\partial x^2} = \frac{\partial^2 \varepsilon(x, \mathbf{p}^o)}{\partial x^2} + \sum_i \left. \frac{\partial^2 \varepsilon(x, \mathbf{p})}{\partial x \partial p_i} \right|_{\mathbf{p}=\mathbf{p}^o} \frac{\partial p_i^o}{\partial x} \quad (2.67)$$

Here, the linear-response vector $\partial p_i^o/\partial x$ needs to be calculated. To obtain it when all the parameters are variational, we start from the stationary condition which is true for all x :

$$\forall x, \quad \left. \frac{\partial \varepsilon(x, \mathbf{p})}{\partial p_i} \right|_{\mathbf{p}=\mathbf{p}^o} = 0 \quad (2.68)$$

We can thus take the derivative of this equation with respect to x :

$$\left. \frac{\partial^2 \varepsilon(x, \mathbf{p})}{\partial x \partial p_i} \right|_{\mathbf{p}=\mathbf{p}^o} + \sum_j \left. \frac{\partial \varepsilon^2(x, \mathbf{p})}{\partial p_i \partial p_j} \right|_{\mathbf{p}=\mathbf{p}^o} \frac{\partial p_j^o}{\partial x} = 0 \quad (2.69)$$

which leads to the linear-response equations:

$$\sum_j \left. \frac{\partial^2 \varepsilon(x, \mathbf{p})}{\partial p_i \partial p_j} \right|_{\mathbf{p}=\mathbf{p}^o} \frac{\partial p_j^o}{\partial x} = - \left. \frac{\partial^2 \varepsilon(x, \mathbf{p})}{\partial x \partial p_i} \right|_{\mathbf{p}=\mathbf{p}^o} \quad (2.70)$$

This is a linear system of equations for the linear-response vector $\partial p_i^o/\partial x$. Since we are interested in energy derivatives evaluated at $x = 0$, we need to calculate the unperturbed electronic Hessian $\partial^2 \varepsilon(x = 0, \mathbf{p})/\partial p_i \partial p_j$.

2.3.1.3 Coupled-perturbed Hartree-Fock (CPHF)

For optimizing the orbitals in the HF determinant wavefunction, it is convenient to use an exponential parametrization:

$$|\Psi(\boldsymbol{\kappa})\rangle = e^{\hat{\kappa}(\boldsymbol{\kappa})} |\Psi_0\rangle \quad (2.71)$$

where $e^{\hat{\kappa}}$ is a unitary operator performing rotations between occupied and virtual spin-orbitals in a reference determinant wave function Ψ_0 . This rotation operator is constructed from a single-excitation operator, $\hat{\kappa}$, which can be written in the second-quantization formalism as:

$$\hat{\kappa}(\boldsymbol{\kappa}) = \sum_a^{\text{occ}} \sum_r^{\text{vir}} (\kappa_{ar} \hat{a}_r^\dagger \hat{a}_a - \kappa_{ar}^* \hat{a}_a^\dagger \hat{a}_r) \quad (2.72)$$

where \hat{a}_k^\dagger and \hat{a}_k are respectively the creation and annihilation operators of the spin-orbital k and the indices a and r refer respectively to occupied and virtual spin-orbitals in the reference determinant. The parameters $\boldsymbol{\kappa} = \{\kappa_{ar}\}$ are called the orbital rotation parameters. In comparison to the orbital coefficients on the atomic basis functions, the orbital rotation parameters have the advantage of providing a non-redundant parametrization of the wave function, so that one can vary them independently without having to impose any constraints. For the static case, we can take real-valued orbital rotation parameters,

i.e. $\kappa_{ar} = \kappa_{ar}^*$. Without perturbation, the HF energy function is:

$$\varepsilon_{HF}(\boldsymbol{\kappa}) = \frac{\langle \Psi(\boldsymbol{\kappa}) | \hat{H}_0 | \Psi(\boldsymbol{\kappa}) \rangle}{\langle \Psi(\boldsymbol{\kappa}) | \Psi(\boldsymbol{\kappa}) \rangle} \quad (2.73)$$

For linear response theory, we need first to calculate the HF electronic Hessian below:

$$\left. \frac{\partial^2 \varepsilon_{HF}(\boldsymbol{\kappa})}{\partial \kappa_{ar} \partial \kappa_{bs}} \right|_{\boldsymbol{\kappa}=\mathbf{0}} = 2(A_{ar,bs} + B_{ar,bs}) \quad (2.74)$$

with:

$$A_{ar,bs} = (\epsilon_r - \epsilon_a) \delta_{ab} \delta_{rs} + \langle rb|as \rangle - \langle rb|sa \rangle \quad (2.75)$$

$$B_{ar,bs} = \langle rs|ab \rangle - \langle rs|ba \rangle \quad (2.76)$$

where ϵ_a and ϵ_r are respectively the HF energies of the occupied and virtual spin-orbitals, $\langle rb|as \rangle$ and $\langle rs|ab \rangle$ are respectively two-electron integrals of exchange type and Coulomb type.

Let's consider now a perturbation by a static electric field \mathbf{F} . The perturbed HF energy is given by:

$$\varepsilon_{HF}(\mathbf{F}, \boldsymbol{\kappa}) = \frac{\langle \Psi(\boldsymbol{\kappa}) | \hat{H}_0 - \hat{\mu} \mathbf{F} | \Psi(\boldsymbol{\kappa}) \rangle}{\langle \Psi(\boldsymbol{\kappa}) | \Psi(\boldsymbol{\kappa}) \rangle} \quad (2.77)$$

where $\hat{\mu}$ is the dipole moment operator. The CPHF electric dipole polarizability is:

$$\alpha_{ij}^{CPHF} = - \left. \frac{\partial^2 E_{HF}}{\partial F_i \partial F_j} \right|_{\mathbf{F}=\mathbf{0}} = - \left[\frac{\partial^2 \varepsilon_{HF}}{\partial F_i \partial F_j} + \sum_a^{occ} \sum_r^{vir} \left(\left. \frac{\partial^2 \varepsilon_{HF}}{\partial F_i \partial \kappa_{ar}} \right|_{\boldsymbol{\kappa}=\mathbf{0}} \frac{\partial \kappa_{ar}}{\partial F_j} \right) \right] \quad (2.78)$$

Since the explicit dependence of $\varepsilon_{HF}(\mathbf{F}, \boldsymbol{\kappa})$ on \mathbf{F} is linear, we have $\partial^2 \varepsilon_{HF} / \partial F_i \partial F_j = 0$. The HF perturbed electronic gradient is:

$$\left. \frac{\partial^2 \varepsilon_{HF}}{\partial F_i \partial \kappa_{ar}} \right|_{\boldsymbol{\kappa}=\mathbf{0}} = -2 \langle r | \hat{\mu}_i | a \rangle \quad (2.79)$$

where $\langle r | \hat{\mu}_i | a \rangle$ are the transition dipole moment one-electron integrals. The CPHF polarizability can thus be written as:

$$\alpha_{ij}^{CPHF} = \sum_a^{occ} \sum_r^{vir} \left(2 \langle r | \hat{\mu}_i | a \rangle \frac{\partial \kappa_{ar}}{\partial F_j} \right) \quad (2.80)$$

The linear-response vector $\partial \kappa_{ar} / \partial F_j$ is obtained from the HF linear-response equations:

$$\sum_b^{occ} \sum_s^{vir} \left((A_{ar,bs} + B_{ar,bs}) \frac{\partial \kappa_{bs}}{\partial F_j} \right) = \langle r | \hat{\mu}_j | a \rangle \quad (2.81)$$

In vector/matrix notations, we obtain finally:

$$\alpha_{ij}^{CPHF} = 2\boldsymbol{\mu}_i^T (\mathbf{A} + \mathbf{B})^{-1} \boldsymbol{\mu}_j \quad (2.82)$$

where $\boldsymbol{\mu}_i$ is the vector of components $\mu_{i,ar} = \langle r | \hat{\mu}_i | a \rangle$, \mathbf{A} and \mathbf{B} are the so-called orbital rotation Hessian matrices, respectively of elements $A_{ar,bs}$ and $B_{ar,bs}$ (see equations 2.75 and 2.76).

2.3.1.4 Coupled-perturbed Kohn-Sham (CPKS)

The KS-DFT energy function is expressed as:

$$\varepsilon_{KS-DFT}(\boldsymbol{\kappa}) = \frac{\langle \Psi(\boldsymbol{\kappa}) | \hat{T} + \hat{V}_{ne} | \Psi(\boldsymbol{\kappa}) \rangle}{\langle \Psi(\boldsymbol{\kappa}) | \Psi(\boldsymbol{\kappa}) \rangle} + E_H[\rho] + E_{xc}[\rho] \quad (2.83)$$

where $E_H[\rho]$ is the Hartree energy and $E_{xc}[\rho]$ is the exchange-correlation energy. The KS-DFT electronic Hessian has a similar expression as in HF:

$$\left. \frac{\partial^2 \varepsilon_{KS-DFT}(\boldsymbol{\kappa})}{\partial \kappa_{ar} \partial \kappa_{bs}} \right|_{\boldsymbol{\kappa}=\mathbf{0}} = 2(A_{ar,bs} + B_{ar,bs}) \quad (2.84)$$

with, for pure GGA functionals:

$$A_{ar,bs} = (\epsilon_r - \epsilon_a) \delta_{ab} \delta_{rs} + \langle rb | as \rangle + \langle rb | f_{xc} | as \rangle \quad (2.85)$$

$$B_{ar,bs} = \langle rs | ab \rangle + \langle rs | f_{xc} | ab \rangle \quad (2.86)$$

where the $\langle rb | f_{xc} | as \rangle$ terms are the response of the functional. f_{xc} is the first-order XC kernel, *i.e.* the functional derivative of the XC potential with respect to the density:

$$f_{xc}(\mathbf{r}, \mathbf{r}') = \frac{\partial v_{xc}[\rho](\mathbf{r})}{\partial \rho(\mathbf{r}')} = \frac{\partial^2 E_{xc}[\rho]}{\partial \rho(\mathbf{r}) \partial \rho(\mathbf{r}')} \quad (2.87)$$

In the case of hybrid approximations, mixing HF exchange and DFT exchange, $A_{ar,bs}$ and $B_{ar,bs}$ are expressed differently:

$$A_{ar,bs} = \delta_{ab} \delta_{rs} (\epsilon_r - \epsilon_a) + 2(ar | bs) - a_x (ab | rs) + (1 - a_x) (ar | f_{xc} | bs) \quad (2.88)$$

$$B_{ar,bs} = 2(ar | sb) - a_x (as | rb) + (1 - a_x) (ar | f_{xc} | sb) \quad (2.89)$$

where a_x is the amount of HF exchange into the exchange-correlation functional and ranges from 0 to 1. All the rest is identical to CPHF.

2.3.2 Time-Dependent Hartree-Fock (TDHF) and Time-Dependent DFT (TD-DFT)

2.3.2.1 Dynamic molecular properties and quasi-energy

We consider now a periodic time-dependent perturbation:

$$\hat{H}(t) = \hat{H}_0 + x^+ \hat{V} e^{-i\omega t} + x^- \hat{V}^\dagger e^{+i\omega t} \quad (2.90)$$

where x^+ and x^- represent the perturbation strengths (ultimately $x^+ = x^-$). The associated wave function $|\bar{\Psi}(t)\rangle$ satisfies the time-dependent Schrödinger equation:

$$\left[\hat{H}(t) - i \frac{\partial}{\partial t} \right] |\bar{\Psi}(t)\rangle = 0 \quad (2.91)$$

After extracting a phase factor, $|\bar{\Psi}(t)\rangle = e^{-i\mathcal{F}(t)} |\Psi(t)\rangle$, it can be reformulated as:

$$\left[\hat{H}(t) - i \frac{\partial}{\partial t} \right] |\Psi(t)\rangle = \dot{\mathcal{F}}(t) |\Psi(t)\rangle \quad (2.92)$$

where $\dot{\mathcal{F}}(t) = d\mathcal{F}/dt$ is the time-dependent quasi-energy. The quasi-energy Q is defined as the time average of $\dot{\mathcal{F}}(t)$ over a period $T = 2\pi/\omega$:^[36]

$$Q = \frac{1}{T} \int_0^T \dot{\mathcal{F}}(t) dt = \frac{1}{T} \int_0^T \frac{\langle \Psi(t) | \left[\hat{H}(t) - i \frac{\partial}{\partial t} \right] | \Psi(t) \rangle}{\langle \Psi(t) | \Psi(t) \rangle} dt \quad (2.93)$$

The quasi-energy can be expanded with respect to the perturbation strengths x^+ and x^- :

$$Q = Q^{(0)} + Q^{(10)} x^+ + Q^{(01)} x^- + \frac{1}{2} Q^{(20)} x^{+2} + Q^{(11)} x^+ x^- + \frac{1}{2} Q^{(02)} x^{-2} + \dots \quad (2.94)$$

where $Q^{(0)} = E^{(0)}$ is the unperturbed energy and the quasi-energy derivatives are calculated as:

$$Q^{(10)} = \left. \frac{\partial Q}{\partial x^+} \right|_{x=0}; \quad Q^{(01)} = \left. \frac{\partial Q}{\partial x^-} \right|_{x=0}; \quad Q^{(20)} = \left. \frac{\partial^2 Q}{\partial x^{+2}} \right|_{x=0}; \quad Q^{(11)} = 2 \left. \frac{\partial^2 Q}{\partial x^+ \partial x^-} \right|_{x=0}; \dots \quad (2.95)$$

They are the ω -dependent dynamic molecular properties. If we consider the specific case of the electric dipole interaction perturbation, the Hamiltonian of the system can be written as:

$$\hat{H}(t) = \hat{H}_0 - F^+ \cdot \hat{\mu} e^{-i\omega t} - F^- \cdot \hat{\mu} e^{+i\omega t} \quad (2.96)$$

where $\hat{\mu}$ is the dipole moment operator and $F^+ = F^-$ is the amplitude of the oscillating electric field. The dynamic electric dipole polarizability is defined as:

$$\alpha_{ij}(\omega) = - \left. \frac{\partial^2 Q}{\partial F_i^- \partial F_j^+} \right|_{\mathbf{F}=\mathbf{0}} \quad (2.97)$$

Using time-dependent perturbation theory, we obtain the exact expression of the polarizability:

$$\alpha_{ij}(\omega) = - \left[\sum_{n \neq 0} \frac{\langle \Psi_0 | \hat{\mu}_i | \Psi_n \rangle \langle \Psi_n | \hat{\mu}_j | \Psi_0 \rangle}{\omega - \omega_n} - \sum_{n \neq 0} \frac{\langle \Psi_0 | \hat{\mu}_j | \Psi_n \rangle \langle \Psi_n | \hat{\mu}_i | \Psi_0 \rangle}{\omega + \omega_n} \right] \quad (2.98)$$

where Ψ_n are the states of \hat{H}_0 and ω_n are the excitation energies.

2.3.2.2 Polarizability from dynamic response theory

In a time-dependent electronic-structure method, the quasi-energy $Q(\mathbf{F}^+, \mathbf{F}^-)$ is obtained by plugging optimal parameters $\mathbf{p}^o(\mathbf{F}^+, \mathbf{F}^-)$ in a quasi-energy function $\mathcal{Q}(\mathbf{F}^+, \mathbf{F}^-, \mathbf{p}^o)$:

$$Q(\mathbf{F}^+, \mathbf{F}^-) = \mathcal{Q}(\mathbf{F}^+, \mathbf{F}^-, \mathbf{p}^o(\mathbf{F}^+, \mathbf{F}^-)) \quad (2.99)$$

In contrast to the static case, the parameters now depend on time and take complex values. They can be decomposed in Fourier modes:

$$\mathbf{p} = \mathbf{p}^+ e^{-i\omega t} + \mathbf{p}^- e^{+i\omega t} \quad (2.100)$$

We consider only the case where all the parameters are variational, *i.e.* fulfilling the following stationary conditions:

$$\left. \frac{\partial \mathcal{Q}}{\partial \mathbf{p}^+} \right|_{\mathbf{p}=\mathbf{p}^o} = 0 \text{ and } \left. \frac{\partial \mathcal{Q}}{\partial \mathbf{p}^-} \right|_{\mathbf{p}=\mathbf{p}^o} = 0 \quad (2.101)$$

Thanks to the stationarity of the parameters, only the explicit dependence on \mathbf{F}^+ and \mathbf{F}^- in \mathcal{Q} contributes to first-order properties with respect to the quasi-energy:

$$\frac{\partial \mathcal{Q}}{\partial \mathbf{F}_i^-} = \frac{\partial \mathcal{Q}}{\partial \mathbf{F}_i^-} + \underbrace{\left[\frac{\partial \mathcal{Q}}{\partial \mathbf{p}^+} \frac{\partial \mathbf{p}^+}{\partial \mathbf{F}_i^-} + \frac{\partial \mathcal{Q}}{\partial \mathbf{p}^-} \frac{\partial \mathbf{p}^-}{\partial \mathbf{F}_i^-} + c.c. \right]}_{=0} \quad (2.102)$$

For second-order properties with respect to the quasi-energy, the implicit dependence on \mathbf{F}^+ and \mathbf{F}^- via the parameters contributes. In particular, for the dynamic polarizability, we get:

$$\alpha_{ij}(\omega) = - \frac{\partial^2 \mathcal{Q}}{\partial F_i^- \partial F_j^+} = - \frac{\partial^2 \mathcal{Q}}{\partial \mathbf{p}^+ \partial F_i^-} \frac{\partial \mathbf{p}^+}{\partial F_j^+} - \frac{\partial^2 \mathcal{Q}}{\partial \mathbf{p}^- \partial F_i^-} \frac{\partial \mathbf{p}^-}{\partial F_j^+} \quad (2.103)$$

The linear-response vector $(\partial \mathbf{p}^+ / \partial F_j^+, \partial \mathbf{p}^- / \partial F_j^+)$ is found from the linear-response equations:

$$\begin{pmatrix} \frac{\partial^2 \mathcal{Q}}{\partial \mathbf{p}^+ \partial \mathbf{p}^+} & \frac{\partial^2 \mathcal{Q}}{\partial \mathbf{p}^+ \partial \mathbf{p}^-} \\ \frac{\partial^2 \mathcal{Q}}{\partial \mathbf{p}^- \partial \mathbf{p}^+} & \frac{\partial^2 \mathcal{Q}}{\partial \mathbf{p}^- \partial \mathbf{p}^-} \end{pmatrix} \begin{pmatrix} \frac{\partial \mathbf{p}^+}{\partial F_j^+} \\ \frac{\partial \mathbf{p}^-}{\partial F_j^+} \end{pmatrix} = - \begin{pmatrix} \frac{\partial^2 \mathcal{Q}}{\partial F_j^+ \partial \mathbf{p}^+} \\ \frac{\partial^2 \mathcal{Q}}{\partial F_j^+ \partial \mathbf{p}^-} \end{pmatrix} \quad (2.104)$$

The dynamic polarizability has thus the general expression:

$$\alpha_{ij}(\omega) = \begin{pmatrix} \frac{\partial^2 \mathcal{Q}}{\partial \mathbf{p}^+ \partial F_i^-} \\ \frac{\partial^2 \mathcal{Q}}{\partial \mathbf{p}^- \partial F_i^-} \end{pmatrix}^T \begin{pmatrix} \frac{\partial^2 \mathcal{Q}}{\partial \mathbf{p}^+ \partial \mathbf{p}^+} & \frac{\partial^2 \mathcal{Q}}{\partial \mathbf{p}^+ \partial \mathbf{p}^-} \\ \frac{\partial^2 \mathcal{Q}}{\partial \mathbf{p}^- \partial \mathbf{p}^+} & \frac{\partial^2 \mathcal{Q}}{\partial \mathbf{p}^- \partial \mathbf{p}^-} \end{pmatrix}^{-1} \begin{pmatrix} \frac{\partial^2 \mathcal{Q}}{\partial F_j^+ \partial \mathbf{p}^+} \\ \frac{\partial^2 \mathcal{Q}}{\partial F_j^+ \partial \mathbf{p}^-} \end{pmatrix} \quad (2.105)$$

2.3.2.3 Time-Dependent Hartree-Fock (TDHF)

The TDHF quasi-energy function is:

$$\mathcal{Q}_{TDHF}(\mathbf{F}^+, \mathbf{F}^-, \boldsymbol{\kappa}) = \frac{1}{T} \int_0^T \frac{\langle \Psi(\boldsymbol{\kappa}) | \hat{H}(t) - i \frac{\partial}{\partial t} | \Psi(\boldsymbol{\kappa}) \rangle}{\langle \Psi(\boldsymbol{\kappa}) | \Psi(\boldsymbol{\kappa}) \rangle} dt \quad (2.106)$$

After calculating all the derivatives of \mathcal{Q}_{TDHF} with respect to the orbital rotation parameters κ_{ar} , we get the TDHF polarizability (for real-valued orbitals):

$$\alpha_{ij}^{TDHF}(\omega) = \begin{pmatrix} \boldsymbol{\mu}_i \\ \boldsymbol{\mu}_i \end{pmatrix}^T \left[\begin{pmatrix} \mathbf{A} & \mathbf{B} \\ \mathbf{B} & \mathbf{A} \end{pmatrix} - \omega \begin{pmatrix} \mathbf{1} & \mathbf{0} \\ \mathbf{0} & -\mathbf{1} \end{pmatrix} \right]^{-1} \begin{pmatrix} \boldsymbol{\mu}_j \\ \boldsymbol{\mu}_j \end{pmatrix} \quad (2.107)$$

where \mathbf{A} and \mathbf{B} are the same matrices as introduced in CPHF (equations 2.75 and 2.76).

2.3.2.4 Time-Dependent Density Functional Theory (TD-DFT)

The TD-DFT quasi-energy function is:^[37]

$$\mathcal{Q}_{TDFT}(\mathbf{F}^+, \mathbf{F}^-, \boldsymbol{\kappa}) = \frac{1}{T} \int_0^T \left(\frac{\langle \Psi(\boldsymbol{\kappa}) | [\hat{h}(t) - i \frac{\partial}{\partial t}] | \Psi(\boldsymbol{\kappa}) \rangle}{\langle \Psi(\boldsymbol{\kappa}) | \Psi(\boldsymbol{\kappa}) \rangle} + E_H[\rho] + \mathcal{Q}_{xc}[\rho] \right) dt \quad (2.108)$$

where $\hat{h}(t)$ is the one-electron Hamiltonian and $\mathcal{Q}_{xc}[\rho]$ is the exchange-correlation quasi-energy functional depending on the time-dependent density ρ . In practice, we always use the adiabatic approximation:

$$\mathcal{Q}_{xc}[\rho] \approx \frac{1}{T} \int_0^T E_{xc}[\rho] dt \quad (2.109)$$

where $E_{xc}[\rho]$ is the ground-state exchange-correlation functional. We then obtain the same equations as in TDHF with the same matrices \mathbf{A} and \mathbf{B} as in CPKS (equations 2.85 and 2.86, or equations 2.88 and 2.89). In exact TD-DFT, the exchange-correlation kernel f_{xc} should depend on ω but in the adiabatic approximation it does not. This has the consequence that double or higher electronic excitations are not included.

2.3.3 Simplified Linear-Response TD-DFT

The calculation of response properties for systems containing several thousands of atoms remains a challenge for standard TD-DFT. In order to treat very large molecular systems, we employed in this thesis the recently developed Simplified Time-Dependent-Density Functional Theory (sTD-DFT) scheme, which provides response properties of large systems at a much lower computational cost than its TD-DFT parent.^[38, 39] Three simplifications yield the sTD-DFT approach: i) Coulomb and exchange two-electron integrals are approximated by short-range damped Coulomb interactions of transition/charge density monopoles, ii) the response of the exchange-correlation functional is neglected in \mathbf{A} and \mathbf{B} matrices and iii) the configuration space is restricted to a user-specified energy range of excitations. The consequences of these approximations are briefly discussed below.

The computationally demanding four-index two-electron integrals are approximated using the expression below:

$$(ij|kl) = \sum_A^N \sum_B^N q_{ij}^A q_{kl}^B \gamma_{AB} \quad (2.110)$$

where the indices $ijkl$ correspond to general (either occupied or virtual) orbitals, q_{pq}^A and q_{rs}^B are respectively transition density monopoles (atomic charges) centered on atom A and B, and γ_{AB} is the Mataga-Nishimoto-Ohno-Klopman (MNOK) damped Coulomb operator. The latter takes slightly different forms for Coulomb (J) and exchange (K) integrals:

$$\gamma_{AB}^J = \left(\frac{1}{(R_{AB})^{y_J} + (a_x \eta)^{-y_J}} \right)^{\frac{1}{y_J}} \quad (2.111)$$

$$\gamma_{AB}^K = \left(\frac{1}{(R_{AB})^{y_K} + (\eta)^{-y_K}} \right)^{\frac{1}{y_K}} \quad (2.112)$$

In these expressions, a_x is the amount of exact HF exchange in the exchange-correlation functional, η is the mean of the chemical hardness of atoms A and B (whose values are tabulated), and y_J and y_K are two adjustable parameters.

Therefore, the matrices \mathbf{A} and \mathbf{B} are replaced by simplified matrices \mathbf{A}' and \mathbf{B}' of elements:

$$A'_{ar,bs} = \delta_{ab} \delta_{rs} (\epsilon_r - \epsilon_a) + \sum_{A,B}^{N_{atoms}} (2q_{ar}^A q_{bs}^B \gamma_{AB}^K - q_{ab}^A q_{rs}^B \gamma_{AB}^J) \quad (2.113)$$

$$B'_{ar,bs} = \sum_{A,B}^{N_{atoms}} (2q_{ar}^A q_{sb}^B \gamma_{AB}^K - a_x q_{as}^A q_{rb}^B \gamma_{AB}^K) \quad (2.114)$$

Note that the amount of Hartree-Fock exchange is not appearing anymore in equation 2.113. Though, the MNOK Coulomb operator implicitly incorporates it. In addition to the damping of two-electron integrals, the sTD-DFT scheme also involves a massive truncation of the single-excitation expansion space, by selecting only those below a given energy threshold E_{th} . The \mathbf{A}' and \mathbf{B}' matrices include all excitations up to this energy threshold.

To further reduce the computational needs, the tight-binding implementation of the sTD-DFT method (sTD-DFT-xTB), as well as its version restricted to valence molecular orbitals (sTD-DFT-vTB), were used in this work (Chapter 4). The above described sTD-DFT scheme can be interfaced with the xTB tight-binding method,^[40] providing an ultra-fast approach to the response properties for large systems (sTD-DFT-xTB approximation). In this method, the KS-DFT orbitals and eigenvalues are replaced by corresponding data from an extended basis set tight-binding calculation. vTB means that the diffuse AO basis functions have been removed from the xTB basis set, leaving only valence functions. It may be noted that a sTD-DFT calculation is more than 600 time faster with respect to a regular TD-DFT treatment while the xTB version speeds up the entire calculation further by at least two orders of magnitude.

2.3.4 Finite-field method

The finite field (FF) method^[41] is a straightforward, easy-to-implement technique for the calculation of hyperpolarizabilities. In contrast to other methods, the property of interest can be calculated simply from the knowledge of the energy at certain field strengths, and no additional information is needed about excited states or analytical derivatives with respect to the field components. These benefits render the FF method an universally applicable technique to any level of theory, with no additional requirements other than using a method allowing to compute field-dependent energies.

Similarly to the dipole moment (equation 1.4), the dependence of the energy E on an external homogeneous static electric field F is written as a Taylor expansion of the form:

$$\begin{aligned}
 E(F) &= E(0) + \left. \frac{\partial E}{\partial F} \right|_{F=0} F + \frac{1}{2!} \left. \frac{\partial^2 E}{\partial F^2} \right|_{F=0} F^2 + \frac{1}{3!} \left. \frac{\partial^3 E}{\partial F^3} \right|_{F=0} F^3 + \frac{1}{4!} \left. \frac{\partial^4 E}{\partial F^4} \right|_{F=0} F^4 + \dots \\
 &= E(0) - \mu F - \frac{1}{2} \alpha F^2 - \frac{1}{6} \beta F^3 - \frac{1}{24} \gamma F^4 + \dots
 \end{aligned}
 \tag{2.115}$$

The Taylor expansion of equation 2.115 can be splitted into an even and an odd part introducing symmetric and antisymmetric linear combinations of the energy at equal

positive and negative fields:

$$E_S(F) = \frac{E(F) + E(-F)}{2} = E(0) - \frac{1}{2}\alpha F^2 - \frac{1}{24}\gamma F^4 + O(F^6) \quad (2.116)$$

$$E_A(F) = \frac{E(F) - E(-F)}{2} = -\mu F - \frac{1}{6}\beta F^3 - \frac{1}{120}\delta F^5 + O(F^7) \quad (2.117)$$

This allows a completely separated treatment of the even and odd order hyperpolarizabilities. For the evaluation of β , the energy has to be known at two different field strengths, chosen here to be F and $2F$, besides the energy at zero field:

$$\beta(F) = \frac{2E_A(F) - E_A(2F)}{F^3} = \beta + \frac{1}{4}\delta F^2 + O(F^4) \quad (2.118)$$

However, the FF method has also certain downsides. It is, for example, limited to the evaluation of static molecular properties, as time-dependent fields cannot be handled in a straightforward manner. Most crucial, nevertheless, is the dependence of the outcome of a FF calculation on the initially chosen field strength. It is well-known that too small fields introduce numerical noise on the calculated properties due to the finite precision arithmetics of every computer, and can only be mitigated at most. At the other end of the scale, there is also an upper bound for feasible field strengths. A field chosen too strong leads to an inaccurate evaluation of molecular properties driven by two different factors. First of all, the higher-order terms in the Taylor expansion of equation 2.115 lead to non-negligible contributions to the overall energy with increasing field strength. This effect is systematic and can be cancelled out by linear combination of properties obtained at different field strengths, which is usually applied in literature. In conclusion, choosing a reasonable field strength for an FF calculation requires to cope with a rather delicate balance between the two extremes of too weak fields, leading to numerical errors that can be several orders of magnitude larger than the actual property of interest, and too strong fields causing the calculation of properties for an excited state.

In order to remove higher-order contaminations in the FF method, the Romberg differentiation procedure^[42, 43] can be applied. It consists in combining energy values obtained for a succession of k external electric fields, of which the amplitudes form a geometric progression given by $F(k) = a^k F_0$, where F_0 is the smallest field value and a the common ratio. For the different types of β tensor components, the finite difference expression corresponding to the zero-order iteration reads:

$$\beta_{ijm}(k, 0) = \frac{\left([E(F_{-i-j-m}(k)) - E(F_{ijm}(k))] + [E(F_{ij-m}(k)) - E(F_{-i-jm}(k))] \right. \\ \left. + [E(F_{i-jm}(k)) - E(F_{-ij-m}(k))] + [E(F_{-ijm}(k)) - E(F_{i-j-m}(k))] \right)}{8(a^k F_0)^3} \quad (2.119)$$

To remove the contaminations from higher-order hyperpolarizabilities, successive ‘‘Romberg iterations’’ are carried out using a recursive expression where n is the number of iterations:^[44, 45]

$$\beta(k, n) = \frac{a^{2n}\beta(k, n-1) - \beta(k+1, n-1)}{a^{2n} - 1} \quad (2.120)$$

which leads to the so-called ‘‘Romberg triangle’’ where the convergence of the numerical derivative can be monitored (Figure 2.3). Because these expressions are based on molecular energies, their physicochemical nature can impact the convergence of the Romberg procedure. As mentioned in ref. [44], for any molecule there exists a field window where the finite differentiation is stable. Upper and lower bounds define this window.

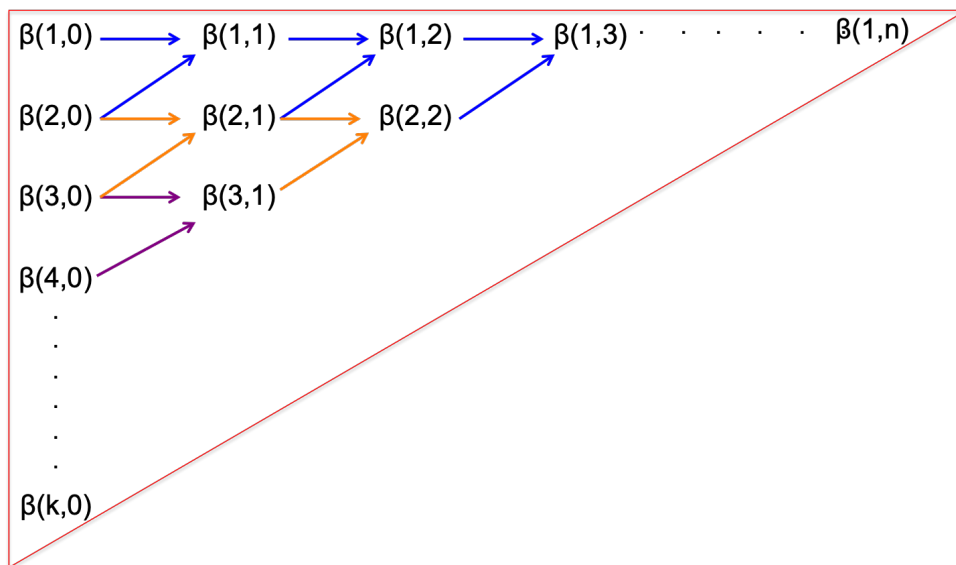


Figure 2.3 – Scheme of the Romberg procedure. The first column is evaluated according to equation 2.119. The other columns correspond to the successive ‘‘Romberg iterations’’ and are calculated using equation 2.120, each column corresponding to an iteration.

2.3.5 Sum-over-states method and the two-state model

The first hyperpolarizability β can also be evaluated using the Sum-Over-States (SOS) method. The SOS formalism defines the response of a system in terms of the linear optical spectroscopic quantities, namely excitations energies and transition moments between various electronic states. The sum-over-state expression of the static second-order NLO response is given by:

$$\beta_{ijk} = \sum_{n, m \neq 0} \frac{\langle 0 | \mu_i | n \rangle \langle n | \mu_j | m \rangle \langle m | \mu_k | 0 \rangle}{\Delta E_{0n}^2} - \langle 0 | \mu_i | 0 \rangle \sum_n \frac{\langle | \mu_j | n \rangle \langle n | \mu_k | 0 \rangle}{\Delta E_{0n}^2} \quad (2.121)$$

where $\mu_i = \langle 0 | \mu_i | n \rangle$ are the transition dipole moments from the ground state $|0\rangle$ to excited state $|n\rangle$, $\langle n | \mu_j | m \rangle$ the transition dipole moments between excited states $|n\rangle$ and $|m\rangle$, $\langle 0 | \mu_i | 0 \rangle$ the dipole moment of the ground state, and ΔE_{0n} the excitation energies

from $|0\rangle$ to $|n\rangle$.

Under the assumption that there are few states which contribute more than others, the summation over the whole spectrum of the Hamiltonian can be reduced to those states. In the case of push-pull π -conjugated compounds, Oudar and Chemla^[46] showed that one low-energy charge-transfer excited state often provides a dominant contribution to β . In such a case, one may apply the two-state approximation (TSA), which assumes that only one electronic excited state dominates the molecular response and contributes to the SOS expression of the second-order NLO response. Moreover, as discussed in Chapter 1, the hyperpolarizability tensor of push-pull π -conjugated derivatives can be reduced to its single β_{zzz} diagonal component, with z being the charge transfer axis. Thus, assuming an ideal 1D character of the second-order NLO response and using the TSA in which β_{zzz} is expressed as a function of the absorption properties of the S_1 state, the static HRS hyperpolarizability can be expressed as:

$$\beta_{HRS}^{TSA} = 9\sqrt{\frac{6}{35}} \times \frac{f_{01}\Delta\mu_{01}}{\Delta E_{01}^3} \quad (2.122)$$

where ΔE_{01} is the $S_0 \rightarrow S_1$ excitation energy, $f_{01} = \frac{2}{3}\Delta E_{01}\mu_{01}^2$ is the associated oscillator strength with $\mu_{01} = \langle 0|\mu_z|1\rangle$, and $\Delta\mu_{01} = \|\vec{\mu}_{S_1} - \vec{\mu}_{S_0}\|$ is the dipole moment variation between the two electronic states. To gain deeper insight on the origin of the light-induced intramolecular charge transfer (ICT), $\Delta\mu_{01}$ can be further decomposed as the product of the photo-induced charge displacement (Δq_{01}) and charge transfer distance (Δr_{01}): $\Delta\mu_{01} = \Delta q_{01} \times \Delta r_{01}$.^[47, 48] The dynamic HRS hyperpolarizability can be easily obtained by multiplying the static one by a frequency dispersion factor F_{disp}^{TSA} :

$$F_{disp}^{TSA} = \frac{\Delta E_{01}^4}{(\Delta E_{01}^2 - (\hbar\omega)^2)(\Delta E_{01}^2 - (2\hbar\omega)^2)} \quad (2.123)$$

with $\hbar\omega$ the photon energy of the incident beam. From equation 2.123, F_{disp}^{TSA} is equal to 1 in the static limit ($\hbar\omega = 0$), to ~ 0.5 if $\hbar\omega = \Delta E_{01}/3$, and tends to infinite in the resonance limit ($\hbar\omega = \Delta E_{01}/2$).

2.4 Basis sets

As presented in previous sections, the LCAO expansion of molecular orbitals yields the best result within a given method when an infinite basis set is used. However, achieving this optimal description of the system is beyond the computational capacities available and various basis sets have been developed, constituted by a limited number of mathematical functions, Slater-type orbitals^[49] (STOs) or Gaussian-type orbitals^[50] (GTOs), to reach accurate results as efficiently as possible. The STOs, although physically more attractive as they are directly deduced from the hydrogenoid orbitals, suffer from calcula-

tory complexity when dealing with polyatomic molecules, as multi-center integrals cannot be efficiently treated. To circumvent this issue, Boys proposed to use GTOs instead.^[50] Computationally convenient as they ensure analytical solutions for all integrals, they are, however, not so well adapted to the description of the shape of the orbital: no discontinuity for $r = 0$ (*i.e.* at the nucleus) and too fast decay for $r \rightarrow \infty$ (Figure 2.4).

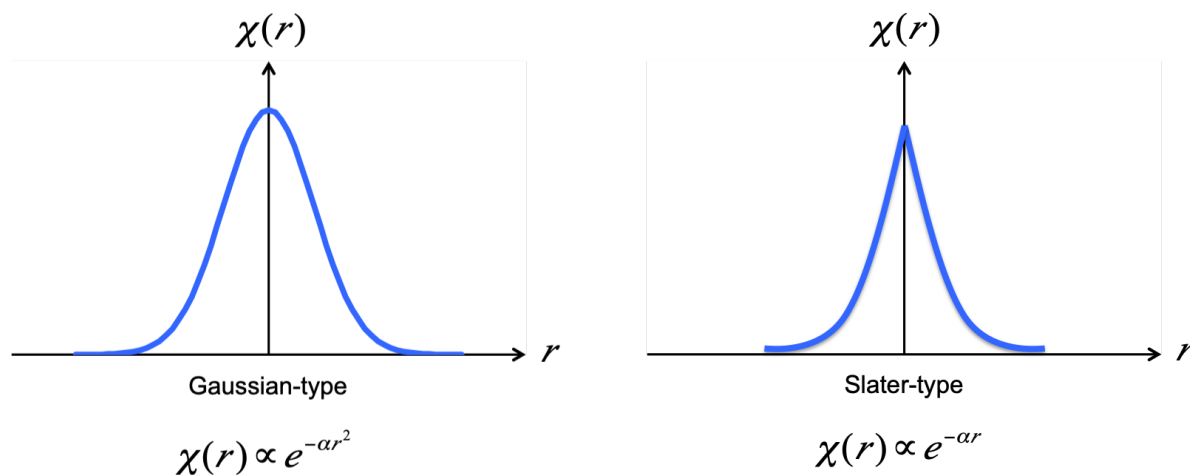


Figure 2.4 – Shape comparison between GTO and STO basis functions.

For these reasons, GTOs are used in a linear combination to reproduce as close as possible a STO. As an example, the STO-nG minimal basis set, in which a single basis function is used for each atomic orbital in the atom, combine n primitive GTOs into a contracted GTO to fit an STO, the most used and optimal being for $n = 3$ (Figure 2.5).

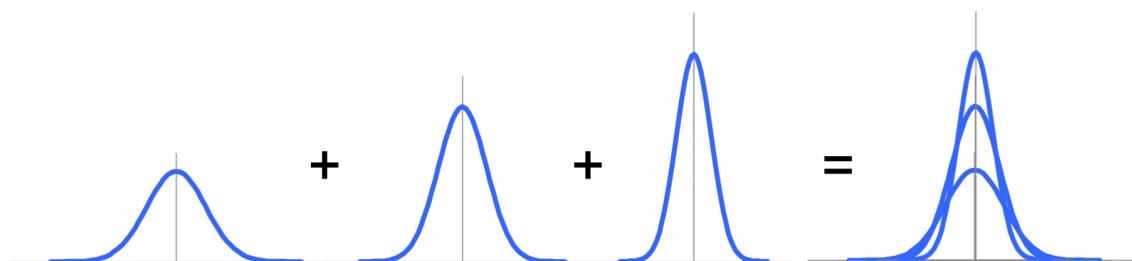


Figure 2.5 – Construction of the STO-3G basis function.

Clearly, the more primitives combined, the better will be the fit with the STO, but the larger the computational effort associated. However, one can reasonably assume that from a chemical point of view, a correct description of the valence orbital is more determining than of the core ones. As a consequence, more flexibility to assess properly for different molecular environment was achieved by Pople and coworkers^[51, 52] with the so-called split-valence basis sets of the type C- v_1v_2 G. The core orbitals are described by

one contracted GTO from C primitives, while two contracted functions are used for the valence orbitals, developed over v_1 and v_2 primitives respectively, for instance as in the 6-31G basis set. Note that basis sets in which there are multiple basis functions corresponding to each valence atomic orbital are called valence double, triple, quadruple-zeta, and so on. One can add diffuse or polarisation functions for better flexibility and reach a more accurate description.^[53] A polarization function is any higher angular momentum orbital used in a basis set that is not normally occupied in the separated atom. For example, for the hydrogen atom, the only orbital type that is occupied is s-type. Therefore, if p-type or d-type basis functions were added to the hydrogen atom they would be known as polarization functions. For first row elements like carbon, d-type and f-type basis functions would be considered to be polarization functions. For transition metals with occupied d-type orbitals, only f-type or higher functions would be considered polarization basis functions. Polarization functions are not thought to be formally fully occupied in molecules. They are included solely to improve the flexibility of the basis set, particularly to better represent electron density in bonding regions. One set of d-type polarization functions can be added to each non-hydrogen atom in the molecule (6-31G(d)), and in addition one set of p-type polarization functions can be added to hydrogens (6-31G(d,p)). Diffuse basis functions are extra basis functions (usually of s-type or p-type) that are added to the basis set to represent very broad electron distributions. They are especially important in representing the electron density in anions or in intermolecular complexes (where there may be particularly long bonds with electron density spread over a large region). The use of diffuse functions in a Pople basis set is indicated by the notation + or ++. The + notation, as in 6-31+G(d), means that one set of sp-type diffuse basis functions is added to non-hydrogen atoms (4 diffuse basis functions per atom: s, p_x , p_y , p_z). The ++ notation, as in 6-31++G(d), means that one set of sp-type diffuse functions is added to each non-hydrogen atom and one s-type diffuse function is added to hydrogen atoms.

Another class of widely used basis sets are those developed by Dunning and coworkers.^[54] They were designed for converging Post-Hartree–Fock calculations systematically to the complete basis set limit using empirical extrapolation techniques. Those basis sets are denoted as cc-pVXZ, where "cc" stands for correlation-consistent, "p" indicates that polarization functions are used for all atoms, and 'V' indicates they are valence-only basis sets, X=D,T,Q,5,6,... (D=double, T=triple, Q=quadruple, ...) means double-, triple- or quadruple- zeta. Diffuse functions can be added by means of augmented correlation-consistent basis sets, aug-cc-pVXZ. While the usual Dunning basis sets are for valence-only calculations, the sets can be augmented with further functions that describe core electron correlation. These core-valence sets (cc-pCVXZ) are necessary for accurate geometric and nuclear property calculations.

2.5 Solvent effects: the polarizable continuum model

The vast majority of chemical reactions as well as experimental measurements take place in solutions. Molecular properties may be greatly affected by the surrounding condensed phase and it is therefore of utmost importance to take properly into account these effects. The most straightforward approach to mimic a solution is to simply add explicitly the solvent molecules around the system investigated. However, as a single solvation shell would clearly be insufficient (absence of long-range effects), it is evident that the system constituted of the solute surrounded by explicit solvent molecules would quickly become enormous and computationally impossible to treat. To cope with this problem, one usually resorts to the use of implicit solvent models in which the solute is treated explicitly, while the solvent molecules are replaced by a continuous medium characterised by the properties of the solvent and surrounding the cavity occupied by the solute (Figure 2.6). Specific solute-solvent interactions can be accounted for by introducing few solvent molecules in the explicit system to give a more reliable and accurate picture. Two types of continuum approaches are commonly used : dielectric Polarizable Continuum Model (PCM) or conductor-like PCM. Implicit solvation has been extensively reviewed and further details are to be found in ref. [55] and [56]. In this work, we have used the PCM in its integral equation formulation (IEFPCM) developed by Tomasi and co-workers,^[57] which falls into the category of dielectric continuum methods.

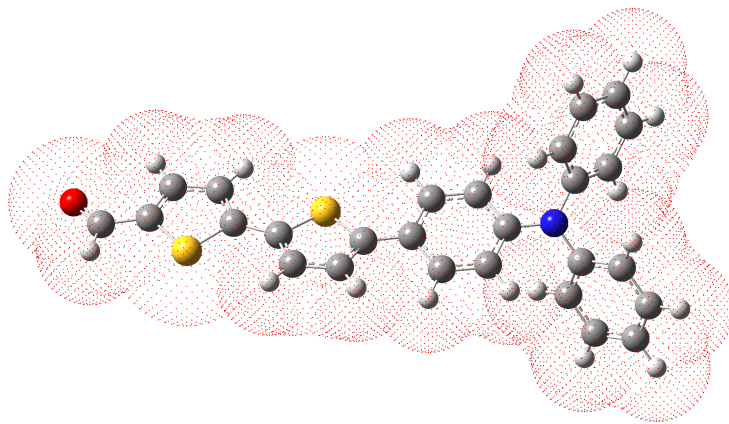


Figure 2.6 – The PCM model. The solute molecule is embedded in a cavity (red dots) which is formed in the continuum with a dielectric constant ϵ .

Within a continuum approach of solvation, the total Hamiltonian can be written as:

$$\hat{H}_{eff} = \hat{H}_{solute} + \hat{V}_{int} \quad (2.124)$$

with \hat{H}_{solute} the Hamiltonian of the isolated solute and \hat{V}_{int} the interaction term describing the solute-solvent interactions.

Solvation is the process by which solvent molecules interact with the solute they surround and is characterised by the free energy of solvation ΔG_{sol} that corresponds to

the change in free energy associated with the transfer of a molecule from the gas phase to the solvent environment. This free energy is partitioned into different contributions as follows:

$$\Delta G_{sol} = \Delta G_{cav} + \Delta G_{rep} + \Delta G_{disp} + \Delta G_{elec} \quad (2.125)$$

and the interaction potential \hat{V}_{int} is equivalently a sum of operators each corresponding to a term of this partition. Here, ΔG_{cav} is the cavitation free energy necessary to create a cavity for the solute in the continuous dielectric medium with an appropriate shape for the solute, which should reproduce as well as possible its molecular shape while excluding the solvent. Many definitions have been proposed for the cavity, reflecting compromises between accuracy and computational cost, as well as the diverse physical requirements for a given system. In the PCM model, the cavity is defined as a superposition of interlocked spheres centred on the solute nuclei assigned with suitable radii. The cavitation energy is not related to the electronic properties of the solute but only depends on its geometry and is evaluated independently according to Pierotti's modified formula (details can be found in ref. [58] and [59]). ΔG_{rep} is associated to solute-solvent repulsion interactions arising from electron exchange contributions while ΔG_{disp} accounts for the dispersion contribution owing to the interactions between instantaneous multipoles due to electrons correlated motion. These quantities are computed in the PCM model according to expressions from Amovilli and Mennucci.^[60] Finally, the last contribution ΔG_{elec} is the free energy associated to the solute-solvent electrostatic interactions and is at the heart of the self-consistent reaction field (SCRF) procedure. Bringing in solution a solute characterised by a given charge distribution in the gas phase will cause a polarisation of the charges in the surrounding dielectric medium, inducing in turn an extra electric field, the so-called reaction field,^[61] in the vicinity of the solute, that will affect its electronic structure. The electrostatic problem relative to a charge distribution inside a cavity surrounded by a dielectric continuum can be solved by considering the Poisson equation and associated boundary conditions:

$$\text{Within the cavity:} \quad -\Delta V = 4\pi\rho_{sol} \quad (2.126)$$

$$\text{Outside the cavity:} \quad -\varepsilon\Delta V = 0 \quad (2.127)$$

$$\text{On the cavity surface:} \quad V_{in} = V_{out} \quad (2.128)$$

$$\text{On the cavity surface:} \quad \left(\frac{\partial V}{\partial n}\right)_{in} = \varepsilon \left(\frac{\partial V}{\partial n}\right)_{out} \quad (2.129)$$

with the total electrostatic potential V , sum of the electrostatic potential generated by the solute's charge distribution ρ_{sol} and the solvent reaction potential, ε the dielectric constant of the solvent, n the unit vector perpendicular to the cavity surface and pointing outwards, and the subscript *in* and *out* to indicate the regions inside and outside the cavity.

Several approaches are available to solve this electrostatic problem such as the apparent surface charge (ASC) method used in the PCM model. Here, the second contribution to the total electrostatic potential aforementioned is the interaction potential of the solute electrons with an apparent surface charge due to the polarisation of the dielectric medium spread on the cavity surface. In practice, this surface is divided into a number of finite triangular non-overlapping elements of known area, called tesserae, at the centre of which is placed a punctual charge. By definition, there is a mutual polarisation between the solute and surrounding solvent, as the solvent reaction field acting upon the solute results from the polarisation it induces in the solvent, and the problem has to be solved iteratively (Poisson equation coupled to Schrödinger equation for the solute). Basically, starting from ρ_{sol}^0 the charge density of the solute without solvent, one can obtain a set of apparent charges by solving the electrostatic problem at the cavity surface. These charges are used to define the interaction potential in \hat{H}_{eff} and solve the corresponding Schrödinger equation, leading to a new ρ_{sol}^1 for the solute that will be used to solve the new electrostatic problem, and so on, until self-consistency.

2.6 Molecular dynamics simulations

Molecular dynamics^[62, 63] (MD) is a simulation method often used to study the conformational rearrangements of molecules and their interactions with other molecular species in a range of environments. A standard MD computer simulation consists in the computation of the trajectory in the phase space of a system of N interacting bodies. MD generates a list of phase points \mathcal{P}_i in the phase space (\mathbf{r}, \mathbf{p}) and ordered in time, where \mathbf{r} and \mathbf{p} are respectively the positions and momenta. The workflow of an MD simulation is described in Figure 2.7. First, the system is initialized by selecting initial positions and velocities. Then, the forces on all particles $i=1, 2, 3, \dots, N$ are computed. Newton's equations of motion are integrated numerically to obtain new positions and momenta. This step and the previous one make up the core of the simulation. They are repeated until we have computed the time evolution of the system for the desired length of time. After completion of the central loop, the averages of measured quantities are computed and printed.

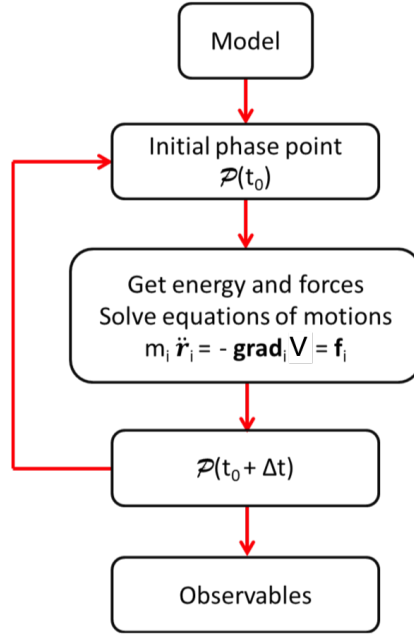


Figure 2.7 – Workflow of an MD simulation.

In MD simulations the collective properties are then determined from the trajectory of all particles, i.e., from the time evolution of positions $\mathbf{r} \equiv \mathbf{r}_i$ and momenta $\mathbf{p} \equiv \mathbf{p}_i$. The method relies on the assumption that stationary values of every average observable \mathcal{A} can be defined as time integrals over the trajectory in the phase space:^[64]

$$\langle \mathcal{A} \rangle = \lim_{\tau \rightarrow \infty} \frac{1}{\tau} \int_0^\tau \mathcal{A}[\mathbf{r}(t), \mathbf{p}(t)] dt \quad (2.130)$$

In practice, the classical mechanics trajectory is computed at discrete times $t=0, t=\Delta t, \dots, t=\tau=N_t\Delta t$, with N_t the number of frames and τ the length of the simulation. The discrete time step Δt determines the time resolution of the trajectory and has to be sufficiently small to ensure proper integration of the equations of motion. For instance, the popular velocity–Verlet integrator (Figure 2.8) is a three step algorithm solving the Newton’s equations and can be described in the following way:

1. The momenta at half time step $t + \frac{\Delta t}{2}$ are computed from those at time t and the forces at time t :

$$\mathbf{p}_i(t + \frac{\Delta t}{2}) = \mathbf{p}_i(t) + \frac{\Delta t}{2} \mathbf{f}_i(t) \quad (2.131)$$

2. The new coordinates at time $t + \Delta t$ are computed from those at time t and the momenta at half time step $t + \frac{\Delta t}{2}$:

$$\mathbf{r}_i(t + \Delta t) = \mathbf{r}_i(t) + \frac{\Delta t}{m} \mathbf{p}_i(t + \frac{\Delta t}{2}) \quad (2.132)$$

3. The new momenta at time $t + \Delta t$ are computed from those at half time step $t + \frac{\Delta t}{2}$ and the forces at time $t + \Delta t$:

$$\mathbf{p}_i(t + \Delta t) = \mathbf{p}_i(t + \frac{\Delta t}{2}) + \frac{\Delta t}{2} \mathbf{f}_i(t + \Delta t) \quad (2.133)$$

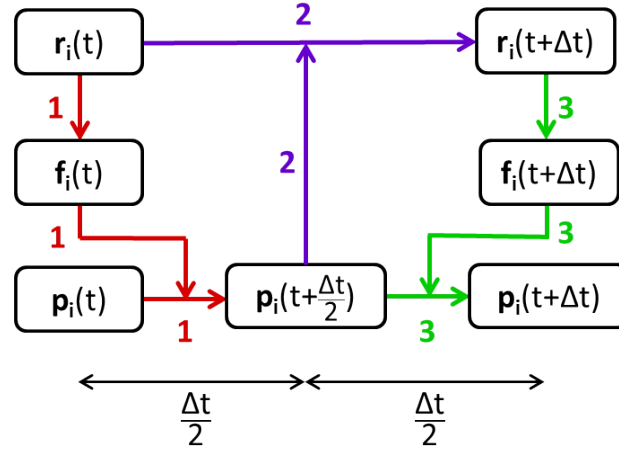


Figure 2.8 – Flowchart of the velocity-Verlet algorithm for the evolution of position \mathbf{r} and linear momentum \mathbf{p} .

The atomic or particle positions and momenta produced by MD simulations are the starting point for the calculation of a variety of physical properties. To prepare the sample, one selects a model system consisting of N particles and solves Newton's equations of motion for this system until its properties no longer change with time, i.e until the equilibration of the system. After equilibration, the actual measurement is performed. It should be mentioned that to measure an observable quantity in a MD simulation, we must first of all be able to express this observable as a function of the positions and momenta of the particles in the system. Then, the instantaneous values of a certain physical observable $\mathcal{A}(t)$ can be computed from the phase points to estimate the corresponding time average, in practice replacing the integral in Equation (2.130) with a discrete summation:

$$\langle \mathcal{A} \rangle \approx \frac{1}{N_t} \sum_{n=1}^{N_t} \mathcal{A}(n\Delta t) \quad (2.134)$$

The knowledge of a mathematical expression for internal energy V , also called interaction potential, is a necessary condition to perform simulations. Every success or failure of the simulation is ascribable to a success or a failure of the interaction potential model. Constructing this model requires many simplifications and approximations. The internal energy of a system of molecules is a complex function of the positions and momenta of all nuclei and electrons. If one is interested in studying the morphology and dynamics at the molecular scale, an effective way of tackling this difficult task is to describe atoms as charged classical particles and completely neglect electrons. Without any approximation,

the potential energy of the system can be expanded into a series of many-body interaction terms:

$$V = \sum_i V_i + \sum_{i<j} V_{ij} + \sum_{i<j<k} V_{ijk} + \sum_{i<j<k<l} V_{ijkl} + \dots \quad (2.135)$$

where the terms represent the self-energy of the atoms, the pairwise interaction between two atoms, and so on. The assumption of fixed connectivity between the atoms allows for further dividing the energy terms between those belonging to the same molecule, giving rise to a set of intramolecular interactions, typically approximated with up to four-body terms, and those belonging to different molecules, responsible of intermolecular interactions. In order to limit the number of interactions to be computed, the intermolecular expansion is usually truncated at the two-body term, although three-body contributions are not negligible. This level of truncation determines the computational cost, growing then proportionally with the number of pair interactions, so roughly with the square of the number of particles. To compensate for neglecting higher terms, some adjustable parameters (e.g., the atomic size and the interaction strength when representing the atoms) are normally fitted to reproduce basic thermodynamic properties, giving rise to effective pairwise potentials rather than exact ones.

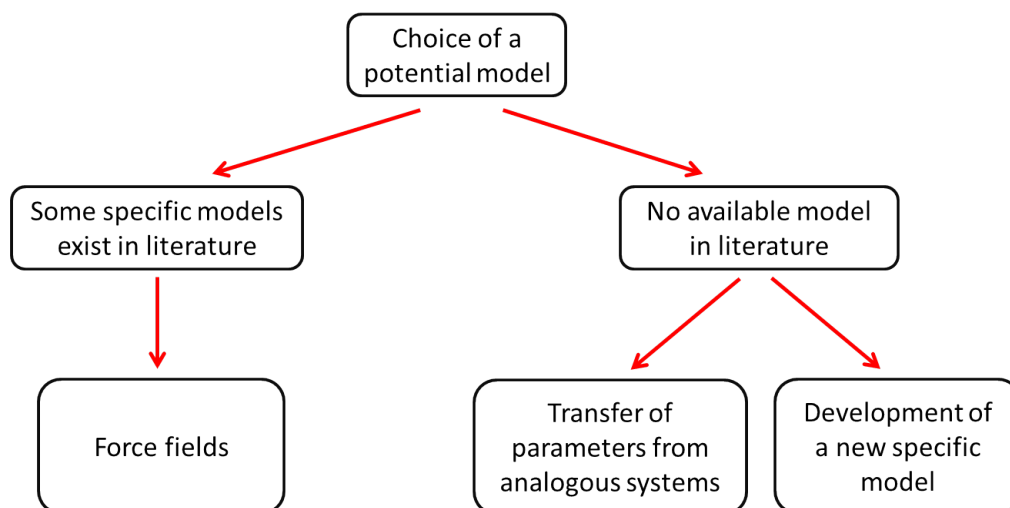


Figure 2.9 – Strategies to get a potential model for simulations.

Different strategies are possible to get a potential model for simulations (Figure 2.9). The set of mathematical functions and parameters used to express the interaction potential is in fact referred to as force field. In the simplest category of force fields, so-called “Class I”, the interactions between atoms have a direct physical meaning. For example, the total energy of the system is divided into bonded (bonds, angles and torsions) and non-bonded (repulsion, dispersion and electrostatic) interactions:

$$V_{total} = V_{bonded} + V_{non-bonded} \quad (2.136)$$

The force fields of this kind rely on intramolecular potential energy functions like the following:

$$V_{bonded} = \sum_{\text{bonds}} K_r (r - r_{eq})^2 + \sum_{\text{angles}} K_\theta (\theta - \theta_{eq})^2 + \sum_{\text{dihedrals}} \sum_n V_n [1 + \cos(n\phi - \gamma_n)] \quad (2.137)$$

where the three contributions represent bond stretching, bending, and internal rotations or torsions. The first two terms are described with simple harmonic potentials, characterized by the equilibrium bond distances r_{eq} and angles θ_{eq} , with force constants K_r and K_θ . The third term is a cosine expansion, with coefficients V_n and phases γ_n , of the torsional potential for each internal rotation angle γ . Note that the three functions involve respectively two-, three-, and four-body intramolecular interactions, referring to the expansion in (2.135). Non-bonded atom-atom interactions are instead assumed to be pairwise additive and include the sum of Lennard-Jones terms, allowing for steric repulsion A_{ij}/r_{ij}^{12} , dispersive Van der Waals attraction B_{ij}/r_{ij}^6 , and unscreened electrostatic Coulomb terms between the partial charges q_i, q_j lying on two atoms i, j at distance r_{ij} :

$$U_{non-bonded} = \sum_{\text{atoms}}^{i < j} \left[\frac{A_{ij}}{r_{ij}^{12}} - \frac{B_{ij}}{r_{ij}^6} + \frac{q_i q_j}{r_{ij}} \right] \quad (2.138)$$

These charges reflect local differences in electronegativity and chemical environment inside the molecule. In practice, partial charges are obtained, often together with the geometrical parameters in (2.137), from preliminary quantum chemistry calculations on isolated molecules. Non-bonded interactions are normally excluded for directly bonded atoms (also labeled as 1-2 interactions) and for atoms sharing a common bonded atom (1-3), while for atoms which are 1-4 connected they are often reduced, with respect to 1-5 or other intramolecular or intermolecular ones, by a factor which depends on the adopted force field. In general, atomistic force fields can offer an adequate description or, in the most favorable cases, prediction of the properties of complex molecular systems at equilibrium. However, it should not be overlooked that parameterization and validation of force fields is carried out on certain classes of compounds and that their transferability to other categories should not be taken for granted. When exploiting the force field for modeling a compound not present in the original training set, its performance should be thoroughly cross-checked against experimental data for the target system, such as density, diffusion coefficient, crystal structures or other physical properties which depend on the correct description of both intra and intermolecular terms. This is discussed in more details in the study reported in Chapter 4 of this thesis, in which refinement of existing force fields was necessary to improve the description of intra and intermolecular interactions within supramolecular assemblies of dipolar π -conjugated dyes.

Finally, the so-called Periodic Boundary Conditions (PBC) are routinely employed in MD simulations to simulate bulk material and remove surface effects. PBC means surrounding the simulation box with its translational images in the 3 directions of space, as illustrated (Figure 2.10). An atom which passes over the cell boundary comes back on the other side. PBC are usually used in conjunction with the minimum image convention for short ranged forces. Here, we only consider interactions between each molecule and the closest periodic image of its neighbours. For consistency with the minimum image convention, the maximum inter-atomic distance which is taken into account, also called cut-off distance r_{cut} , must be equal to half the box length ($r_{cut}=L/2$).

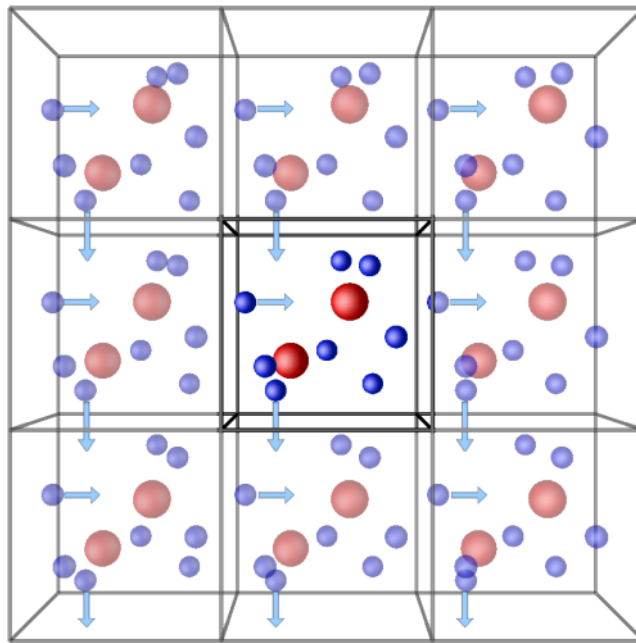


Figure 2.10 – Schematic representation of periodic boundary conditions.

Bibliography

- [1] Planck M. Ueber die Elementarquanta der Materie und der Elektrizität. *Ann. Physik*, 309:564, 1901.
- [2] Einstein A. Über einen die Erzeugung und Verwandlung des Lichtes betreffenden heuristischen Gesichtspunkt. *Ann. Physik*, 322:132, 1905.
- [3] De Broglie L. Recherches sur la théorie des Quanta. *Ann. Phys.*, 10:22, 1925.
- [4] Schrödinger E. Quantisierung als Eigenwertproblem. *Ann. Physik*, 384:361, 1926.
- [5] Born M. and Oppenheimer R. Zur Quantentheorie der Molekeln. *Ann. Physik*, 84:457, 1927.
- [6] Szabo A. and Ostlund N. S. Modern quantum chemistry : introduction to advanced electronic structure theory. 1989.
- [7] Fock V. Näherungsmethode zur Lösung des quantenmechanischen Mehrkörperproblems. *Z. Phys.*, 61:126, 1930.
- [8] Hartree D. R. *Proc. R. Soc. (London)*, A113:621, 1928.
- [9] Roothaan C. C. J. New Developments in Molecular Orbital Theory. *Rev. Mod. Phys.*, 23:69, 1951.
- [10] Hall G. G. The molecular orbital theory of chemical valency VIII. A method of calculating ionization potentials. *Proc. Roy. Soc. (London)*, A205:541, 1951.
- [11] Jensen F. *Introduction to Computational Chemistry*. Wiley, Chichester, 1999.
- [12] Cramer C. J. *Essentials of computational chemistry*. Wiley, Chichester, 2004.
- [13] Cremer D. Møller–Plesset perturbation theory: from small molecule methods to methods for thousands of atoms. *Comp. Mol. Sci.*, 1:509, 2011.
- [14] Thomas L. H. The calculation of atomic fields. *Proc. Camb. Phil. Soc.*, 23:542, 1927.
- [15] Fermi E. Eine statistische Methode zur Bestimmung einiger Eigenschaften des Atoms und ihre Anwendung auf die Theorie des periodischen Systems der Elemente. *Z. Phys.*, 48:73, 1928.
- [16] Dirac P. A. M. Note on Exchange Phenomena in the Thomas Atom. *Proc. Camb. Phil. Soc.*, 26:376, 1930.
- [17] Bloch F. Bemerkung zur Elektronentheorie des Ferromagnetismus und der elektrischen Leitfähigkeit. *Z. Phys.*, 57:545, 1929.

- [18] Teller E. On the Stability of Molecules in the Thomas-Fermi Theory. *Rev. Mod. Phys.*, 34:627, 1962.
- [19] Hohenberg P. and Kohn W. Inhomogeneous Electron Gas. *Phys. Rev.*, 136:B864, 1964.
- [20] Kohn W. and Sham L.J. Self-Consistent Equations Including Exchange and Correlation Effects. *Phys. Rev.*, 140:A1133, 1965.
- [21] Perdew J. P. and Schmidt K. Jacob's ladder of density functional approximations for the exchange-correlation energy. In *Density Functional Theory and its Application to Materials*, volume 577 of *AIP Conference Series*, page 1, 2001.
- [22] Ceperley D. M. and Alder B. J. Ground State of the Electron Gas by a Stochastic Method. *Phys. Rev. Lett.*, 45:566, 1980.
- [23] Vosko S. H., Wilk L., and Nusair M. Accurate spin-dependent electron liquid correlation energies for local spin density calculations: a critical analysis. *Can. J. Phys.*, 58:1200, 1980.
- [24] Perdew J. P. and Wang Y. Accurate and simple analytic representation of the electron-gas correlation energy. *Phys. Rev. B*, 45:13244, 1992.
- [25] Becke A. D. Density-functional exchange-energy approximation with correct asymptotic behavior. *Phys. Rev. A*, 38:3098, 1988.
- [26] Lee C., Yang W., and Parr R. G. Development of the colle-salvetti correlation-energy formula into a functional of the electron density. *Phys. Rev. B*, 37:785, 1988.
- [27] Perdew J. P. In *Electronic Structure of Solids '91*. Ed. P. Ziesche and H. Eschrig (Akademie Verlag, Berlin, 1991) 11.
- [28] Perdew J. P., Burke K., and Ernzerhof M. Generalized Gradient Approximation Made Simple. *Phys. Rev. Lett.*, 77:3865, 1996.
- [29] Becke A. D. Completely numerical calculations on diatomic molecules in the local-density approximation. *Phys. Rev. A*, 33:2786, 1986.
- [30] Bauschlicher C. W. A comparison of the accuracy of different functionals. *Chem. Phys. Lett.*, 246:40, 1995.
- [31] Iikura H., Tsuneda T., Yanai T., and Hirao K. A long-range correction scheme for generalized-gradient-approximation exchange functionals. *J. Chem. Phys.*, 115:3540, 2001.
- [32] Yanai T., Tew D. P., and Handy N. C. A new hybrid exchange–correlation functional using the Coulomb-attenuating method (CAM-B3LYP). *Chem. Phys. Lett.*, 393:51, 2004.

- [33] Chai J-D and Head-Gordon M. Long-range corrected hybrid density functionals with damped atom–atom dispersion corrections. *Phys. Chem. Chem. Phys.*, 10:6615, 2008.
- [34] Langhoff P. W., Karplus M., and Hurst R. P. Approximations to Hartree-Fock Perturbation Theory. *J. Chem. Phys.*, 44:505, 1966.
- [35] Caves T. C. and Karplus M. Perturbed Hartree–Fock Theory. I. Diagrammatic Double-Perturbation Analysis. *J. Chem. Phys.*, 50:3649, 1969.
- [36] Helgaker T., Coriani S., Jørgensen P., Kristensen K., Olsen J., and Ruud K. Recent Advances in Wave Function-Based Methods of Molecular-Property Calculations. *Chem. Rev.*, 112:543, 2012.
- [37] Casida M. E., Chermette H., and Jacquemin D. Time-dependent density-functional theory for molecules and molecular solids. *J. Mol. Struct. Theochem*, 914:1, 2009.
- [38] de Wergifosse M. and Grimme S. Nonlinear-response properties in a simplified time-dependent density functional theory (sTD-DFT) framework: Evaluation of the first hyperpolarizability. *J. Chem. Phys.*, 149:024108, 2018.
- [39] de Wergifosse M. and Grimme S. Perspective on Simplified Quantum Chemistry Methods for Excited States and Response Properties. *J. Phys. Chem. A*, 125:3841, 2021.
- [40] Grimme S. and Bannwarth C. Ultra-fast computation of electronic spectra for large systems by tight-binding based simplified Tamm-Dancoff approximation (sTDA-xTB). *J. Chem. Phys.*, 145:054103, 2016.
- [41] Cohen H. D. and Roothaan C. Electric Dipole Polarizability of Atoms by the Hartree-Fock Method. I. Theory for Closed [U+2010]Shell Systems. *J. Chem. Phys.*, 43:S34, 1965.
- [42] Richardson L. F. and Gaunt J. A. Philosophical transactions of the Royal Society of London. Series A, Containing papers of a mathematical or physical character. 344:299, 1927.
- [43] De Wergifosse M., Liégeois V., and Champagne B. Evaluation of the molecular static and dynamic first hyperpolarizabilities. *Int. J. Quant. Chem.*, 114:900, 2014.
- [44] Mohammed A. A. K., Limacher P. A., and Champagne B. Finding optimal finite field strengths allowing for a maximum of precision in the calculation of polarizabilities and hyperpolarizabilities. *J. Comput. Chem.*, 34:1497, 2013.
- [45] Richardson L. F. and Gaunt J. A. The Deferred Approach to the Limit. Part I. Single Lattice. Part II. Interpenetrating Lattices. *Philos. Trans. R. Soc. London Ser. A*, 226:299, 1927.

- [46] Oudar J. L. and Chemla D. S. Hyperpolarizabilities of the Nitroanilines and Their Relations to the Excited State Dipole Moment. *J. Chem. Phys.*, 66:2664, 1977.
- [47] Le Bahers T., Adamo C., and Ciofini I. A Qualitative Index of Spatial Extent in Charge-Transfer Excitations. *J. Chem. Theory Comput.*, 7:2498, 2011.
- [48] Jacquemin D., Bahers T. L., Adamo C., and Ciofini I. What is the “best” atomic charge model to describe through-space charge-transfer excitations? *Phys. Chem. Chem. Phys.*, 14:5383, 2012.
- [49] Slater J. C. Atomic Shielding Constants. *Phys. Rev.*, 36:57, 1930.
- [50] Boys S. F. Electronic wave functions - I. A general method of calculation for the stationary states of any molecular system. *Proc. R. Soc. London*, A200:542, 1950.
- [51] Binkley J. S., Pople J. A., and Hehre W. J. Self-consistent molecular orbital methods. 21. Small split-valence basis sets for first-row elements. *J. Am. Chem. Soc.*, 102:939, 1980.
- [52] Gordon M. S., Binkley J. S., Pople J. A., Pietro W. J., and Hehre W. J. Self-consistent molecular-orbital methods. 22. Small split-valence basis sets for second-row elements. *J. Am. Chem. Soc.*, 104:2797, 1982.
- [53] Frisch M. J., Pople J. A., and Binkley J. S. Self-consistent molecular orbital methods 25. Supplementary functions for Gaussian basis sets. *J. Chem. Phys.*, 80:3265, 1984.
- [54] Dunning T. H. Gaussian basis sets for use in correlated molecular calculations. I. The atoms boron through neon and hydrogen. *J. Chem. Phys.*, 90:1007, 1989.
- [55] Tomasi J., Mennucci B., and Cammi R. Quantum Mechanical Continuum Solvation Models. *Chem. Rev.*, 105:2999, 2005.
- [56] Cramer C. J. and Truhlar D. G. Implicit Solvation Models: Equilibria, Structure, Spectra, and Dynamics. *Chem. Rev.*, 99:2161, 1999.
- [57] Tomasi J., Mennucci B., and Cancès E. The IEF version of the PCM solvation method: an overview of a new method addressed to study molecular solutes at the QM ab initio level. *J. Mol. Struct. (Theochem)*, 464:211, 1999.
- [58] Pierotti R. A. A scaled particle theory of aqueous and nonaqueous solutions. *Chem. Rev.*, 76:717, 1976.
- [59] Langlet J., Claverie P., Caillet J., and Pullman A. Improvements of the continuum model. 1. Application to the calculation of the vaporization thermodynamic quantities of nonassociated liquids. *J. Phys. Chem.*, 92:1617, 1988.

- [60] Amovilli C. and Mennucci B. Self-Consistent-Field Calculation of Pauli Repulsion and Dispersion Contributions to the Solvation Free Energy in the Polarizable Continuum Model. *J. Phys. Chem. B*, 101:1051, 1997.
- [61] Onsager L. Electric Moments of Molecules in Liquids. *J. Am. Chem. Soc.*, 58:1486, 1936.
- [62] Alder B. J. and Wainwright T. E. Studies in Molecular Dynamics. I. General Method. *J. Chem. Phys.*, 31:459, 1959.
- [63] Alder B. J. and Wainwright T. E. Studies in Molecular Dynamics. II. Behavior of a Small Number of Elastic Spheres. *J. Chem. Phys.*, 33:1439, 1960.
- [64] Muccioli L., D'Avino G., Berardi R., Silvia S., Pizzirusso A., Ricci M., Roscioni O. M., and Zannoni C. *Supramolecular organization of functional organic materials in the bulk and at organic/organic interfaces: a modeling and computer simulation approach*, page 39. Springer Berlin Heidelberg, 2014.

Performance of DFT functionals for calculating the second-order NLO properties of dipolar merocyanines

3.1 Introduction

In this Chapter, we explore the performance of various DFT exchange-correlation functionals (XCFs) for predicting the quadratic NLO responses of recently designed dipolar merocyanines,^[1, 2, 3] in which tricyanopropylidene-based acceptor units are connected to dihexylaminophenyl or dihexylaminothiophenyl donor moieties through polyenic bridges of different lengths (Figure 3.1). HRS measurements demonstrated that these highly dipolar dyes exhibit large first hyperpolarizabilities together with an apparently antagonistic cyanine-like behavior. In particular, the longest derivative incorporating dihexylaminothiophenyl and phthalimide-substituted tricyanopropylidene terminal groups (**II'**[4]) was found to display a record hyperpolarizability together with a negligible bond length alternation (BLA),^[1] in apparent contradiction with the paradigm linking large quadratic NLO responses to an optimal (non zero) BLA value^[4, 5] (see Chapter 1).

The accurate description of the first hyperpolarizabilities of such NLO chromophores, which exhibit large ground-state charge transfer as well as low-lying charge-transfer excited states, is highly challenging for DFT. Many works have reported the inadequacy of exchange-correlation functionals (XCFs) based on the local density approximation (LDA) or the generalized gradient approximation (GGA) for computing the first hyperpolarizabilities of such extended π -conjugated systems. This failure has been attributed to the self-interaction error or overdelocalization of the response to external fields, and originates from the short-range treatment of exchange, as opposed to the exact exchange used in Hartree-Fock theory.^[6, 7, 8] Global hybrid functionals incorporating a low amount of exact exchange were also proved unsuitable for the evaluation of β of conjugated chains terminated by D/A pairs, showing a nearly catastrophic behavior with respect to increasing

the chain length.^[6, 9, 10, 11] This issue can be partially alleviated by using range-separated (RS) hybrids, which offer the possibility to restore the correct asymptotic behavior of the exchange potential at large distances.^[7]

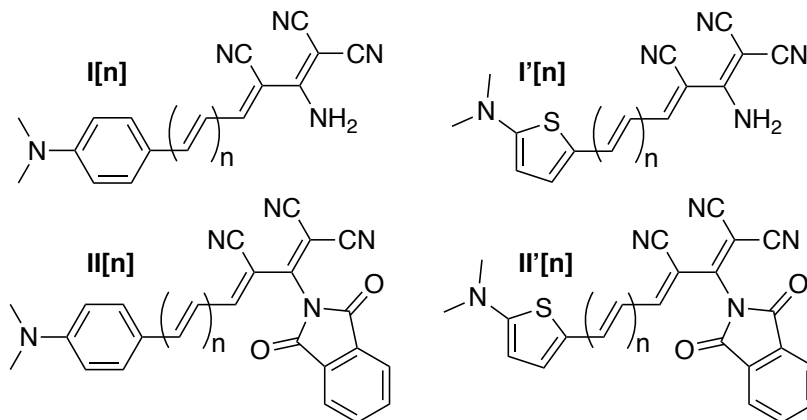


Figure 3.1 – Structures of the tricyanopropylidene-based merocyanines studied herein. The length of the polyenic chain varies from $n = 0$ to $n = 4$.

Here, we examine the relevance of hybrid exchange–correlation functionals (XCFs) incorporating different rates of exact Hartree-Fock exchange (HFX), as well as of several RS hybrids. Since optimizing the range separation parameter ω in RS-XCFs has been shown to improve the description of first hyperpolarizabilities of some prototypical charge-transfer compounds,^[10, 11] hyperpolarizabilities calculated using default ω values are compared to those calculated using ω values tuned according to a system-specific, nonempirical procedure. Still, in this study, more complex, chemically-designed compounds are chosen in order to assess the performance of XCFs, extending the earlier works on prototypical systems like α , ω -nitro,amino-polyenes and -polyyenes.^[7, 9] Here, the smallest compound (**I'[0]**) contains 30 atoms while the largest one (**II[4]**) has 61. The accuracy of the various functionals is discussed depending on their ability to reproduce experimental HRS data, as well as MP2 calculations, used as theoretical references.

3.2 Levels of approximation

Molecular structures were optimized using DFT together with the hybrid M06-2X^[12] XCF and the 6-311G(d) basis set. As shown in previous reports^[13, 14] the M06-2X XCF reliably describes the BLA of extended π -conjugated systems, which is prerequisite for accurate predictions of optical properties. Each structure was characterized as a minimum on the potential energy surface based on its real harmonic vibrational frequencies. Note that terminal N,N-dihexylamino donor groups present in the compounds characterized experimentally have been replaced by simpler N,N-dimethylamino groups in all calculations (see Figure 3.1).

Absorption properties, as well as static and dynamic (frequency-dependent) second-order nonlinear optical responses, were determined using TD-DFT^[15] with the 6-311+G(d) basis set in combination with various XCFs. The 2006 Minnesota family of functionals^[12] was first considered, in order to evaluate the impact of increasing the amount of exact HFX from M06L (0%) to M06 (27%), M06-2X (54%), and M06-HF (100%). The BLYP XCF was employed as well for comparison purposes. Since they have been shown to improve the description of second-order NLO properties of extended π -conjugated systems,^[7, 8, 11] we also addressed the performance of different classes of LRC XCFs. The LRC-XCFs considered in this study are i) LC-BLYP, ii) CAM-B3LYP and iii) ω B97X-D (see Chapter 2 for a detailed description). In addition to calculations using standard values of the RS parameter, we carried out calculations using optimally-tuned ω values in order to obtain a more accurate description of charge-transfer (CT) excitation energies and NLO responses. The procedure used to determine optimal system-dependent ω values is described in the next section.

In addition to DFT, hyperpolarizabilities were calculated using the CPHF method, as well as using MP2 in combination with a finite field (FF) procedure. A fully automated Romberg scheme was used to improve and control the accuracy of the numerical derivatives, using field amplitudes ranging from ± 0.0008 to ± 0.0032 a.u. for compounds with $n = 0$, and from ± 0.0002 to ± 0.0032 a.u. for compounds with $n = 1 - 4$.^[16] Since the MP2 method was shown to closely reproduce the NLO responses obtained with reference CCSD(T) calculations for push-pull π -conjugated systems,^[7] MP2 values are used as theoretical references in this study.

Solvent effects were included in both geometry optimizations and calculations of the optical properties by using the Integral Equation Formalism (IEF) version of the Polarizable Continuum Model (IEF-PCM).^[17, 18] In line with experimental characterizations, chloroform was used as solvent, with dielectric constants $\epsilon_0 = 4.711$ in the static limit and $\epsilon_\infty = 2.091$ at infinite frequency. All calculations were performed with the Gaussian16 package.^[19]

3.3 Optimal tuning of the range separation parameter

The range-separation parameters ω were optimized according to a standard nonempirical system-specific procedure, such that Koopmans' theorem for both neutral and anion is obeyed as closely as possible.^[20, 21, 22, 23] Optimal ω values, denoted as ω_{opt} in the following, corresponds to the minimum of the function below, which is found using the

golden section-search algorithm:^[24]

$$J(\omega) = \sqrt{J_0^2(\omega) + J_1^2(\omega)} \quad (3.1)$$

where

$$J_0(\omega) = |\epsilon_{HOMO}(N) + IP(N)| \quad (3.2)$$

$$J_1(\omega) = |\epsilon_{HOMO}(N + 1) + EA(N)| \quad (3.3)$$

$\epsilon_{HOMO}(N)$ and $\epsilon_{HOMO}(N + 1)$ are the HOMO energies of the system with N (neutral) and $N + 1$ electrons (anion), respectively. The ionization potential (IP) and electron affinity (EA) are calculated as the differences between ground-state energies of systems with N and $N \pm 1$ electrons:

$$IP(N) = E(N - 1) - E(N) \quad (3.4)$$

$$EA(N) = IP(N + 1) = E(N) - E(N + 1) \quad (3.5)$$

Two different ω -tuning schemes were employed, differing in the computation of IP and EA. In the first one, these two quantities are calculated using the standard attenuating parameter (ω_{std}) of the functional, so that their values are kept fixed throughout the optimization procedure. In the second one, IP and EA are calculated self-consistently, *i.e.* using the optimal value of the RS parameter (ω_{opt}) at each step of the process. This second procedure is the most common way of optimizing ω , but results in larger computational times. To the best of our knowledge, we report here the first study comparing the performance of self-consistent (SC) and non self-consistent (NSC) ω -tuning schemes.

While ω -tuning schemes were shown to provide improved fundamental gaps and absorption properties,^[22, 25, 23, 26, 10, 27] the conclusions are more controversial regarding second-order NLO responses. In recent studies, Sun and Autschbach,^[10] as well as Scuseria and coworkers^[11] concluded that LRC-XCFs using physically-adjusted RS parameters lead to improved description of the first hyperpolarizabilities of D-A-substituted organic molecules. Improved correlation with reference CCSD(T) second-hyperpolarizability values was also obtained by Matito, Luis *et al.* by empirically tuning the RS parameter of the LC-BLYP functional for a benchmark set of 60 medium-size molecules.^[28] In contradiction, other investigations reported that the tuning of ω to enforce Koopmans' theorem does not offer real improvement in the description of NLO properties.^[27, 29] In this work, ω values were optimized in the gas phase for the LC-BLYP, CAM-B3LYP and ω B97X-D LRC hybrids. Since it was also demonstrated in previous works that ω values optimized in solvent media using PCM provide reliable hyperpolarizabilities compared to experiments,^[11] the ω values of the LC-BLYP functional were also optimized in the presence of a dielectric continuum.

3.4 Experimental reference data

Experimental UV/Vis data as well as HRS hyperpolarizabilities measured in chloroform using an incident wavelength of 1907 nm are gathered in Table 3.1. Experimental β_{HRS} values are given according to convention T, and are relative to the HRS response of the DR1 reference molecule provided in ref. 30 (see also note ref. 31). As reported in ref. 30, $\lambda_{max} = 481$ nm and $\beta_{zzz}^{\infty} = 160 \times 10^{-30}$ esu = 18516 a.u. for DR1 in chloroform. Assuming that DR1 has a quasi $C_{\infty v}$ symmetry, $\beta_{HRS}^{\infty} = \sqrt{\frac{6}{35}} \times \beta_{zzz}^{\infty} = 7667$ a.u. At 1907 nm, $F_{disp}^{TSA} = 1.43$, so that $\beta_{HRS}^{1907} = \beta_{HRS}^{\infty} \times F_{disp}^{TSA} = 7667 \times 1.43 = 10963$ a.u.). Static first hyperpolarizabilities (*i.e.* at infinite wavelength) were extrapolated from the dynamic ones according to the two-state model, after introducing a homogeneous damping Γ into the frequency dispersion factor (eq 2.123) to attenuate the resonance effects:

$$F_{disp}^{TSA}(\Gamma) = \frac{\beta_{HRS}^{1907}}{\beta_{HRS}^{\infty}} = \frac{\Delta E_{01}^2 (\Delta E_{01} - i\Gamma)^2}{\{(\Delta E_{01} - i\Gamma)^2 - (\hbar\omega)^2\} \{(\Delta E_{01} - i\Gamma)^2 - (2\hbar\omega)^2\}} \quad (3.6)$$

In line with previous studies including a previous report on these derivatives^[32, 33, 34, 3], the static first hyperpolarizabilities were extrapolated by setting Γ to 1.2 times the half width at half maximum (HWHM) of the first absorption band (Table 3.1), in order to account for the change in the absorption bandwidth from one compound to another. For comparison, β_{HRS}^{∞} values were also extrapolated in the absence of homogeneous damping ($\Gamma = 0$).

Table 3.1 – Experimental data (all measured in chloroform) used as references for calculations.^[1, 3] Maximal absorption wavelengths (λ_{max} , nm), half widths at half maximum (HWHM, cm^{-1}) of the main absorption band, dynamic first hyperpolarizabilities (β_{HRS}^{1907} , a.u.), and static ones extrapolated using eq 3.6 with $\Gamma = 0$ ($\beta_{HRS}^{\infty}(0)$, a.u.) and $\Gamma = 1.2 \times \text{HWHM}$ ($\beta_{HRS}^{\infty}(\Gamma)$, a.u.). Relative $\beta[n]/\beta[0]$ values are reported in parentheses for each series of compounds.

	λ_{max}	HWHM	β_{HRS}^{1907}	$F_{disp}^{TSA}(0)$	$\beta_{HRS}^{\infty}(0)$	$F_{disp}^{TSA}(\Gamma)$	$\beta_{HRS}^{\infty}(\Gamma)$
I[0]	470	1700	5800 (1.0)	1.41	4140 (1.0)	1.38	4220 (1.0)
I[1]	529	2350	9190 (1.6)	1.56	5852 (1.4)	1.47	6270 (1.5)
I[2]	565	2550	17900 (3.1)	1.69	10570 (2.6)	1.53	11660 (2.8)
I'[0]	515	950	8710 (1.0)	1.52	5730 (1.0)	1.51	5770 (1.0)
I'[1]	614	850	10640 (1.2)	1.91	5601 (1.0)	1.87	5680 (1.0)
I'[2]	704	1500	24670 (2.8)	2.54	9700 (1.7)	2.27	10870 (1.9)
I'[3]	712	2250	71590 (8.2)	2.62	27250 (4.8)	2.04	35070 (6.1)
I'[4]	720	2550	418430 (48.1)	2.71	154330 (27.0)	1.95	214220 (37.1)
II[0]	566	1100	21280 (1.0)	1.69	12580 (1.0)	1.66	12830 (1.0)
II[1]	668	1025	27090 (1.3)	2.24	12120 (1.0)	2.15	12620 (1.0)
II[2]	759	1400	277670 (13.0)	3.24	85690 (6.8)	2.71	102280 (8.0)
II'[0]	581	650	22740 (1.0)	1.75	12960 (1.0)	1.74	13080 (1.0)
II'[1]	690	450	37730 (1.7)	2.41	15630 (1.2)	2.39	15800 (1.2)
II'[2]	803	415	304760 (13.4)	4.18	72980 (5.6)	4.04	75410 (5.8)
II'[3]	916	400	1886590 (83.0)	16.77	112530 (8.7)	11.19	168620 (12.9)

3.5 Molecular structures

As mentioned above, reliable predictions of the optical properties of π -conjugated systems require an accurate description of the geometrical parameters associated to the electronic delocalization along the molecular backbone, in particular the bond length alternation (BLA). BLA values were calculated at the IEFPCM:M06-2X/6-311G(d) level for the four series of derivatives, according to the following expression:

$$BLA = \frac{1}{2n+1} \sum_{i=1}^{N-2} (-1)^{i+1} \times (d_{i+1} - d_i) \quad (3.7)$$

where d_i is the i^{th} interatomic distance within the polyenic linker of length n connecting the donor and acceptor units (see Figure A.1 and Table A.1). Note that this expression provides BLA values that are negative for all compounds. For simplicity, only the amplitudes are reported in the following.

As shown in Figure 3.2, the evolution of BLA with chain length differs from one series to another. In compounds incorporating a dimethylaminophenyl as donor group (**I[n]** and **II[n]**), BLA values display small variations with n , with values ranging from

0.066 to 0.074 Å for **I[n]** and from 0.052 to 0.064 Å for **II[n]**. In series **I'[n]** and **II'[n]** that include a dimethylaminothiophene donor, BLA values show much larger variations (from 0.024 to 0.067 Å for **I'[n]**, and from 0.002 to 0.054 Å for **II'[n]**). Consistently with the decrease of the π -electron conjugation with respect to increasing n , the pyramidalization angle of the dimethylamino substituent increases, as reported in Table A.2.

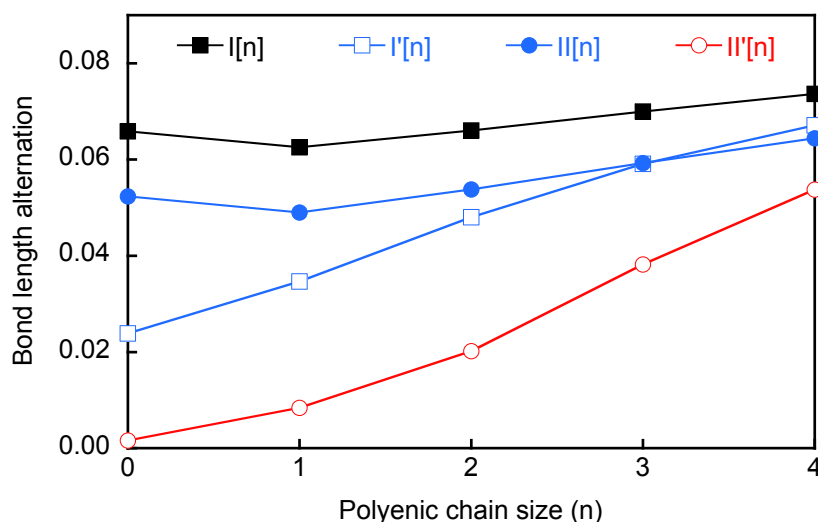


Figure 3.2 – Bond length alternation (in Å) calculated along the polyenic bridge of the four series of derivatives at the IEFPCM:M06-2X/6-311G(d) in chloroform.

3.6 Static first hyperpolarizabilities

3.6.1 Reference *ab initio* calculations

Table 3.2 reports the static HRS hyperpolarizability of the four merocyanine series calculated at the CPHF and MP2 levels. Previous theoretical investigations demonstrated that the MP2 level, as a result of cancellations between higher-order contributions, includes the largest part of electron correlation effects and closely reproduces the first hyperpolarizability of push–pull π -conjugated systems obtained with the CCSD(T) scheme.^[7] β_{HRS}^{MP2} values are thus used as theoretical references in the following, while comparison to β_{HRS}^{CPHF} values provides a direct measure of the magnitude of electron correlation effects.

Table 3.2 – Static HRS hyperpolarizabilities (β_{HRS}^∞ , a.u.) and relative $\beta_{HRS}^\infty[n]/\beta_{HRS}^\infty[0]$ values calculated at the CPHF/6-311+G(d) and MP2/6-311+G(d) levels in chloroform.

	CPHF		MP2	
	β_{HRS}^∞	$\beta_{HRS}^\infty[n]/\beta_{HRS}^\infty[0]$	β_{HRS}^∞	$\beta_{HRS}^\infty[n]/\beta_{HRS}^\infty[0]$
I[0]	4372	1.0	9797	1.0
I[1]	9530	2.2	24979	2.5
I[2]	16782	3.8	47273	4.8
I[3]	25344	5.8	72384	7.4
I[4]	33739	7.7	94967	9.7
I'[0]	3917	1.0	8299	1.0
I'[1]	11120	2.8	29722	3.6
I'[2]	24024	6.1	71680	8.6
I'[3]	35675	9.1	106571	12.8
I'[4]	42662	10.9	123604	14.9
II[0]	7173	1.0	17364	1.0
II[1]	15553	2.2	43885	2.5
II[2]	27055	3.8	82765	4.8
II[3]	40143	5.6	125463	7.2
II[4]	53090	7.4	163570	9.4
II'[0]	5587	1.0	10982	1.0
II'[1]	13591	2.4	32228	2.9
II'[2]	35754	6.4	112592	10.3
II'[3]	67724	12.1	232020	21.1
II'[4]	76914	13.8	250702	22.8

As expected from previous works,^[7, 35, 36, 34, 37, 16] electron correlation enhances the first hyperpolarizability by a factor ranging between 1.97 and 3.43. The $\beta_{HRS}^{MP2}/\beta_{HRS}^{CPHF}$ ratio is system-dependent, which demonstrates the need of including electron correlation effects since the latter introduce a non systematic scaling of the β_{HRS} values that might impact qualitative interpretations. As shown in Figure 3.3, the $\beta_{HRS}^{MP2}/\beta_{HRS}^{CPHF}$ ratios smoothly increase with the size n of the polyenic bridge up to a maximum value obtained for $n = 3$, and then slightly decrease. Although it follows the same trend, the **II'[n]** series, which incorporates the strongest D/A pair, displays stronger variations of the $\beta_{HRS}^{MP2}/\beta_{HRS}^{CPHF}$ ratio as a function of n .

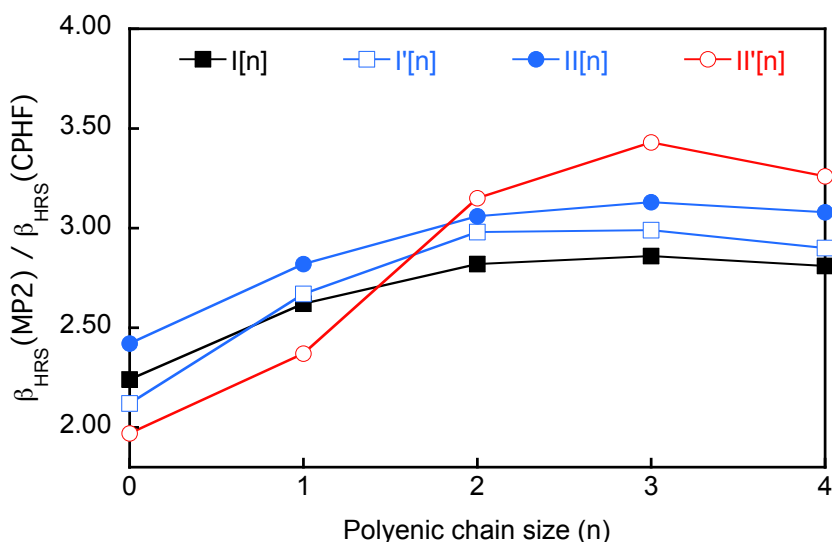


Figure 3.3 – $\beta_{HRS}^{MP2} / \beta_{HRS}^{CPHF}$ ratio as a function of chain length in the four series of derivatives.

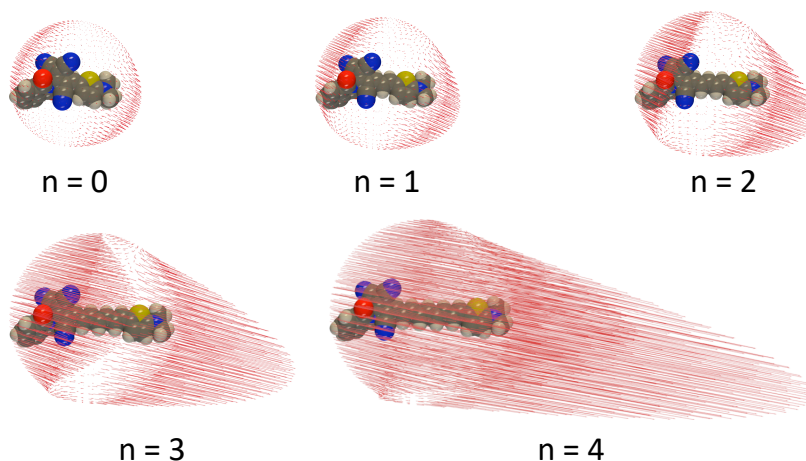


Figure 3.4 – Unit sphere representation of the static first hyperpolarizability tensor for compounds $\mathbf{II}'[n]$ ($n = 0 - 4$), as calculated at the CPHF level. Arrows represent the effective second-order induced dipoles $\vec{\mu}_{eff} = \overleftrightarrow{\beta} : \vec{F}^2(\theta, \phi)$ plotted at each point (θ, ϕ) of the surface of a sphere centered at the center of mass of the molecules, where $\overleftrightarrow{\beta}$ is the first hyperpolarizability tensor and \vec{F} a unit vector of the incident electric field with polarization defined in the spherical coordinates (θ, ϕ) .

As reported in Tables A.25 and A.26, the computed depolarization ratios are typical of one-dimensional push–pull π -conjugated systems; they range from 4.0 to 4.8 at the HF level, and are systematically larger (from 4.5 to 5.0) when introducing electron correlation effects at the MP2 level. Noteworthy, both levels of calculation evidence that increasing the conjugation length from $n = 0$ to $n = 4$ within a molecular series reinforces the 1D character of the NLO response, as also highlighted by unit sphere representations^[38] of the β tensor (see Figure 3.4 for the $\mathbf{II}'[n]$ series).

3.6.2 Two-state approximation

We address in this section the reliability of the two-state approximation, by comparing the static β_{HRS}^{TSA} values calculated using eq 2.122 with those calculated using full-featured CPHF calculations (β_{HRS}^{CPHF}). As shown in Figure 3.5a, the two sets of values correlate well (with correlation coefficients $R^2 \geq 0.99$, see Table A.11b), which proves the suitability of the TSA for describing qualitatively the variations of β_{HRS} . Note that the correlation remains very good ($R^2 = 0.986$) when considering the four series of molecules altogether (Figure A.11). However, as illustrated in Figure 3.5b for the four series of compounds, the relative error is not systematic, the TSA providing underestimated β_{HRS} values for small molecules, and overestimated ones for larger compounds. Besides, large relative errors (ranging between 40% and 46%) are obtained for the largest systems ($n = 4$). The same conclusions hold when the first hyperpolarizabilities are computed at the Coupled-Perturbed Kohn-Sham (CPKS) level. Interestingly, varying the XC functional within a given series of compounds does not induce significant changes in the evolution of β_{HRS}^{TSA} with respect to β_{HRS}^{CPKS} , and gives rise to linear regression equations with very similar slope coefficients (Table A.43). This indicates that the evolution of the error made on the HRS hyperpolarizabilities when using the TSA (see also Tables A.41 and A.42) hardly depends on the level of calculation, which further confirms the robustness of the two-state approximation for qualitative interpretations.

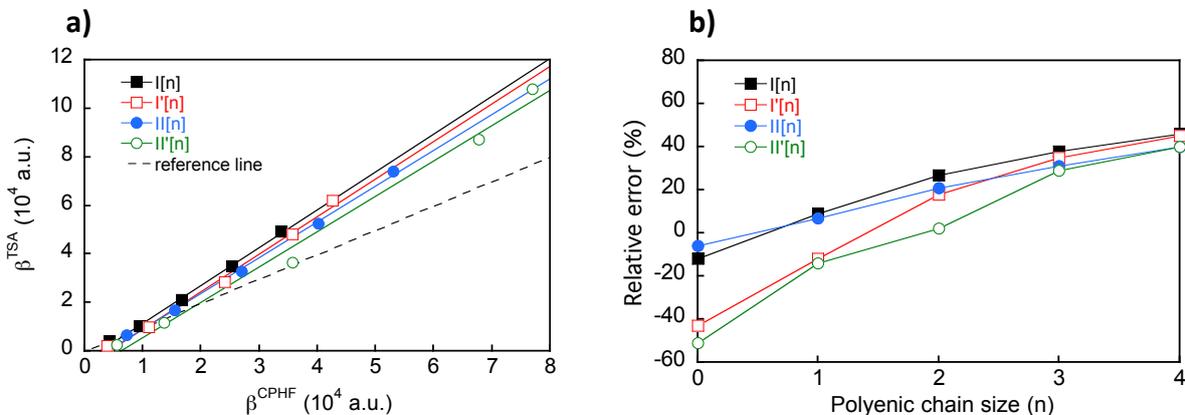


Figure 3.5 – a) Static β_{HRS} values of the four merocyanine series evaluated using the two-state approximation, plotted against the values calculated using CPHF/6-311+G(d) calculations in chloroform. Lines are linear fits. b): Evolution of the relative error (defined as $\text{Err} = (\beta_{HRS}^{TSA} - \beta_{HRS}^{CPHF})/\beta_{HRS}^{CPHF} \times 100$) with the length of the polyenic bridge.

3.6.3 Effect of the amount of exact HF exchange

The static HRS hyperpolarizabilities calculated using the Minnesota family of XCFs are collected in Table 3.3 for the four series of compounds. We first discuss the evolution of β_{HRS}^{∞} with respect to the percentage of HF exchange (%HFX) included in the functional for a given compound. As shown in Figure 3.6, β_{HRS}^{∞} of shorter derivatives hardly depends on %HFX, while it has a strong impact for the larger ones, since the latter are

more affected by conjugation effects.^[39] In series incorporating a dimethylaminophenyl as donor group (**I**[**n**] and **II**[**n**]), β_{HRS}^∞ linearly decreases with %HFX, as previously reported for other extended NLO chromophores.^[8] The series **I'**[**n**] and **II'**[**n**] that include a dimethylaminothiophene donor exhibit a less usual behavior: β_{HRS}^∞ linearly increases with %HFX for shorter compounds ($n = 0 - 2$), whereas it evolves non monotonically for **I'**[**3**] and **II'**[**4**], for which a maximum is found for %HFX= 54% (M06-2X). In the case of **I'**[**4**], β_{HRS}^∞ displays a slightly marked maximum for a lower amount of HF exchange (%HFX= 27%), corresponding to the M06 functional.

These different behaviors can be rationalized by analyzing the independent evolution of the spectroscopic quantities entering in the two-state expression of β_{HRS}^∞ (eq 2.122). As shown in Figures A.3 and A.5, the first charge-transfer excitation energy (ΔE_{01}) linearly increases with %HFX in the **I**[**n**] and **II**[**n**] series, as a result of the increase of the HOMO-LUMO gap. With few exceptions, the dipole moment variation between the ground and first dipole-allowed CT state ($\Delta\mu_{01}$) also increases linearly for shorter compounds ($n = 0 - 2$), while the variation becomes non monotonic for **I**[**3**], **I**[**4**] and **II**[**4**]. Combined with the saturation of the oscillator strengths, these different behaviors result in the regular decrease of β_{HRS}^∞ with %HFX in these two series. The unexpected increase of β_{HRS}^∞ observed for the shortest compounds in the **I'**[**n**] and **II'**[**n**] series mainly originates from the weak dependence of ΔE_{01} on %HFX (Figures A.4 and A.6), while $\Delta\mu_{01}$ and f_{01} globally increase. In derivatives with longer polyenic chains, ΔE_{01} displays a more pronounced increase with %HFX, which translates into the lowering of β_{HRS}^∞ .

Table 3.3 – Static HRS hyperpolarizabilities (β_{HRS}^∞ , a.u.) and relative $\beta_{HRS}^\infty[n]/\beta_{HRS}^\infty[0]$ values calculated in chloroform using the M06 series of XCFs in combination with the 6-311+G(d) basis set.

	M06L		M06		M06-2X		M06-HF	
	β_{HRS}^∞	$\beta[n]/\beta[0]$	β_{HRS}^∞	$\beta[n]/\beta[0]$	β_{HRS}^∞	$\beta[n]/\beta[0]$	β_{HRS}^∞	$\beta[n]/\beta[0]$
I[0]	7800	1.0	7331	1.0	7550	1.0	7215	1.0
I[1]	19261	2.5	18431	2.5	19104	2.5	17318	2.4
I[2]	42325	5.4	39177	5.3	38422	5.1	30792	4.3
I[3]	84258	10.8	72671	9.9	64572	8.6	44320	6.1
I[4]	154269	19.8	120043	16.4	94611	12.5	55179	7.6
I'[0]	4529	1.0	4832	1.0	5676	1.0	6730	1.0
I'[1]	11033	2.4	12869	2.7	16829	3.0	22388	3.3
I'[2]	27713	6.1	33115	6.9	42661	7.5	48973	7.3
I'[3]	63288	14.0	71646	14.8	80109	14.1	66169	9.8
I'[4]	128361	28.3	128759	26.6	117205	20.7	71644	10.6
II[0]	13021	1.0	12522	1.0	12766	1.0	12435	1.0
II[1]	29405	2.3	29581	2.4	31297	2.5	30440	2.4
II[2]	61853	4.8	61284	4.9	62881	4.9	54822	4.4
II[3]	120983	9.3	113035	9.0	106273	8.3	78372	6.3
II[4]	223158	17.1	190547	15.2	157463	12.3	96263	7.7
II'[0]	5836	1.0	6476	1.0	7272	1.0	8769	1.0
II'[1]	11525	2.0	13773	2.1	17496	2.4	25773	2.9
II'[2]	26435	4.5	33966	5.2	49182	6.8	87460	10.0
II'[3]	69848	12.0	90972	14.0	126131	17.3	158799	18.1
II'[4]	162471	27.8	192302	29.7	208061	28.6	150724	17.2

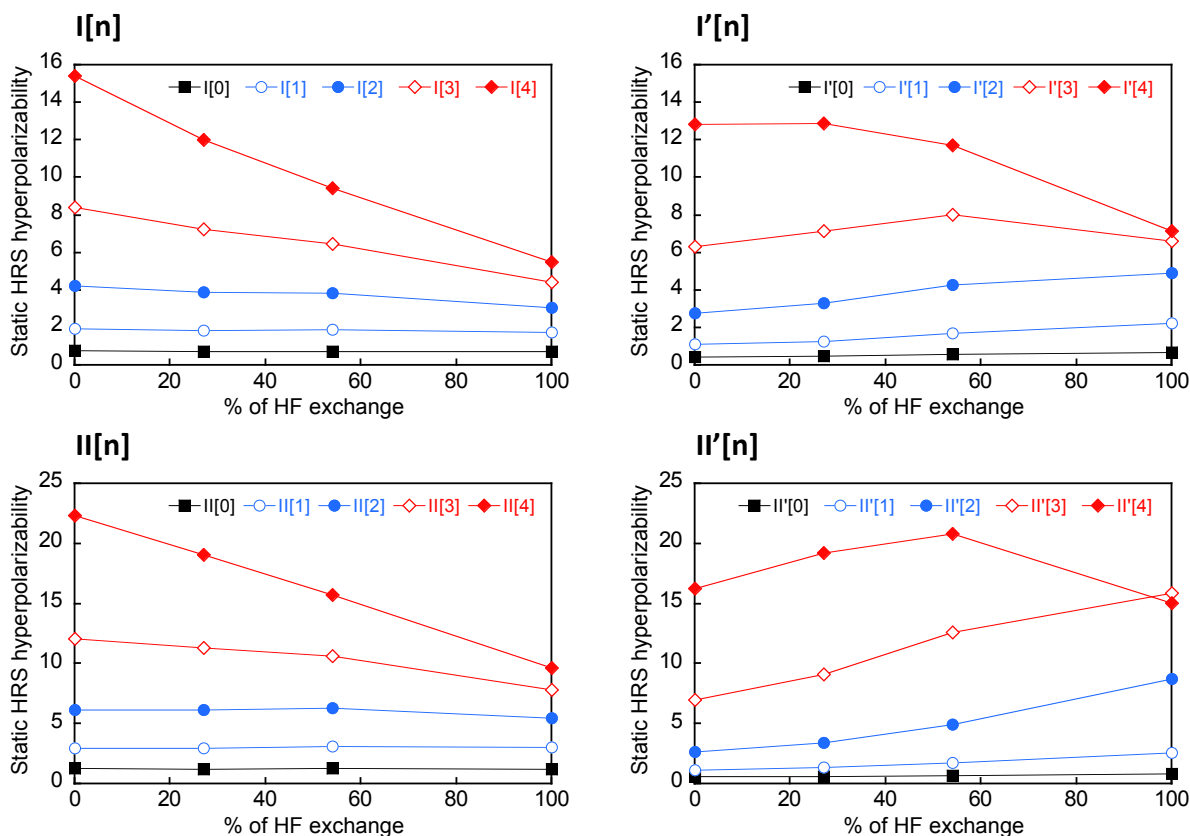


Figure 3.6 – Static HRS hyperpolarizabilities (in 10^4 a.u.) of the four series of merocyanines, calculated in chloroform using the Minnesota’s family of functionals (M06L, M06, M06-2X, M06-HF) in combination with the 6-311+G(d) basis set. Results are reported as a function of the percentage of HF exchange included in the XCF.

It is also informative to compare the evolution with chain length of β_{HRS}^{∞} obtained using the Minnesota functionals and the evolution obtained at the CPHF and MP2 levels (Figure 3.7). For series **I[n]** and **II[n]**, the M06L and M06 XCFs overestimate the size effects and significantly deviate from MP2 reference results for larger compounds. This behavior is consistent with previous investigations that have reported the nearly catastrophic evolution of mild hybrid XCFs with respect to increasing the conjugation length.^[6, 9, 10, 11] Reversely, M06-HF closely follows the size evolution obtained at the CPHF level, as expected owing to the fact that β_{HRS}^{∞} values are hardly impacted by the correlation part of the functional. Nevertheless, one notes that the CPHF and M06-HF β_{HRS}^{∞} values are significantly different, possibly due to the kinetic energy functional. As also shown in previous works,^[8] M06-2X closely reproduces the results obtained at the MP2 level, demonstrating that this XCF incorporates the adequate balance between DFT and HF exchange for computing the NLO properties in conjugated push-pull chromophores.

The situation is more complex for series **I'[n]** and **II'[n]**. Both CPHF and MP2 β_{HRS}^{∞} values show a saturation for long chains, which is more pronounced for **II'[n]**. This behavior is reproduced only by M06-HF, the other XCFs (including M06-2X) showing a

monotonic increase of the static first hyperpolarizability. The difference in the evolution of β_{HRS}^∞ with system size between series including a dimethylaminophenyl and those including a dimethylaminothiophenyl can be directly ascribed to the difference in the evolution of the bond length alternation (Figure 3.2), and qualitatively interpreted using a two-form model mixing neutral and zwitterionic forms.^[40, 41, 42] In this model, the evolution of β_{HRS}^∞ with BLA exhibits a peak between the polyene and the cyanine limits, crosses through zero at the cyanine limit (where BLA = 0), and exhibits another peak between the cyanine and zwitterionic limits. Whereas the BLA hardly changes with n in series **I**[n] and **II**[n], it strongly increases in series **I'**[n] and **II'**[n], starting closer to the cyanine limit in the case of **II'**[0]. When increasing n in the latter series, the BLA increases and shifts the two-form equilibrium close to the polyene limit, where β_{HRS}^∞ saturates before reaching its maximum value.

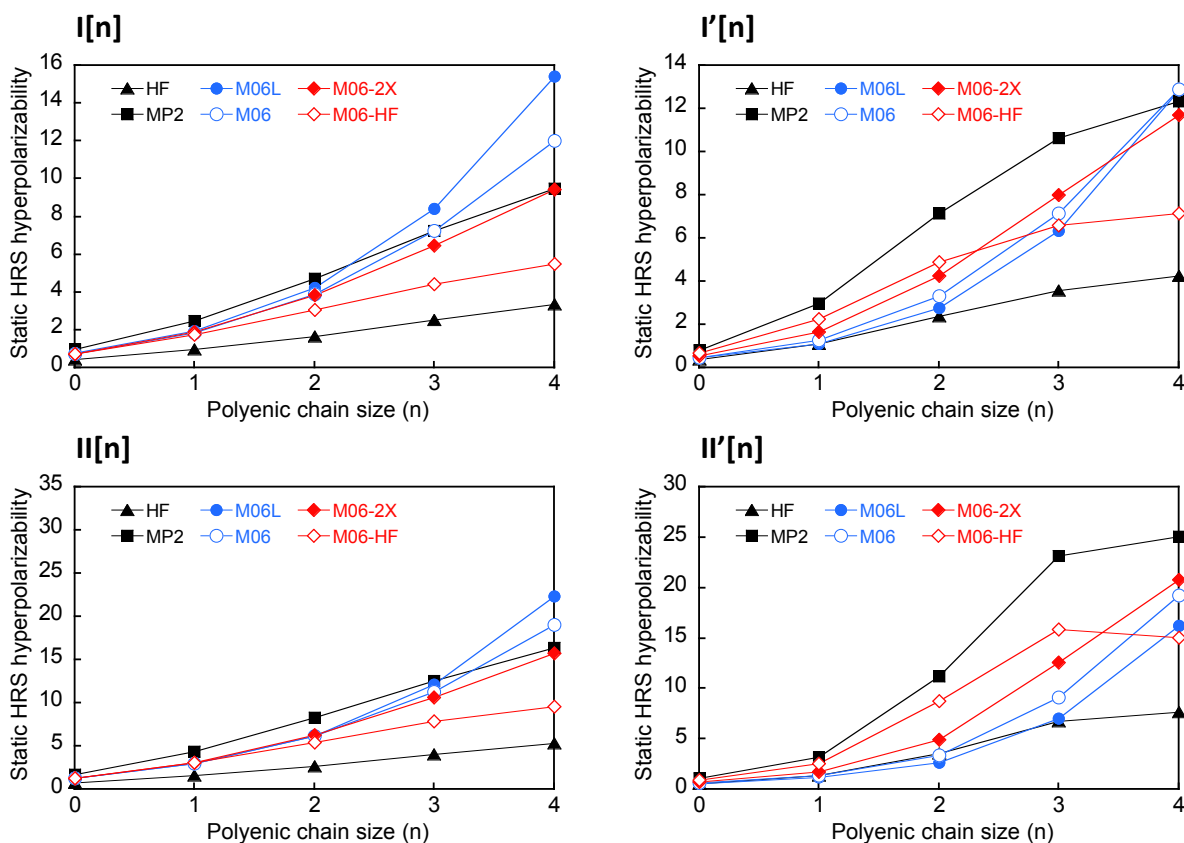


Figure 3.7 – Evolution of the static HRS hyperpolarizabilities (in 10^4 a.u.) with the length of the polyenic bridge in the four series of merocyanines, calculated in chloroform at the HF, MP2 and DFT levels using Minnesota’s family of functionals in combination with the 6-311+G(d) basis set.

3.6.4 Optimal tuning of the range-separation parameter in RS-XCFs

Optimal values of the RS parameters obtained in the gas phase using the self-consistent (SC) and non-self-consistent (NSC) optimization schemes (see Section 3.3) are collected in Table A.3a for the four series of merocyanines. The differences in the ω_{opt} values obtained using the two tuning schemes, as well as the induced differences on the optical properties of the investigated compounds, are discussed in detail in the Appendix A in Figure A.7. Summarizing the main findings, for a given functional, SC and NSC optimization schemes provide close optimal ω values and similar evolution of the first hyperpolarizabilities with chain length. Nevertheless, the accuracy of the NSC scheme with respect to the SC one depends on the choice of the XCF. Significant differences in the β_{HRS} values computed using the two procedures were notably obtained with LC-BLYP, where deviations can reach 15% and 20% for static and dynamic β_{HRS} , respectively. From now on, only properties computed using the self-consistent method will be discussed.

For LC-BLYP and ω B97X-D, the optimally-tuned ω values are comprised in the ranges 0.16-0.20 bohr⁻¹ and 0.11-0.15 bohr⁻¹, respectively, both smaller than the standard ω values. Conversely, ω values optimized for CAM-B3LYP are larger than ω_{std} and range between 0.41 and 0.95 bohr⁻¹. As mentioned in earlier works^[22, 25, 23, 10, 43, 27] ω_{opt} decreases for all XCFs when increasing the system size. Whatever the functional, the variation of ω_{opt} with chain length is larger for series **I[n]** and **II[n]** than for series **I'[n]** and **II'[n]**. For a given molecular family, ω values optimized for LC-BLYP and ω B97X-D display much smaller variations with the system size than CAM-B3LYP, as previously reported by Garret *et al.* for other organic chromophores.^[27]

Table 3.4 reports the β_{HRS}^{∞} values calculated at the LC-BLYP, ω B97X-D and CAM-B3LYP level using default and optimally-tuned ω values. The evolution of β_{HRS}^{∞} with chain length is illustrated in Figure 3.8 for the four families of merocyanines. If one excepts some results calculated with LC-BLYP and ω_{opt} for the larger compounds, the static hyperpolarizabilities computed using LRC functionals globally lie in between values computed at the CPHF and MP2 levels. β_{HRS}^{∞} values computed using LC-BLYP and ω B97X-D with optimally-tuned RS parameters are quite similar, while they differ more significantly when using the default ω values (in part because ω values are getting more similar after optimization).

Table 3.4 – Static HRS hyperpolarizabilities (β_{HRS}^∞ , a.u.) and relative $\beta_{HRS}^\infty[n]/\beta_{HRS}^\infty[0]$ values calculated in chloroform using RS-XCFs in combination with the 6-311+G(d) basis set, using standard (ω_{std}) and optimally-tuned (ω_{opt}) RS parameters.

	LC-BLYP				ω B97X-D				CAM-B3LYP			
	ω_{std}		ω_{opt}		ω_{std}		ω_{opt}		ω_{std}		ω_{opt}	
I[0]	6703	1.0	7770	1.0	6964	1.0	7178	1.0	7159	1.0	6157	1.0
I[1]	16121	2.4	19818	2.6	17263	2.5	18079	2.5	17943	2.5	15418	2.5
I[2]	28744	4.3	40508	5.2	33452	4.8	36778	5.1	35769	5.0	30692	5.0
I[3]	41654	6.2	69994	9.0	53769	7.7	63309	8.8	59596	8.3	5847	8.3
I[4]	52244	7.8	106174	13.7	74881	10.8	95694	13.3	86062	12.0	72699	11.8
I'[0]	6068	1.0	5630	1.0	5346	1.0	5166	1.0	5335	1.0	4815	1.0
I'[1]	19971	3.3	16146	2.9	16101	3.0	14743	2.9	15762	3.0	15142	3.1
I'[2]	43944	7.2	41454	7.4	40318	7.5	37859	7.3	40058	7.5	38600	8.0
I'[3]	60735	10.0	82071	14.6	71132	13.3	74817	14.5	74530	14.0	68981	14.3
I'[4]	67029	11.0	128900	22.9	96112	18.0	116851	22.6	107262	20.1	94970	19.7
II[0]	11408	1.0	13295	1.0	11775	1.0	12295	1.0	12148	1.0	11105	1.0
II[1]	27817	2.4	32548	2.4	28631	2.4	29732	2.4	29551	2.4	27460	2.5
II[2]	50036	4.4	66785	5.0	55580	4.7	60259	4.9	58774	4.8	54520	4.9
II[3]	71721	6.3	117219	8.8	89194	7.6	104703	8.5	98087	8.1	90140	8.1
II[4]	88713	7.8	183070	13.8	124654	10.6	162191	13.2	143376	11.8	129897	11.7
II'[0]	8113	1.0	7142	1.0	7162	1.0	6692	1.0	6976	1.0	6822	1.0
II'[1]	23511	2.9	15899	2.2	17700	2.5	14988	2.2	16543	2.4	16873	2.5
II'[2]	75923	9.4	42440	5.9	51012	7.1	39570	5.9	46665	6.7	48615	7.1
II'[3]	137749	17.0	115381	16.2	123406	17.2	106369	15.9	119329	17.1	121414	17.8
II'[4]	135183	16.7	218829	30.6	177326	24.8	197960	29.6	191549	27.5	184919	27.1

In series **I[n]** and **II[n]**, the static hyperpolarizabilities computed using LC-BLYP and ω B97X-D with optimally-tuned RS parameters are closer to reference MP2 results than those obtained using default ω values. This originates from the fact that $\omega_{opt} < \omega_{std}$, so that the fraction of HFX in those two XCFs is smaller after ω optimization, which increases the β_{HRS}^∞ values. However, optimally-tuned LC-BLYP and ω B97X-D functionals overestimate the enhancement of the first hyperpolarizability with chain length compared to MP2. The situation is reversed in the case of CAM-B3LYP, for which ω -tuning increases the part of HFX in the XCF. In this case, β_{HRS}^∞ values calculated using default ω are closer to MP2 references. Moreover, the increase of β_{HRS}^∞ values with n is better reproduced.

In series **I'[n]** and **II'[n]**, optimally-tuned LRC XCFs all fail to reproduce the evolution of β_{HRS}^∞ values as provided by MP2 calculations. Only LC-BLYP with the default ω value reproduces the saturation observed for larger compounds at the CPHF and MP2 levels. Once again, this behavior is linked to the amount of HFX included in the XCF. Optimizing ω lowers the fraction of HFX, so that the saturation of β_{HRS}^∞ with chain length is expected to appear for chain lengths larger than $n = 4$. It is also interesting to note that ω B97X-D using optimally-tuned RS parameters provides β_{HRS}^∞ values very similar to those calculated at the M06-2X level for the four series of compounds (see Figure A.8).

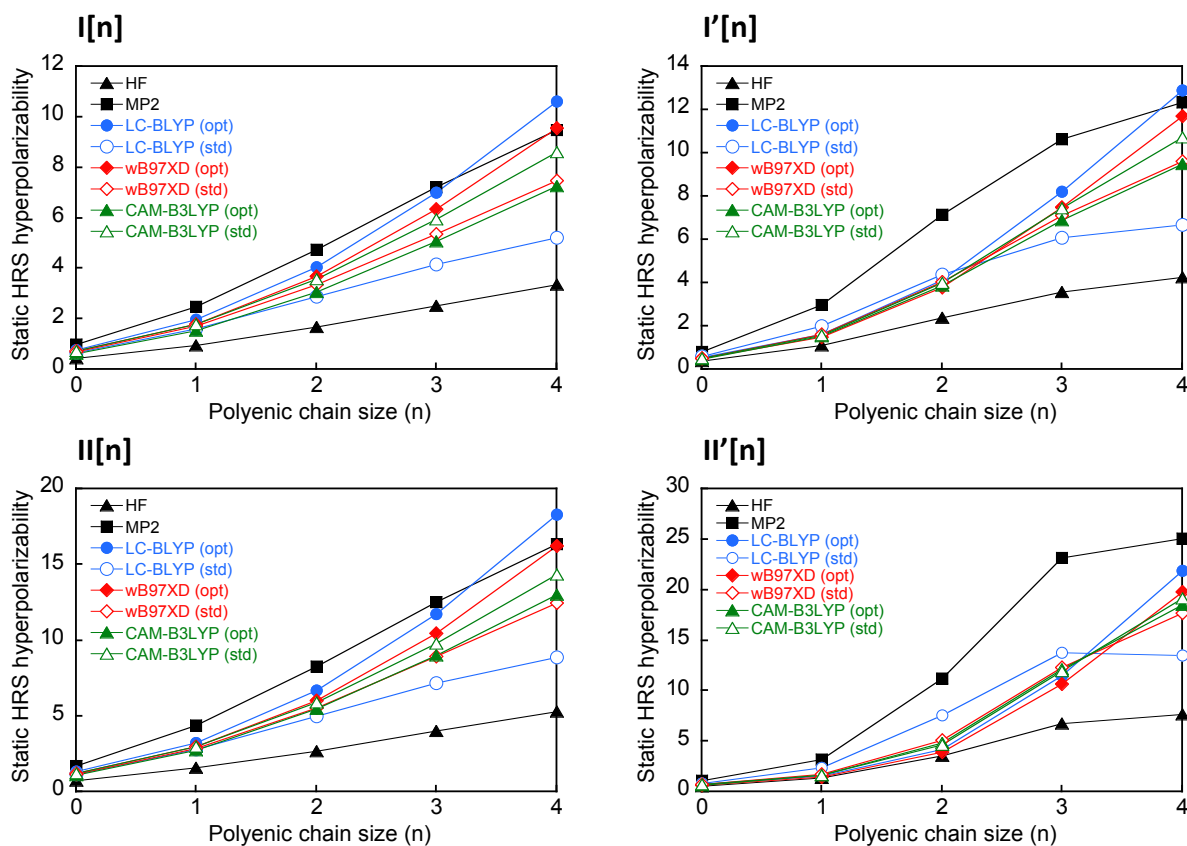


Figure 3.8 – Evolution of the static HRS hyperpolarizabilities (in 10^4 a.u.) with the length of the polyenic bridge in the four series of merocyanines, calculated in chloroform at the HF, MP2 levels in combination with the 6-311+G(d) basis set, as well as at the DFT level using long-range corrected XC functionals with standard (std) and optimally-tuned (opt) RS parameters.

Finally, static hyperpolarizabilities calculated with LC-BLYP using RS parameters optimized in the presence of chloroform are collected in Table A.20c. Consistently with previous calculations carried out in media of similar optical dielectric constant,^[11] the ω values optimized in chloroform (ω_{PCM}) are three times smaller than those optimized in gas phase (Table A.3b), which drastically reduces the fraction of exact HFX in the functional. Not surprisingly, the resulting β_{HRS}^∞ values and their evolution with chain length are very similar to that obtained using the BLYP XCF including only DFT exchange (Table A.20c).

3.7 Frequency dispersion effects

The dynamic HRS hyperpolarizabilities calculated using the Minnesota and long-range corrected functionals, as well as with TDHF are collected in Tables A.27-A.37 for the four series of compounds. In line with experimental characterizations, the dynamic (frequency-dependent) β tensor components were calculated using an infrared incident wavelength (photon energy) of 1907 nm (0.65 eV). Frequency dispersion factors calculated

as $F_{disp} = \beta_{HRS}^{1907} / \beta_{HRS}^{\infty}$, are gathered in Tables A.38-A.39, while those estimated from the TSA (F_{disp}^{TSA} , eq 2.123) are collected in Tables A.4-A.14. Whatever the functional, the two series of values are linearly correlated, which further illustrates the suitability of the TSA to describe this family of compounds. Note that F_{disp} values are systematically smaller than F_{disp}^{TSA} , which originates from the fact that F_{disp} values implicitly include the contribution of higher energy excited states. Note also that the dynamic dielectric constant of chloroform is smaller than the static one, which damps the solvent-induced enhancement of β_{HRS} when going from $\lambda = \infty$ to $\lambda = 1907$ nm, artificially reducing the value of F_{disp} . The same effect is present in F_{disp}^{TSA} , since $\Delta\mu_{01}$ values are calculated using a non-equilibrium solvent approach.

As a result of the lowering of the transition energy, F_{disp} increases with chain length in all families of compounds, with a more pronounced enhancement for the **II** and **II'** series than for **I** and **I'**. In the Minnesota series of functionals, F_{disp} decreases when increasing the amount of HF exchange, as a result of the increase of the transition energy. As for LRC functionals, optimizing the RS parameter induces an exaltation of frequency dispersion effects with LC-BLYP and ω B97X-D, while the ω tuning has no significant effect on F_{disp} values with CAM-B3LYP. For a given compound, frequency dispersion factors calculated using optimally-tuned ω values evolve in the following order: CAM-B3LYP < ω B97X-D < LC-BLYP. Among the Minnesota XCFs, F_{disp} values calculated using M06-2X display the best agreement with those provided by optimally tuned LRC functionals. Thus, M06-2X performs similarly to RS-XCFs not only for evaluating static hyperpolarizabilities as discussed above, but also for gauging the intensification of the NLO responses due to resonance effects. However, none of the selected XCFs reproduces the experimental frequency dispersion ratios ($F_{disp}(0)$ values in Table 3.1). Although their global increase with chain length is qualitatively reproduced, frequency resonance effects are largely underestimated for the larger chains, since excitation energies are systematically overestimated. This discrepancy partly originates from the fact that vertical transitions provided by TD-DFT calculations are not strictly comparable to experimental wavelengths of maximal absorption. More physically sound comparisons would require to compute the full vibronic spectra.

3.8 Comparison to experiments

Comparing calculated first hyperpolarizabilities to experimental data measured in or nearby resonant conditions is very tricky. We make here two attempts, both considering relative $\beta_{HRS}[n] / \beta_{HRS}[0]$ rather than absolute β_{HRS} values to enable more reliable comparisons. On the first hand, static β_{HRS} values are compared, where the experimental ones are extrapolated from HRS measurements by using the two-state model (eq 2.122), either with $\Gamma = 0$ or $\Gamma = 1.2 \times \text{HWHM}$ (see the $\beta_{HRS}^{\infty}(0)$ and $\beta_{HRS}^{\infty}(\Gamma)$ values in Table

3.1). However, the calculated β_{HRS}^∞ values cannot be strictly compared to experimental extrapolations, since they are computed using the static dielectric constants ϵ_0 , which differs from the optical dielectric constant that applies for experimental measurements. The solution we adopted to circumvent that issue is to also determine the theoretical static β_{HRS}^∞ values from the dynamic ones computed at 1907 nm by using the TSA extrapolation procedure (Tables A.44 and A.45).

On the second hand, experimental β_{HRS}^{1907} values are directly compared to the computed dynamic results. Dynamic MP2 values (Tables A.40a-b) have been obtained by applying a multiplicative approximation in which the static MP2 values are corrected by the F_{disp}^{TSA} ratio calculated at the DFT level using the different XCFs, thus assuming that frequency dispersion and electron correlation effects can be treated independently:^[44]

$$\beta_{MP2}^{1907} = \beta_{MP2}^\infty \times F_{disp}^{TSA} \quad (3.8)$$

As illustrated in Figures 3.9, the evolution with chain length of theoretical static $\beta_{HRS}^\infty[n]/\beta_{HRS}^\infty[0]$ ratios correlates at most qualitatively with the experimental data (whether the latter are extrapolated using a damping factor or not). In series **I[n]** and **I'[n]**, the experimental relative hyperpolarizabilities grows more slowly with n than all computed values for small chain lengths. In **I'[n]** they abruptly increase for $n = 4$ as a result of frequency resonance, and get larger than the computed values. The same behavior is observed from $n = 3$ in the **II[n]** series. The agreement between computed and experimental $\beta_{HRS}^\infty[n]/\beta_{HRS}^\infty[0]$ ratios is better in series **II'[n]**. In particular, relative hyperpolarizabilities calculated using hybrid XCFs having a predominant local character (M06L and M06) well reproduces experimental extrapolations issued from the damped TSA. Note that CPHF results are also in good agreement with experiments in this series of compounds.

The evolution with chain length of experimental and theoretical relative β_{HRS}^{1907} values are compared in Figures A.9-A.10. The conclusions do not differ much from the static case. Overall, all calculation levels reproduce qualitatively well the enhancement with chain length of the dynamic first hyperpolarizabilities in the four series of compounds, but fail to reproduce specific results measured in the resonance regime. Whether using the Minnesota (Figure A.9) or LR-XCFs (Figure A.10), DFT calculations overestimate the $\beta_{HRS}^{1907}[n]/\beta_{HRS}^{1907}[0]$ ratios compared to the experimental ones, except in the resonant cases (**I'[4]**, **II[2]** and **II'[3]**). Dynamic MP2 values obtained using the multiplicative scheme (eq 3.8) show a similar enhancement with n as that obtained at the DFT level (Figure 3.10). Note that, except for larger chains ($n = 4$), the choice of the DFT XCF for calculating the frequency dispersion factor F_{disp}^{TSA} has no significant impact.

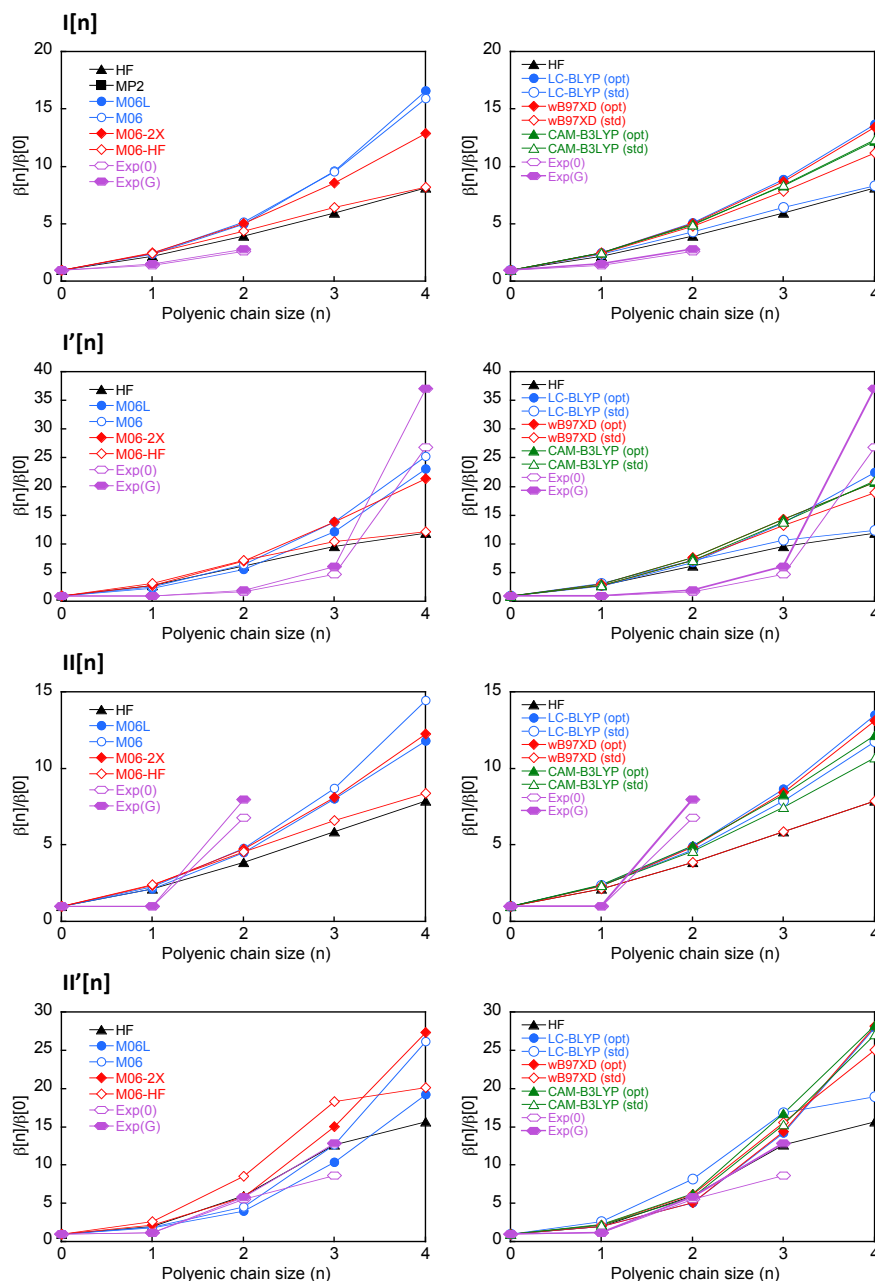


Figure 3.9 – Evolution of the relative static HRS hyperpolarizabilities ($\beta_{HRS}[n]/\beta_{HRS}[0]$) with the length of the polyenic bridge in the four series of merocyanines, calculated in chloroform using various theoretical levels. Results extrapolated from HRS measurements by using the two-state model either with $\Gamma = 0$ or $\Gamma = 1.2 \times \text{HWHM}$ are also reported.

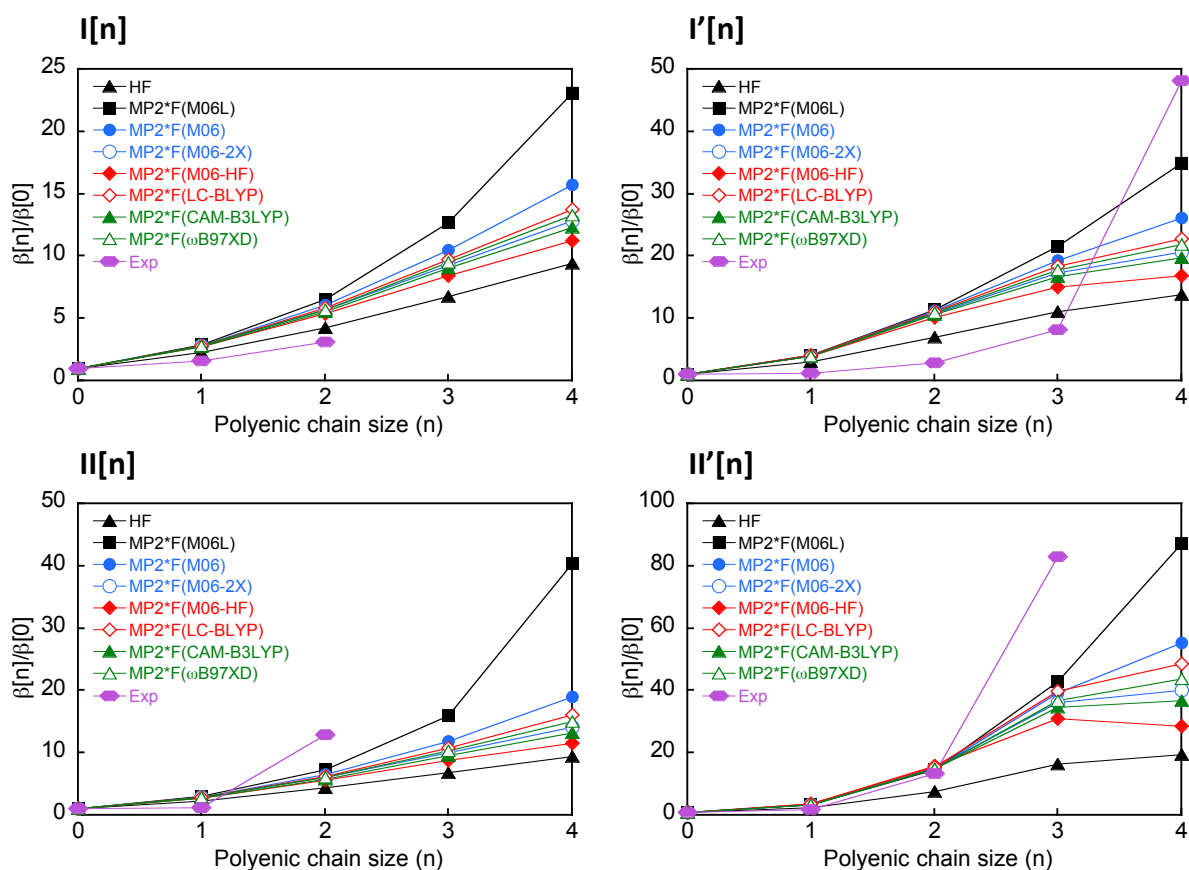


Figure 3.10 – Evolution of the relative dynamic HRS hyperpolarizabilities ($\beta_{HRS}[n]/\beta_{HRS}[0]$) with the length of the polyenic bridge in the four series of merocyanines, calculated in chloroform at the HF and MP2 levels together with the 6-311+G(d) basis set. MP2 values have been obtained using eq 3.8 with frequency dispersion factors calculated using Minnesota and LR-XCFs. Experimental values obtained from HRS measurements are also reported.

3.9 Conclusions

This work investigates the performance of various theoretical levels of approximation to evaluate the second-order NLO responses of recently designed push-pull merocyanine dyes. First hyperpolarizabilities calculated using Minnesota hybrids as well as long-range corrected exchange-correlation functionals are compared to *ab initio* HF and MP2 results, as well as to experimental data obtained from HRS measurements. The evolution of β_{HRS} responses with the nature of the terminal substituents or with the length of the conjugated linker is rationalized by means of the two-state approximation, whose robustness for qualitative interpretations is demonstrated.

The static hyperpolarizabilities calculated using range-separated XCFs globally lie in between values computed at the CPHF and MP2 levels. In most cases, β_{HRS} values computed using LC-BLYP and ω B97X-D with optimally-tuned RS parameters are closer to MP2 results than those obtained using default ω values, although the improvement is not systematic and system-dependent. Interestingly, the ω -tuning is shown to attenuate the intrinsic differences in these two XCFs, the β_{HRS} values computed with optimally-tuned RS parameters being closer than those calculated using the default ω values. Contrary to what was found with LC-BLYP and ω B97X-D, optimizing the RS parameter in CAM-B3LYP increases the ω values and thus the amount of exact HF exchange in the XCF, which reduces the agreement with MP2 reference results.

Calculations performed using the Minnesota family of functionals evidence that the percentage of exact HF exchange in the XCF strongly impacts the magnitude of the β_{HRS} responses. Interestingly, M06-2X is shown to provide β_{HRS} values in close agreement with optimally tuned range-separated functionals, which indicates that a percentage of nearly 50% between DFT and HF exchange is the adequate balance for computing the NLO properties of these highly dipolar conjugated push-pull chromophores.

This work also illustrates the difficulty to compare the calculated dynamic first hyperpolarizabilities to the experimental data measured in resonance conditions. None of the DFT XCFs considered in this study satisfactorily reproduces the frequency resonance enhancement of the β_{HRS} responses, which hampers any quantitative comparison of their relative evolution with chain length. Using a damped two-state model instead to extrapolate experimental static hyperpolarizabilities does not turn out to be a better strategy to compare theoretical and experimental responses in this series of highly dipolar compounds.

Bibliography

- [1] Parthasarathy V., Pandey R., Stolte M., Ghosh S., Castet F., Würthner F., Das P. K., and Blanchard-Desce M. Combination of Cyanine Behaviour and Giant Hyperpolarisability in Novel Merocyanine Dyes: Beyond the Bond Length Alternation (BLA) Paradigm. *Chem. Eur. J.*, 21:14211, 2015.
- [2] Parthasarathy V., Castet F., Pandey R., Mongin O., Das P. K., and Blanchard-Desce M. Unprecedented intramolecular cyclization in strongly dipolar extended merocyanine dyes: A route to novel dyes with improved transparency, nonlinear optical properties and thermal stability. *Dyes Pigm.*, 130:70, 2016.
- [3] Parthasarathy V., Pandey R., Das P. K., Castet F., and Blanchard-Desce M. Linear and Nonlinear Optical Properties of Tricyanopropylidene-Based Merocyanine Dyes: Synergistic Experimental and Theoretical Investigations. *ChemPhysChem*.
- [4] Marder S. R., Cheng L-T, Tiemann B. G., Friedli A. C., Blanchard-Desce M., Perry J. W., and Skindhøj J. Large First Hyperpolarizabilities in Push-Pull Polyenes by Tuning of the Bond Length Alternation and Aromaticity. *Science*, 263:511, 1994.
- [5] Meyers F., Marder S. R., Pierce B. M., and Brédas J. L. Electric Field Modulated Nonlinear Optical Properties of Donor-Acceptor Polyenes: Sum-Over-States Investigation of the Relationship between Molecular Polarizabilities (.alpha., .beta., and .gamma.) and Bond Length Alternation. *J. Am. Chem. Soc.*, 116:10703, 1994.
- [6] Champagne B., Perpète E. A., Jacquemin D., van Gisbergen S. J. A., Baerends E-J, Soubra-Ghaoui C., Robins K. A., and Kirtman B. Assessment of Conventional Density Functional Schemes for Computing the Dipole Moment and (Hyper)polarizabilities of Push–Pull π -Conjugated Systems. *J. Phys. Chem. A*, 104:4755, 2000.
- [7] de Wergifosse M. and Champagne B. Electron correlation effects on the first hyperpolarizability of push–pull π -conjugated systems. *J. Chem. Phys.*, 134:074113, 2011.
- [8] Johnson L. E., Dalton L. R., and Robinson B. H. Optimizing Calculations of Electronic Excitations and Relative Hyperpolarizabilities of Electrooptic Chromophores. *Acc. Chem. Res.*, 47:3258, 2014.
- [9] Bulat F. A., Toro-Labbé A., Champagne B., Kirtman B., and Yang W. Density-functional theory (hyper)polarizabilities of push-pull π -conjugated systems: Treatment of exact exchange and role of correlation. *J. Chem. Phys.*, 123:014319, 2005.
- [10] Sun H. and Autschbach J. Influence of the Delocalization Error and Applicability of Optimal Functional Tuning in Density Functional Calculations of Nonlinear Optical

- Properties of Organic Donor–Acceptor Chromophores. *ChemPhysChem*, 14:2450, 2013.
- [11] Garza A. J., O. I. Osman, Asiri A. M., and Scuseria G. E. Can Gap Tuning Schemes of Long-Range Corrected Hybrid Functionals Improve the Description of Hyperpolarizabilities? *J. Phys. Chem. B*, 119:1202, 2015.
- [12] Zhao Y. and Truhlar D. G. The M06 Suite of Density Functionals for Main Group Thermochemistry, Thermochemical Kinetics, Noncovalent Interactions, Excited States, and Transition Elements: two New Functionals and Systematic Testing of Four M06-Class Functionals and 12 Other Functionals. *Theor. Chem. Acc.*, 120:215, 2008.
- [13] Torrent-Sucarrat M., Navarro S., Cossío F. P., Anglada J. M., and Luis J. M. Relevance of the DFT method to study expanded porphyrins with different topologies. *J. Comput. Chem.*, 38:2819, 2017.
- [14] Casademont-Reig I., Wöller T., Contreras-García J., Alonso M., Torrent-Sucarrat M., and Matito E. New electron delocalization tools to describe the aromaticity in porphyrinoids. *Phys. Chem. Chem. Phys.*, 20:2787, 2018.
- [15] van Gisbergen S. J. A., Snijders J. G., and Baerends E. J. Calculating frequency-dependent hyperpolarizabilities using time-dependent density functional theory. *J. Chem. Phys.*, 109:10644, 1998.
- [16] Champagne B., Beaujean P., de Wergifosse M., Cardenuto M. H., Liégeois V., and Castet F. *Frontiers of Quantum Chemistry*, chapter Quantum Chemical Methods for Predicting and Interpreting Second-Order Nonlinear Optical Properties: From Small to Extended π -Conjugated Molecules, page 117. Springer, Singapore, 2018.
- [17] Mennucci B., Cammi R., and Tomasi J. Medium Effects on the Properties of Chemical Systems: Electric and Magnetic Response of Donor-Acceptor Systems Within the Polarizable Continuum Model. *Int. J. Quantum Chem.*, 75:767, 1999.
- [18] Tomasi J., Mennucci B., and Cammi R. Quantum Mechanical Continuum Solvation Models. *Chem. Rev.*, 105:2999, 2005.
- [19] Frisch M. J., Trucks G. W., Schlegel H. B., Scuseria G. E., Robb M. A., Cheeseman J. R., Scalmani G., Barone V., Petersson G. A., Nakatsuji H., Li X., Caricato M., Marenich A. V., Bloino J., Janesko B. G., Gomperts R., Mennucci B., Hratchian H. P., Ortiz J. V., Izmaylov A. F., Sonnenberg J. L., Williams-Young D., Ding F., Lipparini F., Egidi F., Goings J., Peng B., Petrone A., Henderson T., Ranasinghe D., Zakrzewski V. G., Gao J., Rega N., Zheng G., Liang W., Hada M., Ehara M., Toyota K., Fukuda R., Hasegawa J., Ishida M., Nakajima T., Honda Y., Kitao O., Nakai H., Vreven T., Throssell K., Montgomery J. A. Jr., Peralta J. E., Ogliaro F.,

- Bearpark M. J., Heyd J. J., Brothers E. N., Kudin K. N., Staroverov V. N., Keith T. A., Kobayashi R., Normand J., Raghavachari K., Rendell A. P., Burant J. C., Iyengar S. S., Tomasi J., Cossi M., Millam J. M., Klene M., Adamo C., Cammi R., Ochterski J. W., Martin R. L., Morokuma K., Farkas O., Foresman J. B., and Fox D. J. Gaussian 16 Revision C.01, 2016.
- [20] Stein T., Kronik L., and Baer R. Prediction of charge-transfer excitations in coumarin-based dyes using a range-separated functional tuned from first principles. *J. Chem. Phys.*, 131:244119, 2009.
- [21] Stein T., Kronik L., and Baer R. Reliable Prediction of Charge Transfer Excitations in Molecular Complexes Using Time-Dependent Density Functional Theory. *J. Am. Chem. Soc.*, 131:2818, 2009.
- [22] Stein T., Eisenberg H., Kronik L., and Baer R. Fundamental Gaps in Finite Systems from Eigenvalues of a Generalized Kohn-Sham Method. *Phys. Rev. Lett.*, 105:266802, 2010.
- [23] Karolewski A., Stein T., Baer R., and Kümmel S. Communication: Tailoring the optical gap in light-harvesting molecules. *J. Chem. Phys.*, 134:151101, 2011.
- [24] Kiefer J. Sequential minimax search for a maximum. *Proc. Amer. Math. Soc.*, 4:502, 1953.
- [25] Körzdörfer T., Sears J. S., Sutton C., and J-L Brédas. Long-range corrected hybrid functionals for π -conjugated systems: Dependence of the range-separation parameter on conjugation length. *J. Chem. Phys.*, 135:204107, 2011.
- [26] Pandey L., Doiron C., Sears J. S., and Brédas J-L. Lowest excited states and optical absorption spectra of donor-acceptor copolymers for organic photovoltaics: a new picture emerging from tuned long-range corrected density functionals. *Phys. Chem. Chem. Phys.*, 14:14243, 2012.
- [27] Garrett K., Sosa Vazquez X., Egri S. B., Wilmer J., Johnson L. E., Robinson B. H., and Isborn C. M. Optimum Exchange for Calculation of Excitation Energies and Hyperpolarizabilities of Organic Electro-optic Chromophores, journal = *J. Chem. Theory Comput.* 10:3821, 2014.
- [28] Besalú-Sala P., Sitkiewicz S. P., Salvador P., Matito E., and Luis J. M. A new tuned range-separated density functional for the accurate calculation of second hyperpolarizabilities. *Phys. Chem. Chem. Phys.*, 2020.
- [29] Zaleśny R., Medved' M., S. P. Sitkiewicz, Matito E., and Luis J. M. Can Density Functional Theory Be Trusted for High-Order Electric Properties? The Case of Hydrogen-Bonded Complexes, journal = *J. Chem. Theory Comput.* 15:3570, 2019.

- [30] Campo J., Desmet F., Wenseleers W., and Goovaerts E. Highly sensitive setup for tunable wavelength hyper-rayleigh scattering with parallel detection and calibration data for various solvents. *Opt. Express*, 17:4587, 2009.
- [31] As reported in Ref. 30, $\lambda_{max} = 481$ nm and $\beta_{zzz}^{\infty} = 160 \times 10^{-30}$ esu = 18516 a.u. for DR1 in chloroform. Assuming that DR1 has a quasi $C_{\infty v}$ symmetry, $\beta_{HRS}^{\infty} = \sqrt{\frac{6}{35}} \times \beta_{zzz}^{\infty} = 7667$ a.u. At 1907 nm, $F_{disp}^{TSA} = 1.43$, so that $\beta_{HRS}^{1907} = \beta_{HRS}^{\infty} \times F_{disp}^{TSA} = 7667 \times 1.43 = 10963$ a.u.
- [32] Berkovic G., Meshulam G., and Kotler Z. Measurement and analysis of molecular hyperpolarizability in the two-photon resonance regime. *J. Chem. Phys.*, 112:3997, 2000.
- [33] Mançois F., Pozzo J-L, Pan J., Adamietz F., Rodriguez V., Ducasse L., Castet F., Plaquet A., and Champagne B. Two-Way Molecular Switches with Large Nonlinear Optical Contrast. *Chem. Eur. J.*, 15:2560, 2009.
- [34] Beaujean P., Bondu F., Plaquet A., Garcia-Amorós J., Cusido J., Raymo F. M., Castet F., Rodriguez V., and Champagne B. Oxazines: A New Class of Second-Order Nonlinear Optical Switches. *J. Am. Chem. Soc.*, 138:5052, 2016.
- [35] Plaquet A., Champagne B., Kulhánek J., Bureš F., Bogdan E., Castet F., Ducasse L., and Rodriguez V. Effects of the Nature and Length of the π -Conjugated Bridge on the Second-Order Nonlinear Optical Responses of Push–Pull Molecules Including 4,5-Dicyanoimidazole and Their Protonated Forms. *ChemPhysChem*.
- [36] Castet F., Pic A., and Champagne B. Linear and nonlinear optical properties of arylvinyldiazine dyes: A theoretical investigation. *Dyes Pigm.*, 110:256, 2014.
- [37] Pielak K., Tonnelé C., Sanguinet L., Cariati E., Righetto S., Muccioli L., Castet F., and Champagne B. Dynamical behavior and second harmonic generation responses in acido-triggered molecular switches. *J. Phys. Chem. C*, 122:26160, 2018.
- [38] Tuer A., Krouglov S., Cisek R., Tokarz D., and Barzda V. Three-dimensional visualization of the first hyperpolarizability tensor. *J. Comput. Chem.*, 32:1128, 2011.
- [39] Sancho-García J. C. and Pérez-Jiménez A. J. Improved accuracy with medium cost computational methods for the evaluation of bond length alternation of increasingly long oligoacetylenes. *Phys. Chem. Chem. Phys.*, 9:5874, 2007.
- [40] Bourhill G., Bredas J-L, Cheng L-T, Marder S. R., Meyers F., Perry J. W., and Tie-mann B. G. Experimental Demonstration of the Dependence of the First Hyperpolarizability of Donor-Acceptor-Substituted Polyenes on the Ground-State Polarization and Bond Length Alternation. *J. Am. Chem. Soc.*, 116:2619, 1994.

- [41] Gorman C. B. and Marder S. R. Effect of Molecular Polarization on Bond-Length Alternation, Linear Polarizability, First and Second Hyperpolarizability in Donor-Acceptor Polyenes as a Function of Chain Length. *Chem. Mater.*, 7:215, 1995.
- [42] Barzoukas M., Fort A., and Blanchard-Desce M. Quadratic hyperpolarizability of push—pull polyenes: a two-form analysis of the length effect. *Synth. Met.*, 83:277, 1996.
- [43] Nénon S., Champagne B., and Spassova M. I. Assessing long-range corrected functionals with physically-adjusted range-separated parameters for calculating the polarizability and the second hyperpolarizability of polydiacetylene and polybutatriene chains. *Phys. Chem. Chem. Phys.*, 16:7083, 2014.
- [44] Sekino H. and Bartlett R. J. Hyperpolarizabilities of molecules with frequency dependence and electron correlation. *J. Chem. Phys.*, 94:3665, 1991.

Self-assembling, structure and nonlinear optical properties of fluorescent organic nanoparticles in water

4.1 Introduction

Imaging technologies play a critical role in biological applications such as cancer detection, stem cell transplantation and tissue engineering. Among them, fluorescence imaging has attracted attention because of its capacity to provide strong signal intensity and high resolution images at subcellular level. Molecular fluorescent dyes are widely used, but are limited by the fact that they contain only a single luminescent center that can absorb and emit a limited number of photons per time and space units. In contrast, fluorescent nanoparticles (NPs) concentrate a huge number of fluorescent centers in a narrow region of space, which enables intense and bright spotlight emission. Therefore in the last decades, nanoparticles have attracted increased interest in biology and optoelectronics fields, in particular luminescent metal- and semiconductor-based nanoparticles. A number of them however raise toxicity and biodegradability issues, which are critical with regard to biomedical applications and environmental concerns. In that perspective, molecular-based fluorescent organic nanoparticles (FONs) emerged as a promising less toxic alternative to inorganic ones, offering appealing ways towards the realization of exogenous probes for biomaging applications.^[1, 2, 3, 4]

Some years ago, Blanchard-Desce and coworkers reported bright near-infrared emitting FONs made from dipolar push–pull chromophores incorporating a strong electron-withdrawing group.^[2] By varying the nature of the electron-accepting unit (among which the slightly hydrophilic aldehyde as illustrated in Figure 4.1) and of the π -conjugated systems, FONs showing tuneable emission (from green to near infrared) and exhibiting good colloidal stability in water were obtained.^[5, 6, 7] The analysis of the fluorescence emission spectra and lifetimes of these nanoparticles suggested possible nanostructuring of

dipolar dyes within the FONs, that could result from a specific local organization and orientation of the chromophores in the vicinity of the nanoparticles surface. This hypothesis was further addressed by measuring the second-order nonlinear (NLO) responses of the FONs made from the dipolar dye shown in Figure 4.1, by means of polarization-resolved Hyper-Rayleigh Scattering (HRS) experiments, which is a powerful selective method to investigate interfacial properties.^[8] In contrast to that of constitutive dyes, the measured Second-Harmonic Scattering (SHS) signals of the FONs arise exclusively from the dipolar hyperpolarizability component, with negligible contribution of the octupolar one. These results were attributed to the presence of correlated polar H-type arrangements of the dyes at the water interface, with the hydrophobic triphenylamine end-group pointing toward the center of the NP and the formyl end-group pointing toward water.

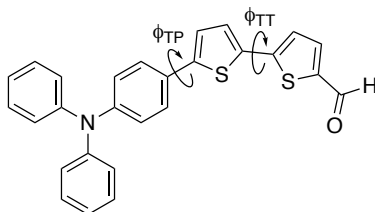


Figure 4.1 – Chemical structure of the dipolar dye investigated in this thesis, with the dihedral angles $\phi_{TT} = \text{S-C-C-S}$ and $\phi_{TP} = \text{C-C-C-S}$.

The objective of this computational study is to complement these experimental investigations by substantiating or not the results and conclusions that were disclosed for NPs based on the dye sketched on Figure 4.1. Molecular dynamics simulations of the nanoparticles formation^[9, 10, 11, 12] in pure water are associated to quantum chemical calculations based on Density Functional Theory (DFT), in order to provide insights on the NPs formation process, the molecular orientation of dipolar dyes within the NPs, as well as the dynamical behavior of their NLO properties. For the first time, the optical response properties of nanoparticles are evaluated fully quantum mechanically by using the tight-binding version of the simplified TD-DFT (sTD-DFT) method, which enables a drastic reduction of computational costs for structures involving several thousands of atoms.^[13, 14]

4.2 Molecular dynamics simulations

Classical MD simulations were carried out using the NAMD software^[15] and analyzed with VMD.^[16] Organic chromophores were modeled using a modified version of the General AMBER Force Field.^[17] Atomic charges were obtained by fitting the electrostatic potential calculated at the B3LYP/cc-pVTZ level of theory, after geometry optimization, using the Gaussian 16 software.^[18] The relaxed B3LYP/cc-pVTZ torsional potentials around the Thienyl-Thienyl and Thienyl-Phenyl dihedrals (ϕ_{TT} and ϕ_{TP} , Figure 4.1) were calculated and implemented in the force field with the methodology described in ref. [19].

Water molecules were described by the flexible variant of the simple point charge model (SPC/Fw),^[20] which well reflects the dynamical and dielectric properties of bulk water. Details on the parameterization of the force fields are provided in the Appendix B.

MD simulations were first performed for 1000 ns in the NPT ensemble ($p = 1$ atm and $T = 300$ K) by employing periodic boundary conditions with a cubic simulation box containing one single organic dye and 1000 water molecules. The self-aggregation of the dyes was simulated by using a 117.2 Å edge cubic simulation box constituted of 100 dipolar dyes surrounded by 46850 water molecules. The initial random spatial distribution of the organic molecules was obtained using the Packmol software.^[21] Then, a MD equilibration procedure was performed on this system for 1 ns within the NpT ensemble and 1 ns within the NVT ensemble, using a temperature of 300 K. To avoid the aggregation of the dyes during this step, the position of their atoms was fixed. In a second step, 8 replicas of the equilibrated system (Figure B.3) were created, and used as starting guesses for 8 different MD simulations performed at 300 K for 250 or 300 ns in the NpT ensemble. A multiple time-stepping integration scheme was used, with a time step of 1 fs for the bonded forces, 2 fs for the Lennard-Jones forces and 4 fs for electrostatic ones. A cutoff of 10 Å was used for intermolecular Lennard-Jones interactions, for which standard Lorentz-Berthelot mixing rules were also applied. Long range electrostatic interactions were evaluated with the Particle Mesh Ewald method with a grid spacing of 1.5 Å. Temperature was controlled with the simple velocity scaling algorithm and pressure with Berendsen barostat.

4.3 Calculation of second-order NLO properties

The static and dynamic (frequency-dependent) components of the first hyperpolarizability tensor of single dyes in solution were computed using the TD-DFT at the M06-2X/6-311+G(d) level.^[22, 23] As evidenced in previous theoretical works, the M06-2X^[24] exchange-correlation functional is well suited for calculating the NLO responses of push-pull conjugated dyes, owing to its substantial amount (54%) of long-range Hartree-Fock (HF) exchange.^[25, 26] Besides, in the case of the chromophore investigated here, M06-2X yields static first hyperpolarizabilities in close agreement with the ones calculated at the second-order Moller-Plesset (MP2) level (see Appendix B).

Frequency-dependent hyperpolarizabilities were calculated using an incident radiation at 1064 nm (1.16 eV), to match the Q-switched Nd:YAG laser source used in the HRS experiments. Solvent effects were included in all TD-DFT calculations by using the integral equation formalism of the polarized continuum model (IEF-PCM).^[27, 28] In order to include the effect of geometry fluctuations, NLO responses calculated using molecular geometries optimized at the DFT level were compared to averaged NLO responses obtained from a statistical sampling of molecular structures extracted at regular time intervals of

the MD trajectories. This sequential MD/DFT scheme was used in previous works for evaluating the second-order NLO responses of dyes in solution^[29, 30, 31] or embedded in complex environments such as biological membranes^[32] or self-assembled monolayers.^[33, 34]

The NLO responses of nanoparticles were calculated using two approaches. The first and crudest approximation consisted in evaluating the first hyperpolarizability of the nanoparticles through the simple summation of the tensor components of the constitutive molecules, using the molecular orientations provided by the MD trajectories. This approach captures the impact of dynamical geometry fluctuations constrained by steric interactions on the NLO properties of the supramolecular structures, but it neglects all mutual polarization effects and intermolecular electronic couplings. In a second step, to take into account these effects, we employed the recently developed sTD-DFT scheme, which provides response properties of large systems at a much lower computational cost than its TD-DFT parent.^[13, 14]

To further reduce the computational needs, the tight-binding implementation of the sTD-DFT method (sTD-DFT-xTB), as well as its version restricted to valence molecular orbitals (sTD-DFT-vTB), were used. Note that the sTD-DFT-xTB default parameterization was primarily fitted to globally reproduce excited state properties and not NLO ones. The strategy consists in fitting the adjustable parameters to reproduce reference calculations on small model systems that retain most of the physics of larger structures, giving to the sTD-DFT-xTB method a similar accuracy as the reference one.^[13, 35] In this spirit, preliminary calculations were performed on the isolated dye as well as on supramolecular clusters containing 12 chromophores, in order to define the optimal values of the y_J , y_K and E_{th} parameters involved in the sTD-DFT equations with respect to M06-2X/6-311G(d) reference calculations. Because of the rather similar performances of the sTD-DFT-xTB and sTD-DFT-vTB methods for this kind of systems, the less computational-demanding sTD-DFT-vTB approach was selected to perform calculations on the NPs. Optimal sTD-DFT-vTB parameters for the systems investigated here are: $y_J = 0.4$, $y_K = 2.0$ and $E_{th} = 5$ eV (see Appendix B for the full discussion).

4.4 Aggregation and structural properties

4.4.1 Aggregation energy of molecular pairs in water

The free-energy profile of a pair of dyes in water was determined as a function of the distance separating their centers of mass, using the dynamically adapted biasing force (ABF) method.^[36] As shown in Figure B.21, the profile clearly shows a minimum around 5 Å, indicating a tendency for the two molecules to aggregate. The aggregation energy, *i.e.* the free-energy difference between their aggregated and separated states, is equal to -6.2 kcal.mol⁻¹, which demonstrates that even the smallest possible aggregate

is thermodynamically more stable than the corresponding solvated molecules. This result suggests that, contrary to the standard cases described by classical nucleation theory (CNT),^[37, 38] there is no critical nucleus size after which supramolecular clusters become stable. According to CNT, the strong driving force for aggregation also indicates that many nuclei can form in a small volume of water, and that the aggregation rate should be very fast.

4.4.2 Self-aggregation of the dyes in water

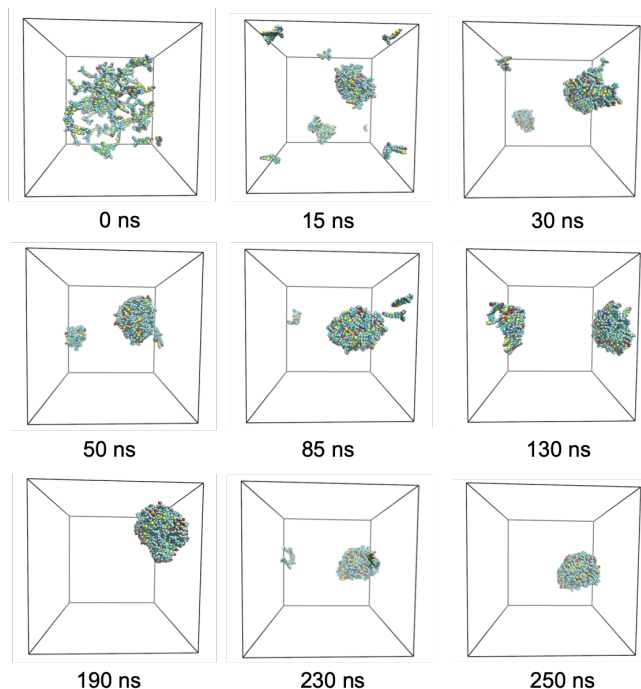


Figure 4.2 – Snapshots of the simulation box showing supramolecular aggregation over time for NP7. Water molecules are not displayed. A video of the time-evolution of the aggregation is provided in Appendix B.

As a consequence of the high aggregation rate in water, the dyes, initially randomly dispersed in the simulation box, start to self-assemble in the first few nanoseconds of the simulation. The first-formed molecular clusters merge to form bigger ones until they all aggregate into a single nanoparticle, as shown in Figure 4.2. However, this process becomes increasingly slow as the size of the aggregates increases, since it is governed by Brownian diffusion that slows down at increasing mass. This is illustrated on Figure 4.3, which reports the number of nanoparticles and the number of dyes composing the biggest aggregate as a function of the simulation time, for the 8 replicated MD trajectories. Figure 4.3 also shows that all MD runs lead to complete aggregation in less than 250 ns, giving rise to nanoparticles (NP1-8) composed of 100 dyes each. To ensure good equilibration of the structure of the NPs, MD trajectories were extended at least 50 ns after the complete dye aggregation, *i.e.* up to 250 ns for replicas NP1, NP3, NP6, NP7 and NP8, and up to 300 ns for NP2, NP3 and NP5.

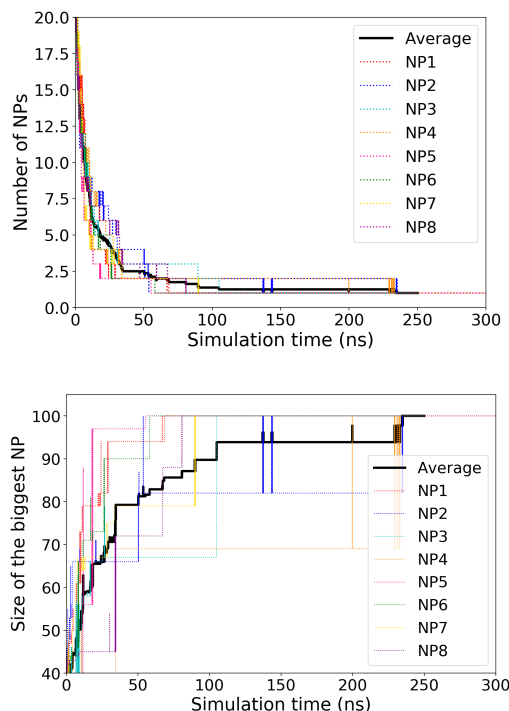


Figure 4.3 – Evolution of the number of NPs (top) and of the size of the biggest NP (bottom) with simulation time for the 8 replicated MD simulations. Abrupt rises in the evolution are due to the coalescence of two "large" aggregates. Two molecules are considered to be in the same aggregate if at least a couple of non-hydrogen atoms is closer than 4.0 Å.

4.4.3 Structure of the nanoparticles

The final nanoparticles globally exhibit an ellipsoidal, nearly spherical shape, more or less elongated depending on the replica (see details in Appendix B), and fluctuating in time (Figures B.22 and B.23). The orientation of the dipolar dyes within a typical NP structure is illustrated on Figure 4.4. Not surprisingly, the hydrophobic triphenylamine groups of the dyes mainly point toward the center of the NP, while the hydrophilic formyl groups point towards the outside. This preferential orientation is also illustrated in the graph of Figure 4.4, which reports the concentration of the different atomic groups as a function of the distance from the NP center.

Interestingly, the time evolution of the average total dipole moment (Figure 4.5) shows that the NPs have a strong polar character (50 D *vs* 6.5 D for the isolated molecule), further evidencing their non-centrosymmetric shape and distribution of molecular orientations. This is also clearly illustrated in Figure 4.4 by the map of the electrostatic potential of NP1, calculated from the atomic charge distribution. Moreover, Figure 4.4 also highlights the presence of domains involving several π -stacked dyes. A statistical analysis of these aggregates, conducted over the 8 final NPs, is detailed in the Appendix B.

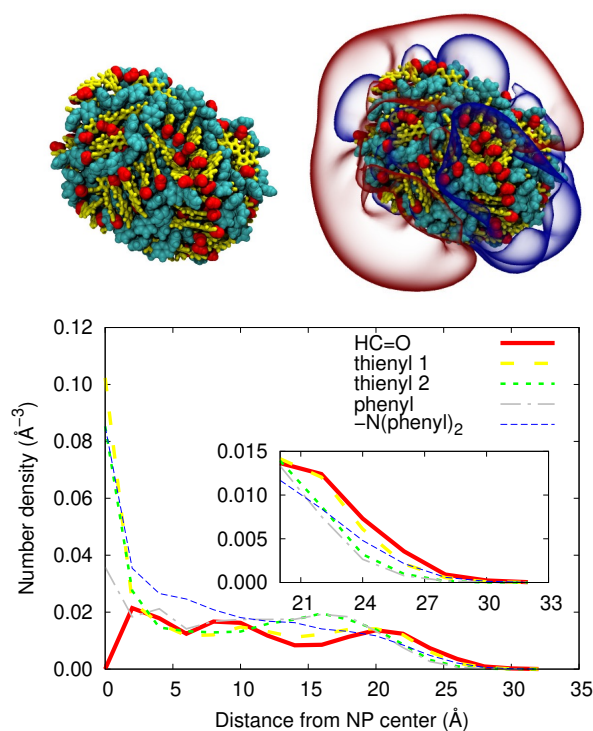


Figure 4.4 – Top Left: Example of ellipsoidal nanoparticle composed of 100 aggregated dyes highlighting the orientation of formyl groups (in red) towards the outside, and the π -stacked domains (in yellow); Top Right: Electrostatic potential calculated from the atomic charge distribution (isovalues range from -4 (blue) to $+4$ (red), in kT/e units, with $T = 300$ K); Bottom: radial number density of the different molecular moieties as a function of the distance from the center of the nanoparticle. Values averaged over the 100 molecules of the 8 final nanoparticles (NP1-NP8).

It reveals that more than 80% of the molecules within a NP develop π -stacking interactions with at least one of their direct neighbour, through at least one of the three central conjugated rings (Figure 4.6). The size of the π -stacked domains is comprised between 2 and 20 molecules. A detailed picture of the relative orientation of π -stacked molecular pairs is provided in Figure 4.7, which evidences that 35% of the dimers adopt a parallel orientation, consistent with the preferential orientation of the hydrophobic triphenylamine termination towards the center of the NPs. However, it is also found that a significant amount (29%) of the dimers stack antiparallely, as a result of stabilizing electrostatic interactions, or even in herringbone-like (16%) or cross (22%) configurations.

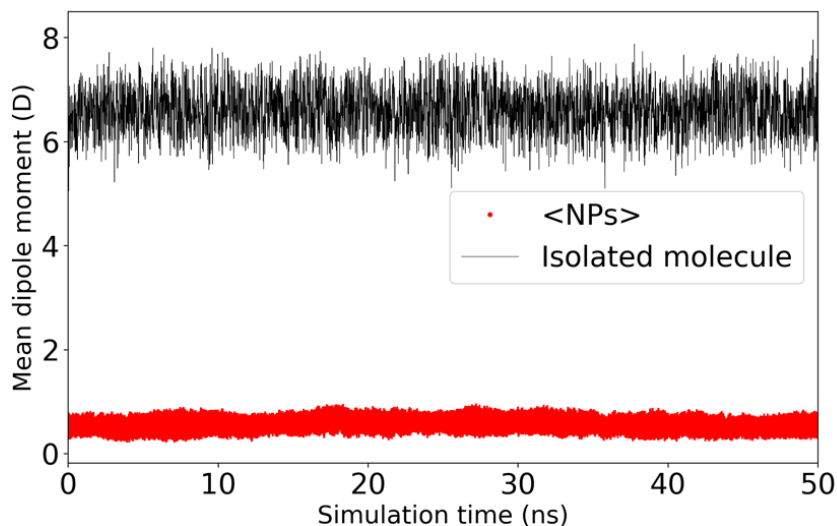


Figure 4.5 – Evolution of the mean dipole moment with simulation time of an isolated dye and of the nanoparticles, divided by the number of their constitutive dyes.

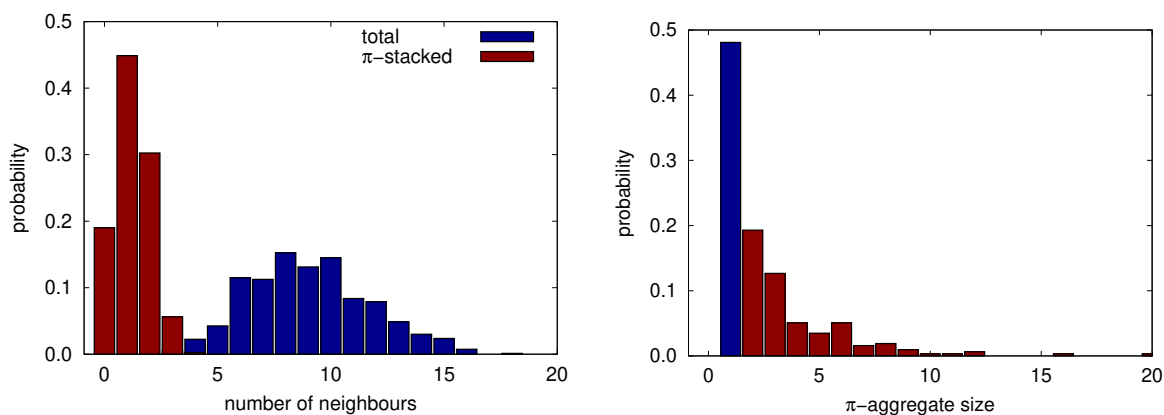


Figure 4.6 – Left: Probability distribution of the number of neighbours (blue) and of the number of π -stacked neighbours (red), assuming the definitions given in the text. Values averaged over the 100 molecules of the 8 final nanoparticles (NP1-NP8). Right: Probability distribution of the number of molecules in the π -stacked aggregates. The blue box on the left panel corresponds to molecules that do not have π -stacked neighbours.

To further characterize the morphology of the NPs at the atomistic scale, statistical distributions of intra- and intermolecular structural parameters were calculated for the 8 replicas along the last 50 ns of the MD trajectories, *i.e.* after full aggregation of all dyes. Figure 4.8 illustrates the distribution of the torsional angle ϕ_{TT} associated to the *cis* ($\phi_{TT} = 0^\circ$) or *trans* ($\phi_{TT} = 180^\circ$) configuration of the bithiophene unit (Figure 4.1), for a single dye in water and for aggregated dyes. In the case of the isolated dye, the probability distribution of ϕ_{TT} values shows two maxima with equal amplitude at 0° and 180° , indicating that *cis* and *trans* configurations are equiprobable, consistently with the close energies of the two isomers and the low rotational energy barriers around the

single bond connecting the thienyl groups (Figure B.2a). The relative magnitude of the two peaks is slightly modified within the NPs, with the *cis* configuration increasing its probability at the expense of the *trans* one. However, the variations with respect to the isolated dye are weak, indicating that aggregation hardly affects the configurational isomerism of the dipolar dyes. The same observation holds true regarding the ϕ_{TP} dihedral angle, which describes the rotation around the single bond connecting the thienyl and phenyl groups (Figure 4.1). The time auto-correlation functions (ACFs) of ϕ_{TT} and ϕ_{TP} angles, calculated for the isolated and aggregated dyes, are plotted in Figure 4.9. The ACF decays provide the time scale of the rotational motions about the thienyl-thienyl and phenyl-thienyl bonds. Compared to molecules in water solution, the ACFs of molecules inserted in nanoparticles show a much slower decay time (approximately 30 ns, versus 1 ns in solution), owing to the sterically hindered environment, but also show that these intramolecular rotations are still possible.

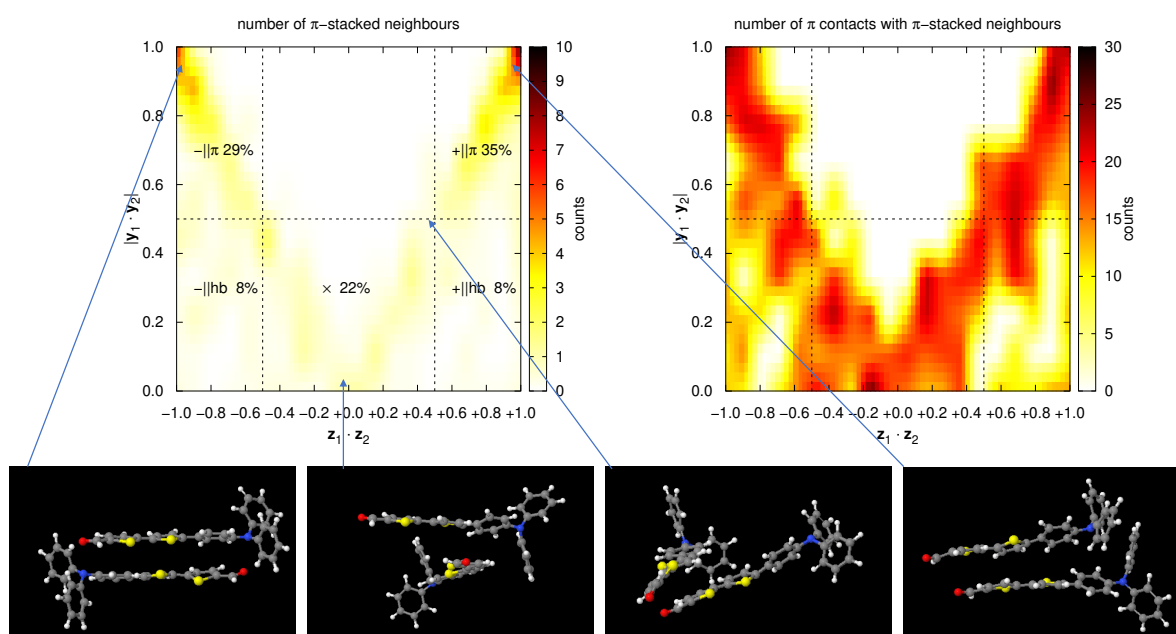


Figure 4.7 – Number of π -stacked molecular pairs as a function of their relative orientation (see the definitions given in the text), as averaged over the 8 final nanoparticles (NP1-NP8). The labels on the left plot correspond to an arbitrary classification of the relative orientation of the long axes of the pair as parallel (+)/ antiparallel (-) or π -stacked (π) or herringbone (hb).

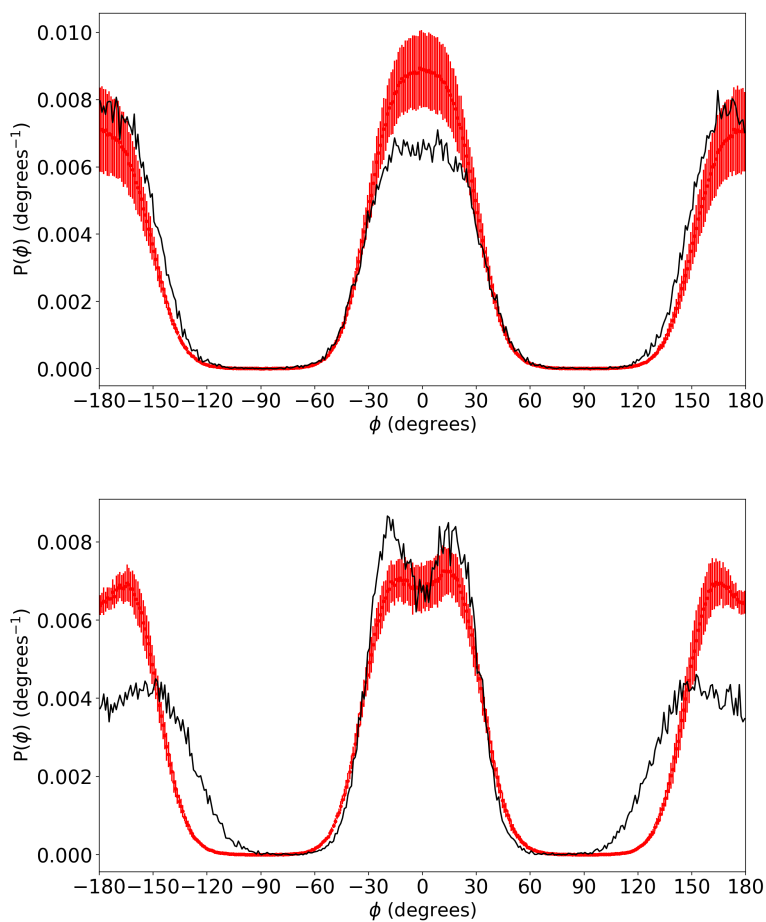


Figure 4.8 – Distribution of the ϕ_{TT} (top) and ϕ_{TP} (bottom) dihedral angles (Figure 4.1) for a single dye in water solution (in black, monitored over 1000 ns) and embedded into a nanoparticle (in red, averaged for the 100 constitutive dyes of the 8 final NPs, over the last 50 ns).

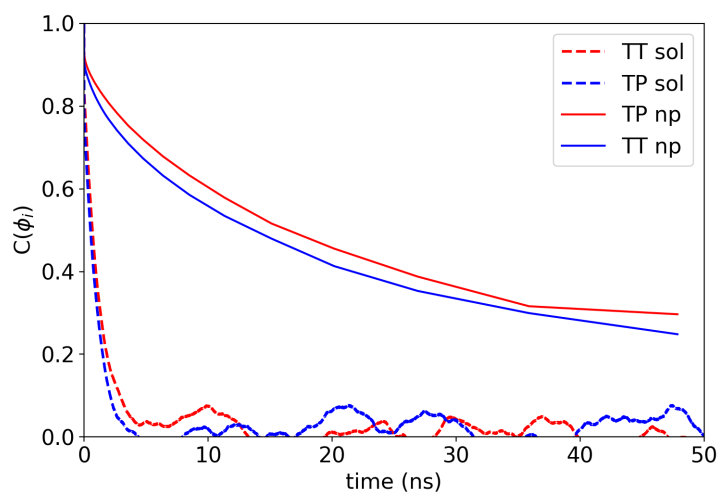


Figure 4.9 – Time autocorrelation function of the dihedral angles ϕ_{TT} and ϕ_{TP} dihedrals, defined as $C(\phi_i) = \langle \cos[\phi_i(t) - \phi_i(0)] \rangle = \langle \cos[\phi_i(0)] \cos[\phi_i(t)] \rangle + \langle \sin[\phi_i(0)] \sin[\phi_i(t)] \rangle$, calculated for the isolated and aggregated dyes.

The evolution of the mean density of neighbours within the nanoparticles as a function of the distance r_{ij} between the centers of mass of molecules (Figures 4.10 and 4.11) reveals that first molecular neighbours are located at average distances of about 6 Å. Note that after 50 Å, $N(r_{ij})$ falls to zero as the distance exceeds the size of the aggregate (Figure B.25), which allows to estimate the average diameter of the NPs to about 5 nm. The evolution of the mean cosine of the angle θ_{ij} between molecular dipoles, also plotted in Figure 4.11, gives complementary information on the orientation of the molecules within the NPs, with positive (negative) values corresponding to parallel (antiparallel) orientation. As shown in Figure 4.11, $\langle \cos \theta_{ij} \rangle$ is positive at the first neighbours distance, suggesting a parallel orientation between first neighbours, which is at the origin of the overall non-zero dipole moments of the NPs (Figure 4.5). At larger distances, $\langle \cos \theta_{ij} \rangle$ approaches zero, indicating that this correlation is lost. The short range preferential parallel ordering of the dipolar dyes is confirmed by the distribution of $\langle \cos \theta_{ij} \rangle$ values for molecules closer than 7.5 Å (Figure B.26), which shows a weak maximum for $\langle \cos \theta_{ij} \rangle = 1$. Note that the distribution displays a second maximum at $\langle \cos \theta_{ij} \rangle = -1$, showing the propensity of neighbouring chromophores to also stack with an anti-antiparallel configuration.

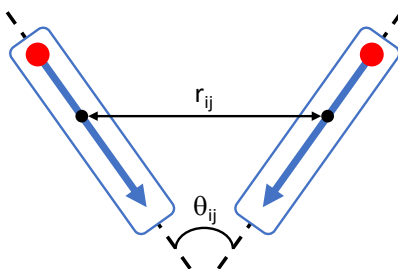


Figure 4.10 – Definition of the angle θ_{ij} between molecular dipoles and the distance r_{ij} , between their centers of mass.

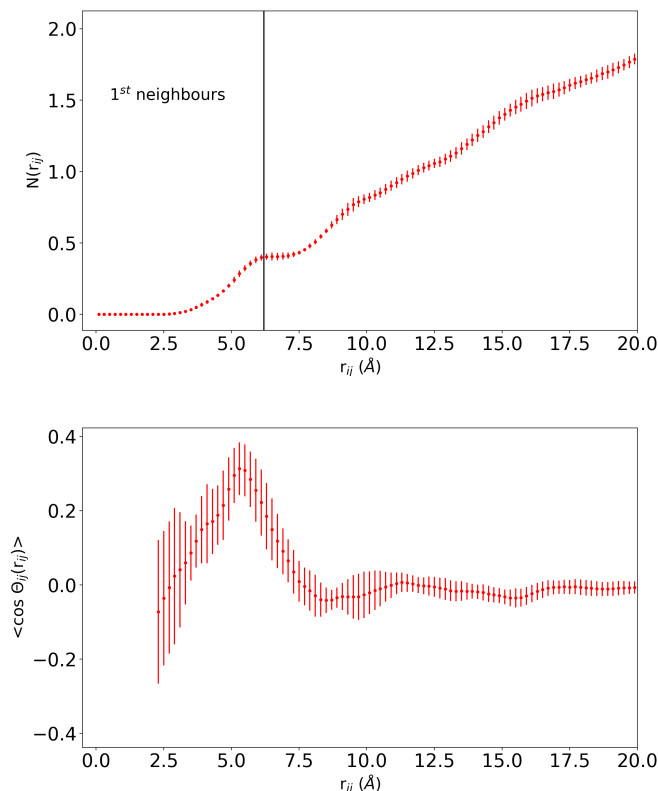


Figure 4.11 – Evolution of the mean density of neighbours $N(r_{ij})$ (top) and of the mean cosine of θ_{ij} (bottom) as a function of r_{ij} .

4.5 Nonlinear optical properties

4.5.1 NLO responses of solvated dyes

The dynamic HRS properties calculated at the DFT level for the *cis* and *trans* forms of the isolated molecule (as well as "averaged" values estimated using relative *trans/cis* Boltzmann populations at room temperature) are compared to those measured in dilute chloroform and acetonitrile solutions in Table 4.1. Although the computed HRS hyperpolarizabilities are about three times larger than the experimental ones, the slight enhancement of the β_{HRS} values from chloroform to acetonitrile is well reproduced. DFT calculations performed in water show that increasing further the solvent polarization effects has no impact on the NLO properties of the dye. Unlike experimental results which show that the NLO response of the dye in chloroform is slightly dominated by its octupolar contribution ($\rho > 1$), DFT calculations predict a low predominance of dipolar character in both solvents, with weak solvatochromism effect. This small discrepancy likely originates from the theoretical treatment of solute-solvent interactions by means a continuum solvation model, where intermolecular interactions are not treated explicitly. DFT calculations and HRS measurements are further compared on the polar plots showing the evolution of the harmonic light intensity as a function of the polarization angle Ψ of the incident beam (Figure 4.12). In acetonitrile, the theoretical curve calculated

using equation 1.31 quasi perfectly matches the experimental fits, while the agreement is worse for data in chloroform, where the thinner shape of the theoretical curve reveals an overestimated dipolar character. Note that part of the discrepancy between experimental and theoretical data might also arise from the lower quality of the experimental fits in the $\Psi = 0^\circ$ and $\Psi = 180^\circ$ zones. Moreover, the large overestimate of calculated β_{HRS} values compared to experiments in both chloroform and acetonitrile may also arise from the increased probability of the formation of small molecular aggregates with a pseudo centrosymmetrical shape (*i. e.* stacked dimers, for which a head-to-tail relative orientation is favored by the dipole-dipole interactions and the better overlap between the conjugated cores).

Table 4.1 – Total dynamic HRS hyperpolarizabilities (β_{HRS}), dipolar ($|\beta_{J=1}|$) and octupolar ($|\beta_{J=3}|$) components (all values in 10^3 a.u.), as well as the associated depolarization (DR) and anisotropy (ρ) ratios deduced from HRS measurements at 1064 nm in chloroform (chl) and acetonitrile (ace), and calculated at the DFT level in chloroform and acetonitrile, and at the DFT and MD+DFT levels in water.

	β_{HRS}	DR	ρ	$ \beta_{J=1} $	$ \beta_{J=3} $
Exp. ^a (chl)	12.5	3.6	1.22 ± 0.03	20.7	25.3
DFT ^b (<i>trans</i> ,chl)	37.5	4.8	0.85	69.5	59.2
DFT ^b (<i>cis</i> ,chl)	32.3	5.0	0.82	60.4	49.5
DFT ^{b,c} (<i>av</i> ,chl)	34.1	4.9	0.83	63.5	52.9
Exp. ^a (ace)	13.3	4.6	0.91 ± 0.03	24.2	22.0
DFT ^b (<i>trans</i> ,ace)	37.9	4.9	0.85	70.3	59.6
DFT ^b (<i>cis</i> ,ace)	34.2	5.0	0.82	63.9	52.2
DFT ^{b,c} (<i>av</i> ,ace)	36.7	4.9	0.83	63.5	52.9
DFT ^b (<i>trans</i> ,water)	38.0	4.9	0.85	70.5	59.7
DFT ^b (<i>cis</i> ,water)	34.1	5.0	0.82	63.9	52.2
DFT ^{b,c} (<i>av</i> ,water)	36.7	4.9	0.84	63.8	57.2
MD+DFT ^d (water)	28.3 ± 14.7	5.0 ± 0.1	0.83 ± 0.03	52.7 ± 27.3	43.8 ± 22.7

^a Taken from ref. [8].

^b IEFPCM:M06-2X/6-311+G(d) calculations using the IEFPCM:B3LYP/cc-pVTZ geometries.

^c *av*: averaged values estimated using relative *trans/cis* Boltzmann populations at room temperature.

^d Averaged over 100 molecular geometries extracted from the MD trajectories.

To gain insight on the impact of thermally-induced geometry distortions, we also compare in Table 4.1 the NLO properties calculated using the DFT-optimized geometries of the dye in water solution to those averaged over 100 molecular geometries extracted from MD trajectories (MD+DFT). The two approaches provide similar DR and ρ values, suggesting that structural fluctuations do not induce significant change in the multipolar character of the NLO responses. On the contrary, the MD-averaged β_{HRS} values show a 30% decrease compared to DFT ones. This is consistent with the low energy barriers for the rotation around the Thienyl-Thienyl and Thienyl-Phenyl bonds (Figures B.2a and B.2b). In fact, many structures extracted from MD runs display non planar shapes, corresponding to lower conjugation along the molecular backbone and damped second-

order NLO response. A similar decrease of the β_{HRS} response when moving from DFT to MD+DFT calculations was observed previously for a push-pull indolino-oxazolidine derivative also incorporating a bithiophene unit.^[39, 29] The strong impact of the dynamical fluctuations is further testified by the large standard deviation of the β_{HRS} values.

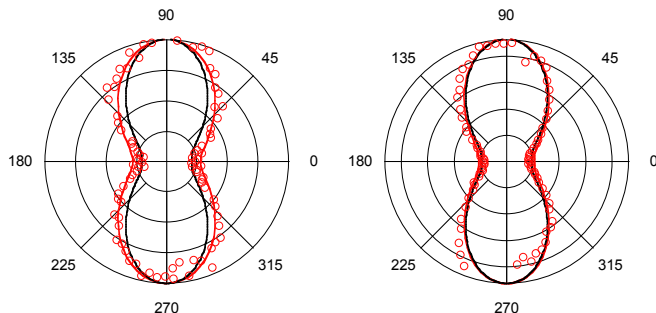


Figure 4.12 – Normalized polar representations of the evolution of the harmonic light intensity as a function of the polarization angle Ψ of the incident beam, as measured in chloroform (left) and acetonitrile (right). Red circles correspond to measured values. Red lines are the best experimental fitted curves. Black lines are calculated using equation 1.31 with β -components calculated at the IEFPCM:M06-2X/6-311+G(d) level.

4.5.2 NLO responses of the nanoparticles

In a first approach, we estimated the first hyperpolarizability tensor of the NPs as the sum of the tensors of the individual constitutive dyes calculated at the TD-DFT level. As mentioned above, although this approximation neglects intermolecular electronic couplings and polarization effects on the NLO properties, it integrates the effects related to the spatial organization of the dyes within the NPs, and to their geometrical fluctuations. As reported in Table B.4, static first hyperpolarizabilities for NP1-8 are spread over a broad range of values, as reflected in the large standard deviation of their distributions $\langle\beta_{HRS}\rangle = (43.8 \pm 11.9)10^3$ a.u. As a result of frequency-dispersion effects, dynamic β_{HRS} values are about three times larger than the static ones ($\langle\beta_{HRS}\rangle = (189.1 \pm 70.5)10^3$ a.u.) with a larger distribution (Table 4.2). The impact of frequency dispersion on the depolarization ratios is less systematic, either increasing or decreasing the DR values depending on the considered NP. Despite these irregular fluctuations, the average static and dynamic depolarization ratios are very close (4.5-4.6), indicating that the NLO responses of the supramolecular structures globally exhibit a 1D character, typical of systems for which the hyperpolarizability tensor is dominated by a single diagonal component.

Data reported in Table B.6 and Figure B.28 show that the NLO responses of individual nanoparticles also display large fluctuations with respect to dynamical geometry fluctuations along the MD simulation. The evolution over time of the cumulative averages

of β_{HRS} and DR values is illustrated in Figure 4.13 for NP5, starting from the time (140 ns) where the 100 molecular dyes collapse into a single structure. Even though individual values vary strongly over time, the cumulative averages rapidly converge to $\langle\beta_{HRS}\rangle = 204$ a.u. and $\langle DR\rangle = 4.3$.

Table 4.2 – Dynamic ($\lambda = 1064$ nm) first hyperpolarizabilities (β_{HRS} in 10^3 a.u.) and depolarization ratios (DR) of the final nanoparticles issued from the 8 replicated MD trajectories, evaluated using the tensor sum approximation at the TD-DFT and sTD-DFT-vTB levels, as well as from sTD-DFT-vTB calculations performed on the whole nanoparticles.

	TD-DFT ^a (tensor sum)		sTD-DFT-vTB ^b (tensor sum)		sTD-DFT-vTB ^b (full calculation)	
	β_{HRS}	DR	β_{HRS}	DR	β_{HRS}	DR
NP1	317.0	6.3	325.8	5.8	3194.5	4.8
NP2	112.0	3.7	248.2	3.4	106.4	3.0
NP3	110.7	3.0	161.2	3.8	616.9	3.6
NP4	160.1	5.1	238.9	5.2	2259.4	5.1
NP5	237.6	5.9	343.1	7.2	369.9	4.7
NP6	185.0	3.6	238.7	4.5	212.7	4.9
NP7	234.0	3.4	827.6	5.0	156.6	2.1
NP8	156.4	5.5	167.9	5.3	634.3	5.0
av.± std. dev.	189.1 ± 70.5	4.6 ± 1.3	318.9 ± 215.4	5.0 ± 1.2	943.8 ± 1145.4	4.2 ± 1.1

^a M06-2X/6-311+G(d) in gas phase.

^b Using $y_J = 4.0$, $y_K = 2.0$ and $E_{th} = 5.0$ eV.

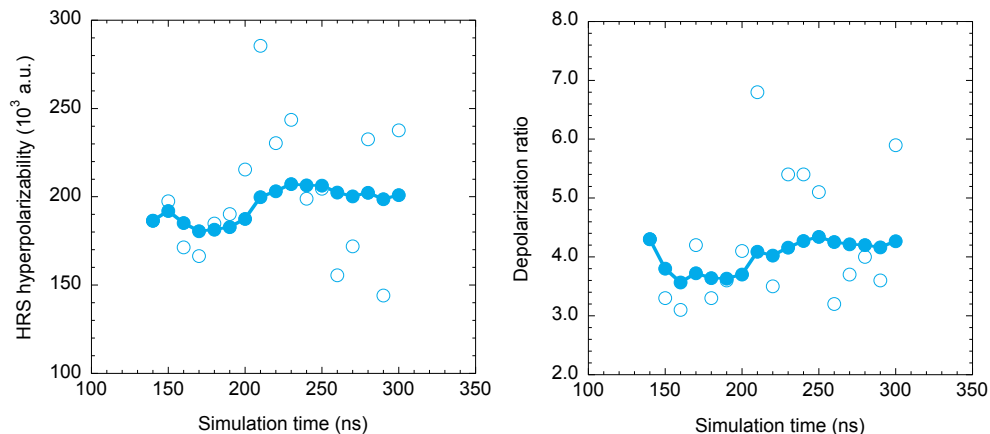


Figure 4.13 – Time evolution of β_{HRS} (left) and DR (right) values for NP5 (empty dots) and of their cumulative moving averages (full dots), as calculated using the tensor-sum approximation at the TD-DFT:M06-2X/6-311+G(d) level.

With the exception of NP7, the static β_{HRS} and DR values evaluated using the tensor-sum approximation at the sTD-DFT-vTB level are very close to those estimated using the full-featured TD-DFT level (the R_1 ratios in Table B.4 and the linear correlation in Figure B.27). In the case of dynamic calculations, the average β_{HRS} value obtained with sTD-DFT-vTB is 1.7 times larger than the TD-DFT one (Table 4.2), while the mean DR value increases from 4.6 to 5.0.

Comparing sTD-DFT-vTB data evaluated using the tensor-sum approximation with those issued from calculations on the whole supramolecular structure provides a direct measure of the effects of intermolecular interactions. In the static case, a good correspondence is found between first hyperpolarizabilities evaluated using the tensor-sum approximation at the TD-DFT and sTD-DFT-vTB levels (Figure B.27), while accounting for intermolecular interactions induces a 20% lowering of the HRS hyperpolarizability. As evidenced in the case of π -stacked dimers (Table B.7 and Figure B.30), this decrease can be ascribed to the slight blue-shift of the main absorption band upon aggregation of the dyes. On the contrary, as a result of resonance effects, dynamic β_{HRS} values display very large and non systematic variations, going from a $\sim 80\%$ decrease for NP7 to a $\sim 900\%$ increase for NP1. Considering data averaged over the 8 NPs, intermolecular interactions enhance the dynamic β_{HRS} response by about a factor 3, while the DR value is lowered from 5.0 to 4.2. We stress however that the very large β_{HRS} values calculated for NP1 and NP4, and therefore the average β_{HRS} value, should be taken with caution, since the response functions diverge at the harmonic frequency inducing numerical instabilities. These results also highlight the important effects of intra and intermolecular structural variations, which reflect in the large standard deviation of the NLO responses. As reported in Table B.6, the relative standard deviations on β_{HRS} calculated for the 8 replicated MD trajectories range from 22% to 47%, and are of similar magnitude (from 26% to 48%) for the depolarization ratio.

4.6 Absorption properties

In order to investigate further the origin of the large enhancement of the dynamic NLO response upon molecular aggregation, we investigated the absorption properties of the dyes in their isolated and aggregated states. In a first step, the vertical excitation energies and oscillator strengths towards low-lying excited states were calculated for three representative π -stacked dimers extracted from the NPs (Figure B.28). As reported in Table B.7 and Figure B.30, TD-DFT calculations performed at the M06-2X/6-311+G(d) level show that, compared to the isolated monomer, dipole-allowed red-shifted transitions appear in the three dimerized structures. Additional calculations using a Boys localization scheme^[40] to decompose the electronic eigenstates into a set of pure (diabatic) intramolecular and intermolecular charge-transfer (CT) electronic configurations further evidenced that some low energy electronic transitions with large oscillator strength have a dominant intermolecular CT character (see details in Appendix B). As also shown in Table B.7 and Figure B.30, despite a global blue-shift of the main absorption bands compared to TD-DFT, the appearance of these new low-energy excited states is qualitatively well reproduced by sTD-DFT-vTB calculations using the same y_J , y_K and E_{th} parameters as those used in NLO calculations.

In a second step, we thus calculated the electronic excited states of a representative NP composed of 100 chromophores using the same sTD-DFT-vTB scheme. The absorption spectrum of the NP (Figure 4.14) is much wider than that of the isolated dye, owing to the structural variety of the constitutive molecular units and, as shown above, the possibility of intermolecular CT excitations.^[41, 42] The global shape of the absorption spectrum is fully consistent with the one measured for FON suspensions in water (see Figure 4 of ref. [5]), which exhibits a red-shifted and broadened main absorption band as compared to dyes dissolved in organic solvents, as well as a residual absorption in the long-wavelength region (500-550 nm \equiv 2.25-2.50 eV). These low-energy absorption bands, in part attributed to intermolecular CT excitations, resonate with the second harmonic light at 532 nm (2.32 eV) and are thus at the origin of the enhancement of the dynamic β_{HRS} response upon aggregation.

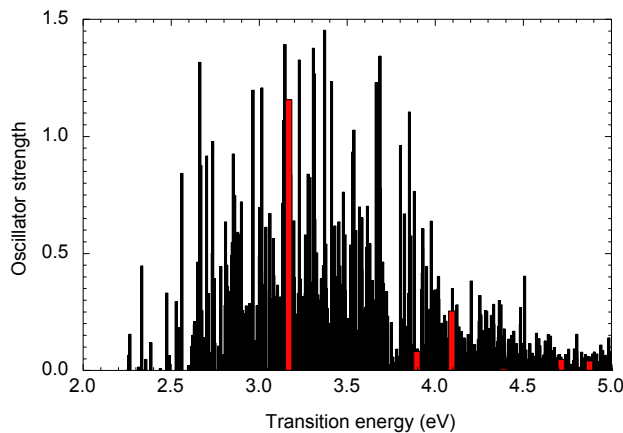


Figure 4.14 – Electronic transitions towards the excited states in NP1 (black bars) and in the *trans* isolated dye (red bars), as calculated at the sTD-DFT-vTB level.

4.7 Comparison to experiments and further discussion

With respect to experiments, this computational study offers complementary insights on the origin of the NLO properties of the molecular-based NPs that are worth being discussed. As reported in ref. [8], the total second-harmonic signal radiated by the nanoparticles in solution can be partitioned in two contributions, respectively ascribed to the bulk and interfacial areas of the NPs:

$$\beta_{NP} = \beta_{bulk} + \beta_{interf} \quad (4.1)$$

The bulk contribution is related to the NLO response of molecular dyes constituting the inner shell of the nanoparticules, *i.e.* not directly in contact with water molecules. A comparison with the three orders of magnitude larger hyperpolarizabilities measured for noncentrosymmetric BaTiO₃ or PbTiO₃ ferroelectric nanocrystals with comparable diameters, suggests that the NPs investigated here exhibit a negligible β_{bulk} contribution.^[43]

On the contrary, owing to their limited size, the NPs issued from the simulations can be considered as having no bulk, with all organic dyes being part of the interfacial region. The interfacial term in equation 4.1 results from second-order and third-order contributions:

$$\beta_{interf} = \beta + (\gamma\phi_0)_{EFISH} \quad (4.2)$$

The second-order term, β , was previously attributed to the locally non-centrosymmetric H-type structuring of the dyes at the water interface.^[8] Our MD simulations confirmed such a specific arrangement, as resulting of π -stacking interactions between the central conjugated rings (Figure 4.4). The second term, referred to as electric field induced second harmonic (EFISH), involves the third-order hyperpolarizability (γ) of the chromophores (which is expected to be strong for such two-photon absorbing dyes) and the interfacial local electric field ϕ_0 , arising from the surface charge density. It is important to note that this term is neglected in the tensor sum approximation, which only considers the second-order ($\beta \equiv \beta_{HRS}$) contribution. On the contrary, sTD-DFT calculations are in principle able to capture the full NLO response of the NPs, including the third-order contribution. However, since water molecules in the interfacial area are not included in the calculations, the magnitude of local field effects is likely underestimated, and so for the third-order response. Note also that the water molecules in the vicinity of the NP are expected to be partially aligned by the electric field of the charged interface, and thus to contribute themselves to the EFISH response. However, the latter contributions due to water molecules is weak and cannot be detected by an experimental setup featuring a picosecond excitation laser source as used in ref. [8]. Therefore, only the NLO signal due to the organic dyes is accounted for in the $\beta_{NP} = (3700 \pm 37)10^3$ a.u. value issued from SHS measurements.

The calculated NLO response of nanoparticles in water is about 30 times larger than that calculated for a single molecular dye. This result is consistent with SHS measurements, although the experimental β_{NP}/β_{dye} ratio is one order of magnitude larger. The underestimation of the simulated β_{NP} is directly related to the smaller size of the nanoparticles (of average diameter ~ 5 nm *versus* 36 nm for the experimental one, *i.e.* with a surface area approximately 50 times smaller) and to the incomplete treatment of local field effects in equation 4.2.

For the same reasons, the DR values predicted by sTD-DFT-vTB calculations, ($DR_{NP} = 4.2 \pm 1.1$), are also underestimated compared to SHS measurements ($DR_{NP} = 8.7 \pm 0.9$). As detailed in ref. [8], it is worth mentioning here that SHS measurements of NPs are expected to generate interferences between the partial waves scattered by the individual molecules, inducing retardation effects at the fundamental and harmonic frequencies. This collective coherent signal, which scales quadratically with the number of correlated molecules, becomes rapidly dominant over the non-coherent one as the size of

the nanoparticle increases. In the present case, the very high experimental DR value is partly attributed to the coherent part of the NLO signal, while calculations do not account for any phase relation between the NLO signals scattered by the various molecules.

Finally, an additional difficulty in comparing theory and experiment lies in the need to include the vibrational contributions, the so-called zero-point vibrational averaging.^[44] In principle, the MD+DFT computational scheme is able to catch, within the simulation time scale, the effects of molecular vibrations, often causing large fluctuations of the NLO responses. The impact of low energy phonon-like modes, associated to global variations in the shape of the nanoparticles, is also taken into account since NLO properties are calculated as averages over several independent trajectories.

4.8 Conclusions and perspectives

The molecular dynamics simulations reported here confirm the spontaneous formation of amorphous nanoparticles based on organic dipolar dyes in water solution, as well as the onset of polar π -stacked domains at the water interface. The soft nature of the nanoparticles allows for rather large shape variations, which are reflected in large fluctuations in time of their second-order NLO responses.

The measured strong enhancement of the first hyperpolarizability upon aggregation of the dyes is well reproduced by the tight-binding implementation of the sTD-DFT method, here employed for the first time to characterize the NLO properties of nanoparticles while fully accounting for their dynamical fluctuations through a sequential MD+QM scheme. This approach allowed to evidence the high impact of mutual polarization effects and intermolecular couplings on the NLO responses. In particular, intermolecular interactions are at the origin of the emergence of low-lying excited states entering into resonance with the second harmonic light. These states are responsible for the high enhancement of the SHS signal upon dyes aggregation.

This thesis also points the difficulty of comparing the calculated and experimental NLO responses of such large and flexible supramolecular assemblies. Limitations of the computational methodology are mainly related to the timescale and size of the objects that can be investigated, to numerical instabilities due to resonance effects, as well as to the probable underestimate of the magnitude of local electric fields since the first solvation shell is not taken into account.

Therefore, this work should be seen as a first step towards accurate simulations of NLO responses of large molecular-based architectures, paving the way toward future calculations and method development. Explicitly including in the calculation the first

shell of water molecules close to the NP interface, which, at least for small particles, may be essential for the quantitative prediction of the EFISH signal, comes out as a natural outlook. The implementation of damped response functions within the the sTD-DFT scheme would also be of great interest in order to avoid disproportionate resonances. Alternatively, the development of parameterized models on the basis of natural response orbitals would allow investigating larger clusters at low computational cost. Finally, an exhaustive study of the NLO responses of nanoparticles of different sizes would provide insights on the relative magnitude of bulk and interfacial contributions.

Bibliography

- [1] Fery-Forgues S. Fluorescent organic nanocrystals and non-doped nanoparticles for biological applications. *Nanoscale*, 5:8428, 2013.
- [2] Genin E., Gao Z., Varela J., Daniel J., Bsaibess T., Gosse I., Groc L., Cognet L., and Blanchard-Desce M. "hyper-bright" near-infrared emitting fluorescent organic nanoparticles for single particle tracking. *Adv. Mater.*, 26:2258, 2014.
- [3] Xing P. and Zhao Y. Multifunctional nanoparticles self-assembled from small organic building blocks for biomedicine. *Adv. Mater.*, 28:7304, 2016.
- [4] Rosendale M., Flores J., Paviolo C., Pagano P., Daniel J., Ferreira J., Verlhac J-B, Groc L., Cognet L., and Blanchard-Desce M. A bottom-up approach to red-emitting molecular-based nanoparticles with natural stealth properties and their use for single-particle tracking deep in brain tissue. *Advanced Materials*, 33:2006644.
- [5] Parthasarathy V., Fery-Forgues S., Campioli E., Recher G., Terenziani F., and Blanchard-Desce M. Dipolar versus Octupolar Triphenylamine-Based Fluorescent Organic Nanoparticles as Brilliant One- and Two-Photon Emitters for (Bio)imaging. *Small*, 7:3219, 2011.
- [6] Amro K., Daniel J., Clermont G., Bsaibess T., Pucheault M., Genin E., Vaultier M., and Blanchard-Desce M. A new route towards fluorescent organic nanoparticles with red-shifted emission and increased colloidal stability. *Tetrahedron*, 70:1903, 2014.
- [7] Mastrodonato C., Pagano P., Daniel J., Vaultier M., and Blanchard-Desce M. Molecular-Based Fluorescent Nanoparticles Built from Dedicated Dipolar Thienothiophene Dyes as Ultra-Bright Green to NIR Nanoemitters. *Molecules*, 21, 2016.
- [8] Daniel J., Bondu F., Adamietz F., Blanchard-Desce M., and Rodriguez V. Interfacial Organization in Dipolar Dye-Based Organic Nanoparticles Probed by Second-Harmonic Scattering. *ACS Photonics*, 2:1209, 2015.
- [9] Levine B. G., LeBard D. N., DeVane R., Shinoda W., Kohlmeyer A., and Klein M. L. Micellization Studied by GPU-Accelerated Coarse-Grained Molecular Dynamics. *J. Chem. Theory Comput.*, 7:4135, 2011.
- [10] Silva D. L., Murugan N. A., Kongsted J., Ågren H., and Canuto S. Self-aggregation and optical absorption of stilbazolium merocyanine in chloroform. *J. Phys. Chem. B*, 118:1715, 2014.
- [11] Guskova O. A., Varanasi S. R., and Sommer J-U. C60-dyad aggregates: Self-organized structures in aqueous solutions. *J. Chem. Phys.*, 141:144303, 2014.

- [12] Potter T. D., Walker M., and Wilson M. R. Self-assembly and mesophase formation in a non-ionic chromonic liquid crystal: insights from bottom-up and top-down coarse-grained simulation models. *Soft Matter*, 16:9488, 2020.
- [13] de Wergifosse M. and Grimme S. Nonlinear-response properties in a simplified time-dependent density functional theory (sTD-DFT) framework: Evaluation of the first hyperpolarizability. *J. Chem. Phys.*, 149:024108, 2018.
- [14] de Wergifosse M. and Grimme S. Perspective on Simplified Quantum Chemistry Methods for Excited States and Response Properties. *J. Phys. Chem. A*, 125:3841, 2021.
- [15] Phillips J. C., Braun R., Wang W., Gumbart J., Tajkhorshid E., Villa E., Chipot C., Skeel R. D., Kalé L., and Schulten K. Scalable molecular dynamics with NAMD. *J. Comput. Chem.*, 26:1781, 2005.
- [16] Humphrey W., Dalke A., and Schulten K. VMD: Visual molecular dynamics. *J. Mol. Graphics*, 14:33, 1996.
- [17] Wang J., Wolf R. M., Caldwell J. W., Kollman P. A., and Case D. A. Development and testing of a general amber force field. *J. Comput. Chem.*, 25:1157, 2004.
- [18] Frisch M. J., Trucks G. W., Schlegel H. B., Scuseria G. E., Robb M. A., Cheeseman J. R., Scalmani G., Barone V., Petersson G. A., Nakatsuji H., Li X., Caricato M., Marenich A. V., Bloino J., Janesko B. G., Gomperts R., Mennucci B., Hratchian H. P., Ortiz J. V., Izmaylov A. F., Sonnenberg J. L., Williams-Young D., Ding F., Lipparini F., Egidi F., Goings J., Peng B., Petrone A., Henderson T., Ranasinghe D., Zakrzewski V. G., Gao J., Rega N., Zheng G., Liang W., Hada M., Ehara M., Toyota K., Fukuda R., Hasegawa J., Ishida M., Nakajima T., Honda Y., Kitao O., Nakai H., Vreven T., Throssell K., Montgomery J. A. Jr., Peralta J. E., Ogliaro F., Bearpark M. J., Heyd J. J., Brothers E. N., Kudin K. N., Staroverov V. N., Keith T. A., Kobayashi R., Normand J., Raghavachari K., Rendell A. P., Burant J. C., Iyengar S. S., Tomasi J., Cossi M., Millam J. M., Klene M., Adamo C., Cammi R., Ochterski J. W., Martin R. L., Morokuma K., Farkas O., Foresman J. B., and Fox D. J. Gaussian 16 Revision C.01. 2016.
- [19] Pizzirusso A., Di Pietro M. E., De Luca G., Celebre G., Longeri M., Muccioli L., and Zannoni C. Order and conformation of biphenyl in cyanobiphenyl liquid crystals: A combined atomistic molecular dynamics and ^1H NMR study. *ChemPhysChem*, 15:1356, 2014.
- [20] Wu Y., Tepper H. L., and Voth G. A. Flexible simple point-charge water model with improved liquid-state properties. *J. Chem. Phys.*, 124:024503, 2006.

- [21] Martínez L., Andrade R., Birgin E. G., and Martínez J. M. PACKMOL: A package for building initial configurations for molecular dynamics simulations. *J. Comput. Chem.*, 30:2157, 2009.
- [22] van Gisbergen S. J. A., Snijders J. G., and Baerends E. J. Calculating frequency-dependent hyperpolarizabilities using time-dependent density functional theory. *J. Chem. Phys.*, 109:10644, 1998.
- [23] Helgaker T., Coriani S., Jørgensen P., Kristensen K., Olsen J., and Ruud K. Recent Advances in Wave Function-Based Methods of Molecular-Property Calculations. *Chem. Rev.*, 112:543, 2012.
- [24] Zhao Y. and Truhlar D. G. The M06 Suite of Density Functionals for Main Group Thermochemistry, Thermochemical Kinetics, Noncovalent Interactions, Excited States, and Transition Elements: two New Functionals and Systematic Testing of Four M06-Class Functionals and 12 Other Functionals. *Theor. Chem. Acc.*, 120:215, 2008.
- [25] Johnson L. E., Dalton L. R., and Robinson B. H. Optimizing Calculations of Electronic Excitations and Relative Hyperpolarizabilities of Electrooptic Chromophores. *Acc. Chem. Res.*, 47:3258, 2014.
- [26] Lescos L., Sitkiewicz S., Beaujean P., Blanchard-Desce M., Champagne B., Matito E., and Castet F. Performance of DFT functionals for calculating the second-order nonlinear optical properties of dipolar merocyanines. *Phys. Chem. Chem. Phys.*, page 16579, 2020.
- [27] Mennucci B., Cammi R., and Tomasi J. Medium Effects on the Properties of Chemical Systems: Electric and Magnetic Response of Donor-Acceptor Systems Within the Polarizable Continuum Model. *Int. J. Quantum Chem.*, 75:767, 1999.
- [28] Tomasi J., Mennucci B., and Cammi R. Quantum Mechanical Continuum Solvation Models. *Chem. Rev.*, 105:2999, 2005.
- [29] Pielak K., Tonnelé C., Sanguinet L., Cariati E., Righetto S., Muccioli L., Castet F., and Champagne B. Dynamical behavior and second harmonic generation responses in acido-triggered molecular switches. *J. Phys. Chem. C*, 122:26160, 2018.
- [30] Ramos T. N., Canuto S., and Champagne B. Unraveling the electric field-induced second harmonic generation responses of stilbazolium ion pairs complexes in solution using a multiscale simulation method. *J. Chem. Inf. Model.*, 60:4817, 2020.
- [31] Ramos T. N., Castet F., and Champagne B. Second Harmonic Generation Responses of Ion Pairs Forming Dimeric Aggregates. *J. Phys. Chem. B*, 125:3386, 2021.

- [32] Bouquiaux C., Tonnelé C., Castet F., and Champagne B. Second-Order Nonlinear Optical Properties of an Amphiphilic Dye Embedded in a Lipid Bilayer. A Combined Molecular Dynamics - Quantum Chemistry Study. *J. Phys. Chem. B*, 124:2101, 2020.
- [33] Tonnelé C., Pielak K., Deviers J., Muccioli L., Champagne B., and Castet F. Nonlinear optical responses of self-assembled monolayers functionalized with indolino-oxazolidine photoswitches. *Phys. Chem. Chem. Phys.*, 20:21590, 2018.
- [34] Tonnelé C., Champagne B., Muccioli L., and Castet F. Nonlinear optical contrast in azobenzene-based self-assembled monolayers. *Chem. Mater.*, 31:6759, 2019.
- [35] Seibert J., Champagne B., Grimme S., and de Wergifosse M. Dynamic structural effects on the second-harmonic generation of tryptophane-rich peptides and gramicidin A. *J. Phys. Chem. B*, 124:2568, 2020.
- [36] Comer J., J. C. Gumbart, Hénin J., Lelièvre T., A. Pohorille, and Chipot C. The Adaptive Biasing Force Method: Everything You Always Wanted To Know but Were Afraid To Ask. *J. Phys. Chem. B*, 119:1129, 2015.
- [37] Erdemir D., Lee A. Y., and Myerson A. S. Nucleation of Crystals from Solution: Classical and Two-Step Models. *Acc. Chem. Res.*, 42:621, 2009.
- [38] Zahn D. Thermodynamics and kinetics of prenucleation clusters, classical and non-classical nucleation. *ChemPhysChem*, 16:2069.
- [39] Pielak K., Bondu F., Sanguinet L., Rodriguez V., Champagne B., and Castet F. Second-Order Nonlinear Optical Properties of Multiaddressable Indolino-oxazolidine Derivatives: Joint Computational and Hyper-Rayleigh Scattering Investigations. *J. Phys. Chem. C*, 121:1851, 2017.
- [40] Subotnik J. E., Yeganeh S., Cave R. J., and Ratner M. A. Constructing diabatic states from adiabatic states: Extending generalized Mulliken-Hush to multiple charge centers with Boys localization. *J. Chem. Phys.*, 129:244101, 2008.
- [41] Sanyal S., Painelli A., Pati S. K., Terenziani F., and Sissa C. Aggregates of quadrupolar dyes for two-photon absorption: the role of intermolecular interactions. *Phys. Chem. Chem. Phys.*, 18:28198, 2016.
- [42] Li W., Peng Q., Ma H., Wen J., Ma J., Peteanu L. A., and Shuai Z. Theoretical Investigations on the Roles of Intramolecular Structure Distortion versus Irregular Intermolecular Packing in Optical Spectra of 6T Nanoparticles. *Chem. Mater.*, 29:2513, 2017.
- [43] Le Dantec R., Mugnier Y., Djanta G., Bonacina L., Extermann J., Badie L., Joulaud C., Germann M., Rytz D., Wolf J-P, and Galez C. Ensemble and Individual Characterization of the Nonlinear Optical Properties of ZnO and BaTiO₃ Nanocrystals. *J. Phys. Chem. C*, 115:15140, 2011.

- [44] Quinet O., Champagne B., and Kirtman B. Zero-point vibrational averaging correction for second harmonic generation in para-nitroaniline. *J. Mol. Struct. (THEOCHEM)*, 633:199, 2003.

Conclusions and perspectives

In the present thesis, different computational approaches have been implemented for the investigation of the NLO properties of different organic systems, ranging from isolated molecules to nanoparticles composed of several hundreds of chromophores. As discussed in Chapters 3 and 4, these computational approaches provide insights on the relationships linking the chemical structure of the chromophores to their optical properties, as well as, in the case of nanoparticles, on the role of the supramolecular organization, of the geometrical fluctuations and of the electronic interactions existing between the molecular units.

More specifically, Chapter 3 reports a comprehensive investigation of the second-order NLO responses of a series of recently designed dipolar merocyanines. First hyperpolarizabilities calculated using the 2006 Minnesota family of hybrids differing by the incorporated amount of Hartree-Fock exchange (%HFX), as well as using the LC-BLYP, ω B97X-D and CAM-B3LYP long-range corrected XCFs are compared to *ab initio* HF and MP2 results, as well as to experimental data obtained from HRS measurements. The impact of the nature of D and A groups, of the size of the π -conjugated linker, of the choice of the XCFs, as well as of frequency-dispersion effects, has been evidenced. The donor group strongly impacts the merocyanines behavior, as shown by the difference in the evolution of the static limit of the HRS hyperpolarizability (β_{HRS}^{∞}) with system size between series including a dimethylaminophenyl and those including a dimethylaminothiophenyl. This behavior has been directly ascribed to the difference in the evolution of the bond length alternation. β_{HRS}^{∞} has also been shown to increase with the length of the polyenic bridge within the four series of merocyanines. Moreover, we evidenced that the NLO response of shorter derivatives hardly depends on %HFX, while it has a strong impact for the larger ones, since the latter are more affected by conjugation effects. Regarding the optimization of the RS parameters, in most cases, β_{HRS} values computed using LC-BLYP and ω B97X-D with optimally-tuned RS parameters are closer to MP2 results than those obtained using default ω values. Contrary to what was found with LC-BLYP and ω B97X-D, optimizing the RS parameter in CAM-B3LYP increases the ω values and thus the amount of exact HF exchange in the XCF, which reduces the agreement with MP2

reference results. Interestingly, M06-2X functional has shown to provide β_{HRS} values in close agreement with optimally tuned range-separated functionals, which indicates that a percentage of nearly 50% between DFT and HF exchange is the adequate balance for computing the NLO properties of these highly dipolar conjugated push-pull chromophores. This study also illustrated the difficulty to compare the calculated dynamic first hyperpolarizabilities to the experimental data measured in resonance conditions. Indeed, none of the DFT XCFs considered in this study satisfactorily reproduces the frequency resonance enhancement of the β_{HRS} responses.

In Chapter 4, we investigated the NLO responses of nanoparticles based on organic dipolar chromophores by means of an original cost-effective modelling strategy that combines molecular dynamics simulations with a recently developed simplified Time-Dependent DFT method (sTD-DFT). The MD simulations confirmed the spontaneous formation of amorphous nanoparticles in water solution observed experimentally. It also evidenced the onset of polar π -stacked domains at the water interface, and that the soft nature of the nanoparticles allows for rather large shape variations, which are reflected in large fluctuations in time of their second-order NLO responses. The sequential coupling of MD simulations with sTD-DFT calculations allowed us to characterize for the first time the second-harmonic scattering (SHS) responses of realistic nanoparticles at a full quantum level, while accounting for their thermally-induced structural fluctuations. Importantly, the high impact of mutual polarization effects and intermolecular couplings on the NLO responses was evidenced. In particular, we demonstrated that intermolecular interactions are at the origin of the emergence of low-lying excited states entering into resonance with the second harmonic light, which are responsible for the experimentally observed enhancement of the SHS signal upon aggregation and for the appearance of a red shifted tail in the linear absorption spectrum. The proposed computational methodology and its challenging application constitute a significant step towards the accurate simulation of the NLO responses of realistic supramolecular assemblies, and should be helpful for providing rational guidelines for the synthesis of new systems with targeted NLO properties. However, it also revealed some limitations, mainly related to the timescale and size of the objects that can be investigated, to numerical instabilities due to resonance effects, as well as to the probable underestimate of the magnitude of local electric fields since the first solvation shell was not explicitly taken into account in the sTD-DFT calculations.

As a whole, this thesis highlights the challenge that represents the modelling of nonlinear optical properties of extended organic systems, even at the level of the isolated molecule, and the subsequent difficulty of comparing theory and experiment. The large number of electrons in such systems prohibits using highly accurate *ab initio* methods such as coupled-cluster, so that DFT remains the only alternative for investigating their NLO properties at a reasonable computational cost, which implies a careful assessment of

the exchange-correlation functional, and most often to make compromises regarding the expected accuracy. Investigating supramolecular systems requires to reduce further the computational resources, at the cost of reducing further the accuracy of the theoretical approximations. Large and flexible molecular aggregates of interacting molecules, such as those considered in Chapter 4, constitute one of the most complicated challenges for computational chemistry. We reported here a first step towards the accurate theoretical description of such systems, though there are many rooms to improvement. The rapid progresses of computers will naturally offer new possibilities for simulating nanoparticles with more realistic size, and their evolution along longer time scales. Including explicit solvent molecules in the quantum chemical calculation of the NLO responses, at least the first solvation shell at the nanoparticle interface, is also one of the prerequisites to enable reliable comparisons with experiments. Looking at the methods themselves, simplified schemes such as sTD-DFT proved to be highly promising for these purposes, and their use should be extended to the investigation of other systems, of various size and composition. As noticed in Chapter 4, further development of the sTD-DFT scheme, such as for instance the implementation of damped response functions, would also be of great interest in order to remove the effects of disproportionate resonances. In another spirit but still with the aim of reducing the computational needs, the development of parameterized models on the basis of natural response orbitals represents an appealing alternative.

Supporting information of Chapter 3

A.1 Molecular geometries

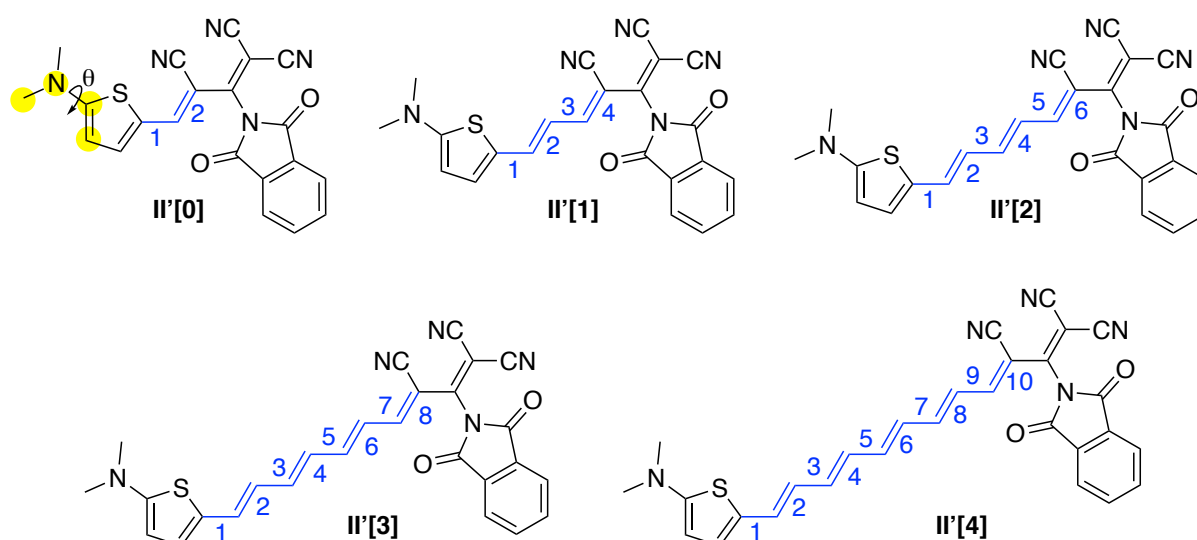


Figure A.1 – Molecular structures of the **II'[n]** series and numbering of the bonds of the conjugated segments (in blue) considered for the calculation of the BLA.

Table A.1 – Bond length alternation (in Å) calculated along the polyenic bridge (see Figure A.1) of the four series of derivatives at the IEFPCM:M06-2X/6-311G(d) level in chloroform.

n	I[n]	I'[n]	II[n]	II'[n]
0	0.066	0.024	0.052	0.002
1	0.063	0.035	0.049	0.008
2	0.066	0.048	0.054	0.020
3	0.070	0.059	0.059	0.038
4	0.074	0.067	0.064	0.054

Table A.2 – Dihedral angle $\Theta_{(C-C-N-C)}$ (in degrees) characterizing the pyramidalization of the NMe_2 group (see Figure A.1), calculated at the IEFPCM:M06-2X/6-311G(d) level in chloroform for the four series of derivatives.

n	I[n]	I'[n]	II[n]	II'[n]
0	0.5	2.1	-0.2	-1.3
1	-0.2	5.5	-0.2	0.0
2	-0.2	9.3	0.2	4.5
3	-0.3	11.6	0.6	8.8
4	0.0	12.4	2.2	11.5

A.2 Optimal range separation parameters

Discussion on the optimal range separation parameters obtained using NSC and SC tuning schemes

As reported in Table A.3a, whatever the XCF used, self-consistent (SC) and non-self-consistent (NSC) optimization schemes provide very close optimal ω values. At the LC-BLYP and $\omega\text{B97X-D}$ levels, ω_{opt} values obtained self-consistently deviate by -0.036 and -0.018 bohr $^{-1}$, respectively, from values calculated using the NSC scheme, with very weak dependence on the molecular structure. Larger average deviations between the two sets of values ($+0.069$ bohr $^{-1}$) are obtained when using CAM-B3LYP, with a larger dependence on the molecular structure. In particular, the differences between ω_{opt}^{NSC} and ω_{opt}^{SC} are larger in the **I[n]** and **I'[n]** series, and decrease with increasing chain length in the four families of molecules.

The differences between ω_{opt}^{NSC} and ω_{opt}^{SC} values translate into differences in the optical properties of the compounds. $S_0 \rightarrow S_1$ excitation energies computed at the LC-BLYP and $\omega\text{B97X-D}$ levels using ω_{opt}^{SC} values are globally red shifted (by 0.06 and 0.03 eV, respectively), compared to those calculated using ω_{opt}^{NSC} values (Tables A.9a and A.13a-b). Reversely, as a result of the global increase of ω_{opt} values, the self-consistent procedure provides slightly blue-shifted ($+0.02$ eV) transition energies when using CAM-B3LYP (Tables A.11a-b).

On the other hand, differences in the first hyperpolarizabilities can be more significant. Whereas they do not exceed 8% (4%) when computed with $\omega\text{B97X-D}$ (CAM-B3LYP), deviations on static β_{HRS} values can be as large as 10-15% when using LC-BLYP (see Tables A.20a-b, A.22a-b, and A.24a-b). Furthermore, dynamic β_{HRS} values calculated using LC-BLYP with the NSC and SC schemes can deviate by more than 20% (Tables A.32a-b, A.34a-b, and A.36a-b). These calculations demonstrate that the accuracy of the non-self-consistent ω -tuning scheme with respect to the self-consistent one depends on the choice of the XCF, as well as on the chemical nature of the investigated molecules. Nevertheless, for a given functional, calculations using ω_{opt}^{NSC} and ω_{opt}^{SC} provide similar

evolution of β_{HRS} values with increasing chain length (see Figure A.7).

Table A.3a – Optimized range separation parameters (ω , bohr⁻¹), calculated for the different LRC hybrid functionals, using the non-self-consistent (NSC) and self-consistent (SC) tuning procedures.

	LC-BLYP (NSC)	LC-BLYP (SC)	CAM-B3LYP (NSC)	CAM-B3LYP (SC)	ω B97X-D (NCS)	ω B97X-D (SC)
I[0]	0.236	0.200	0.792	0.950	0.165	0.153
I[1]	0.227	0.191	0.663	0.792	0.159	0.145
I[2]	0.221	0.183	0.593	0.696	0.154	0.137
I[3]	0.215	0.176	0.545	0.632	0.150	0.131
I[4]	0.211	0.170	0.512	0.588	0.146	0.126
I´[0]	0.216	0.199	0.578	0.936	0.152	0.152
I´[1]	0.210	0.188	0.512	0.681	0.147	0.141
I´[2]	0.206	0.179	0.472	0.588	0.143	0.134
I´[3]	0.203	0.173	0.445	0.545	0.140	0.128
I´[4]	0.201	0.168	0.427	0.521	0.138	0.123
II[0]	0.239	0.183	0.731	0.650	0.164	0.137
II[1]	0.225	0.175	0.590	0.572	0.156	0.130
II[2]	0.216	0.169	0.530	0.523	0.150	0.124
II[3]	0.211	0.162	0.497	0.489	0.146	0.119
II[4]	0.207	0.158	0.476	0.467	0.143	0.115
II´[0]	0.214	0.180	0.539	0.591	0.150	0.135
II´[1]	0.206	0.171	0.461	0.487	0.143	0.126
II´[2]	0.200	0.164	0.418	0.431	0.138	0.118
II´[3]	0.197	0.159	0.400	0.413	0.135	0.114
II´[4]	0.196	0.155	0.396	0.414	0.134	0.112

Table A.3b – Range separation parameters (ω , bohr⁻¹) optimized for LC-BLYP in gas phase and in the presence of chloroform (chl).

	LC-BLYP (NSC, gas)	LC-BLYP (SC, gas)	LC-BLYP (NSC, chl)	LC-BLYP (SC, chl)
I[0]	0.236	0.200	0.076	0.050
I[1]	0.227	0.191	0.075	0.050
I[2]	0.221	0.183	0.075	0.050
I[3]	0.215	0.176	0.177	0.176
I[4]	0.211	0.170	0.075	0.050
I´[0]	0.216	0.199	0.071	0.050
I´[1]	0.210	0.188	0.071	0.050
I´[2]	0.206	0.179	0.072	0.050
I´[3]	0.203	0.173	0.073	0.050
I´[4]	0.201	0.168	0.075	0.050
II[0]	0.239	0.183	0.079	0.050
II[1]	0.225	0.175	0.075	0.050
II[2]	0.216	0.169	0.073	0.050
II[3]	0.211	0.162	0.072	0.050
II[4]	0.207	0.158	0.073	0.050
II´[0]	0.214	0.180	0.071	0.050
II´[1]	0.206	0.171	0.070	0.050
II´[2]	0.200	0.164	0.070	0.050
II´[3]	0.197	0.159	0.071	0.050
II´[4]	0.196	0.155	0.072	0.050

A.3 Absorption optical properties

Transition wavelengths (λ_{ge} , eV), transition energies (ΔE_{ge} , eV), oscillator strengths (f_{ge}) and transition dipole moments (μ_{ge} , D), as well as charge transferred (Δq_{ge} , |e|), charge transfer distance (Δr_{ge} , Å), and dipole moment variation ($\Delta \mu_{ge}$, D) associated to the first dipole-allowed transition ($S_g \rightarrow S_e \equiv S_0 \rightarrow S_1$ otherwise specified) of the investigated merocyanines. The last column reports the frequency dispersion factors calculated using the two-state approximation.

Table A.4 – IEFPCM:M06L/6-311+G(d) calculations.

	λ_{ge}	ΔE_{ge}	f_{ge}	μ_{ge}	Δq_{ge}	Δr_{ge}	$\Delta \mu_{ge}$	$F^{TSA}(\omega)$
I[0]	457	2.710	1.02	15.43	0.42	2.28	4.61	1.38
I[1]	533	2.327	1.43	25.03	0.44	3.21	6.81	1.58
I[2]	608	2.038	1.72	34.35	0.48	4.14	9.49	1.88
I[3]	685	1.811	1.91	43.06	0.52	5.07	12.57	2.37
I[4]	762	1.627	2.02	50.75	0.56	6.02	16.17	3.29
I'[0]	467	2.653	0.92	14.20	0.36	0.65	1.12	1.40
I'[1]	534	2.321	1.51	26.49	0.35	1.09	1.82	1.58
I'[2]	606	2.048	1.95	38.87	0.37	2.53	4.47	1.86
I'[3]	682	1.818	2.19	49.24	0.41	3.80	7.46	2.35
I'[4]	762	1.627	2.28	57.25	0.46	4.97	10.98	3.29
II[0] ¹	538	2.305	0.96	16.99	0.52	3.50	8.77	1.59
II[1] ¹	612	2.025	1.36	27.40	0.49	4.06	9.57	1.90
II[2]	693	1.788	1.56	35.68	0.52	5.02	12.51	2.44
II[3]	774	1.602	1.93	49.07	0.50	5.29	12.71	3.51
II[4]	861	1.439	2.07	58.66	0.53	6.10	15.37	6.83
II'[0] ¹	523	2.372	1.07	18.39	0.38	2.04	3.71	1.55
II'[1] ¹	593	2.091	1.64	31.95	0.34	1.83	3.01	1.80
II'[2] ¹	667	1.860	2.11	46.29	0.35	2.53	4.19	2.23
II'[3]	753	1.647	1.96	48.49	0.48	5.30	12.16	3.14
II'[4]	847	1.463	2.41	67.10	0.43	4.83	9.90	5.92

¹ $S_g \rightarrow S_e \equiv S_0 \rightarrow S_2$

Transition wavelengths (λ_{ge} , eV), transition energies (ΔE_{ge} , eV), oscillator strengths (f_{ge}) and transition dipole moments (μ_{ge} , D), as well as charge transferred (Δq_{ge} , |e|), charge transfer distance (Δr_{ge} , Å), and dipole moment variation ($\Delta \mu_{ge}$, D) associated to the first dipole-allowed transition ($S_g \rightarrow S_e \equiv S_0 \rightarrow S_1$ otherwise specified) of the investigated merocyanines. The last column reports the frequency dispersion factors calculated using the two-state approximation.

Table A.5 – IEFPCM:M06/6-311+G(d) calculations.

	λ_{ge}	ΔE_{ge}	f_{ge}	μ_{ge}	Δq_{ge}	Δr_{ge}	$\Delta \mu_{ge}$	$F^{TSA}(\omega)$
I[0]	431	2.877	1.10	15.65	0.51	2.24	5.44	1.32
I[1]	498	2.491	1.53	25.07	0.54	3.03	7.81	1.47
I[2]	557	2.227	1.90	34.86	0.58	3.90	10.88	1.66
I[3]	609	2.036	2.22	44.55	0.62	4.79	14.34	1.88
I[4]	654	1.896	2.49	53.63	0.67	5.66	18.17	2.14
I'[0]	456	2.717	1.01	15.12	0.42	0.94	1.92	1.38
I'[1]	527	2.353	1.52	26.42	0.43	1.57	3.27	1.56
I'[2]	591	2.099	1.96	38.10	0.47	2.74	6.25	1.79
I'[3]	646	1.921	2.29	48.70	0.54	3.97	10.24	2.08
I'[4]	690	1.796	2.54	57.70	0.61	5.13	14.97	2.42
II[0]	497	2.493	1.12	18.29	0.57	2.85	7.77	1.47
II[1]	569	2.179	1.57	29.47	0.56	3.29	8.80	1.70
II[2]	633	1.959	1.96	40.84	0.58	4.00	11.22	2.01
II[3]	689	1.799	2.28	51.84	0.62	4.83	14.45	2.41
II[4]	741	1.673	2.54	62.04	0.67	5.73	18.42	2.97
II'[0]	513	2.415	1.11	18.72	0.43	1.26	2.60	1.52
II'[1]	590	2.101	1.64	31.85	0.42	1.21	2.45	1.79
II'[2]	664	1.868	2.13	46.58	0.44	1.88	3.95	2.21
II'[3]	729	1.700	2.50	60.02	0.49	3.31	7.86	2.82
II'[4]	783	1.583	2.70	69.68	0.58	4.85	13.54	3.69

Transition wavelengths (λ_{ge} , eV), transition energies (ΔE_{ge} , eV), oscillator strengths (f_{ge}) and transition dipole moments (μ_{ge} , D), as well as charge transferred (Δq_{ge} , |e|), charge transfer distance (Δr_{ge} , Å), and dipole moment variation ($\Delta \mu_{ge}$, D) associated to the first dipole-allowed transition ($S_g \rightarrow S_e \equiv S_0 \rightarrow S_1$ otherwise specified) of the investigated merocyanines. The last column reports the frequency dispersion factors calculated using the two-state approximation.

Table A.6 – IEFPCM:M06-2X/6-311+G(d) calculations.

	λ_{ge}	ΔE_{ge}	f_{ge}	μ_{ge}	Δq_{ge}	Δr_{ge}	$\Delta \mu_{ge}$	$F^{TSA}(\omega)$
I[0]	406	3.050	1.19	15.87	0.53	2.64	6.68	1.28
I[1]	465	2.665	1.62	24.81	0.57	3.47	9.55	1.40
I[2]	510	2.430	2.03	34.05	0.62	4.35	12.96	1.51
I[3]	544	2.278	2.40	43.08	0.66	5.14	16.22	1.61
I[4]	568	2.182	2.76	51.55	0.68	5.86	19.25	1.70
I'[0]	447	2.773	1.06	15.64	0.42	1.48	3.00	1.36
I'[1]	518	2.394	1.57	26.69	0.46	2.32	5.08	1.53
I'[2]	569	2.178	2.00	37.57	0.54	3.64	9.35	1.71
I'[3]	599	2.070	2.38	46.86	0.62	4.80	14.22	1.83
I'[4]	612	2.027	2.72	54.69	0.68	5.75	18.65	1.89
II[0]	466	2.660	1.22	18.70	0.58	3.01	8.32	1.40
II[1]	533	2.325	1.67	29.39	0.59	3.62	10.26	1.58
II[2]	584	2.122	2.08	40.08	0.63	4.43	13.44	1.77
II[3]	621	1.996	2.45	50.12	0.67	5.22	16.88	1.94
II[4]	647	1.915	2.78	59.17	0.71	5.97	20.34	2.10
II'[0]	505	2.456	1.16	19.25	0.43	1.36	2.78	1.49
II'[1]	588	2.109	1.69	32.68	0.43	1.50	3.10	1.78
II'[2]	661	1.875	2.18	47.53	0.47	2.56	5.80	2.19
II'[3]	705	1.759	2.57	59.65	0.58	4.31	11.91	2.55
II'[4]	713	1.740	2.85	66.83	0.68	5.70	18.72	2.63

Transition wavelengths (λ_{ge} , eV), transition energies (ΔE_{ge} , eV), oscillator strengths (f_{ge}) and transition dipole moments (μ_{ge} , D), as well as charge transferred (Δq_{ge} , |e|), charge transfer distance (Δr_{ge} , Å), and dipole moment variation ($\Delta \mu_{ge}$, D) associated to the first dipole-allowed transition ($S_g \rightarrow S_e \equiv S_0 \rightarrow S_1$ otherwise specified) of the investigated merocyanines. The last column reports the frequency dispersion factors calculated using the two-state approximation.

Table A.7 – IEFPCM:M06-HF/6-311+G(d) calculations.

	λ_{ge}	ΔE_{ge}	f_{ge}	μ_{ge}	Δq_{ge}	Δr_{ge}	$\Delta \mu_{ge}$	$F^{TSA}(\omega)$
I[0]	385	3.217	1.22	15.49	0.59	2.68	7.58	1.25
I[1]	433	2.861	1.64	23.45	0.65	3.46	10.72	1.33
I[2]	462	2.684	2.07	31.53	0.68	4.17	13.56	1.39
I[3]	479	2.591	2.49	39.21	0.69	4.68	15.42	1.43
I[4]	487	2.547	2.89	46.32	0.68	4.99	16.38	1.45
I'[0]	448	2.769	1.06	15.62	0.49	1.76	4.10	1.36
I'[1]	518	2.392	1.52	25.98	0.58	2.78	7.70	1.53
I'[2]	544	2.281	1.96	35.00	0.70	3.97	13.28	1.61
I'[3]	536	2.312	2.38	42.02	0.73	4.75	16.74	1.59
I'[4]	521	2.378	2.82	48.42	0.72	5.14	17.69	1.54
II[0]	440	2.817	1.25	18.10	0.64	2.94	9.06	1.34
II[1]	499	2.486	1.68	27.58	0.69	3.61	12.02	1.48
II[2]	532	2.331	2.08	36.50	0.74	4.29	15.19	1.57
II[3]	548	2.264	2.46	44.33	0.76	4.78	17.44	1.63
II[4]	553	2.241	2.80	51.01	0.77	5.11	18.77	1.65
II'[0]	511	2.429	1.15	19.40	0.48	1.35	3.14	1.51
II'[1]	608	2.041	1.66	33.20	0.53	1.75	4.41	1.87
II'[2]	679	1.825	2.13	47.55	0.66	3.32	10.52	2.33
II'[3]	666	1.862	2.51	55.05	0.82	4.79	18.90	2.22
II'[4]	613	2.024	2.86	57.73	0.83	5.38	21.34	1.90

Transition wavelengths (λ_{ge} , eV), transition energies (ΔE_{ge} , eV), oscillator strengths (f_{ge}) and transition dipole moments (μ_{ge} , D), as well as charge transferred (Δq_{ge} , |e|), charge transfer distance (Δr_{ge} , Å), and dipole moment variation ($\Delta \mu_{ge}$, D) associated to the first dipole-allowed transition ($S_g \rightarrow S_e \equiv S_0 \rightarrow S_1$ otherwise specified) of the investigated merocyanines. The last column reports the frequency dispersion factors calculated using the two-state approximation.

Table A.8 – IEFPCM:LC-BLYP(ω_{std})/6-311+G(d) calculations.

	λ_{ge}	ΔE_{ge}	f_{ge}	μ_{ge}	Δq_{ge}	Δr_{ge}	$\Delta \mu_{ge}$	$F^{TSA}(\omega)$
I[0]	376	3.297	1.24	15.35	0.62	2.37	7.11	1.23
I[1]	423	2.931	1.69	23.48	0.68	3.14	10.23	1.31
I[2]	452	2.746	2.14	31.76	0.71	3.81	13.01	1.37
I[3]	469	2.646	2.57	39.67	0.72	4.30	14.87	1.40
I[4]	477	2.598	2.99	47.02	0.72	4.58	15.78	1.42
I'[0]	432	2.870	1.10	15.58	0.53	1.44	3.64	1.33
I'[1]	499	2.485	1.58	26.01	0.62	2.43	7.16	1.48
I'[2]	525	2.360	2.04	35.23	0.72	3.60	12.51	1.55
I'[3]	522	2.377	2.48	42.55	0.76	4.36	15.90	1.54
I'[4]	509	2.434	2.94	49.23	0.74	4.72	16.81	1.51
II[0]	427	2.905	1.29	18.06	0.68	2.61	8.50	1.32
II[1]	484	2.563	1.74	27.64	0.73	3.25	11.37	1.44
II[2]	517	2.400	2.16	36.75	0.77	3.89	14.43	1.53
II[3]	533	2.327	2.55	44.81	0.79	4.36	16.59	1.58
II[4]	539	2.298	2.91	51.76	0.80	4.69	17.94	1.60
II'[0]	490	2.533	1.20	19.40	0.55	1.12	2.92	1.45
II'[1]	580	2.136	1.73	33.10	0.59	1.49	4.27	1.75
II'[2]	647	1.915	2.22	47.27	0.71	2.90	9.93	2.10
II'[3]	639	1.940	2.62	55.10	0.85	4.32	17.65	2.04
II'[4]	594	2.088	2.98	58.35	0.85	4.92	20.11	1.81

Transition wavelengths (λ_{ge} , eV), transition energies (ΔE_{ge} , eV), oscillator strengths (f_{ge}) and transition dipole moments (μ_{ge} , D), as well as charge transferred (Δq_{ge} , |e|), charge transfer distance (Δr_{ge} , Å), and dipole moment variation ($\Delta \mu_{ge}$, D) associated to the first dipole-allowed transition ($S_g \rightarrow S_e \equiv S_0 \rightarrow S_1$ otherwise specified) of the investigated merocyanines. The last column reports the frequency dispersion factors calculated using the two-state approximation.

Table A.9a – IEFPCM:LC-BLYP(ω_{opt})/6-311+G(d) calculations with ω_{opt} values calculated using the NSC procedure.

	λ_{ge}	ΔE_{ge}	f_{ge}	μ_{ge}	Δq_{ge}	Δr_{ge}	$\Delta \mu_{ge}$	$F^{TSA}(\omega)$
I[0]	415	2.990	1.15	15.66	0.52	2.61	6.45	1.29
I[1]	473	2.620	1.59	24.73	0.56	3.44	9.25	1.41
I[2]	517	2.400	2.02	34.28	0.60	4.28	12.31	1.53
I[3]	549	2.257	2.42	43.83	0.62	5.03	14.99	1.63
I[4]	572	2.167	2.81	52.99	0.63	5.66	17.18	1.72
I'[0]	457	2.714	1.03	15.50	0.42	1.52	3.07	1.38
I'[1]	530	2.341	1.52	26.57	0.46	2.33	5.11	1.57
I'[2]	581	2.135	1.97	37.70	0.53	3.62	9.18	1.75
I'[3]	609	2.037	2.38	47.60	0.60	4.76	13.62	1.88
I'[4]	620	2.001	2.76	56.38	0.64	5.64	17.21	1.93
II[0]	481	2.576	1.18	18.66	0.55	3.00	7.93	1.43
II[1]	549	2.259	1.64	29.60	0.57	3.61	9.83	1.63
II[2]	599	2.071	2.07	40.72	0.61	4.39	12.75	1.83
II[3]	634	1.955	2.46	51.37	0.64	5.13	15.71	2.02
II[4]	659	1.882	2.82	61.21	0.66	5.82	18.48	2.17
II'[0]	521	2.381	1.11	19.08	0.42	1.39	2.79	1.54
II'[1]	605	2.050	1.64	32.57	0.42	1.47	3.00	1.86
II'[2]	679	1.825	2.13	47.66	0.46	2.48	5.52	2.33
II'[3]	724	1.713	2.54	60.64	0.56	4.25	11.35	2.75
II'[4]	730	1.699	2.88	69.21	0.65	5.64	17.57	2.83

Transition wavelengths (λ_{ge} , eV), transition energies (ΔE_{ge} , eV), oscillator strengths (f_{ge}) and transition dipole moments (μ_{ge} , D), as well as charge transferred (Δq_{ge} , |e|), charge transfer distance (Δr_{ge} , Å), and dipole moment variation ($\Delta \mu_{ge}$, D) associated to the first dipole-allowed transition ($S_g \rightarrow S_e \equiv S_0 \rightarrow S_1$ otherwise specified) of the investigated merocyanines. The last column reports the frequency dispersion factors calculated using the two-state approximation.

Table A.9b – IEFPCM:LC-BLYP(ω_{opt})/6-311+G(d) calculations with ω_{opt} values calculated using the SC procedure.

	λ_{ge}	ΔE_{ge}	f_{ge}	μ_{ge}	Δq_{ge}	Δr_{ge}	$\Delta \mu_{ge}$	$F^{TSA}(\omega)$
I[0]	425	2.917	1.12	15.69	0.49	2.60	6.11	1.31
I[1]	486	2.550	1.56	25.03	0.53	3.45	8.76	1.45
I[2]	535	2.318	1.99	34.99	0.57	4.34	11.79	1.58
I[3]	574	2.159	2.39	45.14	0.59	5.16	14.63	1.73
I[4]	605	2.049	2.77	55.10	0.61	5.90	17.20	1.86
I'[0]	463	2.680	1.01	15.41	0.40	1.45	2.76	1.39
I'[1]	535	2.316	1.51	26.64	0.42	2.20	4.45	1.58
I'[2]	592	2.095	1.96	38.23	0.48	3.49	8.06	1.80
I'[3]	630	1.969	2.36	48.91	0.55	4.71	12.34	1.99
I'[4]	652	1.901	2.73	58.57	0.59	5.73	16.31	2.13
II[0]	494	2.508	1.15	18.74	0.53	3.05	7.70	1.47
II[1]	564	2.198	1.62	30.04	0.53	3.64	9.27	1.69
II[2]	620	2.000	2.04	41.74	0.56	4.44	11.97	1.94
II[3]	664	1.866	2.44	53.33	0.59	5.26	14.93	2.21
II[4]	700	1.771	2.80	64.46	0.62	6.08	18.03	2.51
II'[0]	526	2.356	1.09	18.96	0.40	1.42	2.69	1.56
II'[1]	608	2.039	1.62	32.41	0.39	1.42	2.68	1.88
II'[2]	683	1.814	2.12	47.63	0.42	2.31	4.63	2.36
II'[3]	738	1.679	2.53	61.60	0.49	4.04	9.49	2.94
II'[4]	764	1.622	2.86	72.03	0.58	5.61	15.53	3.33

Transition wavelengths (λ_{ge} , eV), transition energies (ΔE_{ge} , eV), oscillator strengths (f_{ge}) and transition dipole moments (μ_{ge} , D), as well as charge transferred (Δq_{ge} , |e|), charge transfer distance (Δr_{ge} , Å), and dipole moment variation ($\Delta \mu_{ge}$, D) associated to the first dipole-allowed transition ($S_g \rightarrow S_e \equiv S_0 \rightarrow S_1$ otherwise specified) of the investigated merocyanines. The last column reports the frequency dispersion factors calculated using the two-state approximation.

Table A.10 – IEFPCM:CAM-B3LYP(ω_{std})/6-311+G(d) calculations.

	λ_{ge}	ΔE_{ge}	f_{ge}	μ_{ge}	Δq_{ge}	Δr_{ge}	$\Delta \mu_{ge}$	$F^{TSA}(\omega)$
I[0]	402	3.082	1.19	15.78	0.55	2.43	6.37	1.27
I[1]	459	2.700	1.64	24.78	0.59	3.21	9.09	1.38
I[2]	502	2.467	2.07	34.18	0.63	4.02	12.24	1.49
I[3]	535	2.318	2.47	43.45	0.66	4.77	15.21	1.58
I[4]	557	2.224	2.85	52.22	0.68	5.41	17.75	1.66
I'[0]	442	2.806	1.07	15.59	0.45	1.28	2.75	1.35
I'[1]	511	2.424	1.58	26.61	0.49	2.06	4.80	1.51
I'[2]	561	2.209	2.03	37.56	0.56	3.32	8.95	1.67
I'[3]	588	2.107	2.43	47.07	0.64	4.44	13.58	1.78
I'[4]	599	2.070	2.80	55.27	0.68	5.32	17.46	1.83
II[0]	460	2.695	1.23	18.61	0.60	2.78	7.94	1.38
II[1]	525	2.361	1.70	29.30	0.61	3.33	9.84	1.55
II[2]	574	2.161	2.12	40.06	0.65	4.07	12.77	1.72
II[3]	608	2.038	2.51	50.24	0.69	4.78	15.86	1.88
II[4]	633	1.960	2.86	59.53	0.72	5.49	18.98	2.01
II'[0]	498	2.489	1.17	19.17	0.46	1.17	2.58	1.48
II'[1]	580	2.139	1.71	32.53	0.47	1.28	2.89	1.75
II'[2]	651	1.904	2.21	47.32	0.52	2.26	5.60	2.12
II'[3]	692	1.792	2.61	59.49	0.62	3.93	11.64	2.43
II'[4]	695	1.783	2.93	66.95	0.71	5.27	18.01	2.46

Transition wavelengths (λ_{ge} , eV), transition energies (ΔE_{ge} , eV), oscillator strengths (f_{ge}) and transition dipole moments (μ_{ge} , D), as well as charge transferred (Δq_{ge} , |e|), charge transfer distance (Δr_{ge} , Å), and dipole moment variation ($\Delta \mu_{ge}$, D) associated to the first dipole-allowed transition ($S_g \rightarrow S_e \equiv S_0 \rightarrow S_1$ otherwise specified) of the investigated merocyanines. The last column reports the frequency dispersion factors calculated using the two-state approximation.

Table A.11a – IEFPCM:CAM-B3LYP(ω_{opt})/6-311+G(d) calculations with ω_{opt} values calculated using the NSC procedure.

	λ_{ge}	ΔE_{ge}	f_{ge}	μ_{ge}	Δq_{ge}	Δr_{ge}	$\Delta \mu_{ge}$	$F^{TSA}(\omega)$
I[0]	379	3.269	1.25	15.57	0.60	2.17	6.28	1.24
I[1]	437	2.838	1.70	24.40	0.64	2.96	9.04	1.34
I[2]	480	2.583	2.13	33.63	0.67	3.77	12.13	1.43
I[3]	512	2.423	2.53	42.68	0.69	4.50	14.95	1.51
I[4]	534	2.323	2.92	51.24	0.71	5.11	17.31	1.58
I'[0]	424	2.925	1.11	15.52	0.50	1.12	2.71	1.31
I'[1]	497	2.494	1.61	26.42	0.54	1.97	5.05	1.47
I'[2]	546	2.272	2.06	37.10	0.61	3.23	9.45	1.62
I'[3]	569	2.177	2.47	46.24	0.68	4.31	14.02	1.71
I'[4]	577	2.149	2.85	54.18	0.71	5.14	17.54	1.74
II[0]	441	2.814	1.27	18.46	0.64	2.59	7.93	1.34
II[1]	508	2.441	1.73	28.94	0.65	3.19	10.00	1.50
II[2]	557	2.225	2.15	39.49	0.69	3.93	12.99	1.66
II[3]	592	2.095	2.54	49.43	0.72	4.65	16.04	1.80
II[4]	616	2.014	2.89	58.49	0.74	5.31	18.93	1.91
II'[0]	486	2.552	1.20	19.22	0.50	1.03	2.48	1.44
II'[1]	572	2.166	1.73	32.60	0.50	1.22	2.94	1.72
II'[2]	646	1.918	2.22	47.34	0.54	2.26	5.90	2.09
II'[3]	684	1.812	2.63	59.17	0.65	3.94	12.23	2.36
II'[4]	683	1.815	2.94	66.14	0.74	5.21	18.43	2.36

Transition wavelengths (λ_{ge} , eV), transition energies (ΔE_{ge} , eV), oscillator strengths (f_{ge}) and transition dipole moments (μ_{ge} , D), as well as charge transferred (Δq_{ge} , |e|), charge transfer distance (Δr_{ge} , Å), and dipole moment variation ($\Delta \mu_{ge}$, D) associated to the first dipole-allowed transition ($S_g \rightarrow S_e \equiv S_0 \rightarrow S_1$ otherwise specified) of the investigated merocyanines. The last column reports the frequency dispersion factors calculated using the two-state approximation.

Table A.11b – IEFPCM:CAM-B3LYP(ω_{opt})/6-311+G(d) calculations with ω_{opt} values calculated using the SC procedure.

	λ_{ge}	ΔE_{ge}	f_{ge}	μ_{ge}	Δq_{ge}	Δr_{ge}	$\Delta \mu_{ge}$	$F^{TSA}(\omega)$
I[0]	376	3.296	1.25	15.51	0.61	2.12	6.18	1.23
I[1]	433	2.867	1.71	24.33	0.64	2.87	8.87	1.33
I[2]	475	2.609	2.14	33.56	0.68	3.67	11.91	1.42
I[3]	507	2.446	2.55	42.61	0.70	4.39	14.69	1.50
I[4]	528	2.346	2.94	51.14	0.71	5.00	17.02	1.56
I'[0]	419	2.958	1.12	15.45	0.52	1.06	2.61	1.30
I'[1]	493	2.513	1.62	26.34	0.54	1.91	4.99	1.46
I'[2]	542	2.286	2.07	37.01	0.62	3.18	9.42	1.61
I'[3]	566	2.192	2.48	46.12	0.68	4.26	13.98	1.69
I'[4]	573	2.165	2.87	54.03	0.72	5.08	17.43	1.72
II[0]	437	2.837	1.28	18.41	0.64	2.55	7.87	1.34
II[1]	504	2.461	1.74	28.85	0.66	3.13	9.96	1.49
II[2]	553	2.243	2.16	39.35	0.70	3.88	12.94	1.64
II[3]	587	2.113	2.55	49.23	0.73	4.59	15.98	1.78
II[4]	610	2.032	2.90	58.21	0.75	5.25	18.83	1.89
II'[0]	483	2.566	1.21	19.19	0.51	1.01	2.45	1.44
II'[1]	571	2.172	1.73	32.58	0.51	1.21	2.94	1.71
II'[2]	645	1.921	2.23	47.32	0.55	2.26	5.92	2.08
II'[3]	683	1.815	2.63	59.10	0.65	3.94	12.29	2.36
II'[4]	680	1.823	2.95	65.96	0.74	5.20	18.49	2.33

Transition wavelengths (λ_{ge} , eV), transition energies (ΔE_{ge} , eV), oscillator strengths (f_{ge}) and transition dipole moments (μ_{ge} , D), as well as charge transferred (Δq_{ge} , |e|), charge transfer distance (Δr_{ge} , Å), and dipole moment variation ($\Delta \mu_{ge}$, D) associated to the first dipole-allowed transition ($S_g \rightarrow S_e \equiv S_0 \rightarrow S_1$ otherwise specified) of the investigated merocyanines. The last column reports the frequency dispersion factors calculated using the two-state approximation.

Table A.12 – IEFPCM: ω B97X-D(ω_{std})/6-311+G(d) calculations.

	λ_{ge}	ΔE_{ge}	f_{ge}	μ_{ge}	Δq_{ge}	Δr_{ge}	$\Delta \mu_{ge}$	$F^{TSA}(\omega)$
I[0]	398	3.111	1.19	15.61	0.55	2.41	6.34	1.27
I[1]	452	2.742	1.65	24.52	0.60	3.18	9.07	1.37
I[2]	491	2.524	2.09	33.84	0.63	3.94	11.99	1.46
I[3]	519	2.388	2.52	43.04	0.65	4.60	14.46	1.53
I[4]	538	2.307	2.93	51.77	0.66	5.12	16.30	1.59
I'[0]	441	2.813	1.07	15.51	0.45	1.33	2.88	1.34
I'[1]	509	2.435	1.58	26.46	0.50	2.12	5.09	1.51
I'[2]	555	2.235	2.04	37.24	0.58	3.37	9.41	1.65
I'[3]	575	2.157	2.46	46.56	0.65	4.42	13.79	1.73
I'[4]	578	2.144	2.88	54.76	0.68	5.16	16.83	1.74
II[0]	454	2.729	1.23	18.44	0.60	2.76	7.92	1.37
II[1]	516	2.402	1.70	28.93	0.63	3.31	9.94	1.53
II[2]	560	2.214	2.14	39.46	0.66	4.01	12.78	1.67
II[3]	589	2.104	2.54	49.36	0.69	4.65	15.46	1.79
II[4]	608	2.040	2.92	58.38	0.71	5.20	17.76	1.87
II'[0]	497	2.492	1.17	19.10	0.47	1.21	2.71	1.47
II'[1]	579	2.140	1.70	32.49	0.49	1.35	3.15	1.75
II'[2]	650	1.907	2.21	47.22	0.55	2.39	6.26	2.11
II'[3]	681	1.820	2.63	58.86	0.66	4.05	12.78	2.34
II'[4]	671	1.848	2.98	65.78	0.73	5.19	18.20	2.26

Transition wavelengths (λ_{ge} , eV), transition energies (ΔE_{ge} , eV), oscillator strengths (f_{ge}) and transition dipole moments (μ_{ge} , D), as well as charge transferred (Δq_{ge} , |e|), charge transfer distance (Δr_{ge} , Å), and dipole moment variation ($\Delta \mu_{ge}$, D) associated to the first dipole-allowed transition ($S_g \rightarrow S_e \equiv S_0 \rightarrow S_1$ otherwise specified) of the investigated merocyanines. The last column reports the frequency dispersion factors calculated using the two-state approximation.

Table A.13a – IEFPCM: ω B97X-D(ω_{opt})/6-311+G(d) calculations with ω_{opt} values calculated using the NSC procedure.

	λ_{ge}	ΔE_{ge}	f_{ge}	μ_{ge}	Δq_{ge}	Δr_{ge}	$\Delta \mu_{ge}$	$F^{TSA}(\omega)$
I[0]	406	3.053	1.18	15.73	0.53	2.42	6.14	1.28
I[1]	464	2.673	1.63	24.91	0.57	3.21	8.77	1.39
I[2]	509	2.438	2.07	34.63	0.61	4.02	11.74	1.50
I[3]	543	2.282	2.48	44.41	0.63	4.77	14.47	1.61
I[4]	569	2.180	2.88	53.85	0.65	5.41	16.84	1.70
I'[0]	444	2.792	1.06	15.53	0.43	1.27	2.65	1.35
I'[1]	514	2.412	1.58	26.68	0.47	2.02	4.50	1.52
I'[2]	567	2.188	2.04	37.99	0.53	3.26	8.31	1.70
I'[3]	598	2.072	2.45	48.18	0.60	4.41	12.70	1.83
I'[4]	614	2.020	2.83	57.21	0.65	5.33	16.50	1.90
II[0]	468	2.651	1.21	18.67	0.57	2.83	7.76	1.40
II[1]	533	2.324	1.69	29.63	0.58	3.37	9.46	1.58
II[2]	584	2.122	2.12	40.84	0.62	4.10	12.18	1.77
II[3]	622	1.994	2.53	51.70	0.65	4.83	15.10	1.95
II[4]	650	1.908	2.89	61.91	0.68	5.54	17.99	2.11
II'[0]	502	2.468	1.15	19.10	0.44	1.22	2.57	1.49
II'[1]	582	2.129	1.69	32.47	0.44	1.28	2.73	1.76
II'[2]	655	1.894	2.20	47.45	0.48	2.17	4.99	2.14
II'[3]	702	1.766	2.62	60.58	0.56	3.84	10.41	2.52
II'[4]	715	1.734	2.96	69.57	0.66	5.26	16.57	2.66

Transition wavelengths (λ_{ge} , eV), transition energies (ΔE_{ge} , eV), oscillator strengths (f_{ge}) and transition dipole moments (μ_{ge} , D), as well as charge transferred (Δq_{ge} , |e|), charge transfer distance (Δr_{ge} , Å), and dipole moment variation ($\Delta \mu_{ge}$, D) associated to the first dipole-allowed transition ($S_g \rightarrow S_e \equiv S_0 \rightarrow S_1$ otherwise specified) of the investigated merocyanines. The last column reports the frequency dispersion factors calculated using the two-state approximation.

Table A.13b – IEFPCM: ω B97X-D(ω_{opt})/6-311+G(d) calculations with ω_{opt} values calculated using the SC procedure.

	λ_{ge}	ΔE_{ge}	f_{ge}	μ_{ge}	Δq_{ge}	Δr_{ge}	$\Delta \mu_{ge}$	$F^{TSA}(\omega)$
I[0]	409	3.033	1.17	15.76	0.52	2.43	6.07	1.28
I[1]	468	2.648	1.62	25.04	0.56	3.22	8.65	1.40
I[2]	516	2.404	2.06	34.91	0.60	4.05	11.63	1.52
I[3]	554	2.240	2.46	44.89	0.62	4.83	14.47	1.65
I[4]	583	2.127	2.85	54.60	0.64	5.54	17.08	1.76
I'[0]	445	2.784	1.06	15.53	0.43	1.25	2.57	1.35
I'[1]	516	2.405	1.58	26.74	0.45	1.97	4.30	1.52
I'[2]	570	2.174	2.04	38.23	0.51	3.21	7.92	1.71
I'[3]	607	2.043	2.44	48.69	0.58	4.39	12.24	1.87
I'[4]	628	1.975	2.81	58.04	0.63	5.38	16.26	1.98
II[0]	472	2.626	1.21	18.73	0.56	2.85	7.72	1.41
II[1]	540	2.297	1.68	29.84	0.57	3.39	9.28	1.60
II[2]	594	2.089	2.11	41.29	0.60	4.14	11.93	1.81
II[3]	636	1.951	2.51	52.51	0.63	4.91	14.92	2.02
II[4]	669	1.853	2.87	63.19	0.66	5.68	18.04	2.25
II'[0]	504	2.461	1.15	19.09	0.43	2.53	2.53	1.49
II'[1]	583	2.126	1.69	32.46	0.43	1.26	2.61	1.76
II'[2]	656	1.890	2.20	47.49	0.46	2.10	4.61	2.15
II'[3]	708	1.750	2.62	61.04	0.53	3.75	9.58	2.59
II'[4]	732	1.695	2.94	70.77	0.62	5.25	15.72	2.85

Transition wavelengths (λ_{ge} , eV), transition energies (ΔE_{ge} , eV), oscillator strengths (f_{ge}) and transition dipole moments (μ_{ge} , D), as well as charge transferred (Δq_{ge} , |e|), charge transfer distance (Δr_{ge} , Å), and dipole moment variation ($\Delta \mu_{ge}$, D) associated to the first dipole-allowed transition ($S_g \rightarrow S_e \equiv S_0 \rightarrow S_1$ otherwise specified) of the investigated merocyanines. The last column reports the frequency dispersion factors calculated using the two-state approximation.

Table A.14 – IEFPCM:HF/6-311+G(d) calculations.

	λ_{ge}	ΔE_{ge}	f_{ge}	μ_{ge}	Δq_{ge}	Δr_{ge}	$\Delta \mu_{ge}$	$F^{TSA}(\omega)$
I[0]	336	3.690	1.30	14.34	0.72	1.47	5.05	1.18
I[1]	381	3.254	1.80	22.56	0.73	1.91	6.71	1.24
I[2]	414	2.995	2.32	31.59	0.73	2.37	8.33	1.29
I[3]	437	2.837	2.83	40.68	0.73	2.74	9.58	1.34
I[4]	452	2.743	3.32	49.47	0.72	2.99	10.40	1.37
I'[0]	384	3.229	1.15	14.59	0.66	0.70	2.23	1.24
I'[1]	445	2.786	1.67	24.43	0.71	1.25	4.29	1.35
I'[2]	477	2.599	2.17	34.14	0.76	2.13	7.78	1.42
I'[3]	485	2.556	2.69	42.91	0.76	2.77	10.14	1.44
I'[4]	484	2.562	3.22	51.28	0.74	3.08	10.96	1.44
II[0]	376	3.297	1.36	16.80	0.77	1.63	6.00	1.23
II[1]	428	2.897	1.85	26.09	0.79	1.96	7.43	1.32
II[2]	463	2.678	2.34	35.71	0.80	2.37	9.10	1.39
II[3]	486	2.551	2.81	45.00	0.80	2.73	10.53	1.44
II[4]	501	2.475	3.26	53.71	0.80	3.02	11.66	1.48
II'[0]	428	2.897	1.29	18.18	0.71	0.51	1.73	1.32
II'[1]	551	2.250	1.85	30.51	0.76	0.66	2.43	1.64
II'[2]	558	2.222	2.37	43.60	0.83	1.44	5.72	1.66
II'[3]	569	2.179	2.84	53.13	0.87	2.57	10.74	1.70
II'[4]	548	2.262	3.30	59.44	0.85	3.16	12.83	1.63

A.4 Static nonlinear optical properties

Static HRS hyperpolarizabilities (β_{HRS} , in a.u. and 10^{-30} esu), depolarization ratios (DR), and relative $\beta_{HRS}[n]/\beta_{HRS}[0]$ values for the investigated merocyanines.

Table A.15 – IEFPCM:M06L/6-311+G(d) calculations.

	β_{HRS} (a.u.)	β_{HRS} (10^{-30} esu)	DR	$\beta_{HRS}[n]/\beta_{HRS}[0]$
I[0]	7800	67	4.5	1.00
I[1]	19261	166	4.7	2.47
I[2]	42325	366	4.9	5.43
I[3]	84258	728	4.9	10.80
I[4]	154269	1333	5.0	19.78
I'[0]	4529	39	4.3	1.00
I'[1]	11033	95	4.6	2.44
I'[2]	27713	239	4.8	6.12
I'[3]	63288	547	4.9	13.97
I'[4]	128361	1109	5.0	28.34
II[0]	13021	113	4.3	1.00
II[1]	29405	254	4.6	2.26
II[2]	61853	534	4.8	4.75
II[3]	120983	1045	4.9	9.29
II[4]	223158	1928	4.9	17.14
II'[0]	5836	50	3.7	1.00
II'[1]	11525	100	4.1	1.97
II'[2]	26435	228	4.5	4.53
II'[3]	69848	604	4.8	11.97
II'[4]	162471	1404	4.9	27.84

Static HRS hyperpolarizabilities (β_{HRS} , in a.u. and 10^{-30} esu), depolarization ratios (DR), and relative $\beta_{HRS}[n]/\beta_{HRS}[0]$ values for the investigated merocyanines.

Table A.16 – IEFPCM:M06/6-311+G(d) calculations.

	β_{HRS} (a.u.)	β_{HRS} (10^{-30} esu)	DR	$\beta_{HRS}[n]/\beta_{HRS}[0]$
I[0]	7331	63	4.4	1.00
I[1]	18431	159	4.7	2.51
I[2]	39177	339	4.8	5.34
I[3]	72671	628	4.9	9.91
I[4]	120043	1037	4.9	16.38
I'[0]	4832	42	4.3	1.00
I'[1]	12869	111	4.6	2.66
I'[2]	33115	286	4.8	6.85
I'[3]	71646	619	4.9	14.83
I'[4]	128759	1113	4.9	26.65
II[0]	12522	108	4.3	1.00
II[1]	29581	256	4.6	2.36
II[2]	61284	530	4.8	4.89
II[3]	113035	977	4.9	9.03
II[4]	190547	1647	4.9	15.22
II'[0]	6476	56	3.9	1.00
II'[1]	13773	119	4.2	2.13
II'[2]	33966	293	4.6	5.25
II'[3]	90972	786	4.9	14.05
II'[4]	192302	1662	4.9	29.70

Static HRS hyperpolarizabilities (β_{HRS} , in a.u. and 10^{-30} esu), depolarization ratios (DR), and relative $\beta_{HRS}[n]/\beta_{HRS}[0]$ values for the investigated merocyanines.

Table A.17 – IEFPCM:M06-2X/6-311+G(d) calculations.

	β_{HRS} (a.u.)	β_{HRS} (10^{-30} esu)	DR	$\beta_{HRS}[n]/\beta_{HRS}[0]$
I[0]	7550	65	4.5	1.00
I[1]	19104	165	4.7	2.53
I[2]	38422	332	4.9	5.09
I[3]	64572	558	4.9	8.55
I[4]	94611	818	4.9	12.53
I'[0]	5676	49	4.4	1.00
I'[1]	16829	145	4.7	2.97
I'[2]	42661	369	4.9	7.52
I'[3]	80109	692	4.9	14.11
I'[4]	117205	1013	5.0	20.65
II[0]	12766	110	4.5	1.00
II[1]	31297	270	4.7	2.45
II[2]	62881	543	4.9	4.93
II[3]	106273	918	4.9	8.32
II[4]	157463	1361	5.0	12.33
II'[0]	7272	63	4.1	1.00
II'[1]	17496	151	4.4	2.41
II'[2]	49182	425	4.8	6.76
II'[3]	126131	1090	4.9	17.35
II'[4]	208061	1798	5.0	28.61

Static HRS hyperpolarizabilities (β_{HRS} , in a.u. and 10^{-30} esu), depolarization ratios (DR), and relative $\beta_{HRS}[n]/\beta_{HRS}[0]$ values for the investigated merocyanines.

Table A.18 – IEFPCM:M06-HF/6-311+G(d) calculations.

	β_{HRS} (a.u.)	β_{HRS} (10^{-30} esu)	DR	$\beta_{HRS}[n]/\beta_{HRS}[0]$
I[0]	7215	62	4.5	1.00
I[1]	17318	150	4.7	2.40
I[2]	30792	266	4.8	4.27
I[3]	44320	383	4.9	6.14
I[4]	55179	477	4.9	7.65
I'[0]	6730	58	4.5	1.00
I'[1]	22388	193	4.8	3.33
I'[2]	48973	423	4.9	7.28
I'[3]	66169	572	4.9	9.83
I'[4]	71644	619	4.9	10.65
II[0]	12435	107	4.6	1.00
II[1]	30440	263	4.8	2.45
II[2]	54822	474	4.9	4.41
II[3]	78372	677	4.9	6.30
II[4]	96263	832	5.0	7.74
II'[0]	8769	76	4.4	1.00
II'[1]	25773	223	4.6	2.94
II'[2]	87460	756	4.9	9.97
II'[3]	158799	1372	5.0	18.11
II'[4]	150724	1302	5.0	17.19

Static HRS hyperpolarizabilities (β_{HRS} , in a.u. and 10^{-30} esu), depolarization ratios (DR), and relative $\beta_{HRS}[n]/\beta_{HRS}[0]$ values for the investigated merocyanines.

Table A.19 – IEFPCM:LC-BLYP(ω_{std})/6-311+G(d) calculations.

	β_{HRS} (a.u.)	β_{HRS} (10^{-30} esu)	DR	$\beta_{HRS}[n]/\beta_{HRS}[0]$
I[0]	6703	58	4.4	1.00
I[1]	16121	139	4.7	2.40
I[2]	28744	248	4.8	4.29
I[3]	41654	360	4.9	6.21
I[4]	52244	451	4.9	7.79
I'[0]	6068	52	4.4	1.00
I'[1]	19971	173	4.7	3.29
I'[2]	43944	380	4.9	7.24
I'[3]	60735	525	4.9	10.01
I'[4]	67029	579	4.9	11.05
II[0]	11408	99	4.5	1.00
II[1]	27817	240	4.7	2.44
II[2]	50036	432	4.9	4.39
II[3]	71721	620	4.9	6.29
II[4]	88713	767	4.9	7.78
II'[0]	8113	70	4.3	1.00
II'[1]	23511	203	4.6	2.90
II'[2]	75923	656	4.9	9.36
II'[3]	137749	1190	5.0	16.98
II'[4]	135183	1168	5.0	16.66

Static HRS hyperpolarizabilities (β_{HRS} , in a.u. and 10^{-30} esu), depolarization ratios (DR), and relative $\beta_{HRS}[n]/\beta_{HRS}[0]$ values for the investigated merocyanines.

Table A.20a – IEFPCM:LC-BLYP($\omega_{opt}/6-311+G(d)$) calculations with ω_{opt} values calculated using the NSC procedure.

	β_{HRS} (a.u.)	β_{HRS} (10^{-30} esu)	DR	$\beta_{HRS}[n]/\beta_{HRS}[0]$
I[0]	7634	66	4.5	1.00
I[1]	19381	167	4.7	2.54
I[2]	38523	333	4.9	5.05
I[3]	63803	551	4.9	8.36
I[4]	91616	792	4.9	12.00
I'[0]	5861	51	4.4	1.00
I'[1]	17429	151	4.7	2.97
I'[2]	43961	380	4.9	7.50
I'[3]	81434	704	4.9	13.89
I'[4]	117295	1014	5.0	20.01
II[0]	13119	113	4.4	1.00
II[1]	32403	280	4.7	2.47
II[2]	65045	562	4.8	4.96
II[3]	108968	942	4.9	8.31
II[4]	159290	1376	4.9	12.14
II'[0]	7498	65	4.1	1.00
II'[1]	17613	152	4.4	2.35
II'[2]	49391	427	4.7	6.59
II'[3]	129253	1117	4.9	17.24
II'[4]	215223	1860	5.0	28.70

Static HRS hyperpolarizabilities (β_{HRS} , in a.u. and 10^{-30} esu), depolarization ratios (DR), and relative $\beta_{HRS}[n]/\beta_{HRS}[0]$ values for the investigated merocyanines.

Table A.20b – IEFPCM:LC-BLYP($\omega_{opt}/6-311+G(d)$) calculations with ω_{opt} values calculated using the SC procedure.

	β_{HRS} (a.u.)	β_{HRS} (10^{-30} esu)	DR	$\beta_{HRS}[n]/\beta_{HRS}[0]$
I[0]	7770	67	4.5	1.00
I[1]	19818	171	4.7	2.55
I[2]	40508	350	4.9	5.21
I[3]	69994	605	4.9	9.01
I[4]	106174	917	4.9	13.66
I'[0]	5630	49	4.4	1.00
I'[1]	16149	140	4.7	2.87
I'[2]	41454	358	4.9	7.36
I'[3]	82071	709	4.9	14.58
I'[4]	128900	1114	5.0	22.89
II[0]	13295	115	4.4	1.00
II[1]	32548	281	4.7	2.45
II[2]	66785	577	4.8	5.02
II[3]	117219	1013	4.9	8.82
II[4]	183070	1582	4.9	13.77
II'[0]	7142	62	4.0	1.00
II'[1]	15899	137	4.3	2.23
II'[2]	42440	367	4.7	5.94
II'[3]	115381	997	4.9	16.16
II'[4]	218829	1891	5.0	30.64

Static HRS hyperpolarizabilities (β_{HRS} , in a.u.), depolarization ratios (DR), and relative $\beta_{HRS}[n]/\beta_{HRS}[0]$ values for the investigated merocyanines.

Table A.20c – IEFPCM:LC-BLYP(ω_{opt})/6-311+G(d) calculations with ω_{opt} values calculated using the SC procedure in the presence of chloroform, and comparison to BLYP results.

	LC-BLYP (ω_{opt})			BLYP		
	β_{HRS} (a.u.)	DR	$\beta_{HRS}[n]/\beta_{HRS}[0]$	β_{HRS} (a.u.)	DR	$\beta_{HRS}[n]/\beta_{HRS}[0]$
I[0]	8453	4.5	1.0	8536	4.5	1.0
I[1]	20646	4.7	2.4	20689	4.7	2.4
I[2]	45242	4.9	5.4	45304	4.9	5.3
I[3]	69994	4.9	8.3	90341	4.9	10.5
I[4]	159379	5.0	18.9	166505	5.0	19.4
I'[0]	4862	4.3	1.0	4828	4.3	1.0
I'[1]	11729	4.6	2.4	11452	4.6	2.4
I'[2]	29663	4.8	6.1	28497	4.8	5.9
I'[3]	67996	4.9	14.0	64962	4.9	13.4
I'[4]	136691	5.0	28.1	132448	5.0	27.2
II[0]	13700	4.3	1.0	13778	4.3	1.0
II[1]	30653	4.6	2.2	30509	4.6	2.2
II[2]	64822	4.8	4.7	64169	4.8	4.7
II[3]	126785	4.9	9.3	126117	4.9	9.2
II[4]	231361	4.9	16.9	233824	4.9	17.0
II'[0]	5935	3.6	1.0	5896	3.6	1.0
II'[1]	11457	4.0	1.9	11306	4.0	1.9
II'[2]	26707	4.5	4.5	25868	4.5	4.4
II'[3]	73145	4.8	12.4	68880	4.8	11.7
II'[4]	173542	4.9	29.4	161808	4.9	27.4

Static HRS hyperpolarizabilities (β_{HRS} , in a.u. and 10^{-30} esu), depolarization ratios (DR), and relative $\beta_{HRS}[n]/\beta_{HRS}[0]$ values for the investigated merocyanines.

Table A.21 – IEFPCM:CAM-B3LYP(ω_{std})/6-311+G(d) calculations.

	β_{HRS} (a.u.)	β_{HRS} (10^{-30} esu)	DR	$\beta_{HRS}[n]/\beta_{HRS}[0]$
I[0]	7159	62	4.4	1.00
I[1]	17943	155	4.7	2.51
I[2]	35769	309	4.8	5.00
I[3]	59596	515	4.9	8.33
I[4]	86062	744	4.9	12.02
I'[0]	5335	46	4.3	1.00
I'[1]	15762	136	4.7	2.95
I'[2]	40058	346	4.9	7.51
I'[3]	74530	644	4.9	13.97
I'[4]	107262	927	5.0	20.11
II[0]	12148	105	4.5	1.00
II[1]	29551	255	4.7	2.43
II[2]	58774	508	4.8	4.84
II[3]	98087	848	4.9	8.07
II[4]	143376	1239	4.9	11.80
II'[0]	6976	60	4.1	1.00
II'[1]	16543	143	4.4	2.37
II'[2]	46665	403	4.7	6.69
II'[3]	119329	1031	4.9	17.10
II'[4]	191549	1655	5.0	27.46

Static HRS hyperpolarizabilities (β_{HRS} , in a.u. and 10^{-30} esu), depolarization ratios (DR), and relative $\beta_{HRS}[n]/\beta_{HRS}[0]$ values for the investigated merocyanines.

Table A.22a – IEFPCM:CAM-B3LYP(ω_{opt})/6-311+G(d) calculations with ω_{opt} values calculated using the NSC procedure.

	β_{HRS} (a.u.)	β_{HRS} (10^{-30} esu)	DR	$\beta_{HRS}[n]/\beta_{HRS}[0]$
I[0]	6323	55	4.3	1.00
I[1]	15997	138	4.6	2.53
I[2]	31872	275	4.8	5.04
I[3]	52792	456	4.9	8.35
I[4]	75517	653	4.9	11.94
I'[0]	4993	43	4.3	1.00
I'[1]	15522	134	4.6	3.11
I'[2]	39298	340	4.8	7.87
I'[3]	70360	608	4.9	14.09
I'[4]	97346	841	4.9	19.50
II[0]	11333	98	4.4	1.00
II[1]	28056	242	4.7	2.48
II[2]	55737	482	4.8	4.92
II[3]	92318	798	4.9	8.15
II[4]	133496	1154	4.9	11.78
II'[0]	6887	60	4.1	1.00
II'[1]	16909	146	4.4	2.46
II'[2]	48521	419	4.7	7.05
II'[3]	121439	1049	4.9	17.63
II'[4]	186592	1612	5.0	27.09

Static HRS hyperpolarizabilities (β_{HRS} , in a.u. and 10^{-30} esu), depolarization ratios (DR), and relative $\beta_{HRS}[n]/\beta_{HRS}[0]$ values for the investigated merocyanines.

Table A.22b – IEFPCM:CAM-B3LYP(ω_{opt})/6-311+G(d) calculations with ω_{opt} values calculated using the SC procedure.

	β_{HRS} (a.u.)	β_{HRS} (10^{-30} esu)	DR	$\beta_{HRS}[n]/\beta_{HRS}[0]$
I[0]	6157	53	4.3	1.00
I[1]	15418	133	4.6	2.50
I[2]	30692	265	4.8	4.99
I[3]	50847	439	4.9	8.26
I[4]	72699	628	4.9	11.81
I'[0]	4815	42	4.2	1.00
I'[1]	15142	131	4.6	3.14
I'[2]	38600	334	4.8	8.02
I'[3]	68981	596	4.9	14.33
I'[4]	94970	821	4.9	19.72
II[0]	11105	96	4.4	1.00
II[1]	27460	237	4.7	2.47
II[2]	54520	471	4.8	4.91
II[3]	90140	779	4.9	8.12
II[4]	129897	1122	4.9	11.70
II'[0]	6822	59	4.1	1.00
II'[1]	16873	146	4.4	2.47
II'[2]	48615	420	4.7	7.13
II'[3]	121414	1049	4.9	17.80
II'[4]	184919	1598	5.0	27.11

Static HRS hyperpolarizabilities (β_{HRS} , in a.u. and 10^{-30} esu), depolarization ratios (DR), and relative $\beta_{HRS}[n]/\beta_{HRS}[0]$ values for the investigated merocyanines.

Table A.23 – IEFPCM: ω B97X-D(ω_{std})/6-311+G(d) calculations.

	β_{HRS} (a.u.)	β_{HRS} (10^{-30} esu)	DR	$\beta_{HRS}[n]/\beta_{HRS}[0]$
I[0]	6964	60	4.4	1.00
I[1]	17263	149	4.7	2.48
I[2]	33452	289	4.8	4.80
I[3]	53769	465	4.9	7.72
I[4]	74881	647	4.9	10.75
I'[0]	5346	46	4.4	1.00
I'[1]	16101	139	4.7	3.01
I'[2]	40318	348	4.9	7.54
I'[3]	71132	615	4.9	13.30
I'[4]	96112	831	4.9	17.98
II[0]	11775	102	4.4	1.00
II[1]	28631	247	4.7	2.43
II[2]	55580	480	4.8	4.72
II[3]	89194	771	4.9	7.57
II[4]	124654	1077	4.9	10.59
II'[0]	7162	62	4.1	1.00
II'[1]	17700	153	4.4	2.47
II'[2]	51012	441	4.8	7.12
II'[3]	123406	1066	4.9	17.23
II'[4]	177326	1532	5.0	24.76

Static HRS hyperpolarizabilities (β_{HRS} , in a.u. and 10^{-30} esu), depolarization ratios (DR), and relative $\beta_{HRS}[n]/\beta_{HRS}[0]$ values for the investigated merocyanines.

Table A.24a – IEFPCM: ω B97X-D(ω_{opt})/6-311+G(d) calculations with ω_{opt} values calculated using the NSC procedure.

	β_{HRS} (a.u.)	β_{HRS} (10^{-30} esu)	DR	$\beta_{HRS}[n]/\beta_{HRS}[0]$
I[0]	7125	62	4.4	1.00
I[1]	17874	154	4.7	2.51
I[2]	35855	310	4.8	5.03
I[3]	60531	523	4.9	8.50
I[4]	89048	769	4.9	12.50
I'[0]	5218	45	4.4	1.00
I'[1]	15111	131	4.7	2.90
I'[2]	38654	334	4.9	7.41
I'[3]	74315	642	4.9	14.24
I'[4]	111379	962	4.9	21.35
II[0]	12194	105	4.4	1.00
II[1]	29543	255	4.7	2.42
II[2]	59187	511	4.8	4.85
II[3]	100443	868	4.9	8.24
II[4]	150544	1301	4.9	12.35
II'[0]	6817	59	4.0	1.00
II'[1]	15626	135	4.3	2.29
II'[2]	42309	366	4.7	6.21
II'[3]	111914	967	4.9	16.42
II'[4]	195014	1685	5.0	28.61

Static HRS hyperpolarizabilities (β_{HRS} , in a.u. and 10^{-30} esu), depolarization ratios (DR), and relative $\beta_{HRS}[n]/\beta_{HRS}[0]$ values for the investigated merocyanines.

Table A.24b – IEFPCM: ω B97X-D(ω_{opt})/6-311+G(d) calculations with ω_{opt} values calculated using the SC procedure.

	β_{HRS} (a.u.)	β_{HRS} (10^{-30} esu)	DR	$\beta_{HRS}[n]/\beta_{HRS}[0]$
I[0]	7178	62	4.4	1.00
I[1]	18079	156	4.7	2.52
I[2]	36778	318	4.8	5.12
I[3]	63309	547	4.9	8.82
I[4]	95694	827	4.9	13.33
I'[0]	5166	45	4.3	1.00
I'[1]	14743	127	4.7	2.85
I'[2]	37859	327	4.8	7.33
I'[3]	74817	646	4.9	14.48
I'[4]	116851	1010	5.0	22.62
II[0]	12295	106	4.4	1.00
II[1]	29732	257	4.7	2.42
II[2]	60256	521	4.8	4.90
II[3]	104703	905	4.9	8.52
II[4]	162191	1401	4.9	13.19
II'[0]	6692	58	4.0	1.00
II'[1]	14988	130	4.3	2.24
II'[2]	39570	342	4.7	5.91
II'[3]	106369	919	4.9	15.90
II'[4]	197960	1711	5.0	29.58

Static HRS hyperpolarizabilities (β_{HRS} , in a.u. and 10^{-30} esu), depolarization ratios (DR), and relative $\beta_{HRS}[n]/\beta_{HRS}[0]$ values for the investigated merocyanines.

Table A.25 – IEFPCM:HF/6-311+G(d) calculations.

	β_{HRS} (a.u.)	β_{HRS} (10^{-30} esu)	DR	$\beta_{HRS}[n]/\beta_{HRS}[0]$
I[0]	4372	38	4.0	1.00
I[1]	9530	82	4.3	2.18
I[2]	16782	145	4.5	3.84
I[3]	25344	219	4.6	5.80
I[4]	33739	292	4.7	7.72
I'[0]	3917	34	4.0	1.00
I'[1]	11120	96	4.4	2.84
I'[2]	24024	208	4.6	6.13
I'[3]	35675	308	4.7	9.11
I'[4]	42662	369	4.8	10.89
II[0]	7173	62	4.2	1.00
II[1]	15553	134	4.4	2.17
II[2]	27055	234	4.6	3.77
II[3]	40143	347	4.7	5.60
II[4]	53090	459	4.8	7.40
II'[0]	5587	48	4.0	1.00
II'[1]	13591	117	4.2	2.43
II'[2]	35754	309	4.5	6.40
II'[3]	67724	585	4.8	12.12
II'[4]	76914	665	4.8	13.77

Static HRS hyperpolarizabilities (β_{HRS} , in a.u. and 10^{-30} esu), depolarization ratios (DR), and relative $\beta_{HRS}[n]/\beta_{HRS}[0]$ values for the investigated merocyanines.

Table A.26 – IEFPCM:MP2/6-311+G(d) calculations.

	β_{HRS} (a.u.)	β_{HRS} (10^{-30} esu)	DR	$\beta_{HRS}[n]/\beta_{HRS}[0]$
I[0]	9797	85	4.6	1.00
I[1]	24979	216	4.8	2.55
I[2]	47273	408	5.0	4.83
I[3]	72384	625	5.0	7.39
I[4]	94967	821	5.0	9.69
I'[0]	8299	72	4.5	1.00
I'[1]	29722	257	4.8	3.58
I'[2]	71680	619	5.0	8.64
I'[3]	106571	921	5.0	12.84
I'[4]	123604	1068	5.0	14.89
II[0]	17364	150	4.7	1.00
II[1]	43885	379	4.9	2.53
II[2]	82765	715	5.0	4.77
II[3]	125463	1084	5.0	7.23
II[4]	163570	1413	5.0	9.42
II'[0]	10982	95	4.5	1.00
II'[1]	32228	278	4.7	2.93
II'[2]	112592	973	4.9	10.25
II'[3]	232020	2005	5.0	21.13
II'[4]	250702	2166	5.0	22.83

A.5 Dynamic nonlinear optical properties

Dynamic HRS hyperpolarizabilities (β_{HRS} , in a.u. and 10^{-30} esu), depolarization ratios (DR), and relative $\beta_{HRS}[n]/\beta_{HRS}[0]$ values for the investigated merocyanines.

Table A.27 – IEFPCM:M06L/6-311+G(d) calculations.

	β_{HRS} (a.u.)	β_{HRS} (10^{-30} esu)	DR	$\beta_{HRS}[n]/\beta_{HRS}[0]$
I[0]	7687	66	4.6	1.0
I[1]	20803	180	4.8	2.7
I[2]	52507	454	4.9	6.9
I[3]	126715	1095	5.0	16.6
I[4]	303904	2626	5.0	39.8
I'[0]	4236	37	4.4	1.0
I'[1]	11015	95	4.7	2.6
I'[2]	31486	272	4.9	7.4
I'[3]	86474	747	5.0	20.2
I'[4]	229492	1983	5.0	53.6
II[0]	14584	126	4.5	1.0
II[1]	37190	321	4.7	2.6
II[2]	100835	871	4.9	6.9
II[3]	258887	2237	5.0	17.8
II[4]	741008	6403	5.0	50.8
II'[0]	6019	52	3.9	1.0
II'[1]	12959	112	4.3	2.2
II'[2]	34807	301	4.7	5.8
II'[3]	127067	1098	4.9	21.1
II'[4]	443179	3830	5.0	73.6

Dynamic HRS hyperpolarizabilities (β_{HRS} , in a.u. and 10^{-30} esu), depolarization ratios (DR), and relative $\beta_{HRS}[n]/\beta_{HRS}[0]$ values for the investigated merocyanines.

Table A.28 – IEFPCM:M06/6-311+G(d) calculations.

	β_{HRS} (a.u.)	β_{HRS} (10^{-30} esu)	DR	$\beta_{HRS}[n]/\beta_{HRS}[0]$
I[0]	7098	61	4.5	1.0
I[1]	19407	168	4.8	2.7
I[2]	45974	397	4.9	6.5
I[3]	96694	836	4.9	13.6
I[4]	183448	1585	5.0	25.8
I'[0]	4524	39	4.4	1.0
I'[1]	12953	112	4.7	2.9
I'[2]	37636	325	4.9	8.3
I'[3]	94388	816	4.9	20.9
I'[4]	200301	1731	5.0	44.3
II[0]	13225	114	4.5	1.0
II[1]	34726	300	4.7	2.6
II[2]	86922	751	4.9	6.6
II[3]	188923	1632	4.9	14.3
II[4]	386216	3337	5.0	29.2
II'[0]	6408	55	4.0	1.0
II'[1]	14734	127	4.4	2.3
II'[2]	42560	368	4.7	6.6
II'[3]	150557	1301	4.9	23.5
II'[4]	407457	3521	5.0	63.6

Dynamic HRS hyperpolarizabilities (β_{HRS} , in a.u. and 10^{-30} esu), depolarization ratios (DR), and relative $\beta_{HRS}[n]/\beta_{HRS}[0]$ values for the investigated merocyanines.

Table A.29 – IEFPCM:M06-2X/6-311+G(d) calculations.

	β_{HRS} (a.u.)	β_{HRS} (10^{-30} esu)	DR	$\beta_{HRS}[n]/\beta_{HRS}[0]$
I[0]	7185	62	4.6	1.0
I[1]	19515	169	4.8	2.7
I[2]	42585	368	4.9	5.9
I[3]	77738	672	4.9	10.8
I[4]	123048	1063	5.0	17.1
I'[0]	5292	46	4.5	1.0
I'[1]	16825	145	4.8	3.2
I'[2]	47240	408	4.9	8.9
I'[3]	98502	851	5.0	18.5
I'[4]	157782	1363	5.0	29.6
II[0]	12968	112	4.6	1.0
II[1]	34801	301	4.8	2.7
II[2]	77666	671	4.9	6.0
II[3]	145738	1259	5.0	11.2
II[4]	238357	2060	5.0	18.4
II'[0]	7054	61	4.3	1.0
II'[1]	18400	159	4.6	2.6
II'[2]	60193	520	4.9	8.5
II'[3]	182005	1573	5.0	25.8
II'[4]	340347	2941	5.0	48.2

Dynamic HRS hyperpolarizabilities (β_{HRS} , in a.u. and 10^{-30} esu), depolarization ratios (DR), and relative $\beta_{HRS}[n]/\beta_{HRS}[0]$ values for the investigated merocyanines.

Table A.30 – IEFPCM:M06-HF/6-311+G(d) calculations.

	β_{HRS} (a.u.)	β_{HRS} (10^{-30} esu)	DR	$\beta_{HRS}[n]/\beta_{HRS}[0]$
I[0]	6827	59	4.5	1.0
I[1]	17525	151	4.8	2.6
I[2]	33155	286	4.9	4.9
I[3]	50261	434	4.9	7.4
I[4]	65196	563	5.0	9.5
I'[0]	6342	55	4.6	1.0
I'[1]	22846	197	4.8	3.6
I'[2]	54358	470	4.9	8.5
I'[3]	77681	671	5.0	12.2
I'[4]	87066	752	5.0	13.7
II[0]	12407	107	4.7	1.0
II[1]	33117	286	4.8	2.7
II[2]	66021	570	4.9	5.3
II[3]	99987	864	5.0	8.1
II[4]	128031	1106	5.0	10.3
II'[0]	8497	73	4.5	1.0
II'[1]	27803	240	4.7	3.3
II'[2]	112623	973	4.9	13.3
II'[3]	228913	1978	5.0	27.1
II'[4]	215590	1863	5.0	25.5

Dynamic HRS hyperpolarizabilities (β_{HRS} , in a.u. and 10^{-30} esu), depolarization ratios (DR), and relative $\beta_{HRS}[n]/\beta_{HRS}[0]$ values for the investigated merocyanines.

Table A.31 – IEFPCM:LC-BLYP(ω_{std})/6-311+G(d) calculations.

	β_{HRS} (a.u.)	β_{HRS} (10^{-30} esu)	DR	$\beta_{HRS}[n]/\beta_{HRS}[0]$
I[0]	6273	54	4.5	1.0
I[1]	16052	139	4.8	2.6
I[2]	30352	262	4.9	4.9
I[3]	46224	399	4.9	7.4
I[4]	60337	521	4.9	9.7
I'[0]	5601	48	4.5	1.0
I'[1]	19794	171	4.8	3.6
I'[2]	47214	408	4.9	8.5
I'[3]	69149	598	4.9	12.4
I'[4]	79215	684	5.0	14.3
II[0]	11173	97	4.6	1.0
II[1]	29471	255	4.8	2.6
II[2]	57091	493	4.9	5.1
II[3]	86708	749	4.9	7.7
II[4]	111969	968	5.0	10.0
II'[0]	7621	66	4.4	1.0
II'[1]	24137	209	4.7	3.2
II'[2]	90932	786	4.9	11.9
II'[3]	180546	1560	5.0	23.6
II'[4]	180212	1557	5.0	23.6

Dynamic HRS hyperpolarizabilities (β_{HRS} , in a.u. and 10^{-30} esu), depolarization ratios (DR), and relative $\beta_{HRS}[n]/\beta_{HRS}[0]$ values for the investigated merocyanines.

Table A.32a – IEFPCM:LC-BLYP(ω_{opt})/6-311+G(d) calculations with ω_{opt} values calculated using the NSC procedure.

	β_{HRS} (a.u.)	β_{HRS} (10^{-30} esu)	DR	$\beta_{HRS}[n]/\beta_{HRS}[0]$
I[0]	7343	63	4.6	1.0
I[1]	20088	174	4.8	2.8
I[2]	43299	374	4.9	5.9
I[3]	77674	671	4.9	10.7
I[4]	119925	1036	5.0	16.4
I'[0]	5559	48	4.6	1.0
I'[1]	17851	154	4.8	3.2
I'[2]	49997	432	4.9	9.0
I'[3]	102526	886	5.0	18.5
I'[4]	160585	1388	5.0	28.9
II[0]	13586	117	4.6	1.0
II[1]	36989	320	4.8	2.7
II[2]	85704	741	4.9	6.3
II[3]	158883	1373	5.0	11.7
II[4]	254405	2198	5.0	18.8
II'[0]	7451	64	4.2	1.0
II'[1]	19179	166	4.5	2.6
II'[2]	63595	550	4.8	8.6
II'[3]	207394	1792	5.0	28.0
II'[4]	384872	3326	5.0	52.0

Dynamic HRS hyperpolarizabilities (β_{HRS} , in a.u. and 10^{-30} esu), depolarization ratios (DR), and relative $\beta_{HRS}[n]/\beta_{HRS}[0]$ values for the investigated merocyanines.

Table A.32b – IEFPCM:LC-BLYP(ω_{opt})/6-311+G(d) calculations with ω_{opt} values calculated using the SC procedure.

	β_{HRS} (a.u.)	β_{HRS} (10^{-30} esu)	DR	$\beta_{HRS}[n]/\beta_{HRS}[0]$
I[0]	7521	65	4.6	1.00
I[1]	20738	179	4.8	2.76
I[2]	46347	400	4.9	6.16
I[3]	87906	760	5.0	11.69
I[4]	146151	1263	5.0	19.43
I'[0]	5362	46	4.5	1.00
I'[1]	16599	143	4.8	3.10
I'[2]	47608	411	4.9	8.88
I'[3]	105939	915	5.0	19.76
I'[4]	185381	1602	5.0	34.57
II[0]	13964	121	4.5	1.00
II[1]	37870	327	4.8	2.71
II[2]	91307	789	4.9	6.54
II[3]	181689	1570	5.0	13.01
II[4]	322016	2783	5.0	23.06
II'[0]	7167	62	4.1	1.00
II'[1]	17451	151	4.5	2.43
II'[2]	55147	477	4.8	7.69
II'[3]	192115	1660	4.9	26.80
II'[4]	428268	3701	5.0	59.75

Dynamic HRS hyperpolarizabilities (β_{HRS} , in a.u.), depolarization ratios (DR), and relative $\beta_{HRS}[n]/\beta_{HRS}[0]$ values for the investigated merocyanines.

Table A.32c – IEFPCM:LC-BLYP(ω_{opt})/6-311+G(d) calculations with ω_{opt} values calculated using the SC procedure in the presence of chloroform, and comparison to BLYP results.

	LC-BLYP (ω_{opt})			BLYP		
	β_{HRS} (a.u.)	DR	$\beta_{HRS}[n]/\beta_{HRS}[0]$	β_{HRS} (a.u.)	DR	$\beta_{HRS}[n]/\beta_{HRS}[0]$
I[0]	8579	4.6	1.00	8730	4.6	1.01
I[1]	23135	4.8	2.70	23518	4.8	2.71
I[2]	58630	4.9	6.85	60634	4.9	6.99
I[3]	87906	5.0	10.26	152753	5.0	17.60
I[4]	316635	5.0	36.97	398666	5.0	45.93
I'[0]	4682	4.5	1.01	4651	4.4	1.00
I'[1]	12156	4.7	2.63	11885	4.7	2.57
I'[2]	35512	4.9	7.67	34473	4.9	7.45
I'[3]	98835	5.0	21.35	97800	5.0	21.13
I'[4]	257367	5.0	55.60	277689	5.0	59.99
II[0]	16119	4.5	1.00	16607	4.5	1.00
II[1]	40996	4.7	2.55	42601	4.7	2.56
II[2]	112240	4.9	6.98	121229	4.9	7.27
II[3]	284325	5.0	17.68	340791	5.0	20.45
II[4]	750247	5.0	46.64	1243741	5.0	74.63
II'[0]	6411	3.8	1.01	6471	3.8	1.00
II'[1]	13616	4.3	2.14	13851	4.3	2.14
II'[2]	37894	4.7	5.95	38508	4.7	5.94
II'[3]	145421	4.9	22.85	150017	4.9	23.15
II'[4]	509315	5.0	80.02	624050	5.0	96.29

Dynamic HRS hyperpolarizabilities (β_{HRS} , in a.u. and 10^{-30} esu), depolarization ratios (DR), and relative $\beta_{HRS}[n]/\beta_{HRS}[0]$ values for the investigated merocyanines.

Table A.33 – IEFPCM:CAM-B3LYP(ω_{std})/6-311+G(d) calculations.

	β_{HRS} (a.u.)	β_{HRS} (10^{-30} esu)	DR	$\beta_{HRS}[n]/\beta_{HRS}[0]$
I[0]	6790	59	4.5	1.0
I[1]	18238	158	4.8	2.7
I[2]	39287	339	4.9	5.8
I[3]	70695	611	4.9	10.4
I[4]	109580	947	5.0	16.0
I'[0]	4954	43	4.5	1.0
I'[1]	15676	135	4.8	3.2
I'[2]	43965	380	4.9	8.8
I'[3]	90210	780	5.0	18.1
I'[4]	140937	1218	5.0	28.3
II[0]	12231	106	4.6	1.0
II[1]	32462	281	4.8	2.6
II[2]	71332	616	4.9	5.8
II[3]	131138	1133	4.9	10.7
II[4]	209441	1810	5.0	17.1
II'[0]	6675	58	4.2	1.0
II'[1]	17070	148	4.5	2.5
II'[2]	55971	484	4.8	8.3
II'[3]	167625	1448	5.0	25.0
II'[4]	300444	2596	5.0	44.8

Dynamic HRS hyperpolarizabilities (β_{HRS} , in a.u. and 10^{-30} esu), depolarization ratios (DR), and relative $\beta_{HRS}[n]/\beta_{HRS}[0]$ values for the investigated merocyanines.

Table A.34a – IEFPCM:CAM-B3LYP(ω_{opt})/6-311+G(d) calculations with ω_{opt} values calculated using the NSC procedure.

	β_{HRS} (a.u.)	β_{HRS} (10^{-30} esu)	DR	$\beta_{HRS}[n]/\beta_{HRS}[0]$
I[0]	5925	51	4.4	1.0
I[1]	16039	139	4.7	2.7
I[2]	34414	297	4.9	5.8
I[3]	61272	529	4.9	10.4
I[4]	93584	809	5.0	15.9
I'[0]	4582	40	4.4	1.0
I'[1]	15301	132	4.7	3.3
I'[2]	42715	369	4.9	9.2
I'[3]	83828	724	5.0	18.1
I'[4]	124864	1079	5.0	27.0
II[0]	11247	97	4.5	1.0
II[1]	30393	263	4.8	2.7
II[2]	68738	594	4.9	6.1
II[3]	124736	1078	4.9	11.1
II[4]	195813	1692	5.0	17.4
II'[0]	6509	56	4.2	1.0
II'[1]	17331	150	4.5	2.7
II'[2]	58147	502	4.8	9.0
II'[3]	177533	1534	5.0	27.4
II'[4]	298895	2583	5.0	46.1

Dynamic HRS hyperpolarizabilities (β_{HRS} , in a.u. and 10^{-30} esu), depolarization ratios (DR), and relative $\beta_{HRS}[n]/\beta_{HRS}[0]$ values for the investigated merocyanines.

Table A.34b – IEFPCM:CAM-B3LYP(ω_{opt})/6-311+G(d) calculations with ω_{opt} values calculated using the SC procedure.

	β_{HRS} (a.u.)	β_{HRS} (10^{-30} esu)	DR	$\beta_{HRS}[n]/\beta_{HRS}[0]$
I[0]	5756	50	4.4	1.00
I[1]	15401	133	4.7	2.68
I[2]	32975	285	4.9	5.73
I[3]	58634	507	4.9	10.19
I[4]	89378	772	5.0	15.53
I'[0]	4400	38	4.4	1.00
I'[1]	14866	128	4.7	3.38
I'[2]	41790	361	4.9	9.50
I'[3]	81777	707	4.9	18.59
I'[4]	121031	1046	5.0	27.51
II[0]	10984	95	4.5	1.00
II[1]	29607	256	4.8	2.70
II[2]	66790	577	4.9	6.08
II[3]	120771	1044	4.9	11.00
II[4]	188528	1629	5.0	17.16
II'[0]	6427	56	4.2	1.00
II'[1]	17246	149	4.5	2.68
II'[2]	58155	503	4.8	9.05
II'[3]	176982	1529	5.0	27.54
II'[4]	294371	2544	5.0	45.80

Dynamic HRS hyperpolarizabilities (β_{HRS} , in a.u. and 10^{-30} esu), depolarization ratios (DR), and relative $\beta_{HRS}[n]/\beta_{HRS}[0]$ values for the investigated merocyanines.

Table A.35 – IEFPCM: ω B97X-D(ω_{std})/6-311+G(d) calculations.

	β_{HRS} (a.u.)	β_{HRS} (10^{-30} esu)	DR	$\beta_{HRS}[n]/\beta_{HRS}[0]$
I[0]	6596	57	4.5	1.0
I[1]	17459	151	4.8	2.6
I[2]	36321	314	4.9	5.5
I[3]	62443	540	4.9	9.5
I[4]	92287	797	5.0	14.0
I'[0]	4965	43	4.5	1.0
I'[1]	16008	138	4.8	3.2
I'[2]	44026	380	4.9	8.8
I'[3]	84645	731	5.0	17.0
I'[4]	122195	1056	5.0	24.6
II[0]	11841	102	4.6	1.0
II[1]	31257	270	4.8	2.6
II[2]	66332	573	4.9	5.6
II[3]	115545	998	4.9	9.8
II[4]	173213	1497	5.0	14.7
II'[0]	6869	59	4.2	1.0
II'[1]	18258	158	4.5	2.7
II'[2]	61164	529	4.9	9.0
II'[3]	170576	1474	5.0	25.0
II'[4]	264574	2286	5.0	38.7

Dynamic HRS hyperpolarizabilities (β_{HRS} , in a.u. and 10^{-30} esu), depolarization ratios (DR), and relative $\beta_{HRS}[n]/\beta_{HRS}[0]$ values for the investigated merocyanines.

Table A.36a – IEFPCM: ω B97X-D($\omega_{opt}/6-311+G(d)$) calculations with ω_{opt} values calculated using the NSC procedure.

	β_{HRS} (a.u.)	β_{HRS} (10^{-30} esu)	DR	$\beta_{HRS}[n]/\beta_{HRS}[0]$
I[0]	6787	59	4.5	1.0
I[1]	18273	158	4.8	2.7
I[2]	39692	343	4.9	5.8
I[3]	72603	627	4.9	10.6
I[4]	115149	995	5.0	16.9
I'[0]	4870	42	4.5	1.0
I'[1]	15118	131	4.8	3.1
I'[2]	42776	370	4.9	8.8
I'[3]	91128	787	5.0	18.7
I'[4]	149280	1290	5.0	30.7
II[0]	12412	107	4.5	1.0
II[1]	32902	284	4.8	2.7
II[2]	75839	655	4.9	6.1
II[3]	142340	1230	4.9	11.5
II[4]	234702	2028	5.0	19.0
II'[0]	6607	57	4.2	1.0
II'[1]	16365	141	4.5	2.5
II'[2]	51562	446	4.8	7.8
II'[3]	169265	1463	4.9	25.7
II'[4]	332253	2871	5.0	50.4

Dynamic HRS hyperpolarizabilities (β_{HRS} , in a.u. and 10^{-30} esu), depolarization ratios (DR), and relative $\beta_{HRS}[n]/\beta_{HRS}[0]$ values for the investigated merocyanines.

Table A.36b – IEFPCM: ω B97X-D(ω_{opt})/6-311+G(d) calculations with ω_{opt} values calculated using the SC procedure.

	β_{HRS} (a.u.)	β_{HRS} (10^{-30} esu)	DR	$\beta_{HRS}[n]/\beta_{HRS}[0]$
I[0]	6847	59	4.5	1.00
I[1]	18533	160	4.8	2.71
I[2]	40973	354	4.9	5.98
I[3]	76859	664	4.9	11.23
I[4]	126380	1092	5.0	18.46
I'[0]	4824	42	4.5	1.00
I'[1]	14753	127	4.8	3.06
I'[2]	41995	363	4.9	8.70
I'[3]	92549	800	5.0	19.18
I'[4]	159817	1381	5.0	33.13
II[0]	12571	109	4.5	1.00
II[1]	33334	288	4.8	2.65
II[2]	78371	677	4.9	6.23
II[3]	152286	1316	4.9	12.11
II[4]	263857	2280	5.0	20.99
II'[0]	6502	56	4.1	1.00
II'[1]	15725	136	4.4	2.42
II'[2]	48301	417	4.8	7.43
II'[3]	163193	1410	4.9	25.10
II'[4]	350811	3031	5.0	53.96

Dynamic HRS hyperpolarizabilities (β_{HRS} , in a.u. and 10^{-30} esu), depolarization ratios (DR), and relative $\beta_{HRS}[n]/\beta_{HRS}[0]$ values for the investigated merocyanines.

Table A.37 – IEFPCM:HF/6-311+G(d) calculations.

	β_{HRS} (a.u.)	β_{HRS} (10^{-30} esu)	DR	$\beta_{HRS}[n]/\beta_{HRS}[0]$
I[0]	3985	34	4.1	1.00
I[1]	9181	79	4.4	2.30
I[2]	17102	148	4.6	4.29
I[3]	27113	234	4.8	6.80
I[4]	37589	325	4.8	9.43
I'[0]	3480	30	4.1	1.00
I'[1]	10463	90	4.5	3.01
I'[2]	24497	212	4.7	7.04
I'[3]	38675	334	4.8	11.11
I'[4]	48275	417	4.9	13.87
II[0]	6745	58	4.3	1.00
II[1]	15588	135	4.5	2.31
II[2]	29569	256	4.7	4.38
II[3]	46316	400	4.8	6.87
II[4]	63988	553	4.9	9.49
II'[0]	4970	43	4.1	1.00
II'[1]	12611	109	4.3	2.54
II'[2]	37685	326	4.7	7.58
II'[3]	81368	703	4.9	16.37
II'[4]	96147	831	4.9	19.35

Table A.38 – Frequency dispersion factors, defined as $F(\omega) = \beta_{HRS}(-2\omega; \omega, \omega)/\beta_{HRS}(0; 0, 0)$, as calculated at the CPHF level, and using the Minnesota XC functionals.

	HF	M06L	M06	M06-2X	M06-HF
I[0]	0.91	0.99	0.97	0.95	0.95
I[1]	0.96	1.08	1.05	1.02	1.01
I[2]	1.02	1.24	1.17	1.11	1.08
I[3]	1.07	1.50	1.33	1.20	1.13
I[4]	1.11	1.97	1.53	1.30	1.18
I'[0]	0.89	0.94	0.94	0.93	0.94
I'[1]	0.94	1.00	1.01	1.00	1.02
I'[2]	1.02	1.14	1.14	1.11	1.11
I'[3]	1.08	1.37	1.32	1.23	1.17
I'[4]	1.13	1.79	1.56	1.35	1.22
II[0]	0.94	1.12	1.06	1.02	1.00
II[1]	1.00	1.26	1.17	1.11	1.09
II[2]	1.09	1.63	1.42	1.24	1.20
II[3]	1.15	2.14	1.67	1.37	1.28
II[4]	1.21	3.32	2.03	1.51	1.33
II'[0]	0.89	1.03	0.99	0.97	0.97
II'[1]	0.93	1.12	1.07	1.05	1.08
II'[2]	1.05	1.32	1.25	1.22	1.29
II'[3]	1.20	1.82	1.65	1.44	1.44
II'[4]	1.25	2.73	2.12	1.64	1.43

Table A.39 – Frequency dispersion factors, defined as $F(\omega) = \beta_{HRS}(-2\omega; \omega, \omega) / \beta_{HRS}(0; 0, 0)$, as calculated using LRC XC functionals (with ω_{opt} values calculated using the SC procedure).

	LC-BLYP (ω_{std})	LC-BLYP (ω_{opt})	CAM-B3LYP (ω_{std})	CAM-B3LYP (ω_{opt})	ω B97X-D (ω_{std})	ω B97X-D (ω_{opt})
I[0]	0.94	0.97	0.95	0.93	0.95	0.95
I[1]	1.00	1.05	1.02	1.00	1.01	1.03
I[2]	1.06	1.14	1.10	1.07	1.09	1.11
I[3]	1.11	1.26	1.19	1.15	1.16	1.21
I[4]	1.15	1.38	1.27	1.23	1.23	1.32
I'[0]	0.92	0.95	0.93	0.91	0.93	0.93
I'[1]	0.99	1.03	0.99	0.98	0.99	1.00
I'[2]	1.07	1.15	1.10	1.08	1.09	1.11
I'[3]	1.14	1.29	1.21	1.19	1.19	1.24
I'[4]	1.18	1.44	1.31	1.27	1.27	1.37
II[0]	0.98	1.05	1.01	0.99	1.01	1.02
II[1]	1.06	1.16	1.10	1.08	1.09	1.12
II[2]	1.14	1.37	1.21	1.23	1.19	1.30
II[3]	1.21	1.55	1.34	1.34	1.30	1.45
II[4]	1.26	1.76	1.46	1.45	1.39	1.63
II'[0]	0.94	1.00	0.96	0.94	0.96	0.97
II'[1]	1.03	1.10	1.03	1.02	1.03	1.05
II'[2]	1.20	1.30	1.20	1.20	1.20	1.22
II'[3]	1.31	1.67	1.40	1.46	1.38	1.53
II'[4]	1.33	1.96	1.57	1.59	1.49	1.77

Table A.40a – MP2 dynamic HRS hyperpolarizabilities (a.u.) evaluated using the multiplicative scheme ($\beta_{MP2}^{1907} = \beta_{MP2}^{\infty} \times F(\omega)$) using frequency dispersion factors calculated with the various functionals.

	M06L	M06	M06-2X	M06-HF	LC-BLYP (ω_{std})
I[0]	9655	9486	9323	9270	9169
I[1]	26979	26302	25516	25278	24872
I[2]	58645	55475	52395	50901	49918
I[3]	108858	96312	87143	82087	80325
I[4]	187081	145127	123511	112207	109678
I'[0]	7762	7770	7738	7821	7660
I'[1]	29674	29916	29715	30330	29459
I'[2]	81439	81466	79374	79562	77014
I'[3]	145614	140399	131040	125112	121335
I'[4]	220987	192282	166396	150211	146075
II[0]	19448	18339	17639	17325	17006
II[1]	55504	51518	48798	47744	46494
II[2]	134926	117390	102225	99672	94435
II[3]	268474	209695	172054	160066	151680
II[4]	543143	331537	247601	217550	206450
II'[0]	11326	10867	10653	10641	10316
II'[1]	36238	34477	33893	34766	33086
II'[2]	148250	141080	137799	144986	134850
II'[3]	422089	383989	334801	334463	304106
II'[4]	683850	531197	410099	358595	334210
	LC-BLYP (ω_{opt})	CAM-B3LYP (ω_{std})	CAM-B3LYP (ω_{opt})	ω B97X-D (ω_{std})	ω B97X-D (ω_{opt})
I[0]	9483	9292	9159	9279	9345
I[1]	26139	25390	24951	25263	25606
I[2]	54087	51922	50789	51327	52665
I[3]	90908	85865	83469	84061	87876
I[4]	130724	120918	116755	117042	125420
I'[0]	7904	7706	7584	7708	7750
I'[1]	30550	29560	29180	29550	29742
I'[2]	82321	78671	77604	78272	79511
I'[3]	137564	128992	126340	126816	131829
I'[4]	177764	162410	157523	157148	169053
II[0]	18238	17483	17175	17461	17754
II[1]	51061	48208	47316	47910	49202
II[2]	113155	100449	101392	98776	107647
II[3]	194467	167739	168097	162529	182481
II[4]	287716	238940	237400	227289	266100
II'[0]	11020	10508	10346	10533	10670
II'[1]	35374	33255	32940	33244	33813
II'[2]	146303	135045	134687	134999	137435
II'[3]	386325	325925	338209	320706	355969
II'[4]	490646	393225	399090	374052	444277

Table A.40b – Relative $\beta_{MP2}^{1907}[n]/\beta_{MP2}^{1907}[0]$ values calculated using β_{MP2}^{1907} values reported in Table A.40a.

	M06L	M06	M06-2X	M06-HF	LC-BLYP (ω_{std})
I[0]	1.00	1.00	1.00	1.00	1.00
I[1]	2.79	2.77	2.74	2.73	2.71
I[2]	6.07	5.85	5.62	5.49	5.44
I[3]	11.27	10.15	9.35	8.85	8.76
I[4]	19.38	15.30	13.25	12.10	11.96
I'[0]	1.00	1.00	1.00	1.00	1.00
I'[1]	3.82	3.85	3.84	3.88	3.85
I'[2]	10.49	10.48	10.26	10.17	10.05
I'[3]	18.76	18.07	16.94	16.00	15.84
I'[4]	28.47	24.75	21.51	19.21	19.07
II[0]	1.00	1.00	1.00	1.00	1.00
II[1]	2.85	2.81	2.77	2.76	2.73
II[2]	6.94	6.40	5.80	5.75	5.55
II[3]	13.80	11.43	9.75	9.24	8.92
II[4]	27.93	18.08	14.04	12.56	12.14
II'[0]	1.00	1.00	1.00	1.00	1.00
II'[1]	3.20	3.17	3.18	3.27	3.21
II'[2]	13.09	12.98	12.94	13.62	13.07
II'[3]	37.27	35.34	31.43	31.43	29.48
II'[4]	60.38	48.88	38.50	33.70	32.40
	LC-BLYP (ω_{opt})	CAM-B3LYP (ω_{std})	CAM-B3LYP (ω_{opt})	ω B97X-D (ω_{std})	ω B97X-D (ω_{opt})
I[0]	1.00	1.00	1.00	1.00	1.00
I[1]	2.76	2.73	2.72	2.72	2.74
I[2]	5.70	5.59	5.55	5.53	5.64
I[3]	9.59	9.24	9.11	9.06	9.40
I[4]	13.79	13.01	12.75	12.61	13.42
I'[0]	1.00	1.00	1.00	1.00	1.00
I'[1]	3.87	3.84	3.85	3.83	3.84
I'[2]	10.42	10.21	10.23	10.16	10.26
I'[3]	17.40	16.74	16.66	16.45	17.01
I'[4]	22.49	21.07	20.77	20.39	21.81
II[0]	1.00	1.00	1.00	1.00	1.00
II[1]	2.80	2.76	2.75	2.74	2.77
II[2]	6.20	5.75	5.90	5.66	6.06
II[3]	10.66	9.59	9.79	9.31	10.28
II[4]	15.78	13.67	13.82	13.02	14.99
II'[0]	1.00	1.00	1.00	1.00	1.00
II'[1]	3.21	3.16	3.18	3.16	3.17
II'[2]	13.28	12.85	13.02	12.82	12.88
II'[3]	35.06	31.02	32.69	30.45	33.36
II'[4]	44.52	37.42	38.57	35.51	41.64

A.6 Two-state approximation

Table A.41 – Static HRS hyperpolarizabilities (β_{HRS}^{TSA} , in a.u.) calculated with the two-state approximation (equation 2.122 of the main text) using the spectroscopic data calculated at the HF level, and using the Minnesota family of XCFs. % Errors with respect to full-featured TDHF or TD-DFT calculations are also reported.

	HF		M06L		M06		M06-2X		M06-HF	
	β_{HRS}^{TSA}	Err(%)	β_{HRS}^{TSA}	Err(%)	β_{HRS}^{TSA}	Err(%)	β_{HRS}^{TSA}	Err(%)	β_{HRS}^{TSA}	Err(%)
I[0]	3860	-12	7012	-10	7426	1	8245	8	8179	13
I[1]	10353	9	22775	18	22836	24	24108	25	22120	28
I[2]	21253	27	56766	34	55282	41	54088	38	42899	39
I[3]	35066	38	119378	42	111419	53	97129	46	65400	48
I[4]	49417	46	224179	45	196181	63	150895	52	84740	54
Γ[0]	2251	-43	1639	-64	2856	-41	4402	-18	6056	-10
Γ[1]	9785	-12	6468	-41	11268	-12	17181	9	25212	13
Γ[2]	28398	18	29967	8	39130	18	53391	30	64944	33
Γ[3]	48229	35	80395	27	97768	36	112732	43	95086	44
Γ[4]	62014	45	171945	34	193856	51	180216	51	109340	53
II[0]	6723	-6	20305	56	16592	33	15920	15	14952	20
II[1]	16703	7	46292	57	39432	33	40210	24	38887	28
II[2]	32756	21	101019	63	86337	41	86296	33	73730	34
II[3]	52642	31	175931	45	167137	48	153498	39	109424	40
II[4]	74083	40	314985	41	294984	55	237355	43	137749	43
II'[0]	2712	-51	8772	50	6051	-7	6437	-21	7468	-15
II'[1]	11655	-14	15920	38	12803	-7	16507	-5	25500	-1
II'[2]	36504	2	40582	54	38100	12	56595	22	108716	24
II'[3]	87086	29	157239	125 ¹	118192	30	166228	36	217195	37
II'[4]	107987	40	224553	38	272379	42	299716	44	217888	45

¹ The large error (125%) obtained with M06L for **II'[3]** is due to the fact that the S_1 ($\Delta E_{01} = 1.647$ eV, $f_{01} = 1.957$) and S_2 ($\Delta E_{02} = 1.670$ eV, $f_{02} = 0.447$) electronic excited states are quasi degenerate and both contribute to the NLO response.

Table A.42 – Static HRS hyperpolarizabilities (β_{HRS}^{TSA} , in a.u.) calculated with the two-state approximation (equation 2.122 of the main text) using the spectroscopic data calculated using LRC XC functionals with ω_{opt} values obtained using the SC procedure. % Errors with respect to full-featured TD-DFT calculations are also reported.

	LC-BLYP(ω_{std})		LC-BLYP(ω_{opt})		CAM-B3LYP(ω_{std})	
	β_{HRS}^{TSA}	Err(%)	β_{HRS}^{TSA}	Err(%)	β_{HRS}^{TSA}	Err(%)
I[0]	7268	8	8148	7	7632	7
I[1]	20226	25	24395	26	22343	25
I[2]	39661	38	55562	44	49677	39
I[3]	60959	46	102554	61	89162	50
I[4]	79566	52	163434	78	135488	57
I'[0]	4982	-18	4291	-27	3938	-26
I'[1]	21827	9	16015	-8	15684	0
I'[2]	57270	30	50781	16	49716	24
I'[3]	86619	43	112561	38	103975	40
I'[4]	101124	51	191143	63	162845	52
II[0]	13162	15	16610	27	14733	21
II[1]	34617	24	41740	29	37516	27
II[2]	66638	33	90412	39	79351	35
II[3]	99392	39	165550	52	138669	41
II[4]	127219	43	268081	68	213385	49
II'[0]	6392	-21	6658	-11	5778	-17
II'[1]	22413	-5	15140	-14	14944	-10
II'[2]	92606	22	48514	-2	52919	13
II'[3]	187035	36	150036	16	156028	31
II'[4]	194850	44	307579	43	274553	43
	CAM-B3LYP(ω_{opt})		ω B97X-D(ω_{std})		ω B97X-D(ω_{opt})	
	β_{HRS}^{TSA}	Err(%)	β_{HRS}^{TSA}	Err(%)	β_{HRS}^{TSA}	Err(%)
I[0]	6391	1	7372	6	7524	6
I[1]	18999	19	21419	24	22355	25
I[2]	42506	33	45973	37	50828	42
I[3]	75693	43	78952	47	93713	55
I[4]	114424	52	115264	54	149204	68
I'[0]	3338	-33	4096	-23	3719	-29
I'[1]	15043	-3	16437	2	14380	-5
I'[2]	48268	23	50862	26	46368	20
I'[3]	97084	38	99952	41	103308	39
I'[4]	145420	49	145061	51	175185	57
II[0]	13024	15	14128	20	15175	24
II[1]	34310	22	35981	26	37956	28
II[2]	73218	31	74439	34	81721	38
II[3]	127522	38	124360	39	148935	48
II[4]	192121	44	180646	45	240297	60
II'[0]	5158	-25	6033	-16	5777	-15
II'[1]	14702	-13	16110	-9	13547	-13
II'[2]	54976	13	58884	15	44318	5
II'[3]	159551	31	164520	33	138114	23
II'[4]	265541	42	253949	43	280320	44

Table A.43 – Slopes and intercepts (a.u.), as well as correlation coefficients (R^2) obtained after performing linear regressions between HRS hyperpolarizabilities computed using the two-state approximation and using TD-DFT in the four series of merocyanines.

XC functional	Serie	Slope	Intercept	R2
HF	I	1.560	-4024	0.998
	I'	1.547	-6191	0.992
	II	1.472	-5522	0.997
	II'	1.455	-8892	0.990
M06L	I	1.487	-5534	1.000
	I'	1.393	-7366	0.999
	II	1.389	7143	0.998
	II'	1.426	10680	0.924 ¹
M06	I	1.682	-8026	0.999
	I'	1.551	-8953	0.998
	II	1.570	-6856	0.999
	II'	1.443	-7899	0.999
M06-2X	I	1.643	-6776	0.998
	I'	1.578	-9258	0.996
	II	1.535	-7165	0.999
	II'	1.463	-10291	0.997
M06-HF	I	1.599	-4831	0.998
	I'	1.573	-7805	0.993
	II	1.466	-4918	0.999
	II'	1.456	-10308	0.995
LC-BLYP (ω_{std})	I	1.591	-4742	0.998
	I'	1.566	-7570	0.994
	II	1.476	-5482	0.999
	II'	1.459	-10356	0.995
LC-BLYP (ω_{opt})	I	1.850	-10945	0.999
	I'	1.667	-13704	0.987
	II	1.719	-13788	0.994
	II'	1.434	-14595	0.988
ω B97XD (ω_{std})	I	1.593	-5573	0.999
	I'	1.555	-7940	0.994
	II	1.478	-5648	0.999
	II'	1.459	-10013	0.997
ω B97XD (ω_{opt})	I	1.733	-8224	0.997
	I'	1.614	-10314	0.993
	II	1.630	-9922	0.997
	II'	1.456	-11830	0.994
CAM-B3LYP (ω_{std})	I	1.627	-6331	0.999
	I'	1.561	-8629	0.996
	II	1.515	-6871	0.999
	II'	1.457	-10209	0.997
CAM-B3LYP (ω_{opt})	I	1.566	-5568	0.998
	I'	1.541	-8283	0.996
	II	1.470	-6321	0.999
	II'	1.451	-10425	0.998

¹ the smaller correlation coefficient obtained for series **II'** with M06L is due to the fact that the NLO properties of **II'**[**3**] cannot be described using the two-state model owing to the close degeneracy of the S_1 and S_2 excited states. See comment on Table A.41.

Table A.44 – Static HRS hyperpolarizabilities (a.u.) extrapolated using the dynamic ones computed at 1907 nm by using the two-state approximation.

	M06L	M06	M06-2X	M06-HF	LC-BLYP (ω_{std})
I[0]	5570	5377	5613	5462	5100
I[1]	13166	13202	13939	13177	12253
I[2]	27929	27695	28202	23853	22155
I[3]	53466	51433	48284	35148	33017
I[4]	92372	85723	72381	44963	42491
I'[0]	3026	3278	3891	4663	4211
I'[1]	6972	8303	10997	14932	13374
I'[2]	16928	21026	27626	33763	30461
I'[3]	36797	45379	53826	48856	44902
I'[4]	69754	82769	83483	56536	52460
II[0]	9172	8997	9263	9259	8464
II[1]	19574	20427	22026	22376	20466
II[2]	41326	43245	43879	42052	37314
II[3]	73757	78391	75123	61342	54878
II[4]	108493	130039	113503	77595	69981
II'[0]	3883	4216	4734	5627	5256
II'[1]	7199	8231	10337	14868	13793
II'[2]	15609	19258	27485	48336	43301
II'[3]	40467	53389	71375	103114	88503
II'[4]	74861	110422	129410	113468	99565
	LC-BLYP (ω_{opt})	CAM-B3LYP (ω_{std})	CAM-B3LYP (ω_{opt})	ω B97X-D (ω_{std})	ω B97X-D (ω_{opt})
I[0]	5741	5346	4680	5194	5349
I[1]	14302	13216	11580	12744	13238
I[2]	29334	26367	23222	24877	26956
I[3]	50813	44744	39089	40812	46581
I[4]	78576	66012	57294	58042	71807
I'[0]	3858	3670	3385	3705	3573
I'[1]	10506	10381	10182	10601	9706
I'[2]	26449	26326	25957	26682	24558
I'[3]	53236	50680	48389	48928	49491
I'[4]	87033	77015	70367	70227	80716
II[0]	9499	8863	8197	8643	8916
II[1]	22408	20943	19870	20429	20834
II[2]	47065	41472	40726	39720	43299
II[3]	82212	69754	67849	64550	75389
II[4]	128293	104200	99750	92627	117270
II'[0]	4594	4510	4463	4673	4364
II'[1]	9282	9754	10085	10433	8935
II'[2]	23367	26401	27959	28988	22466
II'[3]	65345	68981	74992	72896	63009
II'[4]	128609	122132	126339	117068	123092

Table A.45 – Relative static HRS hyperpolarizabilities ($\beta_{HRS}[n]/\beta_{HRS}[0]$) extrapolated using the dynamic ones computed at 1907 nm by using the two-state approximation.

	M06L	M06	M06-2X	M06-HF	LC-BLYP (ω_{std})
I[0]	1.00	1.00	1.00	1.00	1.00
I[1]	2.36	2.46	2.48	2.41	2.40
I[2]	5.01	5.15	5.02	4.37	4.34
I[3]	9.60	9.56	8.60	6.44	6.47
I[4]	16.58	15.94	12.89	8.23	8.33
I'[0]	1.00	1.00	1.00	1.00	1.00
I'[1]	2.30	2.53	2.83	3.20	3.18
I'[2]	5.59	6.41	7.10	7.24	7.23
I'[3]	12.16	13.84	13.83	10.48	10.66
I'[4]	23.05	25.25	21.45	12.12	12.46
II[0]	1.00	1.00	1.00	1.00	1.00
II[1]	2.13	2.27	2.38	2.42	2.42
II[2]	4.51	4.81	4.74	4.54	4.41
II[3]	8.04	8.71	8.11	6.63	6.48
II[4]	11.83	14.45	12.25	8.38	8.27
II'[0]	1.00	1.00	1.00	1.00	1.00
II'[1]	1.85	1.95	2.18	2.64	2.62
II'[2]	4.02	4.57	5.81	8.59	8.24
II'[3]	10.42	12.66	15.08	18.32	16.84
II'[4]	19.28	26.19	27.33	20.16	18.94
	LC-BLYP (ω_{opt})	CAM-B3LYP (ω_{std})	CAM-B3LYP (ω_{opt})	ω B97X-D (ω_{std})	ω B97X-D (ω_{opt})
I[0]	1.00	1.00	1.00	1.00	1.00
I[1]	2.49	2.47	2.47	2.45	2.47
I[2]	5.11	4.93	4.96	4.79	5.04
I[3]	8.85	8.37	8.35	7.86	8.71
I[4]	13.69	12.35	12.24	11.18	13.42
I'[0]	1.00	1.00	1.00	1.00	1.00
I'[1]	2.72	2.83	3.01	2.86	2.72
I'[2]	6.86	7.17	7.67	7.20	6.87
I'[3]	13.80	13.81	14.30	13.21	13.85
I'[4]	22.56	20.99	20.79	18.95	22.59
II[0]	1.00	1.00	1.00	1.00	1.00
II[1]	2.36	2.36	2.42	2.36	2.34
II[2]	4.95	4.68	4.97	4.60	4.86
II[3]	8.65	7.87	8.28	7.47	8.46
II[4]	13.51	11.76	12.17	10.72	13.15
II'[0]	1.00	1.00	1.00	1.00	1.00
II'[1]	2.02	2.16	2.26	2.23	2.05
II'[2]	5.09	5.85	6.26	6.20	5.15
II'[3]	14.22	15.29	16.80	15.60	14.44
II'[4]	27.99	27.08	28.31	25.05	28.21

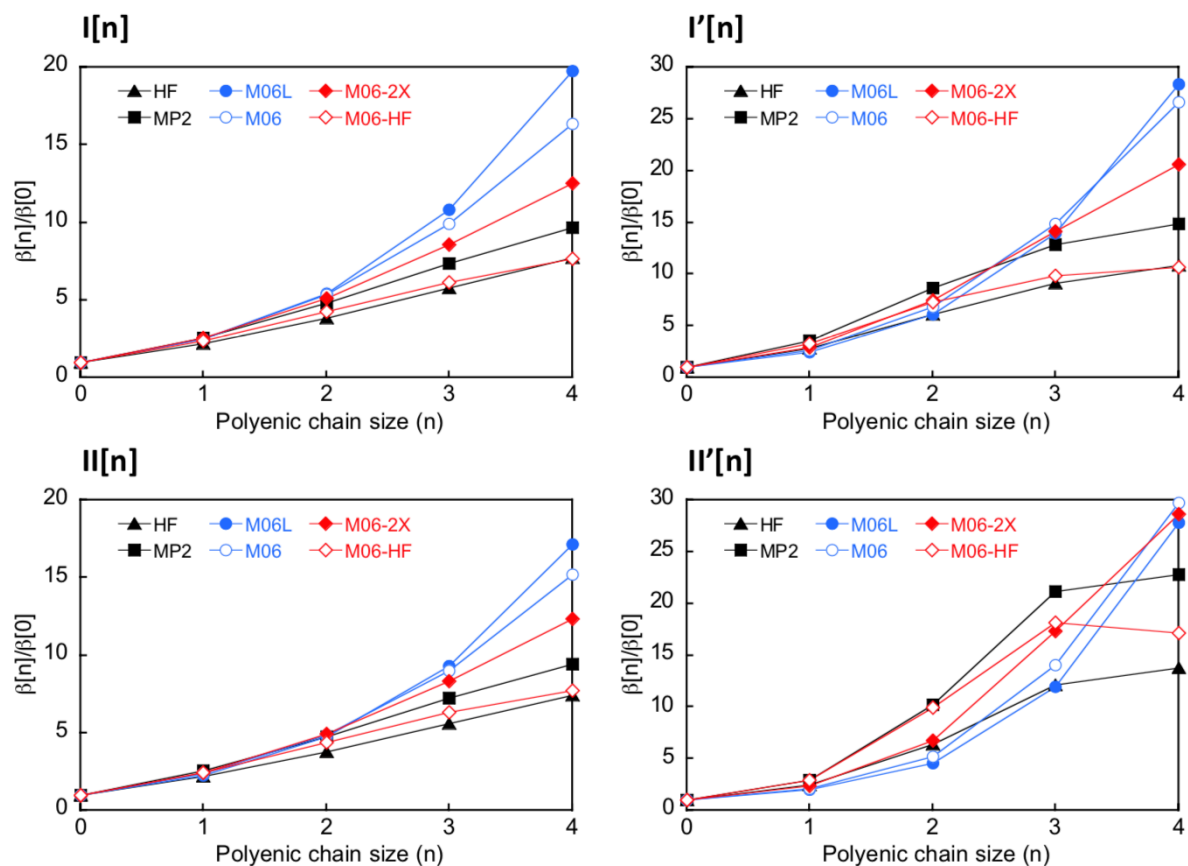


Figure A.2 – Evolution of the relative values of the static HRS hyperpolarizabilities ($\beta_{HRS}[n]/\beta_{HRS}[0]$) with the length of the polyenic bridge in the four series of merocyanines, calculated in chloroform at the HF, MP2 and DFT levels using the Minnesota's family of functionals in combination with the 6-311+G(d) basis set.

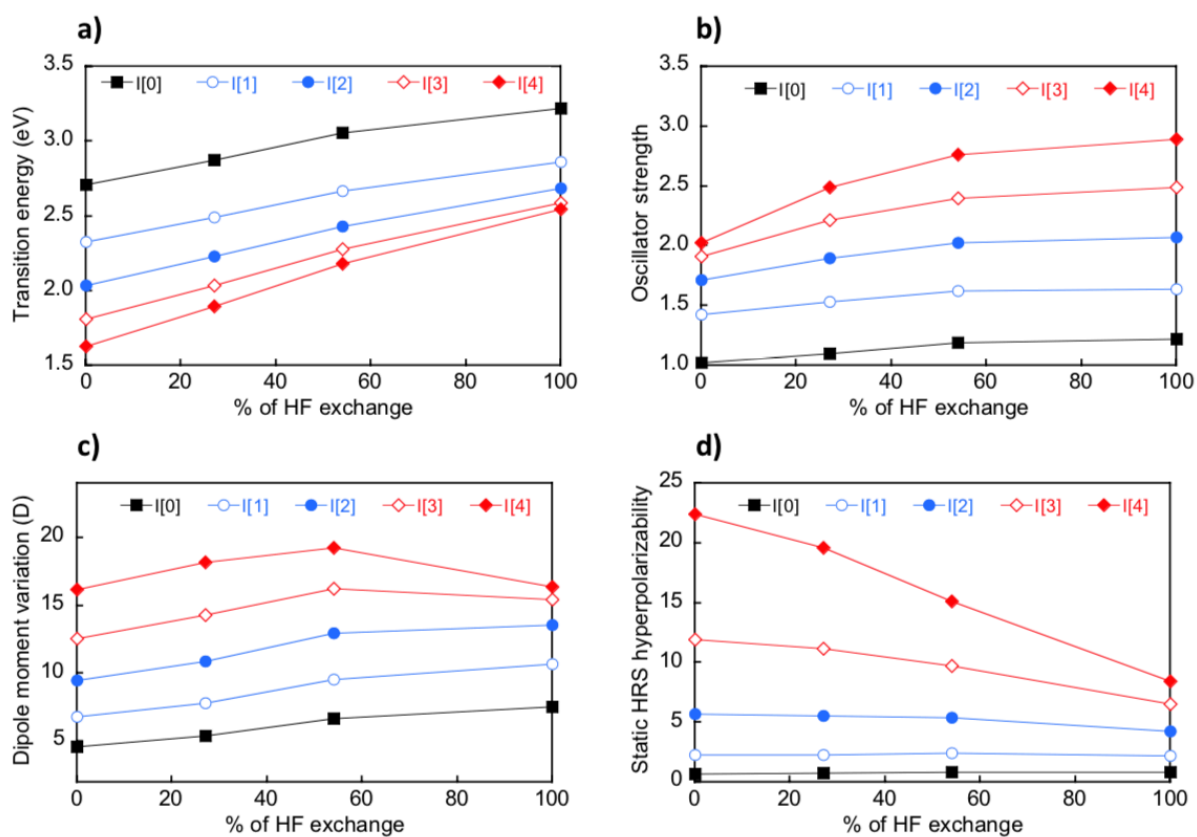


Figure A.3 – Evolution of a) the $S_0 \rightarrow S_1$ transition energy, b) oscillator strength c), dipole moment variation and d) and static HRS hyperpolarizabilities (in 10^4 a.u.) in the merocyanine series $I[n]$, calculated in chloroform using the Minnesota’s family of functionals (M06L, M06, M06-2X, M06-HF) in combination with the 6-311+G(d) basis set. Results are reported in function of the percentage of HF exchange included in the XCF.

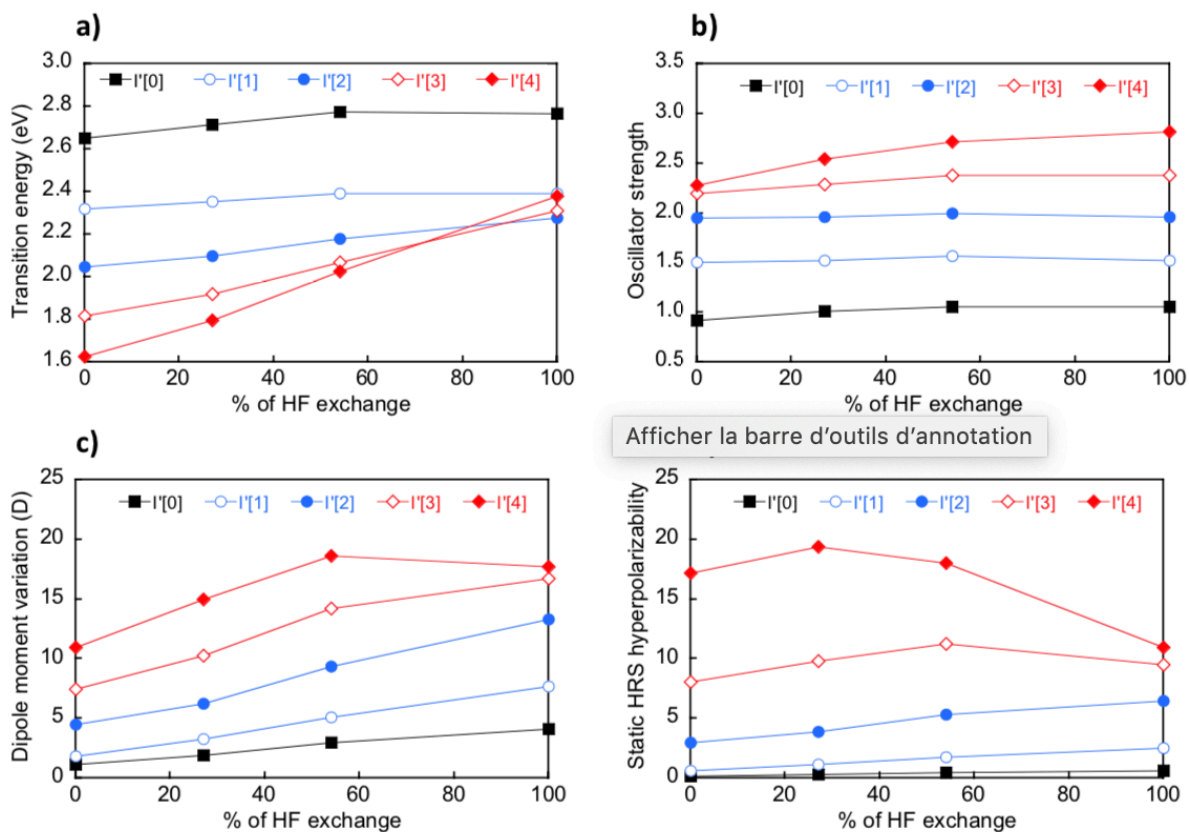


Figure A.4 – Evolution of a) the $S_0 \rightarrow S_1$ transition energy, b) oscillator strength c), dipole moment variation and d) and static HRS hyperpolarizabilities (in 10^4 a.u.) in the merocyanine series $I'[n]$, calculated in chloroform using the Minnesota's family of functionals (M06L, M06, M06-2X, M06-HF) in combination with the 6-311+G(d) basis set. Results are reported in function of the percentage of HF exchange included in the XCF.

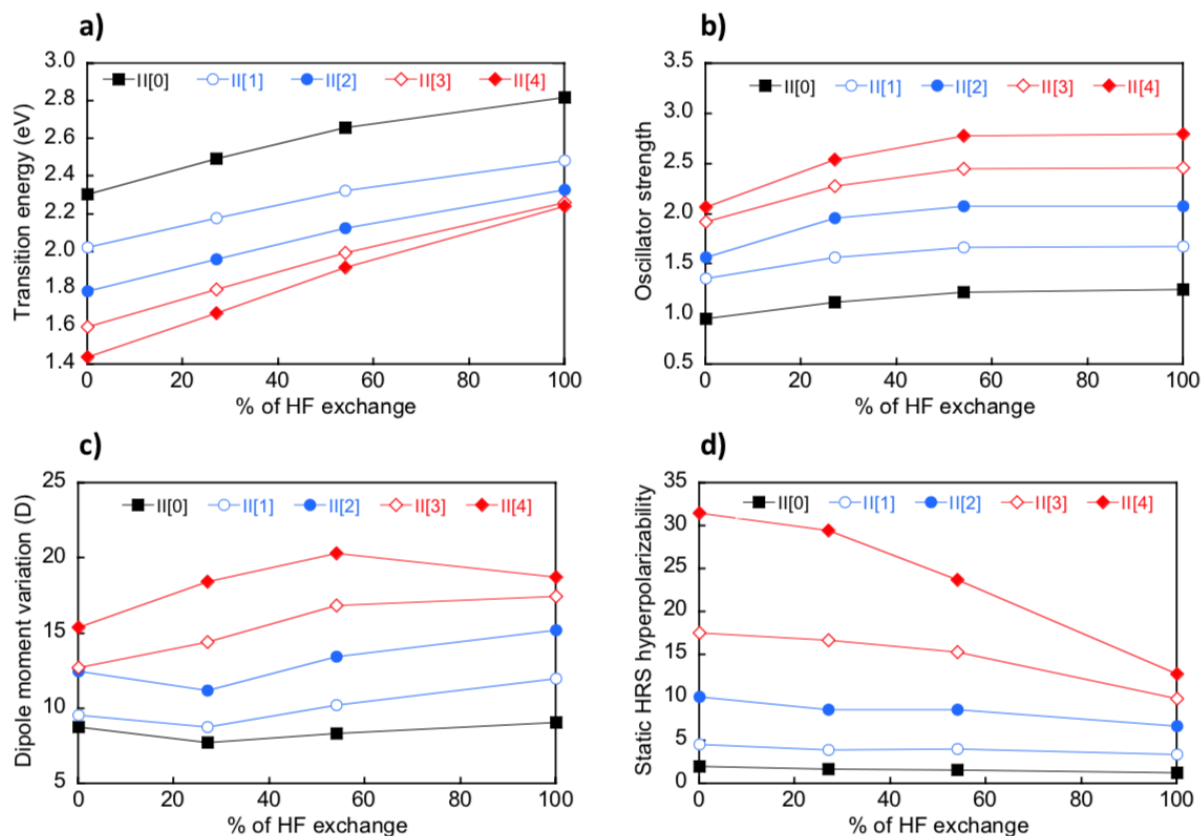


Figure A.5 – Evolution of a) the $S_0 \rightarrow S_1$ transition energy, b) oscillator strength c), dipole moment variation and d) and static HRS hyperpolarizabilities (in 10^4 a.u.) in the merocyanine series $\text{II}[n]$, calculated in chloroform using the Minnesota’s family of functionals (M06L, M06, M06-2X, M06-HF) in combination with the 6-311+G(d) basis set. Results are reported in function of the percentage of HF exchange included in the XCF.

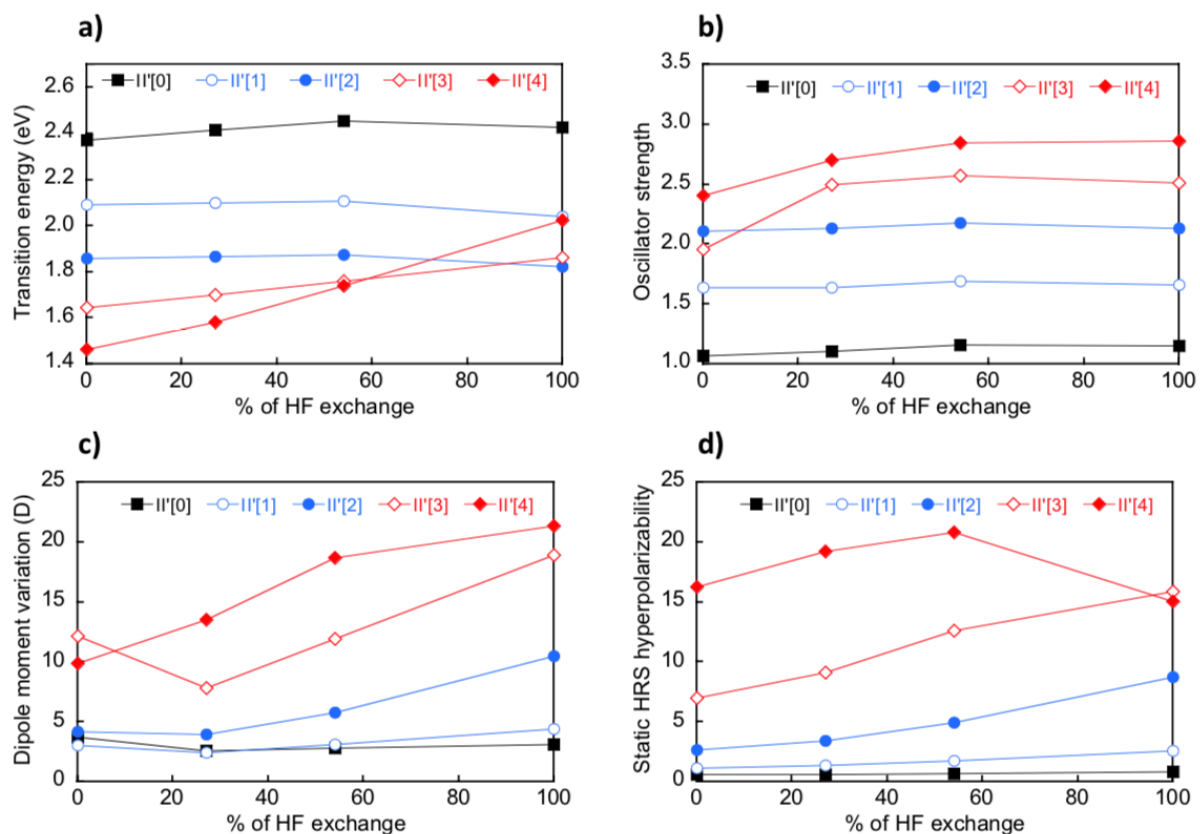


Figure A.6 – Evolution of a) the $S_0 \rightarrow S_1$ transition energy, b) oscillator strength c), dipole moment variation and d) and static HRS hyperpolarizabilities (in 10^4 a.u.) in the merocyanine series $\mathbf{II}'[n]$, calculated in chloroform using the Minnesota's family of functionals (M06L, M06, M06-2X, M06-HF) in combination with the 6-311+G(d) basis set. Results are reported in function of the percentage of HF exchange included in the XCF.

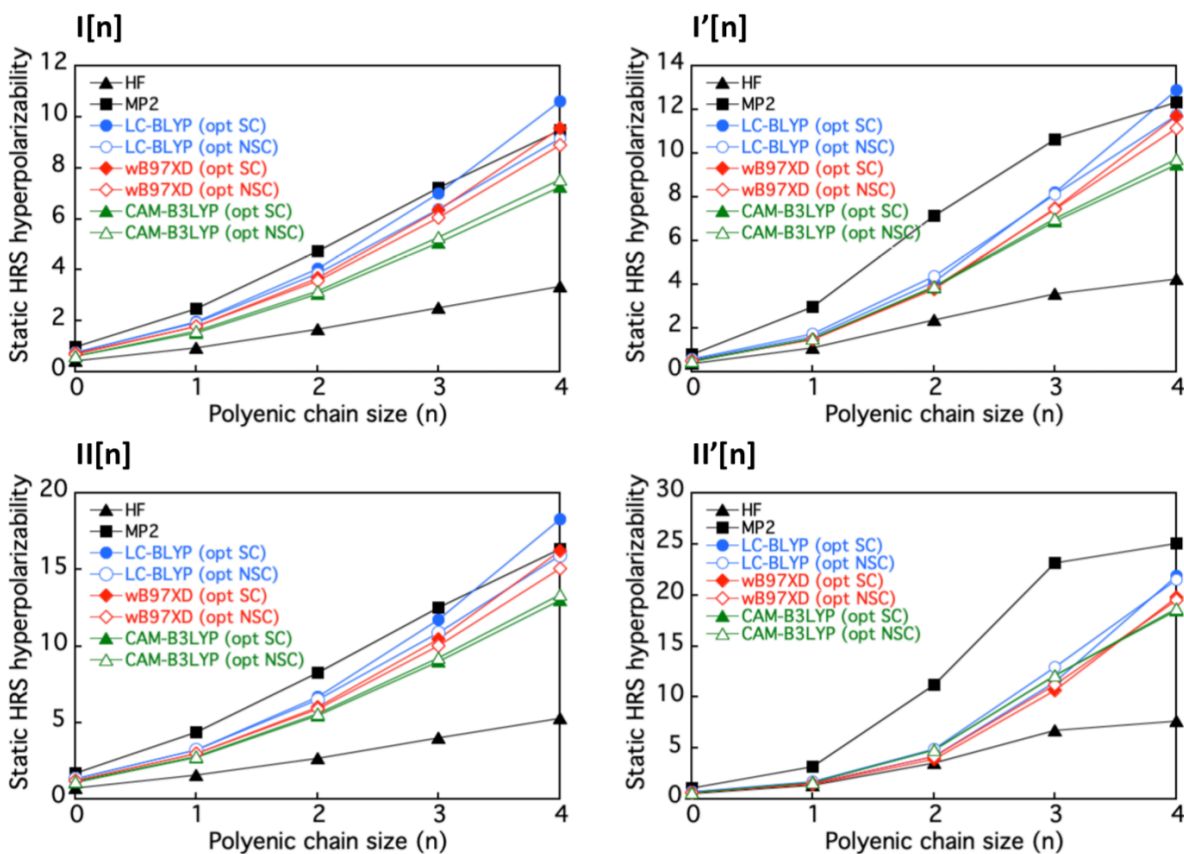


Figure A.7 – Evolution of the static HRS hyperpolarizabilities (in 10^4 a.u.) with the length of the polyenic bridge in the four series of merocyanines, calculated in chloroform with the long-range corrected functionals using optimally-tuned RS parameters (obtained using the self-consistent (SC) and non-self-consistent (NSC) procedures) and the 6-311+G(d) basis set. Results obtained at the HF, MP2 and M06-2X levels are also reported for comparison.

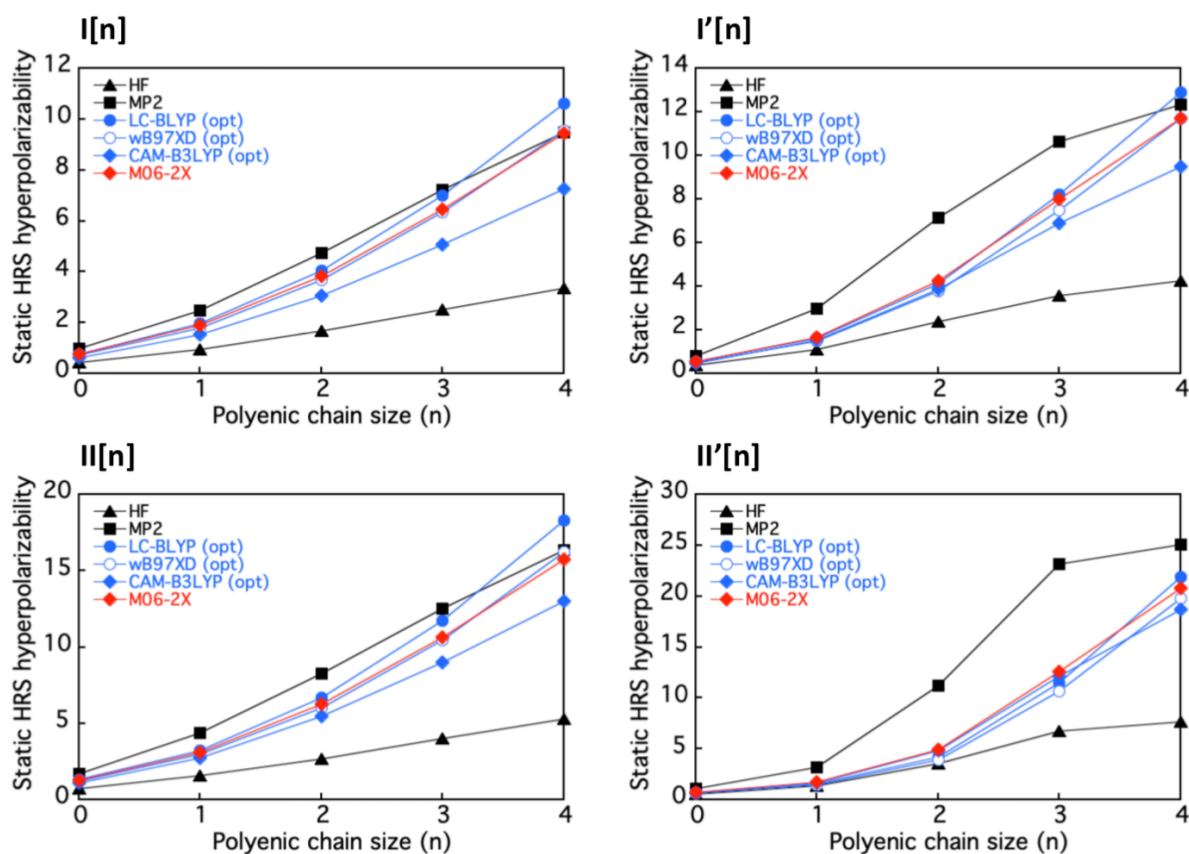


Figure A.8 – Evolution of the static HRS hyperpolarizabilities (in 10^4 a.u.) with the length of the polyenic bridge in the four series of merocyanines, calculated in chloroform with the long-range corrected functionals using optimally-tuned RS parameters (obtained using the self-consistent procedure) and the 6-311+G(d) basis set. Results obtained at the HF, MP2 and M06-2X levels are also reported for comparison.

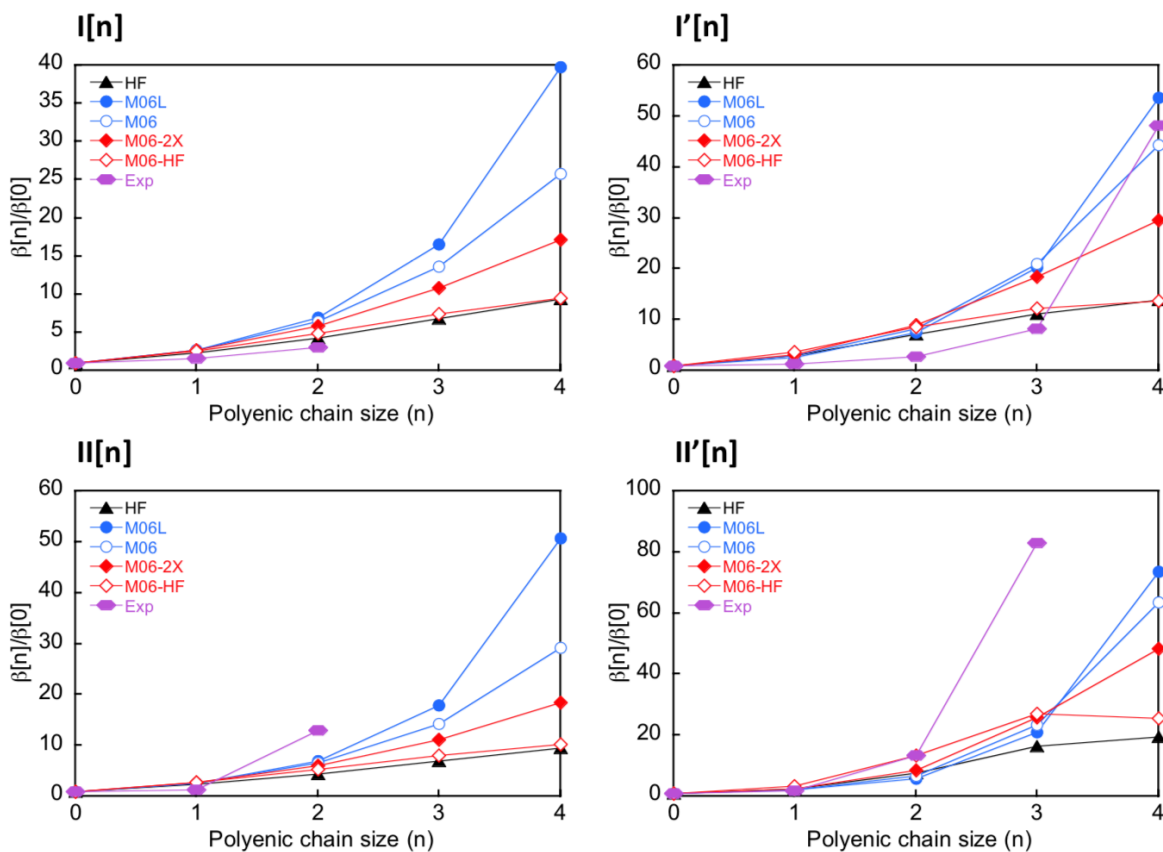


Figure A.9 – Evolution of the relative dynamic HRS hyperpolarizabilities ($\beta_{HRS}[n]/\beta_{HRS}[0]$ in a.u.) with the length of the polyenic bridge in the four series of merocyanines, calculated in chloroform at the HF level, and with the Minnesota series of XCFs together with the 6-311+G(d) basis set. Experimental values obtained from HRS measurements are also reported.

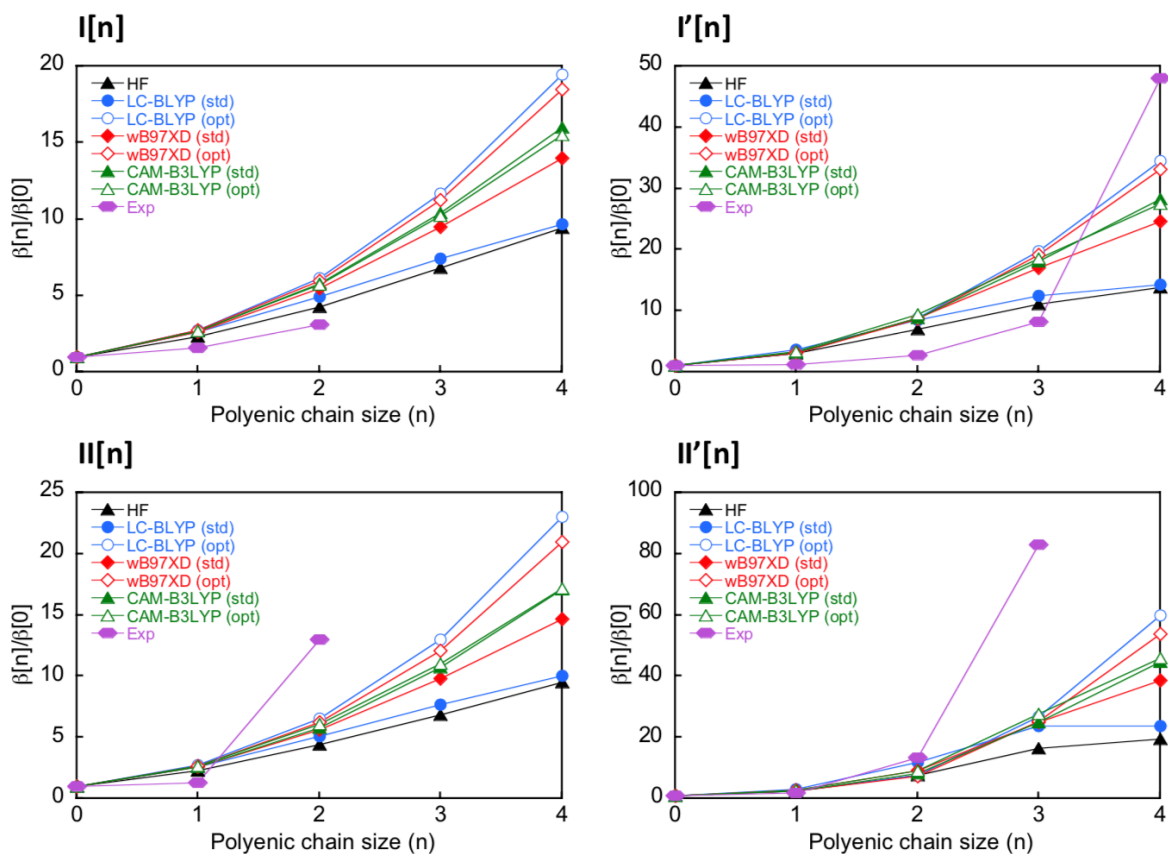


Figure A.10 – Evolution of the relative dynamic HRS hyperpolarizabilities ($\beta_{HRS}[n]/\beta_{HRS}[0]$ in a.u.) with the length of the polyenic bridge in the four series of merocyanines, calculated in chloroform at the HF level, and with the long-range corrected functionals using standard and optimally-tuned RS parameters (obtained using the self-consistent procedure) together with the 6-311+G(d) basis set. Experimental values obtained from HRS measurements are also reported.

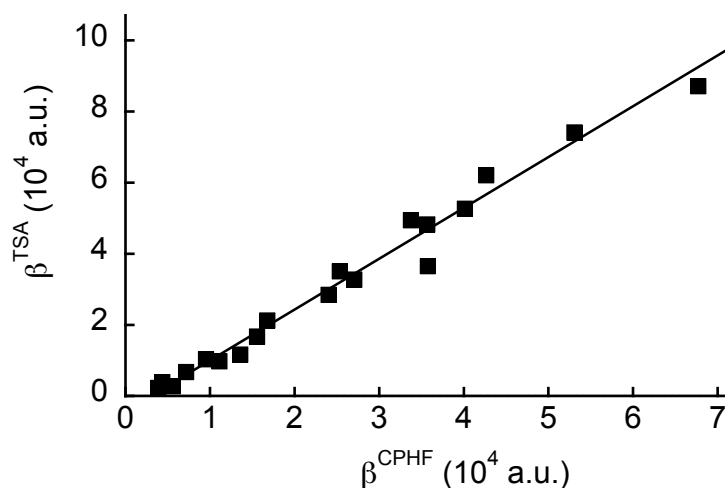


Figure A.11 – Static β_{HRS} values of the whole set of compounds evaluated using the two-state approximation, plotted against the values calculated using CPHF/6-311+G(d) calculations in chloroform. The line is a linear fit; $R^2 = 0.986$.

Supporting information of Chapter 4

B.1 Force field parameterization and MD simulations

B.1.1 Validation of the force field used for water

In order to validate the force field used to describe water, preliminary MD simulations were run for pure solvent molecules, from which key physical observables were extracted and compared to experimental data. Bulk properties such as the mass density and local structure were first calculated. The mass density ρ_m is defined as:

$$\rho_m = \frac{ZM}{N_A V}$$

where Z is the number of molecules in the simulation box, M is the molar mass of the water molecule, N_A is the Avogadro constant and V is the volume of the simulation box. The local structure is characterized by radial distribution functions (RDF) $g(r)$ between atoms or mass centers of molecules, given by:

$$g(r) = \frac{N(r, r + dr)}{\frac{Z}{V} 4\pi r^2 dr}$$

where N is the number of water molecules at a distance comprised between r and $r + dr$ from a reference one. As shown in Table B.1 and Figure B.1, the water model SPC/Fw^[1] reproduces very well the mass density and water bulk properties, giving results very close to the experimental ones.

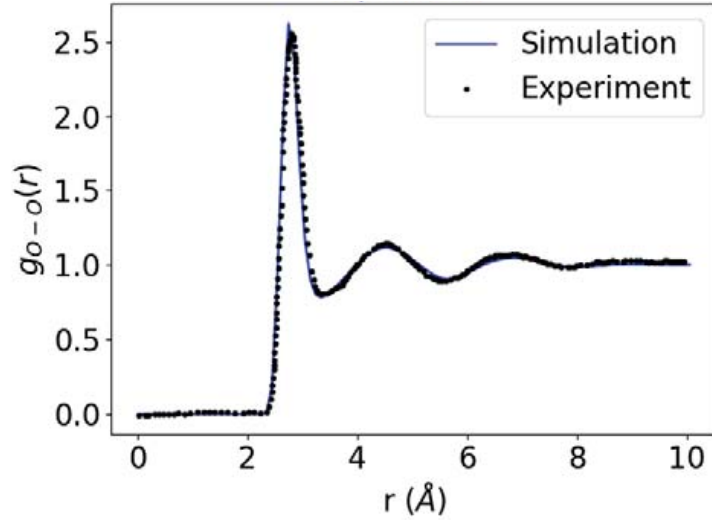


Figure B.1 – RDF between oxygens at 300 K, comparing simulation and experiment. Simulations at equilibrium were run for 20 ns on a box of 500 solvent molecules, using the NpT ensemble at $p = 1.01325$ bar. Experimental data were extracted from ref. [2].

The self-diffusion coefficient and the static dielectric constant, which are directly related to the solvent dynamics and solvent-mediated electrostatic interactions, were also evaluated. The self-diffusion coefficient D is defined by:

$$D = \lim_{t \rightarrow \infty} \frac{1}{6t} \langle [\mathbf{r}(t) - \mathbf{r}(0)]^2 \rangle$$

where t is the elapsed time, \mathbf{r} is the position of all particles and $\langle [\mathbf{r}(t) - \mathbf{r}(0)]^2 \rangle$ is the mean square displacement. The static dielectric constant ε can be written as:

$$\varepsilon = 1 + \frac{1}{3\varepsilon_0} \frac{\sum_i \mu_i}{Vk_B T} + \frac{N\alpha}{V\varepsilon_0}$$

where ε_0 is the vacuum permittivity, μ_i is the dipole moment of the water molecule, V is the volume of the simulation box, k_B is the Boltzmann constant, T is the temperature, N is the number of solvent molecules and α is the molecular polarizability. The second term in the right-hand side describes the permanent dipole contribution, while the last term describes the induced dipole contribution. The latter term is neglected in non-polarizable force fields. Results presented in Table B.1 show that all the experimental and calculated values of the self-diffusion coefficient and static dielectric constant are in the same range.

Moreover, the self-diffusion activation energy was deduced from the self-diffusion coefficient D , which follows an Arrhenius-like relation with temperature T :^[3]

$$\ln D = \ln D_0 - \frac{E_A}{k_B T}$$

where E_A is the self-diffusion activation energy, D_0 is the diffusion coefficient at infinite temperature. The calculated activation energy, deduced from the linear evolution of the self-diffusion coefficient as a function of the reciprocal of temperature, is very close to the experimental value (Table B.1).

Table B.1 – Calculated and experimental physical properties of water at $T = 300$ K. Simulations at equilibrium were run for 20 ns on a box of 500 solvent molecules, using the NpT ensemble at $p = 1.01325$ bar. Experimental data are from references [4] and [5].

Physical property	Calc.	Exp.
ρ_m (g/cm^3)	1.002	0.997
D ($10^{-8}m^2/s$)	0.231	0.245
ϵ	80.0	77.4
$E_A(kJ/mol)$	17	18

B.1.2 Torsional energy profiles of organic chromophores

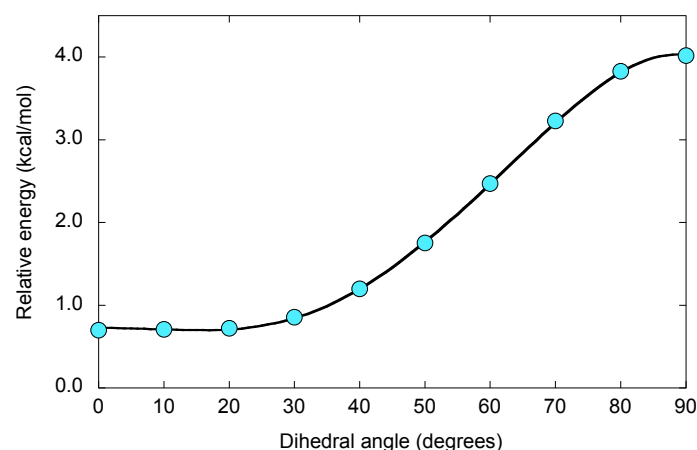


Figure B.2a – Comparison of the free energy profile associated to the rotation around the Thienyl-Thienyl dihedral angle ($\phi_{TT} = S-C-C-S$, see Figure 4.1), obtained at the B3LYP/cc-pVTZ level in gas phase at $T=300K$ (dots) and using the reparameterized force field (line).

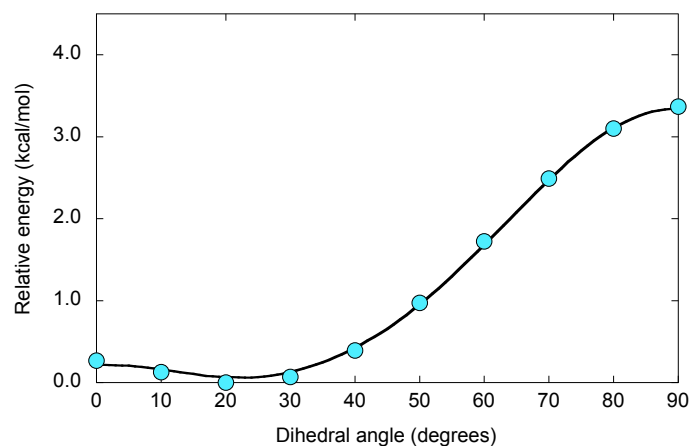


Figure B.2b – Comparison of the free energy profile associated to the rotation around the Thienyl-Phenyl dihedral angle (ϕ_{TP} , see Figure 4.1), obtained at the B3LYP/cc-pVTZ level in gas phase at T=300K (dots) and using the reparameterized force field (line).

B.1.3 MD simulations of organic chromophores in water

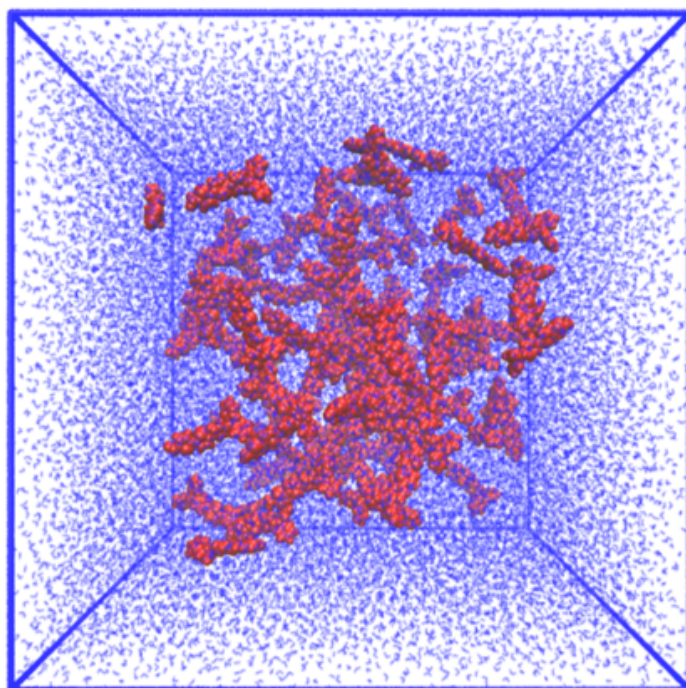


Figure B.3 – Starting configuration of the 8 simulations in pure water.

B.2 Determination of the optimal parameters of the sTD-DFT method

This section reports calculations of the first hyperpolarizability of the isolated dye in three different geometries randomly extracted from the MD trajectory (Figure B.4a), and on a supramolecular cluster containing 12 chromophores (Figure B.4b). These benchmarks have for objective of defining the optimal values of the y_J and y_K parameters used to damp the two-electron Coulomb and exchange integrals (equations 2.111-2.112). The energy threshold E_{th} used to truncate the number of configuration state functions in the SCI (Configuration Interaction Singles) procedure is also optimized.

B.2.1 Test molecular and supramolecular geometries

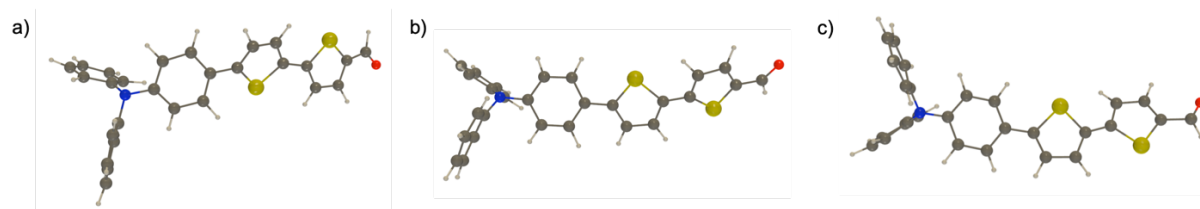


Figure B.4a – Different geometries of the isolated dyes considered in the sTD-DFT benchmarks.

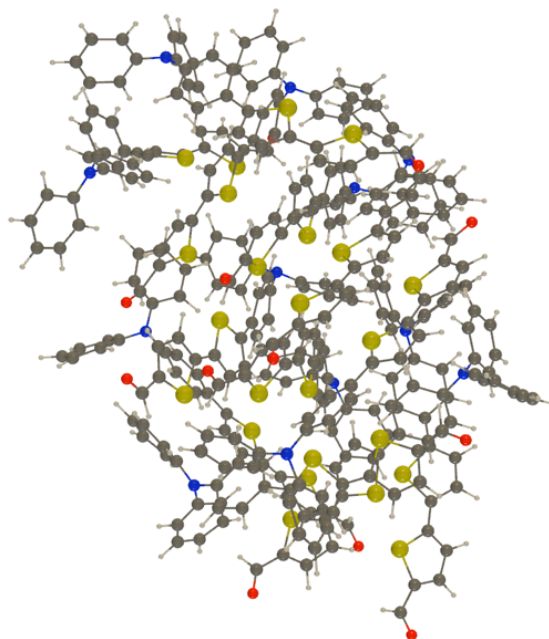


Figure B.4b – Geometry of the aggregate composed of 12 dyes considered in the sTD-DFT benchmarks.

B.2.2 Optimization of the sTD-DFT-xTB parameters

In this Section, the y_J and E_{th} parameters of the sTD-DFT-xTB method are adjusted by comparison to reference TD-DFT/M06-2X/6-311G(d) calculations in gas phase, while y_K is kept fixed to its default value of 2.0. The y_J parameter is first tuned on the three test geometries of the isolated molecule (Figures B.5, B.6 and B.7). It can be observed that default parameter value $y_J = 4.0$ satisfactorily reproduces the evolution of the first hyperpolarizabilities with the energy of the incident light ($E = \hbar\omega$), as calculated using the reference TD-DFT level. Numerical β values calculated at the TD-DFT and sTD-DFT-xTB levels using $\omega = 0.000$ eV, $\omega = 0.827$ eV and $\omega = 1.165$ eV are reported in Table B.2. For $\omega = 1.165$ eV, the absolute errors of the sTD-DFT-xTB approach compared to the TD-DFT reference are lower than 5% whatever the geometry. Smaller ω values lead to larger errors, which however remain acceptably small ($< 17\%$).

In a second step, we addressed the impact of varying the energy threshold in sTD-DFT-xTB calculations, using default parameters. As shown in Figures B.8, B.9 and B.10 for the isolated molecules, the frequency dispersion curves of the first hyperpolarizabilities calculated using sTD-DFT-xTB are downshifted compared to reference TD-DFT calculations. Moreover, reducing E_{th} from 10 to 6 eV negligibly impacts the sTD-DFT-xTB results, while those obtained with $E_{th} = 5.0$ eV show larger deviations. A similar conclusion can be drawn for calculations performed for the supramolecular aggregate (Figure B.11). Therefore, an energy threshold value of $E_{th} = 6.0$ eV can be used to minimize the calculation time in sTD-DFT-xTB calculations without any significant loss of accuracy.

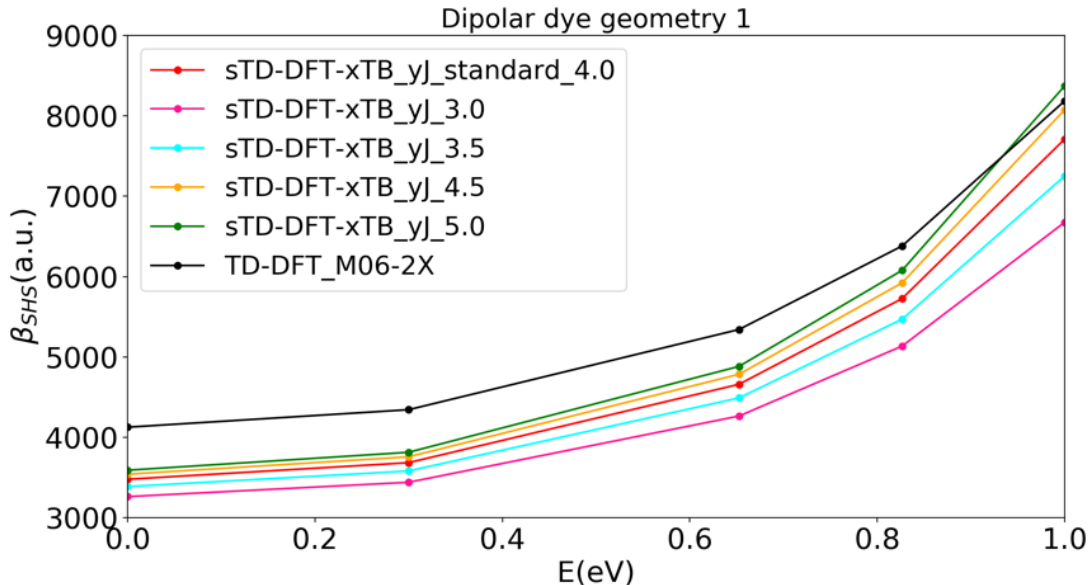


Figure B.5 – Tuning of the y_J parameter for the geometry 1 of the isolated molecule (Fig. B.4a). In all sTD-DFT-xTB calculations, $y_K = 2.0$ and $E_{th} = 10$ eV.

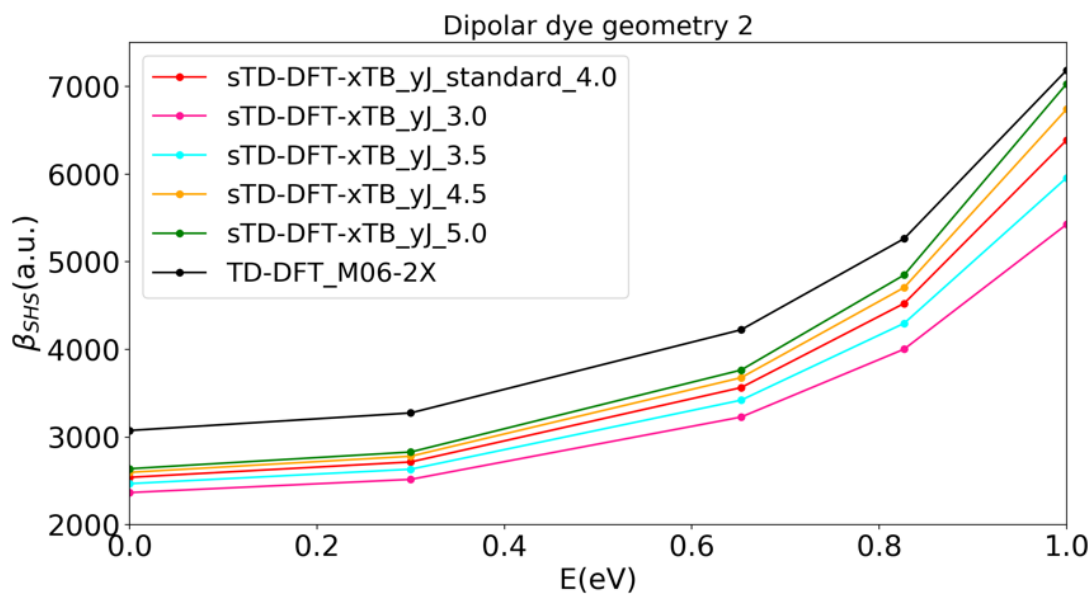


Figure B.6 – Tuning of the y_J parameter for the geometry 2 of the isolated molecule (Fig. B.4a). In all sTD-DFT-xTB calculations, $y_K = 2.0$ and $E_{th} = 10$ eV.

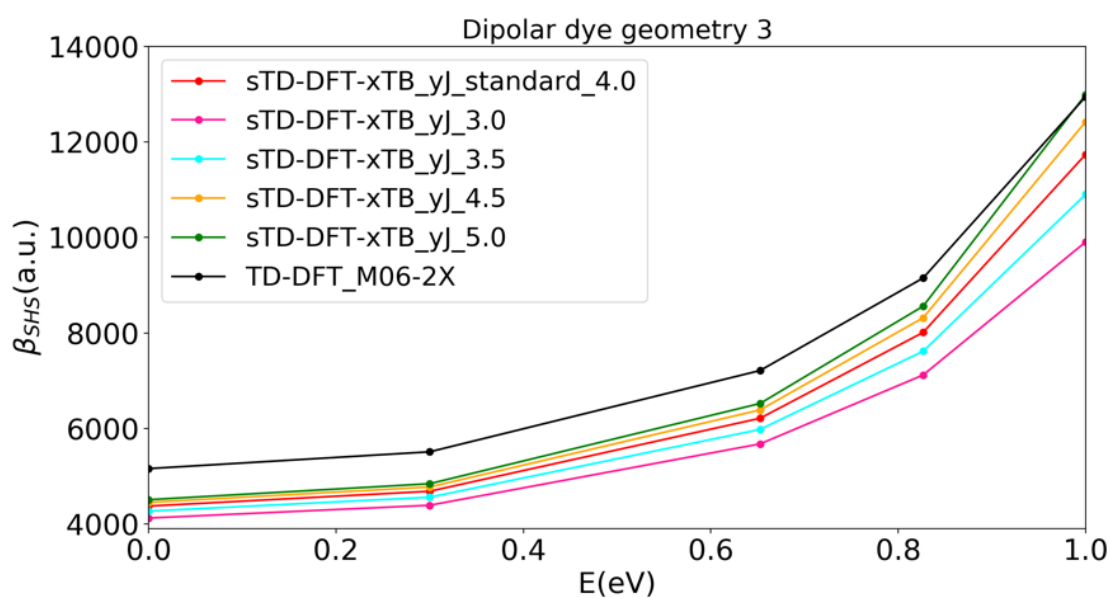


Figure B.7 – Tuning of the y_J parameter for the geometry 3 of the isolated molecule (Fig. B.4a). In all sTD-DFT-xTB calculations, $y_K = 2.0$ and $E_{th} = 10$ eV.

Table B.2 – Comparison between static and dynamic first hyperpolarizabilities calculated at the sTD-DFT-xTB and TD-DFT levels for the three test geometries of the isolated molecule shown Figure B.4a. First hyperpolarizabilities β are calculated at three different excitation energies ω . In all sTD-DFT-xTB calculations, $y_J = 4.0$, $y_K = 2.0$ and $E_{th} = 10$ eV.

Geometry 1

$\beta(-2\omega;\omega,\omega)$	sTD-DFT-xTB	TD-DFT	error
$\omega = 0.000$ eV	3 478	4 126	-16%
$\omega = 0.827$ eV	5 727	6 381	-10%
$\omega = 1.165$ eV	11 827	11 490	+3%

Geometry 2

$\beta(-2\omega;\omega,\omega)$	sTD-DFT-xTB	TD-DFT	error
$\omega = 0.000$ eV	2 540	3 075	-17%
$\omega = 0.827$ eV	4 524	5 263	-14%
$\omega = 1.165$ eV	10 524	11 063	-5%

Geometry 3

$\beta(-2\omega;\omega,\omega)$	sTD-DFT-xTB	TD-DFT	error
$\omega = 0.000$ eV	4 374	5 159	-15%
$\omega = 0.827$ eV	8 012	9 151	-12%
$\omega = 1.165$ eV	21 439	21 613	-1%

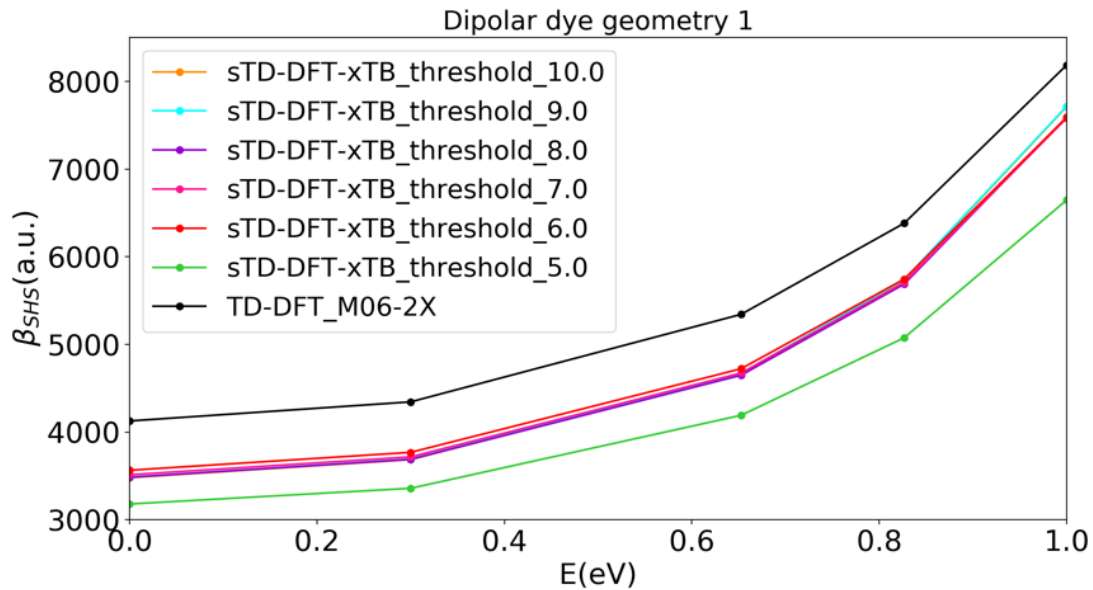


Figure B.8 – Tuning of the energy threshold E_{th} for the geometry 1 of the isolated molecule (Fig. B.4a). In all sTD-DFT-xTB calculations, $y_J = 4.0$ and $y_K = 2.0$.

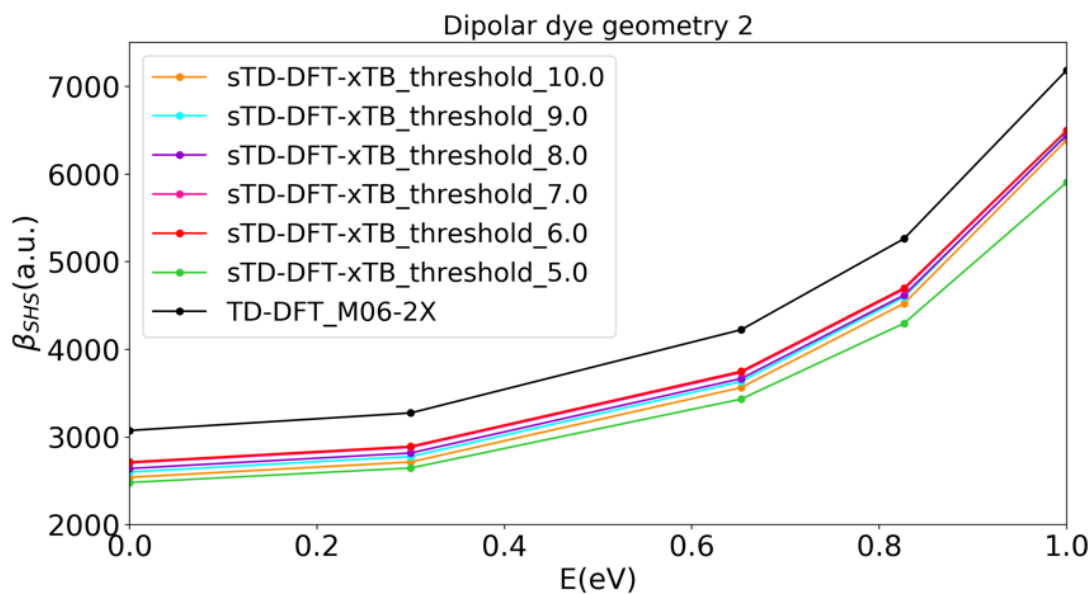


Figure B.9 – Tuning of the energy threshold E_{th} for the geometry 2 of the isolated molecule (Fig. B.4a). In all sTD-DFT-xTB calculations, $y_J = 4.0$ and $y_K = 2.0$.

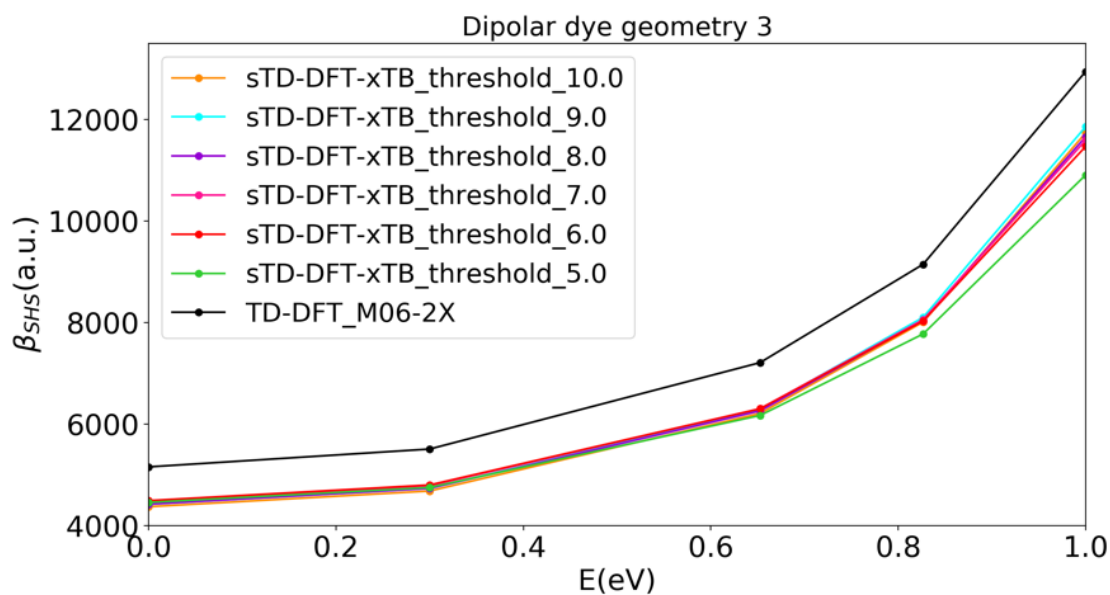


Figure B.10 – Tuning of the energy threshold E_{th} for the geometry 3 of the isolated molecule (Fig. B.4a). In all sTD-DFT-xTB calculations, $y_J = 4.0$ and $y_K = 2.0$.

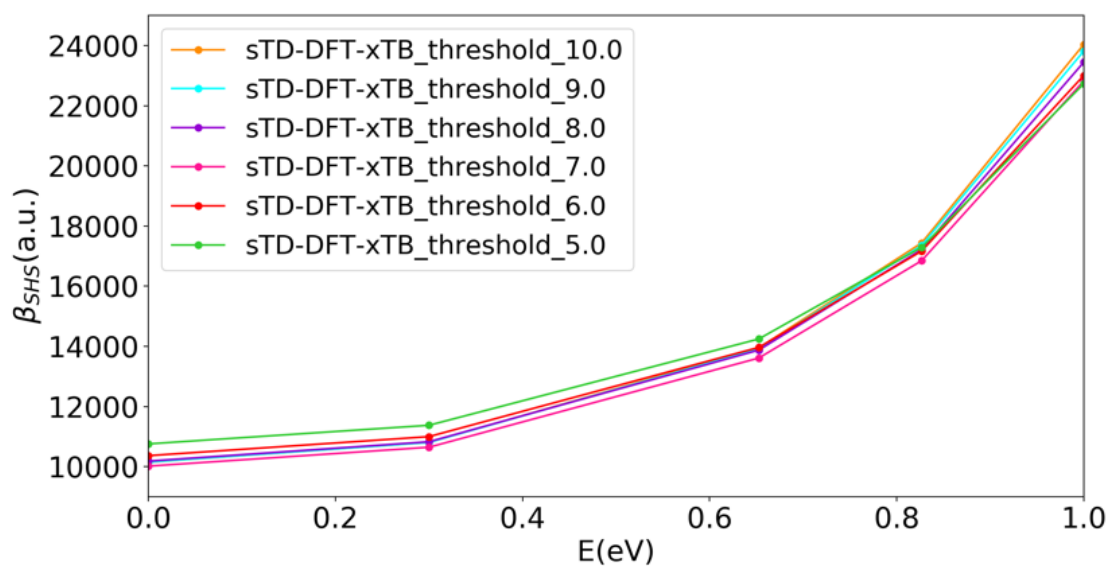


Figure B.11 – Tuning of the energy threshold E_{th} for the supramolecular aggregate shown Figure B.4b. In all sTD-DFT-xTB calculations, $y_J = 4.0$ and $y_K = 2.0$.

B.2.3 Optimization of the sTD-DFT-vTB parameters

We compare now the first hyperpolarizabilities calculated using the sTD-DFT-vTB method, restricted to valence-shell molecular orbitals, with those computed using the TD-DFT and sTD-DFT-xTB approaches. The y_J parameter is first tuned on the three test geometries of the isolated molecule, while y_K is kept fixed at 2.0. Figures B.12, B.13 and B.14 show that reference TD-DFT β values are well reproduced when using $y_J = 0.4$, a much smaller value than that optimized in the case of sTD-DFT-xTB.

Then, the sTD-DFT-vTB method with $y_J = 0.4$ and $y_K = 2.0$ is tested using energy thresholds decreasing from 10 to 5 eV. As shown in Figures B.15, B.16 and B.17, decreasing E_{th} slightly shifts upward the frequency dispersion curves, without any change in their shape. All E_{th} values provide frequency dispersion profiles of β in quite good agreement with TD-DFT, which allows us to consider the smallest E_{th} value for speeding up calculations. Again, the conclusion drawn for the isolated dyes can be extended to the case of larger aggregates, as shown in Figure B.18. Therefore, one can conclude that a threshold of 5 eV can be used for sTD-DFT-vTB calculations on large aggregates.

Finally, the frequency dispersion curves of the first hyperpolarizability, calculated at the sTD-DFT-xTB ($y_J = 4.0$, $y_K = 2.0$ and $E_{th} = 6$ eV) and sTD-DFT-vTB ($y_J = 0.4$, $y_K = 2.0$ and $E_{th} = 5$ eV) levels for the three test geometries of the isolated molecule, are compared in Figure B.19. Results obtained for the supramolecular aggregate are displayed in Figure B.20. The curves show that restricting the MO space to the valence shell from sTD-DFT-xTB to sTD-DFT-vTB does not introduce significant loss in accuracy, while the execution times are reduced by a factor 2.

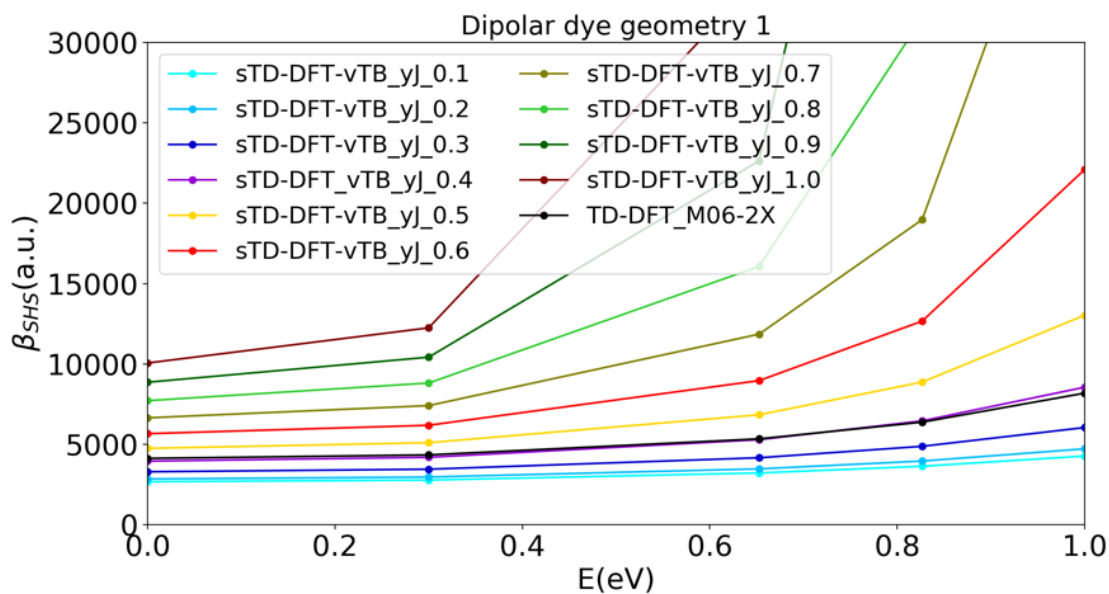


Figure B.12 – Tuning of the y_J parameter for the geometry 1 of the isolated molecule (Fig. B.4a). In all sTD-DFT-vTB calculations, $y_K = 2.0$ and $E_{th} = 10$ eV.

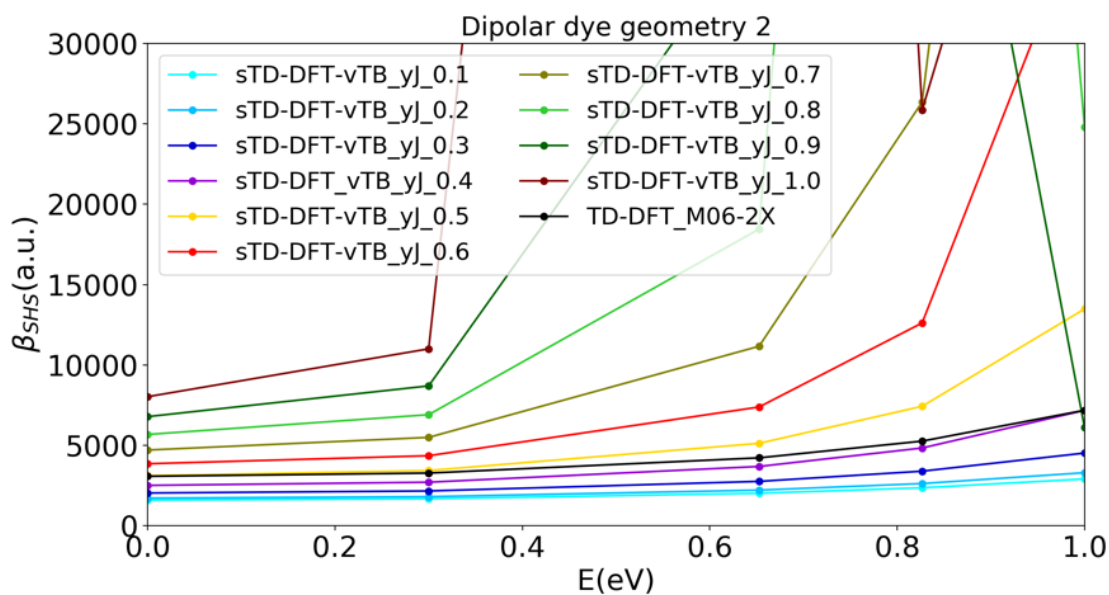


Figure B.13 – Tuning of the y_J parameter for the geometry 2 of the isolated molecule (Fig. B.4a). In all sTD-DFT-vTB calculations, $y_K = 2.0$ and $E_{th} = 10$ eV.

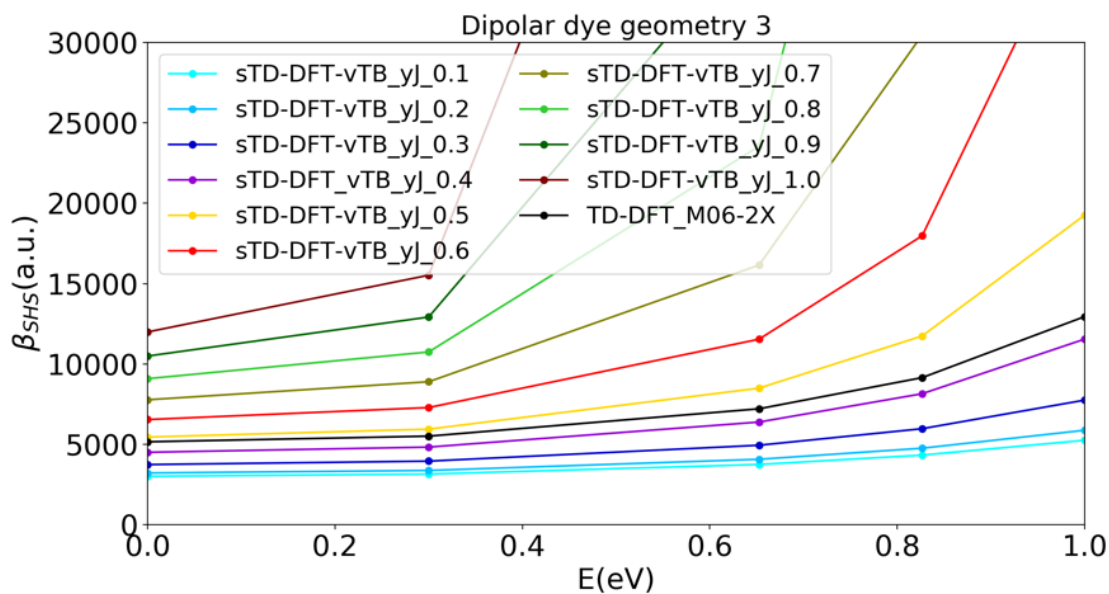


Figure B.14 – Tuning of the y_J parameter for the geometry 3 of the isolated molecule (Fig. B.4a). In all sTD-DFT-vTB calculations, $y_K = 2.0$ and $E_{th} = 10$ eV.

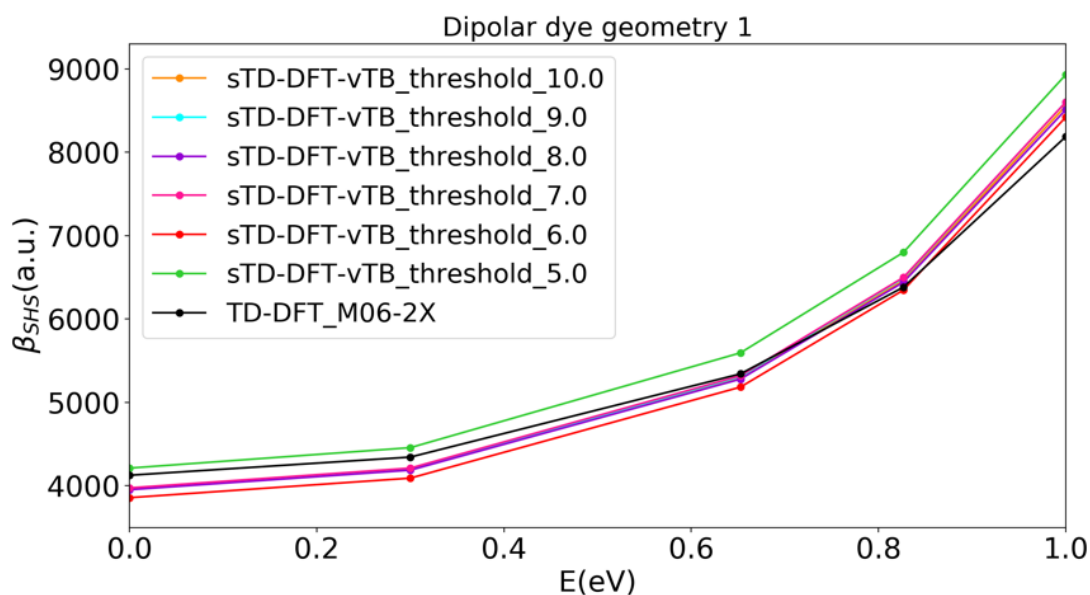


Figure B.15 – Tuning of the energy threshold E_{th} for the geometry 1 of the isolated molecule (Fig. B.4a). In all sTD-DFT-vTB calculations, $y_J = 0.4$ and $y_K = 2.0$.

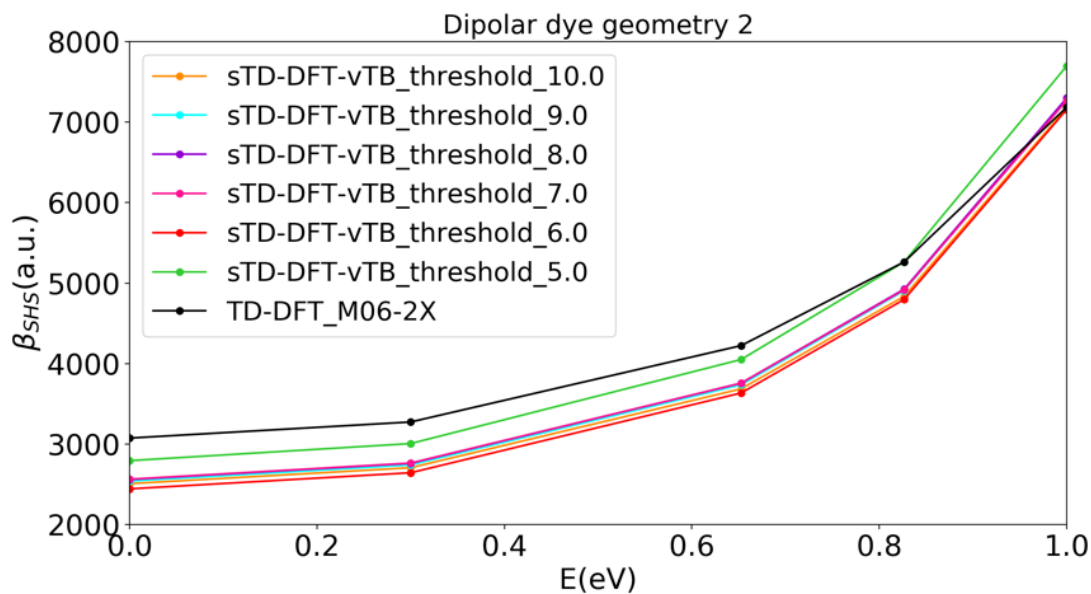


Figure B.16 – Tuning of the energy threshold E_{th} for the geometry 2 of the isolated molecule (Fig. B.4a). In all sTD-DFT-vTB calculations, $y_J = 0.4$ and $y_K = 2.0$.

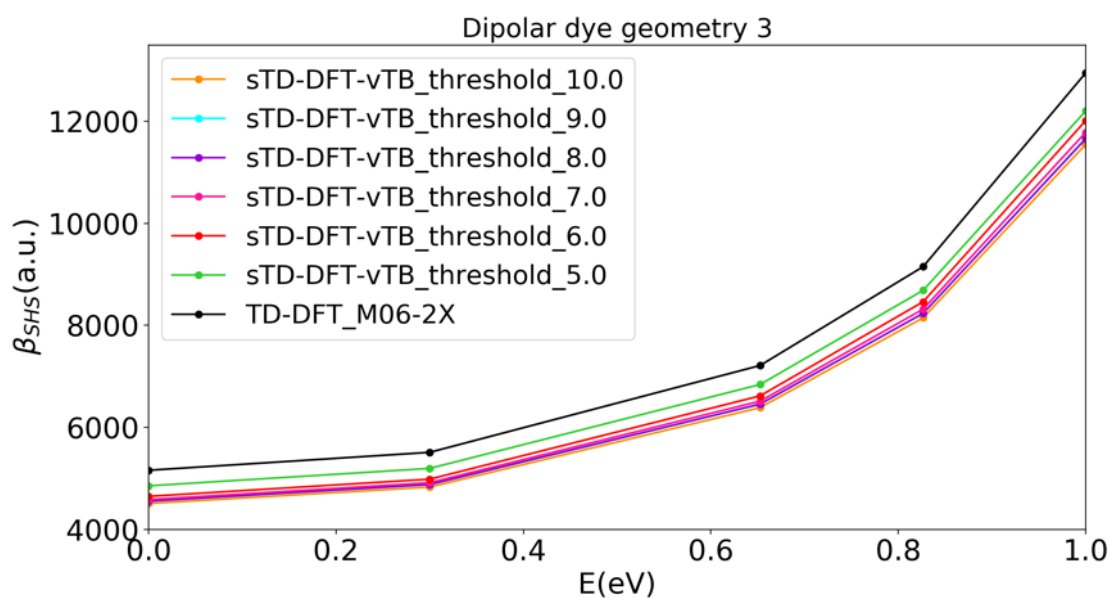


Figure B.17 – Tuning of the energy threshold E_{th} for the geometry 3 of the isolated molecule (Fig. B.4a). In all sTD-DFT-vTB calculations, $y_J = 0.4$ and $y_K = 2.0$.

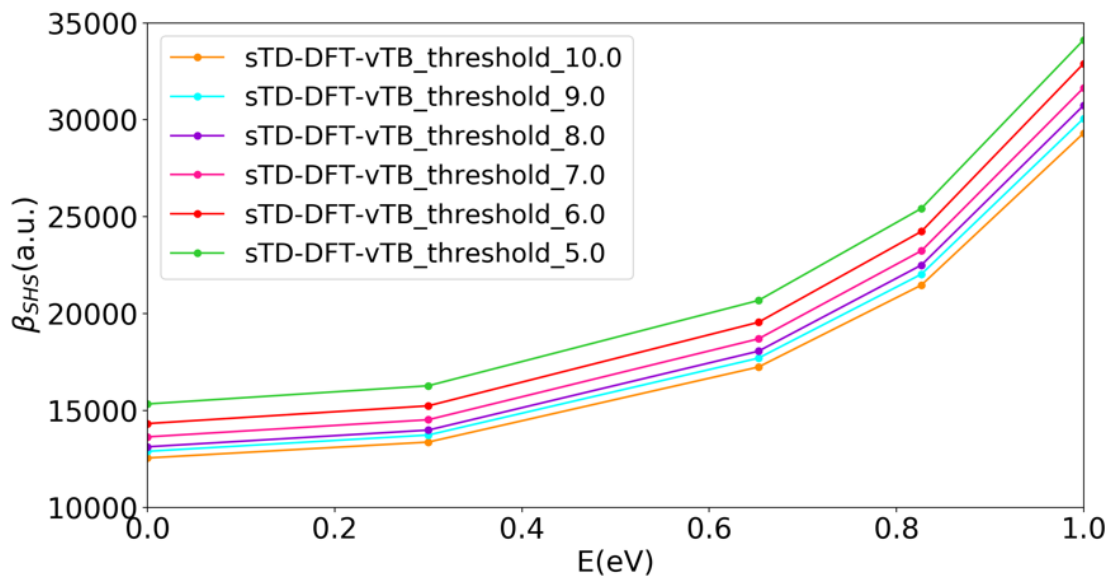


Figure B.18 – Tuning of the energy threshold E_{th} for the supramolecular aggregate shown Figure B.4b. In all sTD-DFT-vTB calculations, $y_J = 0.4$ and $y_K = 2.0$.

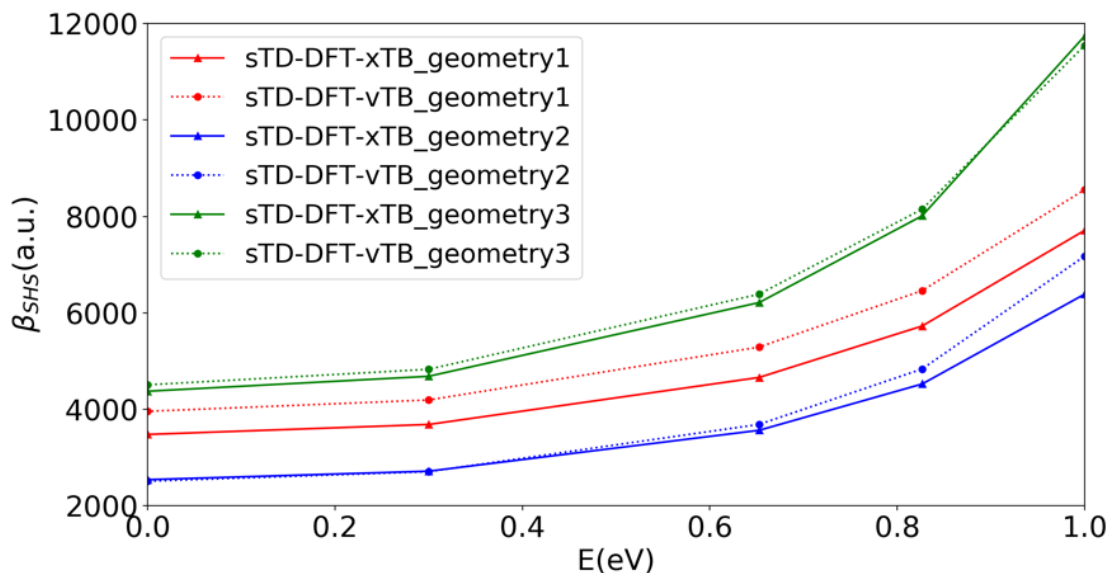


Figure B.19 – Frequency dispersion curves of the first hyperpolarizability for the three test geometries of the isolated molecule (Fig. B.4a), as calculated at the sTD-DFT-xTB ($y_J = 4.0$, $y_K = 2.0$ and $E_{th} = 6$ eV) and sTD-DFT-vTB ($y_J = 0.4$, $y_K = 2.0$ and $E_{th} = 5$ eV) levels.

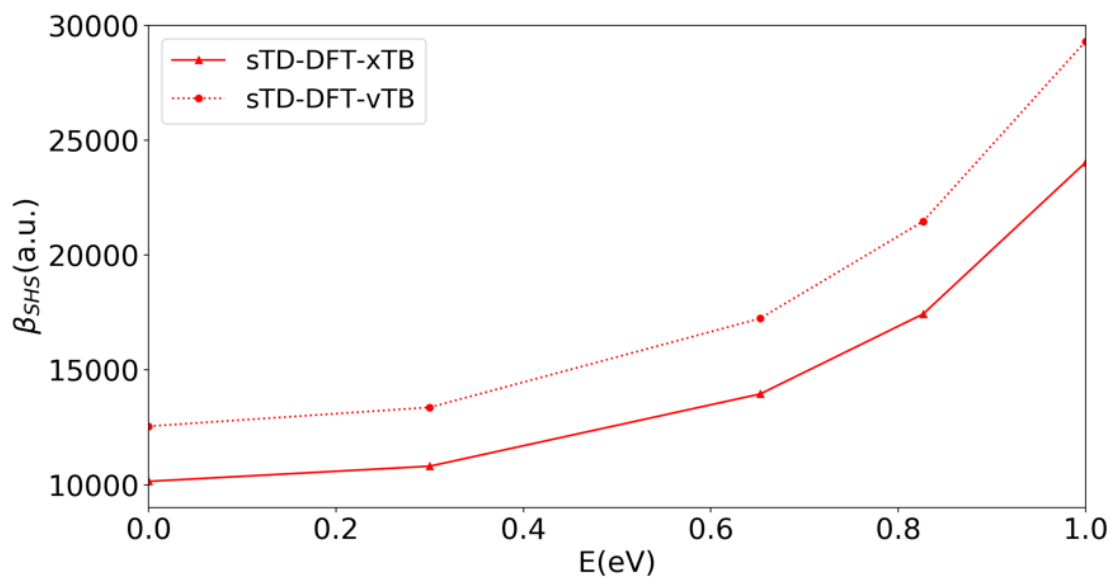


Figure B.20 – Frequency dispersion curves of the first hyperpolarizability for the supramolecular aggregate (Fig. B.4b), as calculated at the sTD-DFT-xTB ($y_J = 4.0$, $y_K = 2.0$ and $E_{th} = 6$ eV) and sTD-DFT-vTB ($y_J = 0.4$, $y_K = 2.0$ and $E_{th} = 5$ eV) levels.

B.3 Free energy of pairs of chromophores in water

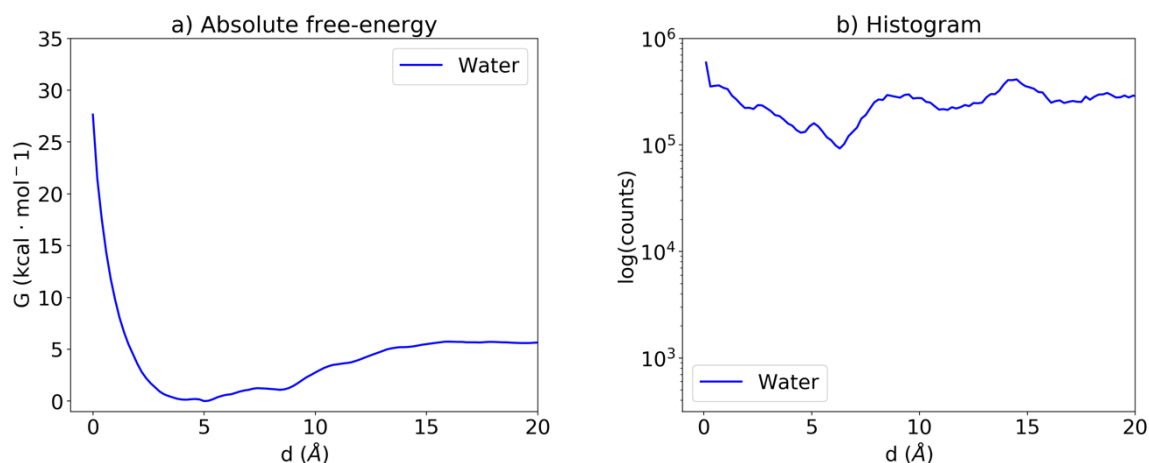


Figure B.21 – Free-energy as a function of the distance d between mass centers of the two dyes (a), as well as counts of distance values along the dynamics, showing that every distance d is statistically explored. Simulations at equilibrium were run for 20 ns on boxes containing two dipolar dyes in solvent, using the NpT ensemble at $p = 1.01325$ bar and $T = 300$ K, and the adaptive biasing force method for the calculation of free energy.^[6]

B.4 Morphology of the nanoparticles

B.4.1 Global shape of the nanoparticles

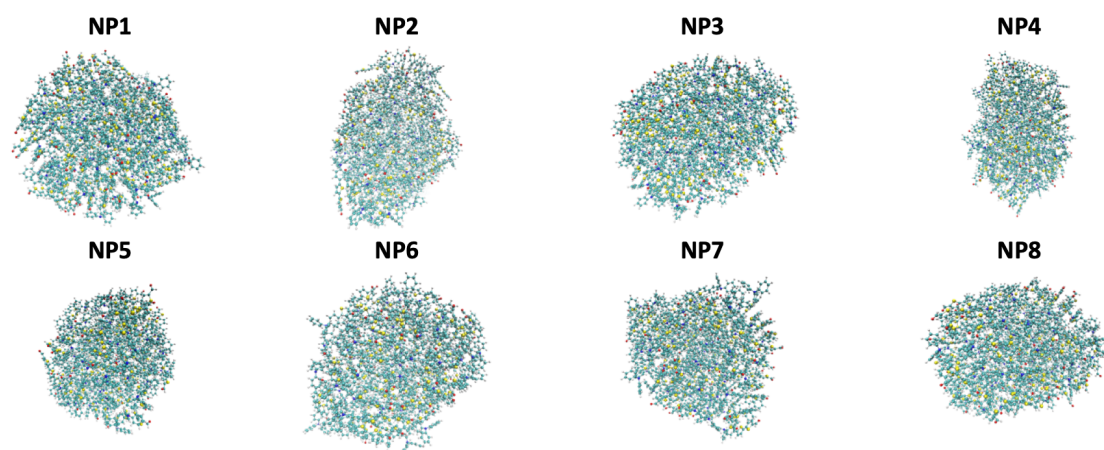


Figure B.22 – Shape of the nanoparticles issued from the 8 replicated MD trajectories.

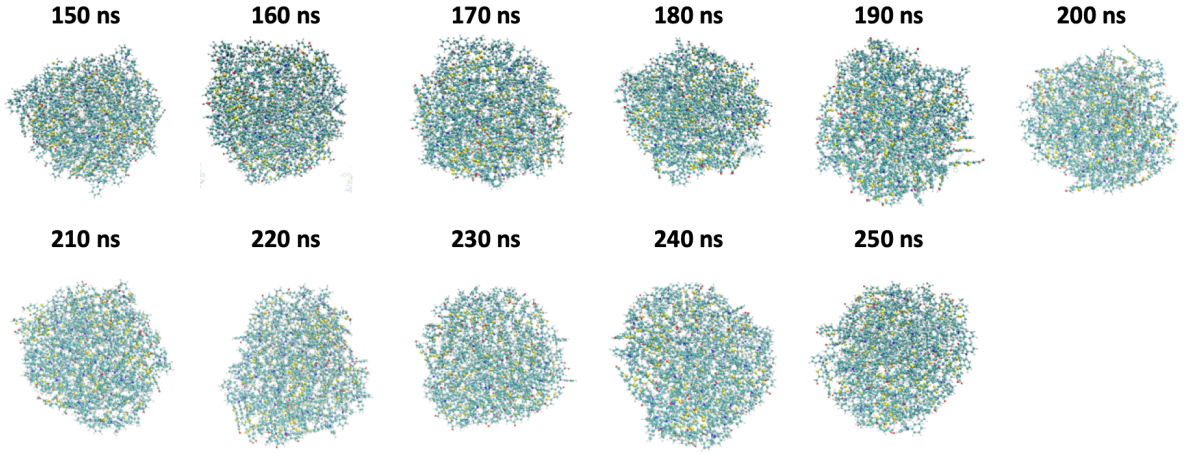


Figure B.23 – Time evolution of the shape of NP1 along the MD simulation.

B.4.2 Characterization of the shape of the nanoparticles

The moment of inertia tensor was calculated as a function of time for the largest nanoparticles for the 8 aggregation experiments and diagonalized, obtaining the eigenvalues $I_{zz} > I_{yy} > I_{xx}$, from which the corresponding component of the radius of gyration was obtained as $r_i = \sqrt{I_{ii}/M}$ where M is the NP mass (Figure B.24). Following Varga and coworkers,^[7] the shape of the particles was further characterized by calculating the two aspect ratios $\kappa_1 = r_z/r_x > \kappa_2 = r_z/r_y > 1$ and the biaxiality parameter $\theta = (\kappa_1 - 1)^{-1}(\kappa_1/\kappa_2 - \kappa_2)$, which takes the value of -1 for a perfectly uniaxial disc, +1 for a perfectly uniaxial rod, and 0 for a perfectly biaxial ellipsoid (Table B.3). Most NPs assume nearly spherical shape (with aspect ratios close to 1) with a certain disc-like character ($\theta < 0$), without any evident correlation between the orientation of the electric dipole moment and the ones the principal inertia axes, although a much larger number of simulations would be needed to confirm this result.

Table B.3 – Components of the radius of gyration (r_i , in Å), aspect ratios (κ_1 , and κ_2) and biaxiality parameter θ , calculated over the last 50 ns of the trajectories for each NP, and (last line) averaged over the 8 NPs.

	r_x	r_y	r_z	κ_1	κ_2	θ
NP1	14.3±0.1	14.5±0.1	15.6±0.3	1.10±0.02	1.02±0.01	0.6±0.3
NP2	13.5±0.2	15.5±0.2	16.2±0.2	1.20±0.02	1.15±0.02	-0.5±0.1
NP3	12.8±0.2	16.1±0.3	16.8±0.2	1.32±0.03	1.25±0.04	-0.6±0.1
NP4	13.2±0.1	15.8±0.1	16.7±0.2	1.26±0.01	1.20±0.02	-0.5±0.1
NP5	13.7±0.1	15.1±0.1	15.7±0.1	1.15±0.02	1.10±0.02	-0.4±0.1
NP6	13.9±0.2	15.1±0.2	15.5±0.1	1.12±0.02	1.09±0.02	-0.6±0.2
NP7	13.5±0.1	15.6±0.1	15.9±0.2	1.17±0.02	1.15±0.02	-0.7±0.1
NP8	13.8±0.1	14.9±0.1	16.0±0.1	1.16±0.01	1.08±0.01	0.0±0.1
Av.	13.6±0.4	15.3±0.5	16.0±0.5	1.18±0.07	1.13±0.07	-0.4±0.4

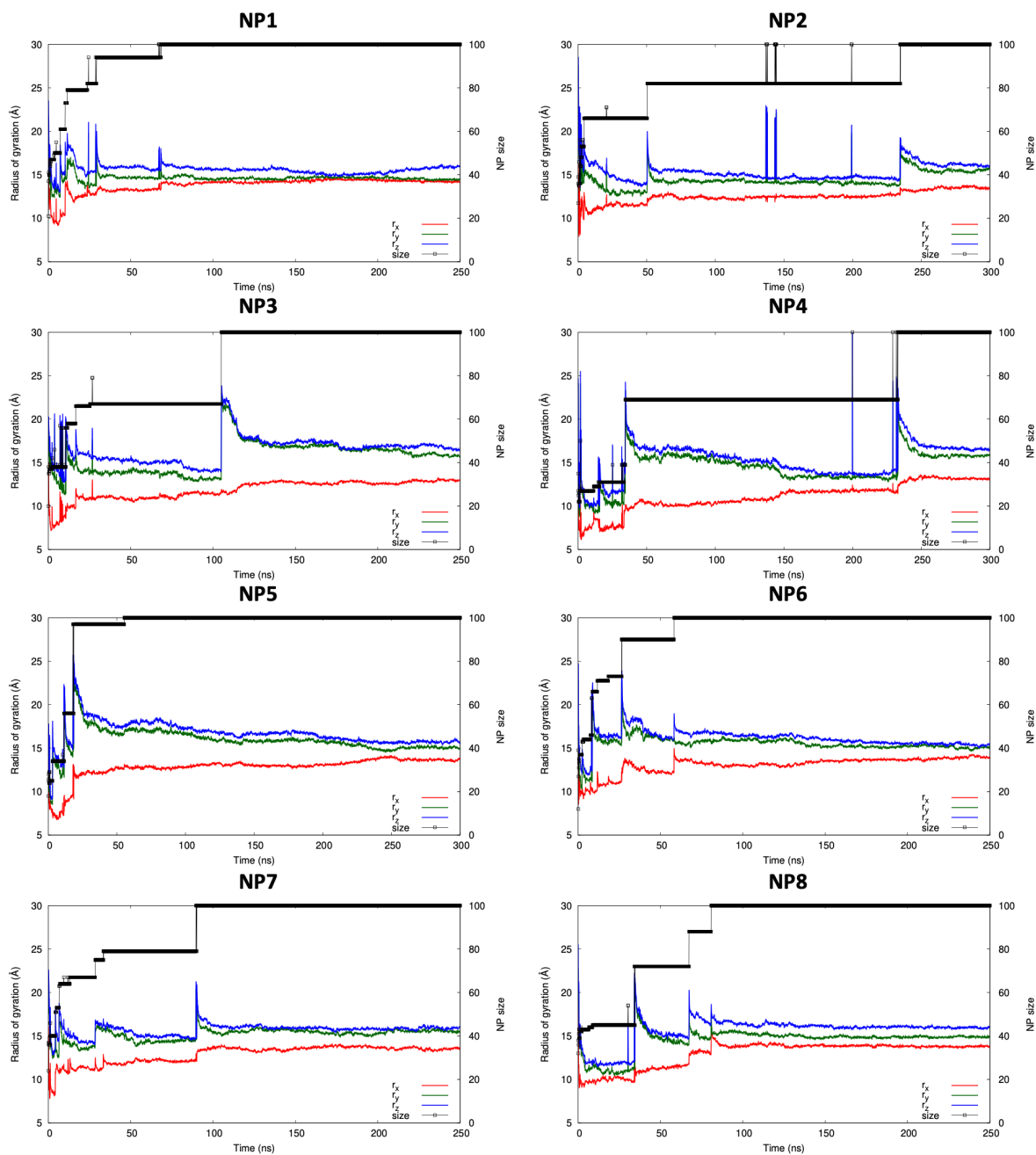


Figure B.24 – Time-evolution of the size and radius of gyration of the biggest nanoparticle with simulation time for the 8 replicated MD simulations.

B.4.3 Time-evolution and statistical distributions of structural and electronic properties

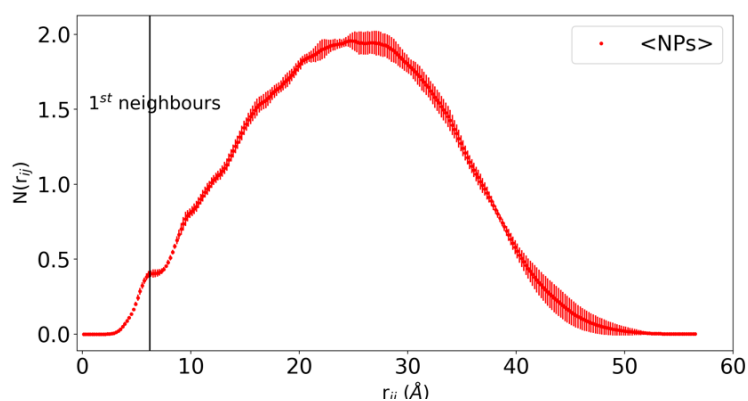


Figure B.25 – Evolution of the mean density of neighbours as a function of the distance r_{ij} between the centers of mass of molecules.

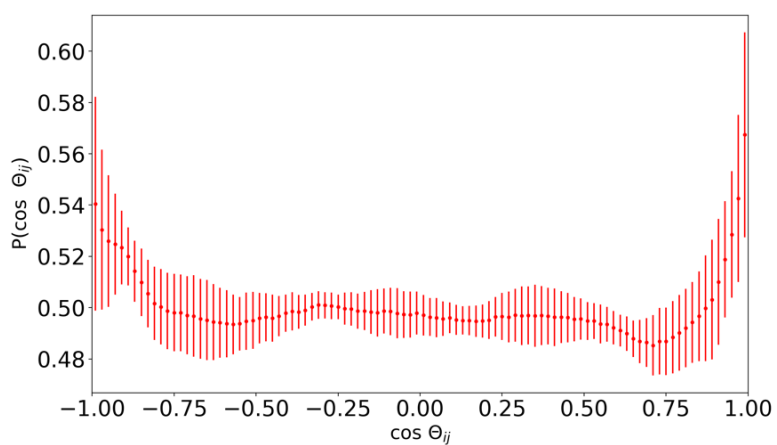


Figure B.26 – Distribution of $\cos \theta_{ij}$, where θ_{ij} is the angle between the dipole moment vectors of any pair of dyes at a distance lower than 7.5 Å.

B.4.4 π -aggregation of the molecular units

In this section, the π -stacking of the molecular units within the NP is investigated, using the following definitions:

Neighbour: a molecule with at least one non-H atom at a distance lower than 4 Å from the non-H atoms of the target molecule.

π -stacked neighbour: a molecule which is neighbour and has at least ten interatomic distances below 4 Å. Only distances between atoms 14, 15, 16, 17, 18, 19, 20, 35, 36, 37, 38, 41, 42, 43, 44, 45 of the two molecules are considered (see the scheme below for atom labels). Note that this is actually a loose definition, which includes also possible herringbone situations.

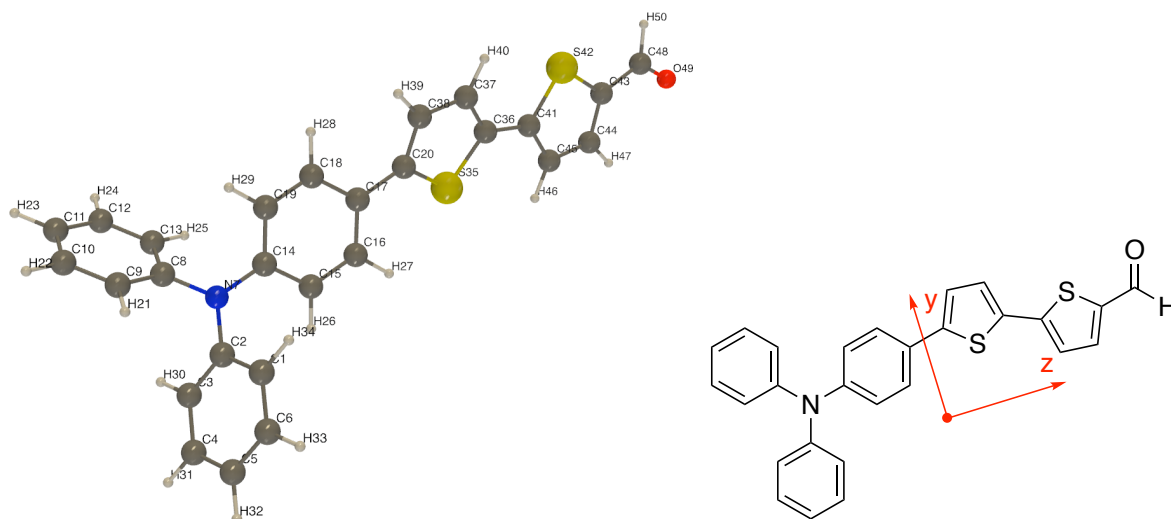
z-axis: unit vector parallel to the atom 14-atom 43 distance vector.

y-axis: unit vector perpendicular to z, obtained from the atom 35-atom 37 distance vector (removing its projection along z).

Relative orientation of π -stacked neighbours: defined by the scalar products between the unit vectors of the pair of interacting molecules:

$$\vec{z}_1 \cdot \vec{z}_2 = \cos(\angle \vec{z}_1, \vec{z}_2)$$

$$|\vec{y}_1 \cdot \vec{y}_2| = |\cos(\angle \vec{y}_1, \vec{y}_2)|$$



B.5 NLO properties of the nanoparticles

B.5.1 NLO properties of the final nanoparticles of each MD run

Table B.4 – Static first hyperpolarizabilities (β_{HRS} , in 10^3 a.u.) and depolarization ratios (DR) of the final nanoparticles issued from the 8 replicated MD trajectories (Figure B.21), evaluated using the tensor sum approximation at the TD-DFT and sTD-DFT-vTB levels, as well as from sTD-DFT-vTB calculations performed on the full nanoparticles.

	TD-DFT ^a (tensor sum)		sTD-DFT-vTB ^b (tensor sum)		sTD-DFT-vTB ^b (full calculation)			
	β_{HRS}	DR	β_{HRS}	DR	β_{HRS}	DR	R_1^c	R_2^d
NP1	58.3	5.5	55.2	4.9	45.9	4.8	0.9	0.83
NP2	23.4	2.9	22.1	3.4	22.4	4.3	0.9	1.01
NP3	31.4	4.1	31.1	4.3	19.6	2.7	1.0	0.63
NP4	39.0	5.1	31.5	4.3	25.2	5.1	0.8	0.80
NP5	56.1	5.6	63.7	6.3	55.5	6.2	1.1	0.87
NP6	47.9	3.7	51.5	4.4	40.4	4.4	1.1	0.78
NP7	46.8 ^e	3.6 ^e	44.9	4.2	34.3	4.7	1.0	0.76
NP8	47.8	5.6	43.0	5.0	33.5	5.1	0.9	0.78
av.	43.8	4.5	42.9	4.6	34.6	4.7	1.0	0.8
\pm std. dev.	± 11.9	± 1.1	± 14.0	± 0.8	± 12.3	± 1.0	± 0.10	± 0.11

^a M06-2X/6-311+G(d) in gas phase

^b using $y_J = 0.4$, $y_K = 2.0$ and $E_{th} = 5.0$ eV

^c $R_1 = \beta_{HRS}^{sTD-DFT-vTB}(\text{tensor sum}) / \beta_{HRS}^{TD-DFT}(\text{tensor sum})$

^d $R_2 = \beta_{HRS}^{sTD-DFT-vTB}(\text{full calc.}) / \beta_{HRS}^{sTD-DFT-vTB}(\text{tensor sum})$

^e one molecule was removed from the calculations due to numerical instability

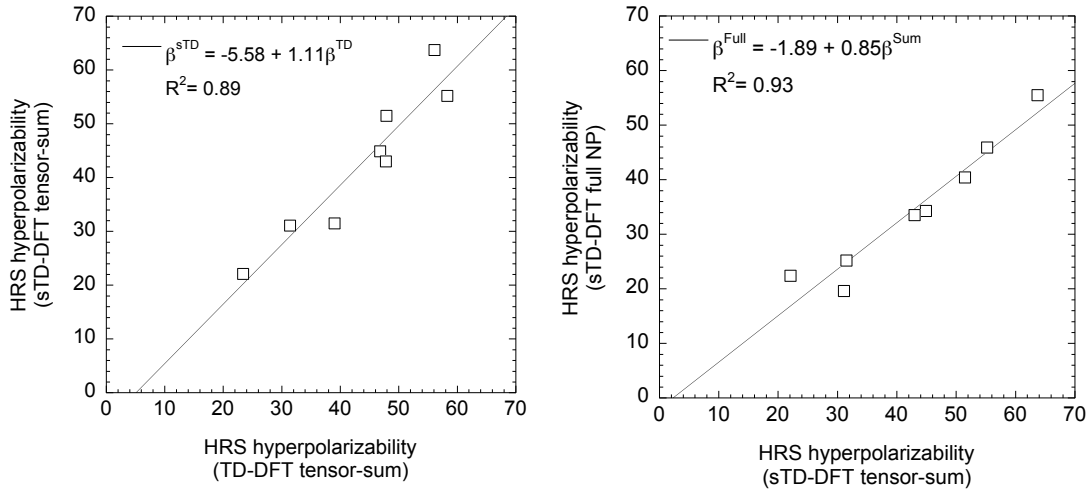


Figure B.27 – Linear correlations between (a) static first hyperpolarizabilities (in 10^3 a.u.) evaluated using the tensor sum approximation at the TD-DFT and sTD-DFT-vTB levels, and between (b) sTD-DFT-vTB static first hyperpolarizabilities calculated using the tensor sum approximation and calculations performed on the full nanoparticles.

Table B.5 – Dynamic ($\lambda = 1064$ nm) first hyperpolarizabilities (β_{HRS} , in 10^3 a.u.) and depolarization ratios (DR) of the final nanoparticles issued from the 8 replicated MD trajectories (Figure B.21), evaluated using the tensor sum approximation at the TD-DFT and sTD-DFT-vTB levels, as well as from sTD-DFT-vTB calculations performed on the full nanoparticles.

	TD-DFT ^a (tensor sum)		sTD-DFT-vTB ^b (tensor sum)		sTD-DFT-vTB ^b (full calculation)			
	β_{HRS}	DR	β_{HRS}	DR	β_{HRS}	DR	R_1^c	R_2^d
NP1	317.0	6.3	325.8	5.8	3194.5	4.8	1.0	9.81
NP2	112.0	3.7	248.2	3.4	106.4	3.0	2.2	0.43
NP3	110.7	3.0	161.2	3.8	616.9	3.6	1.5	3.83
NP4	160.1	5.1	238.9	5.2	2259.4	5.1	1.5	9.46
NP5	237.6	5.9	343.1	7.2	369.9	4.7	1.4	1.08
NP6	185.0	3.6	238.7	4.5	212.7	4.9	1.3	0.89
NP7	234.0	3.4	827.6	5.0	156.6	2.1	3.5	0.19
NP8	156.4	5.5	167.9	5.3	634.3	5.0	1.1	3.78
av.	189.1	4.6	318.9	5.0	943.8	4.2	/	/
\pm std. dev.	± 70.5	± 1.3	± 215.4	± 1.2	± 1145.4	± 1.1		

^a M06-2X/6-311+G(d) in gas phase

^b using $y_J = 0.4$, $y_K = 2.0$ and $E_{th} = 5.0$ eV

^c $R_1 = \beta_{HRS}^{sTD-DFT-vTB}(\text{tensor sum}) / \beta_{HRS}^{TD-DFT}(\text{tensor sum})$

^d $R_2 = \beta_{HRS}^{sTD-DFT-vTB}(\text{full calc.}) / \beta_{HRS}^{sTD-DFT-vTB}(\text{tensor sum})$

B.5.2 Evolution in time of the NLO properties

Table B.6 – Evolution in time of the dynamic ($\lambda = 1064$ nm) first hyperpolarizabilities (β_{HRS} , in 10^3 a.u.) and depolarization ratios (DR) of the nanoparticles along the 8 replicated MD trajectories, evaluated using the tensor sum approximation at the TD-DFT/M06-2X/6-311+G(d) level in gas phase. The starting time is taken when the 100 molecules collapse into a single structure.

NP1

Simulation time (ns)	β_{HRS}	DR
100	104.2	2.0
110	111.5	3.5
120	95.0	5.1
130	172.9	5.8
140	77.9	3.7
150	119.3	3.4
160	102.3	3.5
170	118.6	2.5
180	89.6	3.6
190	102.3	3.9
200	196.1	5.8
210	223.9	4.9
220	260.6	6.4
230	115.5	4.7
240	193.8	6.5
250	317.0	6.3
av. \pm std. dev.	156.1 ± 72.9	4.48 ± 1.42

NP2

Simulation time (ns)	β_{HRS}	DR
250	178.8	4.9
260	172.3	8.7
270	234.4	5.6
280	142.7	2.5
290	116.1	2.9
300	112.0	3.7
av. \pm std. dev.	172.7 ± 70.1	4.72 ± 2.28

NP3

Simulation time (ns)	β_{HRS}	DR
190	126.8	2.3
200	126.3	2.7
210	155.2	1.9
220	142.3	5.0
230	165.3	5.5
240	162.6	4.8
250	110.7	3.0
av. \pm std. dev.	132.7 ± 30.5	3.6 ± 1.5

NP4

Simulation time (ns)	β_{HRS}	DR
250	140.9	2.1
260	156.8	2.8
270	105.8	3.0
280	205.0	3.0
290	111.4	2.0
300	160.1	5.1
av. \pm std. dev.	135.3 \pm 43.4	3.0 \pm 1.1

NP5

Simulation time (ns)	β_{HRS}	DR
140	186.4	4.3
150	197.4	3.3
160	171.4	3.1
170	166.5	4.2
180	184.8	3.3
190	190.3	3.6
200	215.5	4.1
210	285.4	6.8
220	230.3	3.5
230	243.6	5.4
240	198.9	5.4
250	204.6	5.1
260	155.5	3.2
270	171.9	3.7
280	232.5	4.0
290	144.1	3.6
300	237.6	5.9
av. \pm std. dev.	204.4 \pm 39.1	4.3 \pm 1.1

NP6

Simulation time (ns)	β_{HRS}	DR
140	251.0	7.0
150	116.4	5.8
160	137.4	3.8
170	167.2	4.3
180	175.0	6.1
190	211.6	5.3
200	115.5	1.7
210	179.7	3.0
220	179.8	2.2
230	208.6	3.4
240	170.9	4.6
250	185.0	3.6
av. \pm std. dev.	174.8 \pm 39.1	4.2 \pm 1.6

NP7

Simulation time (ns)	β_{HRS}	DR
130	267.7	5.7
140	188.4	4.1
150	277.8	7.0
160	166.4	3.4
170	207.2	4.6
180	178.7	3.6
190	206.6	3.4
200	203.9	5.1
210	318.6	8.1
220	242.0	7.3
230	356.7	6.4
240	180.8	4.4
250	234.0	3.4
av. \pm std. dev.	233.0 ± 57.9	5.1 ± 1.6

NP8

Simulation time (ns)	β_{HRS}	DR
120	134.8	3.5
130	102.2	1.8
140	157.7	2.5
150	161.9	4.8
160	171.2	4.9
170	156.8	6.7
180	178.2	6.6
190	116.2	2.9
200	215.4	7.7
210	179.9	6.6
220	143.4	4.2
230	238.7	7.1
240	193.3	4.2
250	156.4	5.5
av. \pm std. dev.	164.7 ± 36.3	4.9 ± 1.8

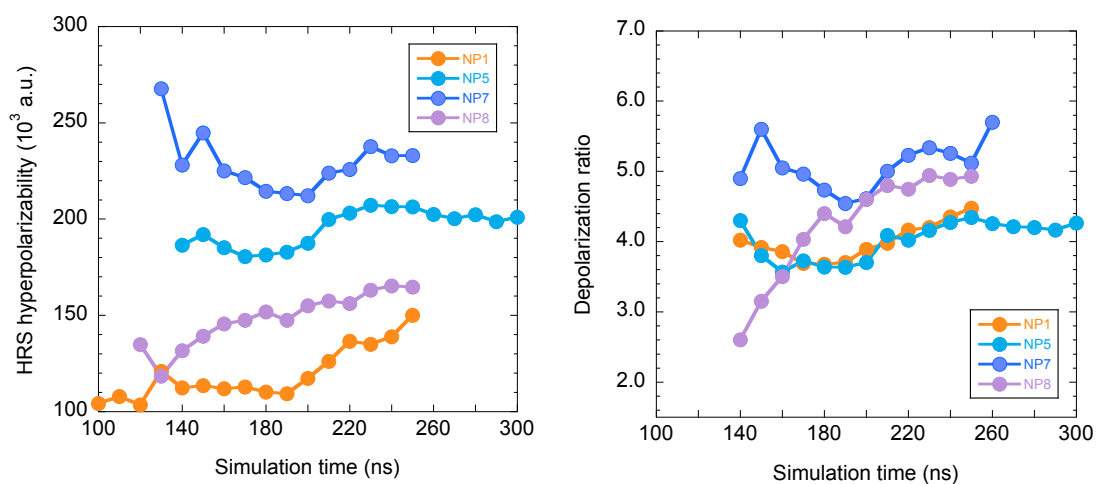


Figure B.28 – Time evolution of the cumulative averages of β_{HRS} (left) and DR (right) values for NP1, 5 7 and 8, as calculated using the tensor-sum approximation at the TD-DFT:M06-2X/6-311+G(d) level.

B.6 Absorption properties of π -stacked dimers

B.6.1 Comparison between TD-DFT and sTD-DFT-vTB calculations

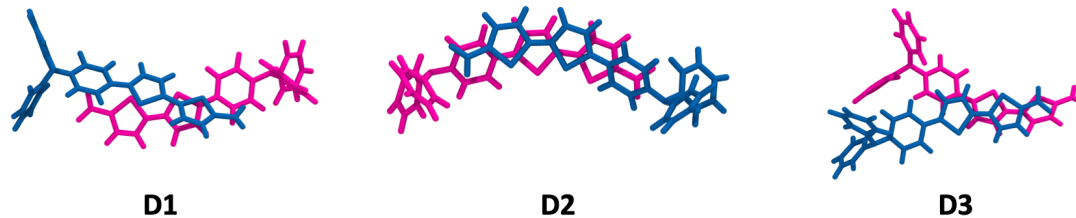


Figure B.29 – Representative π -stacked dimer structures extracted from the NPs.

Table B.7 – Excitation energies (ΔE , eV) and oscillator strengths (f) associated to the main low-lying $S_0 \rightarrow S_i$ electronic transitions ($\Delta E \leq 4$ eV, $f \geq 0.1$) calculated for the isolated dye and of the π -stacked dimers.

	TD-DFT ^a			sTD-DFT-vTB ^b		
	S_i	ΔE	f	S_i	ΔE	f
Monomer ^c	S_1	3.15	1.28	S_1	3.17	1.16
D1	S_1	2.74	0.10	S_3	3.07	0.24
	S_2	3.05	1.81	S_3	3.34	2.59
	S_3	3.23	0.23	S_3	3.73	0.17
D2	S_2	2.85	1.30	S_3	2.86	0.21
	S_3	3.14	0.58	S_4	3.24	1.20
	S_4	3.30	0.09	S_5	3.40	1.22
				S_6	3.80	0.13
D3	S_1	2.49	0.82	S_1	2.58	1.14
	S_3	3.10	1.25	S_4	3.32	1.54
				S_5	3.54	0.10

^a M06-2X/6-311+G(d) calculations in B3LYP/cc-pVTZ geometry. ^b Using $y_J = 4.0$, $y_K = 2.0$ and $E_{th} = 5.0$ eV. ^c In the trans form.

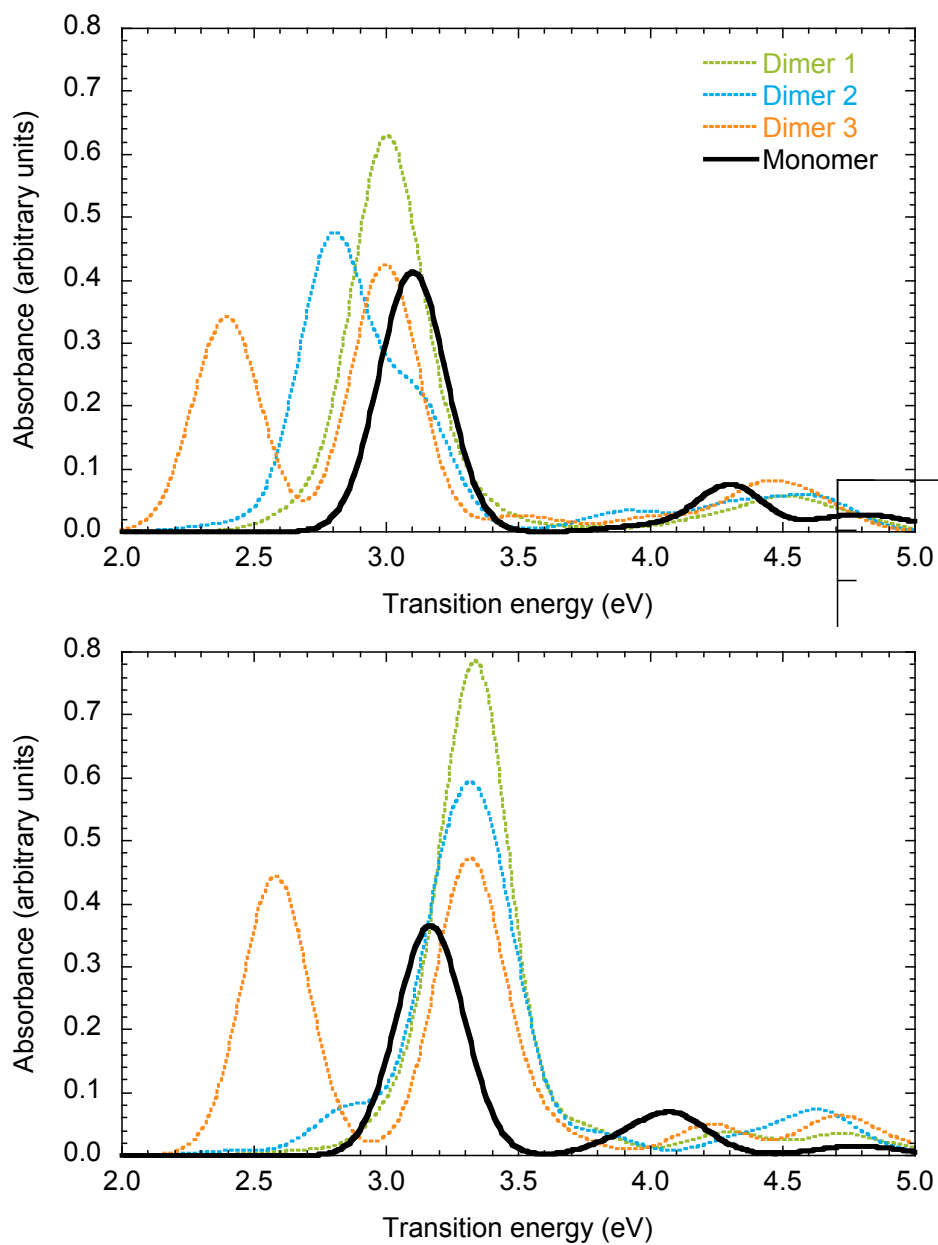


Figure B.30 – Absorption spectra of π -stacked dimer structures represented in Figure B.28, calculated at the TD-DFT (top) and sTD-DFT-vTB (bottom) levels.

B.6.2 Diabatization of low-lying excited states

Diabatization of the electronic transitions was performed for singlet excited states of three representative π -stacked dimers extracted from the NPs (Figure 4.14), by means of the Boys localization scheme^[8] implemented in the Q-Chem program.^[9] Computation of the diabatic states ($\{Z_i\}$) was performed on the basis of adiabatic states calculated in vacuum at the M06-2X/6-311+G(d) level using the Tamm–Dancoff approximation (TDA),^[10] since the localization scheme is not implemented for TD-DFT states. The number of adiabatic states considered corresponds to the number of intramolecular and intermolecular charge-transfer contributions. In practice, only the lowest 4 excited singlets (S_1 - S_4) involving transitions from the HOMO-1 and HOMO to the LUMO and LUMO+1 were considered for dimers D1 and D2. For D3, S_5 has been considered instead of S_4 .

Dimer D1

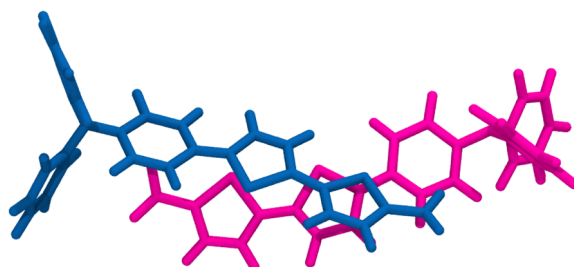


Table B.8a – Energies of adiabatic (S_i) states (in eV), oscillator strengths, and contributions of electronic excitations (in %) in dimer **D1**, as calculated using TD-DFT and TDA. H = HOMO; L = LUMO.

	TD-DFT		TDA		contributions
	ΔE	f	ΔE	f	
S_1	2.742	0.098	2.849	0.096	81% H \rightarrow L
S_2	3.053	1.810	3.191	1.242	82% H \rightarrow L+1 08% H \rightarrow L
S_3	3.237	0.238	3.298	1.414	81% H-1 \rightarrow L
S_4	3.442	0.076	3.466	0.213	81% H-1 \rightarrow L+1 06% H-1 \rightarrow L

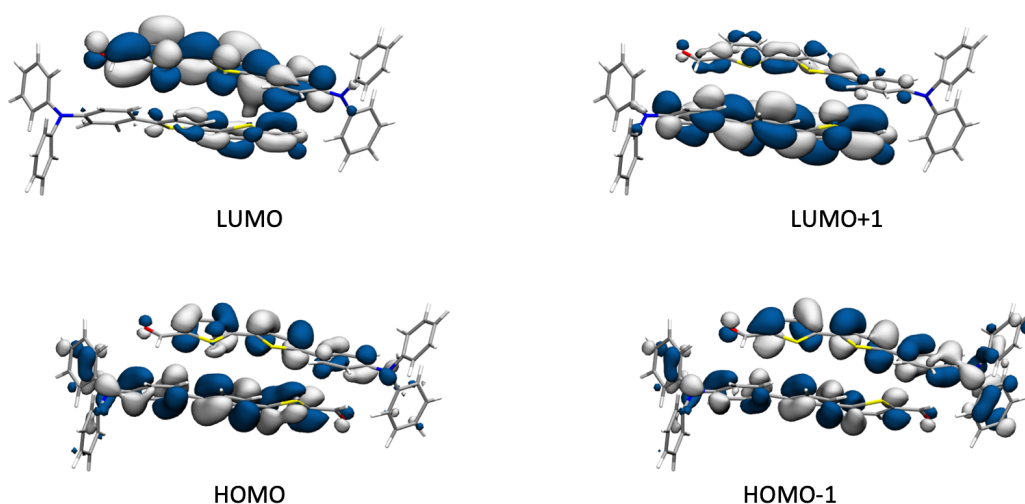


Figure B.31 – Sketch of the frontier orbitals of dimer **D1**.

Table B.8b – Energies of the TDA adiabatic (S_i) states (in eV, oscillator strength in parenthesis) of dimer **D1**, and their diabatic composition in terms of intra (in blue) and intermolecular (in orange) contributions and Z_i states: $Z_{intra} = Z_1 + Z_2$ and $Z_{inter} = Z_3 + Z_4$.

i	S_i	Z_{intra}	Z_{inter}	Z_1	Z_2	Z_3	Z_4
1	2.85 (0.10)	73	27	47	26	21	6
2	3.19 (1.24)	52	48	6	47	34	13
3	3.30 (1.41)	57	43	47	10	43	0
4	3.47 (0.21)	18	82	1	17	1	81

Table B.8c – Excitation energy (in eV) and relative Mulliken fragment charges of diabatic states of dimer **D1** with respect to the ground state charge distribution.

i	Z_i	nature	molecule 1		molecule 2	
			e-	h+	e-	h+
1	3.08	intra	-0.0251	0.0233	-0.9748	0.9767
2	3.16	intra	-0.9758	0.9754	-0.0239	0.0247
3	3.17	inter	-0.0387	0.9652	-0.9615	0.0344
4	3.39	inter	-0.9766	0.0409	-0.0231	0.9589

Dimer D2

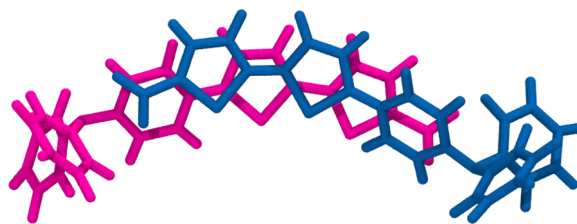


Table B.9a – Energies of adiabatic (S_i) states (in eV), oscillator strengths, and contributions of electronic excitations (in %) in dimer **D2**, as calculated using TD-DFT and TDA. H = HOMO; L = LUMO.

	TD-DFT		TDA		contributions
	ΔE	f	ΔE	f	
S_1	2.501	0.027	2.614	0.022	90% H \rightarrow L
S_2	2.859	1.290	2.980	0.871	89% H \rightarrow L+1
S_3	3.139	0.594	3.226	1.606	80% H-1 \rightarrow L 05% H-1 \rightarrow L+1
S_4	3.294	0.089	3.325	0.232	82% H-1 \rightarrow L+1 06% H-1 \rightarrow L 05% H-3 \rightarrow L+1

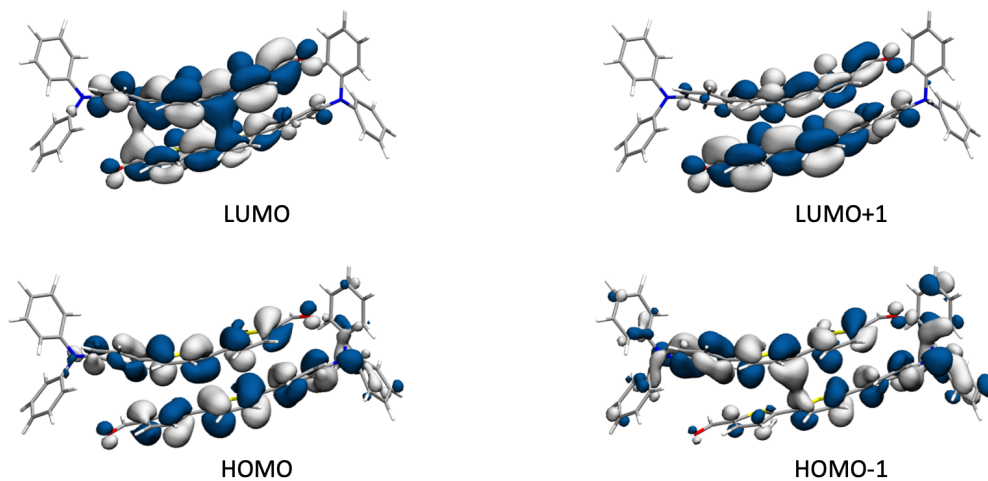


Figure B.32 – Sketch of the frontier orbitals of dimer **D2**.

Table B.9b – Energies of the TDA adiabatic (S_i) states (in eV, oscillator strength in parenthesis) of dimer **D2**, and their diabatic composition in terms of intra (in blue) and intermolecular (in orange) contributions and Z_i states: $Z_{intra} = Z_1 + Z_3$ and $Z_{inter} = Z_2 + Z_4$.

i	S_i	Z_{intra}	Z_{inter}	Z_1	Z_2	Z_3	Z_4
1	2.61 (0.02)	67	33	41	20	26	13
2	2.98 (0.87)	36	64	9	37	28	27
3	3.23 (1.61)	62	38	47	37	15	1
4	3.33 (0.23)	34	66	3	7	31	59

Table B.9c – Excitation energy (in eV) and relative Mulliken fragment charges of diabatic states of dimer **D2** with respect to the ground state charge distribution.

i	Z_i	nature	molecule 1		molecule 2	
			e-	h+	e-	h+
1	2.95	intra	-0.9875	0.9706	-0.0124	0.0293
2	3.02	inter	-0.9935	-0.0038	-0.0064	1.0038
3	3.03	intra	-0.0135	0.0055	-0.9865	0.9945
4	3.14	inter	-0.0151	0.9779	-0.9853	0.0218

Dimer D3

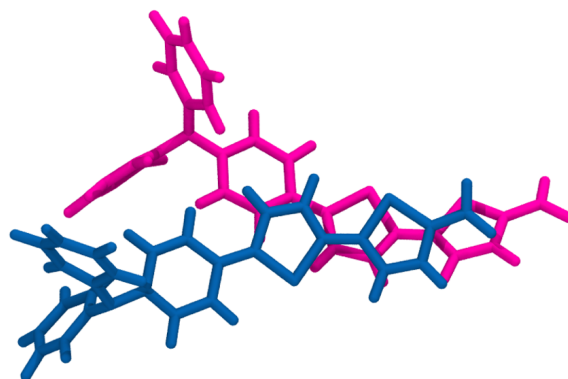


Table B.10a – Energies of adiabatic (S_i) states (in eV), oscillator strengths, and contributions of electronic excitations (in %) in dimer **D3**, as calculated using TD-DFT and TDA. H = HOMO; L = LUMO.

	TD-DFT		TDA		contributions
	ΔE	f	ΔE	f	
S_1	2.490	0.827	2.675	1.014	89% H→L
S_2	2.920	0.026	2.931	0.094	91% H-1→L
S_3	3.106	1.262	3.239	1.712	47% H→L+1 38% H-1→L+1
S_4	3.295	0.001	3.365	0.001	50% H-17→L 29% H-17→L+2
S_5	3.552	0.063	3.566	0.109	41% H-1→L+1 39% H→L+1 05% H-18→L+1

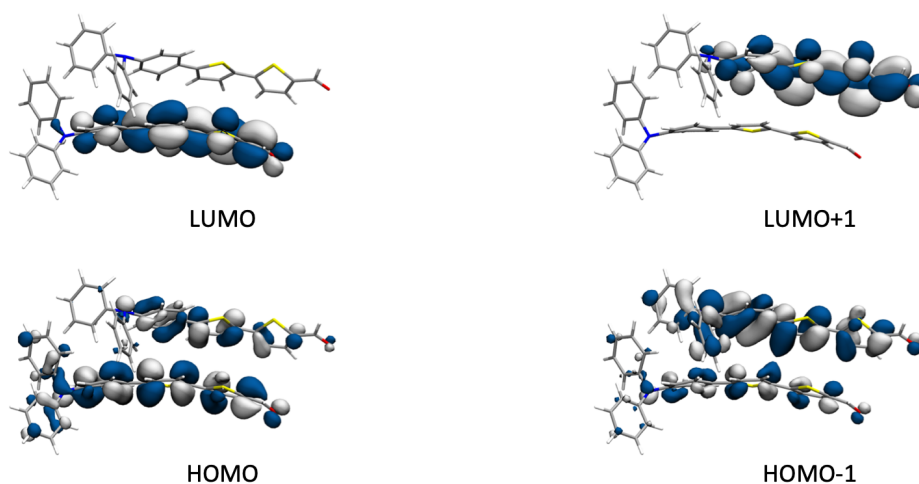


Figure B.33 – Sketch of the frontier orbitals of dimer **D3**.

Table B.10b – Energies of the TDA adiabatic (S_i) states (in eV, oscillator strength in parenthesis) of dimer **D3**, and their diabatic composition in terms of intra (in blue) and intermolecular (in orange) contributions and Z_i states: $Z_{intra} = Z_1 + Z_3 + Z_4$ and $Z_{inter} = Z_2$.

i	S_i	Z_{intra}	Z_{inter}	Z_1	Z_2	Z_3	Z_4
1	2.67 (1.01)	89	11	83	11	5	0
2	2.93 (0.09)	11	89	11	89	0	0
3	3.24 (1.71)	100	0	4	0	87	9
4	3.57 (0.11)	100	0	1	0	7	91

Table B.10c – Excitation energy (in eV) and relative Mulliken fragment charges of diabatic states of dimer **D3** with respect to the ground state charge distribution.

i	Z_i	nature	molecule 1		molecule 2	
			e-	h+	e-	h+
1	2.74	intra	-0.8357	0.8358	-0.1642	0.1639
2	2.90	inter	-0.9929	0.0023	-0.0078	0.9981
3	3.24	intra	-0.1860	0.1812	-0.8140	0.8189
4	3.54	intra	-0.9995	0.9995	-0.0003	0.0004

B.7 Assessment of M06-2X with respect to MP2

Table B.11 – Static β_{HRS} (10^3 a.u.) and DR values computed at the M06-2X/6-311G(d) and MP2/6-311G(d) levels, for the molecule in gas phase in the three geometries illustrated in Figure B.4a.

	Geometry 1		Geometry 2		Geometry 3	
	β_{HRS}	DR	β_{HRS}	DR	β_{HRS}	DR
TD-DFT; M06-2X/6-311G(d); gas phase	4126	4.7	3075	4.4	5159	4.7
FF-MP2/6-311G(d); gas phase	4373	4.9	2651	4.5	4902	4.9

Bibliography

- [1] Wu Y., Tepper H. L., , and Voth G. A. Flexible simple point-charge water model with improved liquid-state properties. *J. Chem. Phys.*, 124:024503, 2006.
- [2] Soper AA. K. *The Radial Distribution Functions of Water as Derived from Radiation Total Scattering Experiments: Is There Anything We Can Say for Sure?* International Scholarly Research Notices, Article ID 279463, 2013.
- [3] Fallahi F. and Mohammadi-Manesh H. Molecular dynamics simulations of carbon monoxide self-diffusion in the nanoporous of the Cu-BTC. *Procedia Materials Science*, 11:449, 2015.
- [4] Ramkumar D. H. S. and Kudchadker A. P. Mixture properties of the water + γ -butyrolactone + tetrahydrofuran system. *J. Chem. Eng. Data*, 34:459, 1989.
- [5] Donaldson S. H., Jahnke J. P., Messinger R. J., Östlund Å., Uhrig D., Israelachvili J. N., and Chmelka B. F. Correlated diffusivities, solubilities, and hydrophobic interactions in ternary polydimethylsiloxane–water–tetrahydrofuran mixtures. *Macromolecules*, 49:6910, 2016.
- [6] Comer J., Gumbart J. C., Hénin J., Lelièvre T., Pohorille A., and Chipot C. The adaptive biasing force method: Everything you always wanted to know but were afraid to ask. *J. Phys. Chem. B*, 119:1129, 2015.
- [7] González-Pinto M., Martínez-Ratón Y., Velasco E., and Varga S. Effect of shape biaxiality on the phase behavior of colloidal liquid-crystal monolayers. *Phys. Chem. Chem. Phys.*, 17:6389, 2015.
- [8] Subotnik J. E., Yeganeh S., Cave R. J., and Ratner M. A. Constructing diabatic states from adiabatic states: Extending generalized Mulliken–Hush to multiple charge centers with Boys localization. *J. Chem. Phys.*, 129:244101, 2008.
- [9] Shao Y. and al. Advances in molecular quantum chemistry contained in the Q-Chem 4 program package. *Mol. Phys.*, 113:184, 2015.
- [10] Hirata S. and Head-Gordon M. Time-dependent density functional theory within the Tamm-Dancoff approximation. *Chem. Phys. Lett.*, 314:291, 1999.